HAL
open science

Origin of seismicity related to a flooded abandoned coal mining district at Gardanne, Provence, France

Dalija Namjesnik

To cite this version:

Dalija Namjesnik. Origin of seismicity related to a flooded abandoned coal mining district at Gardanne, Provence, France. Earth Sciences. Université de Lorraine, 2021. English. NNT : 2021LORR0116 . tel-03367922

HAL Id: tel-03367922

https://hal.univ-lorraine.fr/tel-03367922v1

Submitted on 6 Oct 2021

HAL is a multi-disciplinary open access archive for the deposit and dissemination of scientific research documents, whether they are published or not. The documents may come from teaching and research institutions in France or abroad, or from public or private research centers.

L'archive ouverte pluridisciplinaire **HAL**, est destinée au dépôt et à la diffusion de documents scientifiques de niveau recherche, publiés ou non, émanant des établissements d'enseignement et de recherche français ou étrangers, des laboratoires publics ou privés.

UNIVERSITÉ DE LORRAINE

AVERTISSEMENT

Ce document est le fruit d'un long travail approuvé par le jury de soutenance et mis à disposition de l'ensemble de la communauté universitaire élargie.

Il est soumis à la propriété intellectuelle de l'auteur. Ceci implique une obligation de citation et de référencement lors de l'utilisation de ce document.

D'autre part, toute contrefaçon, plagiat, reproduction illicite encourt une poursuite pénale.

Contact : ddoc-theses-contact@univ-lorraine.fr

LIENS

Code de la Propriété Intellectuelle. articles L 122. 4
Code de la Propriété Intellectuelle. articles L 335.2- L 335.10
http://www.cfcopies.com/V2/leg/leg_droi.php
http://www.culture.gouv.fr/culture/infos-pratiques/droits/protection.htm

UNIVERSITÉ DE LORRAINE
Ecole Doctorale SIReNa - Sciences et Ingénierie des Ressources Naturelles
Laboratoire GeoRessources

Thèse

Présentée et soutenue publiquement pour l'obtention du titre de

DOCTEUR DE l'UNIVERSITE DE LORRAINE

En **Géosciences**

Par **Dalija NAMJESNIK**

Origin of seismicity related to a flooded abandoned coal mining district at Gardanne, Provence, France

Date de soutenance : 29. Juin 2021

Membres du jury :

Mme. Beata ORLECKA-SIKORA (Pr)	Institute of Geophysics, Polish Academy of Sciences, Poland	**Rapporteuse**
M. Heinz KONIETZKY (Pr)	Geotechnical Institute, Germany	**Rapporteur**
Mme. Gloria SENFAUTE (PhD)	EDF Lab Paris-Saclay, France	**Examinatrice**
Mme. Evelyne FOERSTER (PhD)	Commissariat à l'énergie atomique et aux énergies alternatives, France	**Examinatrice**
Mme. Alessia MAGGI (Pr)	Université de Strasbourg, France	**Examinatrice**
M. Pascal BERNARD (Pr)	Institut de Physique du Globe de Paris, France	**Invité**
Mme. Monique TERRIER (PhD)	Bureau de Recherches Géologiques et Minières, France	**Invité**
M. Yann GUNZBURGER (Pr)	GeoRessources, Université de Lorraine, France	**Directeur de thèse**
M. Jannes KINSCHER (PhD)	Institut National de l'Environnement Industriel et des Risques, France	**Co- directeur de thèse**

Acknowledgements

I am grateful that I was able to work within the Ineris team, in scientific collaboration with the BRGM, IPGP and University of Lorraine, on this very interesting project, which introduced me to the world of (post) mining and allowed me enrich my knowledge of seismicity. I am pleased to have had this opportunity to contribute to the better understanding of the problem of post-mining seismicity.

For this, I share my accomplishment with all the people with whom I had pleasure to work with and spend time with during the past 3,5 years.

I would like to thank Yann Gunzburger and Jannes Kinscher, it was a pleasure to work with you both and to have you as my director and co-director of the thesis. Yann, I appreciate your guidance, advice and encouragement. Working with you has allowed me to get the insight into the seismicity problem from the perspective of geomechanics, and I wish there was more time for me to invest and explore more this direction as well. Jannes, thank you for your continuous guidance, support and investment in my thesis work, for always being available for discussion and for answering my questions. I have learned a lot from you.

Special thanks to the jury members: Heinz Konietzky, Beata Orlecka-Sikora, Evelyne Foerster, Gloria Senfaute, Alessia Maggi, Pascal Bernard and Monique Terrier for your interest in this thesis work and great ideas for the continuation of the project. I have enjoyed our discussion. Unfortunately, circumstances did not allow us to gather in person, but hopefully, there will be other opportunities to meet. Pascal Bernard, thank you as well for your contribution and ideas during my PhD.

I wish to thank also to Anne Mangeney and Jean Schmittbuhl for their investment and advice as members of my Comité de suivi de thèse.

Many thanks to BRGM team, for your welcome during my visits to BRGM Orléans and UTAM-Sud, and especially to Pascal Dominique, Hideo Aochi and Jacques Morel for your support, investment and interest in this thesis work, and discussions and sharing knowledge about Gardanne mine. Pascal and Alison, it was great to join you in one of your visits to the seismic network in Provence.

Natalia Poiata, thank you for your welcome to IPGP and helping me with my first steps with the BTBB method, as well as for all further help, your availability and kind words.

Special thanks to the Ineris team. Emmanuelle Klein, thank you for your encouragement, support, and trust in my abilities, and for always being available for any questions. Isabelle Contrucci, you were the first to welcome me to Nancy, and it was great to share a trip to the EGU conference with you, thank you also for all your help. Francesca De Santis, it was nice sharing the office and part of the PhD journey with you, and thank you a lot for your welcome in Nancy. Thanks to all who have been part of this project in any other aspects, provided help or welcomed me to the team: Armand, Catherine, Roxanne, Alain, Marwan, Alice, Philippe, Mountaka, Virginie, Stella, Nicolas, Regis, Vincent,...

Big thanks to everyone in GeoRessources – equipe GOR: Marianne, Rasool, Marie, Agnes, Olivier, Laura, Delphine and others.

Thanks to all PhD students with whom I shared many moments: Ever – thanks for teaching me about Peruvian culture, Elio – for all the lunch breaks at Crous; also Jana, Mimi, Ottone, you were here already when I arrived and it was great sharing this PhD period with you; I hope we would still share some dinners together. Good luck to all the „new“ PhDs and post-docs as well: Emeline – you've become a close friend during confinement periods this past year, thanks for everything, Kamel – it was great sharing the office and cookies with you :D Emilio, Guillaume, Aurélien, Amelia - happy to have met you all, bonne continuation!

To my Croatian friends, for support and visiting me in Nancy - hvala: Tena, Josipa, Benjamin, Ivana, Marija, Jelena :) Many thanks to my international family of friends that I met here: Anna, Didi, Emeline, Hoan, Mahdi, YongHwi, Yujin, and many others - I am glad to have shared with you many great moments and experiences!

Special thanks at the end to my family from Croatia, for their help, encouragement, and support, vidimo se uskoro!! =)

Résumé élargi

Ces travaux de recherche s'inscrivent dans la problématique de la sismicité induite dans le contexte de l'après-mine. Ils portent en particulier sur le cas de l'ancien bassin houiller de Gardanne, en France, dont les travaux miniers ont été partiellement ennoyés après la fermeture de la mine au début des années 2000.

De nombreux pays dans le monde ont une longue tradition minière, dont la France, où plus de 4000 sites ont été exploités (Didier 2008). Lorsque les mines sont abandonnées, le pompage de l'eau souterraine est habituellement interrompu, ce qui permet à l'eau de remplir progressivement les vides résiduels. Une telle intrusion d'eau peut affecter la stabilité mécanique des ouvrages souterrains et conduire à des instabilités des terrains de recouvrement, avec l'apparition en surface d'affaissements ou d'effondrements de plus ou moins grande ampleur. Particulièrement observées dans les mines souterraines peu profondes, ces instabilités peuvent provoquer des dommages importants à la surface et mettre en péril la sécurité des populations. C'est ainsi que la stratégie de prévention des risques de mouvements de terrains à long terme, dans le contexte de l'après mine, a conduit en France à la mise en place de dispositifs de surveillance microsismique, capables de détecter l'occurrence de désordres au niveau de la couche exploitée et de suivre la progression des désordres dans le toit immédiat et dans le recouvrement.

***

Cette thèse porte sur l'étude de la sismicité enregistrée à la suite de l'ennoyage de l'ancien bassin houiller de Gardanne, en Provence. Situé entre les villes d'Aix-en-Provence et de Marseille, ce bassin minier a été exploité par différentes méthodes entre le 19ème et le 20ème siècles, à des profondeurs allant jusqu'à –1350 m NGF. Du temps de l'exploitation, la stabilité des ouvrages souterrains était déjà une préoccupation importante pour l'exploitant. A sa fermeture en 2003, des études sur leur stabilité à long terme ont conduit a identifié des zones à risque d'affaissement, à caractère cassant. Le bassin a été ennoyé progressivement d'Ouest en Est par réduction des pompages d'exhaure pour ramener la nappe de la cote - 1 100 m NGF à - 14 m NGF en 2010 et les zones à risque surveillées par un réseau microsismique permanent.

Le site de Gardanne pose aujourd'hui un problème de sismicité post-minière. En effet, depuis 2010, le bassin est périodiquement affecté par une activité sismique qui se localise hors des zones surveillées par le dispositif de surveillance microsismique. On note l'existence d'une zone particulièrement active (la zone dite de l'essaim de Fuveau) dans le secteur minier de Regagnas (et en partie celui de Gréasque) où des événements sismiques apparaissent périodiquement lors de périodes de « crises » (2012, 2014, 2016-2017), principalement sous la forme d'essaims de séismes. Les événements sismiques les plus importants enregistrés durant ces crises montrent des magnitudes proches de 2, qui ont été pour les plus forts ressentis localement par la population.

***

Cette activité sismique inattendue a conduit à l'installation temporaire d'un réseau sismologique de recherche par le BRGM-DPSM en 2013 dans ce secteur, complété en 2018 et 2019 par de nouvelles stations du BRGM-DPSM et de l'Ineris. Les études préliminaires, en majorité basées sur les analyses de la crise de 2014, estiment que l'activité sismique semble être déclenchée par les fluctuations saisonnières du niveau de la nappe dans les travaux miniers (Dominique 2015 ; Kinscher 2017 ; Matrullo et al., 2015). Sur cette base, les travaux miniers ont donc été assimilés à un aquifère « anthropique » avec des capacités de stockage importantes, notamment dans les zones comportant de nombreux vides miniers (celles exploitées par la méthode des chambres et piliers) où le système hydrogéologique naturel a été modifié significativement par l'exploitation minière.

L'analyse sismique des données de la crise sismique de 2014 dans les secteurs Gréasque et Regagnas a par ailleurs montré que les sources sismiques semblent être principalement situées sous les travaux miniers. Le mécanisme source indique des événements liés à un mécanisme de rupture le long de failles normales orientées NW-SE. La présence de plusieurs événements de type « multiplet » a également été constatée, ce qui indique l'activité de segments de failles qui pourraient soit rompre graduellement en quelques jours seulement, soit demeurer actifs pendant quelques années. Il est à noter que la présence de réseaux de failles est relativement bien documentée et que le bassin de Gardanne est classé comme zone d'aléa de sismicité naturelle modérée.

L'analyse des sources sismiques dans ce secteur de Fuveau Gréasque contredit donc a priori l'hypothèse d'une origine de la sismicité liée à des désordres (rupture de toit, pilier etc.) au niveau de la couche exploitée (par ex. Matrullo). Cependant, la modélisation numérique laisse ouverte la possibilité de la réactivation de failles dans les terrains de recouvrement, ainsi que la possibilité d'une subsidence modérée en surface, liée à la surcharge des ouvrages effondrés ou en cas d'écrasement résiduel des piliers effondrés (Didier, et al., 2003, Didier et al., 2004). C'est pourquoi deux hypothèses concernant l'origine de la sismicité ont été proposées, qui entraînent des conséquences différentes pour l'évaluation de l'aléa sismique post-minier :

Hypothèse N°1 : l'origine de la sismicité est liée à une déformation continue des ouvrages miniers et des terrains de recouvrement, qui peut entraîner des conséquences en surface et/ou une rupture de failles préexistantes. Dans ce cas, l'activité sismique est susceptible de s'arrêter lorsque l'effondrement de la mine finira par atteindre l'équilibre. La magnitude maximale M_{max} prévue des événements sismiques dépendra de la taille de la zone de la mine touchée par les effondrements.

Hypothèse N°2: l'origine de la sismicité est liée à la réactivation de failles plus profondes situées sous les ouvrages miniers. L'estimation de l'aléa est dans ce cas complètement différente de celle de la première hypothèse, tant en termes de persistance de la sismicité à long terme qu'en termes de magnitude maximale attendue, qui dans ce cas dépend de la taille du segment de faille actif.

***

La motivation de cette thèse reposait donc sur deux grandes questions :

- quelle est l'origine de la sismicité, en ce qui concerne 2 hypothèses proposées ?
- quels sont les mécanismes de déclenchement de la sismicité, en ce qui concerne la relation entre le contexte hydrologique et la sismicité?

La thèse a porté sur l'analyse des traces sismiques continues acquises par les stations temporaires à l'aplomb de la zone de l'essaim de Fuveau, mieux instrumentée à partir de 2013. Elle couvre plus particulièrement la période de 4 ans, allant de 2014 à 2017. Les données sismiques de la station la plus proche du réseau de surveillance permanent (à 2 km : station « Fuveau » de l'Ineris), ont également été utilisées sur la période 2010-2017.

En raison du grand volume de données disponibles mais non traitées, l'accent a d'abord été mis sur le développement et l'application de nouveaux outils de traitement pour la détection et la localisation des événements afin d'améliorer les techniques actuelles de surveillance et de traitement. Les procédures manuelles et chronophages habituelles de localisation ne sont plus réalisables, et l'automatisation du traitement était nécessaire. Les nouvelles méthodes de localisation basées sur la cohérence des formes d'ondes complètes présentent un grand avantage par rapport aux méthodes utilisées de manière standard, car elles ne nécessitent pas de pointé de phase manuel et sont donc adaptées au traitement automatique. En particulier, l'approche développée par Poiata et al. (2016), appelée Backtrack (BTBB), a été testée. Cependant, l'application de l'outil de traitement automatique aux données provenant d'un nombre limité de stations était difficile et nécessitait au préalable l'élaboration de nouvelles étapes de traitement, afin de réduire le nombre de faux déclenchements et d'évaluer la qualité de la localisation.

Ainsi, une nouvelle méthodologie de détection et de localisation des événements enregistrés par un réseau peu dense a été développée dans le cadre de cette thèse. Une nouvelle approche d'élimination du bruit a été élaborée pour surmonter les difficultés liées au nombre limité de stations. Un système de classification des événements fondé sur la qualité de la localisation a été mis au point pour permettre de distinguer les événements de grande qualité (magnitude plus élevé et/ou RSB plus élevé qui permettait une visibilité à au moins trois stations) des événements noyés dans le bruit, ce qui a mené à l'identification de clusters d'événements spatiaux.

Ce travail représente une première application de la méthode BTBB, initialement développée pour les réseaux sismiques denses à grande échelle, aux données continues enregistrées par un réseau de surveillance sismique clairsemé dans le cadre post-minier de la mine de Gardanne. Les résultats de l'analyse de quatre années de données sismiques continues montrent que la nouvelle méthodologie fournit une analyse solide du bruit et un nombre accru d'événements microsismiques détectés. Comparée aux résultats des catalogues du BRGM et de l'Ineris, la nouvelle méthodologie permet une plus grande précision de localisation, permettant une meilleure identification des structures sismiques actives. Le traitement est automatisé, ce qui a permis de traiter de grands volumes de données.

En conséquence, un catalogue sismique détaillé pour la période 2014-2017, basé sur les données du réseau de stations déployées à l'aplomb de la zone, permet un aperçu plus détaillé de l'activité sismique et de sa relation potentielle avec les variations du niveau d'eau dans la mine. De plus, l'approche

développée offre une solution pour automatiser la détection et la localisation dans le suivi microsismique opérationnel, en particulier, mais sans s'y limiter, dans les environnements post-miniers où des réseaux de surveillance temporaires clairsemés et constitués de géophones à une seule composante sont très souvent le seul outil disponible pour l'évaluation des dangers, et où des décisions de la plus haute importance, basées sur une localisation précise des événements sismiques, doivent être prise en temps opportun.

***

En outre, l'accent a été mis sur le regroupement des événements sismiques et l'exploration plus détaillée dans l'espace et dans le temps des phénomènes de type multiplets précédemment observés. L'objectif de l'analyse des multiplets et des clusters était d'identifier et de caractériser le mécanisme et les processus sous-jacents qui génèrent la sismicité. Pour l'analyse, les événements sismiques du nouveau catalogue de données sismiques de 2014 à 2017 sont principalement utilisés, complétés par les données et le catalogue sismique du réseau permanent pour obtenir des informations sur la période antérieure à 2014.

Plusieurs analyses de clusters et de multiplets/répéteurs ont été appliquées. D'une part, l'analyse des clusters a révélé la présence de six clusters principaux dans la zone de l'essaim de Fuveau. La plupart de ces clusters sont actifs depuis 2010 et montrent une activité de fond constante, avec des augmentations variables en nombre d'événement et magnitude temporaires pendant la crise principale. Les clusters centraux sont les plus actifs durant les périodes de crise de décembre 2014 et de fin 2016-début 2017, tandis que la dernière crise en août 2017 est marquée par l'activité particulière d'un cluster isolé, plus au Nord-Est.

D'autre part, l'analyse des multiplets à plus grande échelle (à l'aide de la station « Fuveau ») a montré que les familles de multiplets surviennent depuis le début de l'ennoyage du bassin central en 2010 et sont également situées au sud de la zone de l'essaim Fuveau. La plupart des multiplets sont cependant observés dans la zone de l'amas central de l'essaim de Fuveau. Les multiplets se produisent sous forme d'événements transitoires à court terme (semaines à mois), en partie suivant le modèle de la loi d'Omori, en particulier durant les crises microsismiques, mais aussi sous forme de séquences à long terme avec un taux de récurrence partiel périodique de l'ordre de la semaine et de mois, sur une période de plusieurs années.

Une analyse plus détaillée des multiplets du nouveau catalogue sismique d'événements 2014-2017 a confirmé ces observations. De plus, il est observé que la plupart des familles de multiplets se produisent au niveau du cluster central. Les familles de multiplets sont également observées dans le cluster le plus au nord, qui était principalement actif lors de la dernière crise en août 2017, mais, de manière intéressante, dans trois groupes sur six, presque aucune famille de multiplets n'est observée.

La discrimination entre les multiplets et les répéteurs a été étudiée par deux approches, qui ont toutes les deux montré la possibilité d'un chevauchement des sources, ce qui implique l'occurrence de répéteurs (c.-à-d., rupture répétitive d'une même aspérité sur une même faille). Cependant, en raison d'une forte incertitude dans la localisation absolue des événements (en raison du nombre limité de stations), il est malheureusement impossible de quantifier en détail le chevauchement des sources et la classification connexe de la famille de répéteurs/multiplets.

***

Comme le réseau temporaire dans la zone d'étude a été renforcé depuis 2018 et 2019, comprenant désormais treize stations au total, une étude supplémentaire a été réalisée par l'Ineris sur les données nouvellement enregistrées de 2019 pour mieux contraindre les mécanismes des sources sismiques et les profondeurs des sources des segments de failles identifiés. Les résultats de cette étude sont présentés et interprétés dans cette thèse, pour mieux comprendre l'origine de la sismicité locale observée et d'évaluer les deux principales hypothèses. L'analyse de la profondeur de la source et du mécanisme de la source indique constamment que les profondeurs de la source sont supérieures à celles des travaux miniers et sont liées au mécanisme de cisaillement, ce qui est plutôt conforme à l'hypothèse n°2.

Par ailleurs, les premières tentatives de modélisation numérique géomécanique réalisée par l'Ineris pour vérifier l'hypothèse n°2, ont permis de caractériser les conditions sous lesquelles la sismicité post-minière pourrait être liée à la réactivation de failles sous les travaux miniers, d'un point de vue géomécanique.

Les résultats de la thèse sont également en faveur de l'hypothèse n°2 : la nature répétitive de la sismicité, où chaque famille de multiplets identifiée indique un relâchement de contrainte répétitif sur la même structure géologique sismogène, avec le même mécanisme de rupture, ne semble pas être compatible avec un déclenchement de la sismicité engendrée par la dégradation des travaux miniers à la suite de l'ennoyage, qui montrerait plutôt une évolution spatiale progressive de la sismicité comme on le voit généralement dans les environnements souterrains en contexte d'effondrement (p. ex., Kinscher et al. 2015). L'activité sismique liée à l'effondrement minier présenterait des variations dans les mécanismes au fil du temps en raison de changements importants dans les conditions de propagation des ondes sismiques dans l'environnement, la signature sismique serait donc a priori dominée par les évolutions spatio-temporelles ainsi que par les formes d'ondes diverses et évolutives contrairement aux observations.

Les résultats combinés fournissent un ensemble important d'arguments pour évaluer les hypothèses sur l'origine des événements sismiques de l'essaim de Fuveau. En conclusion, toutes les indications sont en faveur de l'origine des sources sismiques sur des failles situées en-dessous de la mine, c'est-à-dire que l'hypothèse n°2 apparaît comme une conclusion plus valide pour expliquer l'origine de la sismicité. On peut donc supposer que les clusters d'événements sismiques correspondent à des failles activées ou à des segments de failles.

***

Même si le lien apparent entre la sismicité et les conditions hydrogéologiques a déjà été observé dans la zone étudiée de la mine, la relation entre l'activité sismique et l'hydrologie, ainsi que le mécanisme de déclenchement ne sont pas bien compris. Les observations précédentes démontrent et confirment que les changements du niveau d'eau dans la couche de la mine, liés aux précipitations et au taux de pompage, influent sur le taux sismique de l'essaim de Fuveau. Le déclenchement sismique des précipitations est un phénomène déjà observé dans quelques autres sites miniers, interprété comme déclenché par le processus de diffusion de la pression interstitielle (p. ex., Ogasawara et al., 2002).

Afin de mieux comprendre le lien entre la sismicité et le système hydrogéologique, les données hydrologiques disponibles sont comparées à celles du nouveau catalogue sismique (2014-2017). Les principales tendances visibles par rapport à chaque cluster sont discutées. Les crises sismiques de décembre 2014 et de fin 2016-début 2017 suivent les changements périodiques du niveau d'eau qui dépendent de la saison des pluies et du pompage. En particulier, la migration spatio-temporelle tend à être plus visible.

Les précipitations semblent représenter un facteur important dans le déclenchement et l'activation des failles. En revanche, la crise sismique d'août 2017 durant la période de sécheresse perturbe ce schéma, probablement affecté par l'augmentation du taux de pompage, qui a par conséquent abaissé le niveau d'eau dans les ouvrages miniers. Au cours de cette crise, le niveau de la nappe a atteint une valeur minimale depuis que le front d'ennoyage a atteint la zone d'étude, diminuant considérablement la pression interstitielle. Malheureusement, en raison du manque d'instruments piézométriques dans la zone d'étude, il n'est pas possible de quantifier le niveau d'eau exact, ni l'amplitude des changements de niveau d'eau. Par conséquent, l'ordre de grandeur de la pression interstitielle dans ces zones minières demeure inconnu.

***

Enfin, l'accent a été mis sur la caractérisation du mécanisme de déclenchement de la sismicité. Même si nous ne disposons pas d'informations précises sur la variation des niveaux d'eau, les questions concernant le mécanisme de déclenchement de la sismicité pendant la saison sèche et le mécanisme de déclenchement pendant la période des pluies sont discutées plus en détail. D'après les observations, de fortes indications montrent que la principale force motrice de tous les clusters (c.-à-d. les clusters n°1 à n°5), sauf pour la crise d'août 2017 (c.-à-d. le cluster n°6), est l'augmentation de la pression interstitielle. L'activité sismique de cette dernière crise semble être déclenchée par l'extraction importante de fluides de la couche minée. La plupart des familles de multiplets, et potentiellement des répéteurs, qui se produisent dans le cluster central et le cluster Nord sont probablement liés à la fois à un glissement lent de segments de failles et/ou aux cycles de chargement accélérés des failles sismogènes. Les clusters dans lesquels peu ou pas de familles multiplets sont observées semblent davantage dominés par des événements plus forts isolés M> 1. Les augmentations observées de l'activité sismique (cluster temporel) dans chacun de ces clusters représentent possiblement la redistribution des contraintes (relaxation) après le glissement de faille induit par la pression des pores sur des plans de faille voisins, comparable au schéma classique des répliques sismiques, sans aucun choc principal visible.

***

En conclusion, malgré les limites en termes de données disponibles (réseau sismique clairsemé et manque de mesures hydrologiques du niveau d'eau dans la couche de la mine dans le secteur sismiquement actif), une question à étudier en termes de risque sismique est la possibilité pour une structure de faille unique de produire des événements de M>3. En se basant sur les connaissances actuelles, cela ne semble pas être le cas puisque cela supposerait la présence d'un segment de faille >500m. L'activité sismique est plutôt présente sous la forme d'essaims de séismes, ce qui signifie que le relâchement de contraintes

(causé par l'augmentation de la pression de pore) se produit plutôt le long de plusieurs structures de petite taille au lieu de se produire lors d'un unique et large événement.

Malgré la compréhension générale du mécanisme affectant le déclenchement et le comportement répétitif ou post-choc des événements sismiques, des observations plus précises de la sismicité, des paramètres mécaniques et des déformations, des changements de niveau d'eau et des changements de pression des pores près des failles sont nécessaires pour améliorer la compréhension du mécanisme et de l'interconnexion entre ces facteurs. L'ampleur maximale de l'événement qui peut être déclenché est actuellement difficile à quantifier et à prédire, principalement en raison de ces limites. Néanmoins, la compréhension actuelle des processus qui sous-tendent le déclenchement d'événements sismiques a permis de tirer des conclusions générales.

Table of Contents

Acknowledgements i

Résumé élargi iii

Table of Contents x

Figures xiv

Tables xvii

Glossary xviii

PART I GENERAL INTRODUCTION: POST-MINING SEISMICITY AND GARDANNE MINE CASE STUDY .1

Introduction 3

1 State of the art regarding seismicity in post-mining conditions 5

1.1 Post mining hazards: ground failures and surface consequences 5

1.2 The role and challenges of microseismic monitoring in post-mining period 9

1.3 Seismicity in post-mining districts 10

2 Case study: Gardanne mine 19

2.1 A brief history of the mine and general context 19

2.2 Mining disorders, rockbursts, induced and natural seismicity 22

2.3 Groundwater management during mining period 22

2.4 Post-mining period 24

2.5 Post mining seismicity – the seismic swarm of Fuveau in Regagnas sector 27

2.6 Discussion on the origin on seismicity and seismic hazard 34

3 Thesis motivation and objectives 37

3.1 Motivation 37

3.2 Methodology and objectives 38

PART II IMPROVEMENT IN DETECTION AND LOCATION OF MICROSEISMICITY WITH A SPARSE NETWORK 41

Introduction 43

4 State of the art regarding detection and location of seismic events 45

4.1 Advantages of full-waveform and array coherency-based methods 45

4.2 Waveform-based detection and location methods: common basic principles 46

4.3 BackTrackBB (BTBB) method overview 48

5 New development for detection and location of events of sparse networks in the case of Gardanne 51
5.1 Testing BTBB parametrization and limitations 51
5.2 Step 1: Detection and first noise removal criteria using STA/LTA approach 55
5.3 Step 2: Location and second noise removal criteria using the amplitude-based approach 58
5.4 BTBB location 62
5.5 Local magnitude determination 63
5.6 Event classification and location quality assessment 64
6 Results – new catalogue of 2014-2017 70
6.1 Application of the new processing scheme to the 2014-2017 dataset 70
6.2 Classification scheme 71
6.3 $\boldsymbol{b}$ –value estimation and magnitude of completeness 73
7 Conclusion 75

PART III CLUSTER AND MULTIPLET ANALYSIS 77

Introduction 79
8 State of the art regarding clustering and multiplets 81
8.1 Clustering and underlying physical phenomena and mechanisms 81
8.2 Multiplets and repeaters 82
8.3 Repeat/Recurrence time 84
9 Spatial cluster analysis 85
9.1 K-means clustering method 85
9.2 Clustering of events of new catalogue 2014-2017 86
10 Multiplets and cluster activity 2010-2017 89
10.1 Cross-correlation technique 89
10.2 Identification of multiplet families using Fuveau station 90
10.3 The spatial resolution of multiplet analysis 91
10.4 Spatio-temporal distribution of multiplet families 92
10.5 Main multiplet families in the Fuveau swarm (study area) 94
10.6 Reconstruction of cluster activity before 2014 97
11 Detailed multiplet analysis 2014-2017 99
11.1 Multiplet families in new catalogue 2014-2017 99
11.2 Spatio temporal distribution of multiplets 101
12 Repeaters or multiplets? 105

12.1 Source parameters determination 105
12.2 First repeater identification method: seismic source overlap 106
12.3 Second repeater identification method: coherency analysis 108
13 Summary of main observations 112

PART IV SEISMICITY ORIGIN AND TRIGGERING MECHANISM 113

Introduction 115
14 Origin of seismicity 116
14.1 The repetitive long term seismic activity 116
14.2 Depth and source mechanism 117
14.3 Conclusion about source origin 122
15 Seismicity-hydrology connection 124
15.1 Influence of the rainfall on the seismicity triggering 124
15.2 Influence of the pumping on seismicity migration 125
15.3 Conclusion about the hydro-seismic connection 128
16 Mechanics behind triggering and clustering of earthquakes 129
16.1 Triggering mechanism of the seismic activity 130
16.2 The secondary, driving mechanism behind clustering and multiplet families' sequences 131
16.3 Interpretations of mechanism for each cluster 134
16.4 Conclusion about triggering 139

GENERAL CONCLUSION AND PERSPECTIVES 141

Summary and conclusions 143
Perspectives 148

BIBLIOGRAPHY 151

ANNEX PART I 167

Geological section 169
Seismic networks and used data 171

ANNEX PART II 173

Data preparation 175

BTBB principle 176
STA LTA method 181
New seismic data catalogue 2014-2017, 364 events of A class 186

ANNEX PART III 195

Fitting the model of K-means algorithm to data catalogue 2014-2017 197
Influence of station configuration changes on the location of events and apparent migration of seismicity 198
Finding the optimal value of the cross-correlation function 200
Corner frequency estimation for families 201

ANNEX PART IV 203

Source mechanism 205

RÉSUMÉ 211

ABSTRACT 213

Figures

Part I

Figure 1.1 Typical failures in abandoned underground mines. 6

Figure 1.2 Illustration of the Coulomb fracture criterion by means of a Mohr diagram 11

Figure 1.3 Schematic diagram of mechanisms for inducing earthquakes. 12

Figure 1.4 Elevation of water level (solid line) and depth of seismic event locations (diamonds) in the flooding area 14

Figure 1.5 Pressure history within the Lacq oil and gas fields. 17

Figure 1.6 Illustration of asperities as contacting surfaces or locked patches on a fault. 18

Figure 2.1 Geographical situation of Gardanne mining basin 19

Figure 2.2 Gardanne mine exploitation methods and position Grande mine layer in space 21

Figure 2.3 Localization of the main sources of water in mining works 24

Figure 2.4 Initially identified zones of high seismic risk 26

Figure 2.5. Flooded abandoned Gardanne mine with observed seismicity. 28

Figure 2.6 A Localizations of around 80 events of crisis 2014 29

Figure 2.7 Waveforms of the events of the three multiplet groups 30

Figure 2.8 Map with information of sector Regagnas (study area) 33

Figure 2.9 Illustration of the mechanical model of the chamber and pillar sector Regagnas. 34

Figure 2.10 Illustration of the two hypotheses 36

Part II

Figure 4.1 Scheme of waveform-based method processing. 47

Figure 4.2 The simplified sketch presenting a general theory of migration and stacking process for PWS methods 48

Figure 5.1 Example of the characteristic function of signal resulted in the first part of BTBB analysis. 52

Figure 5.2 Example of successful detection and location of the seismic event as a result of the application of BTBB 52

Figure 5.3 Challenges of discriminating between detected coherent noise and detected events when applying BTBB directly to continuous data 53

Figure 5.4 Scheme of detection and location methodology developed in this study.. 54

Figure 5.5 Example of step 1 processing 56

Figure 5.6 Setting threshold values in each frequency band for first noise removal criteria 57

Figure 5.7 Illustration of a grid of one station pair and potential sources in a 2D plane at a depth z. 60

Figure 5.8 Example of amplitude ratio-based location method applied to the two detections 61

Figure 5.9 Bi-modal distribution of misfit probability $\boldsymbol{P}(\boldsymbol{l})$ values between observed and theoretical amplitude ratios. 62

Figure 5.10 Comparison of locations determined in this study with 372 matching seismic event locations identified in BRGM catalogue during period of 2014-2015. 66

Figure 5.11 Identification of highest quality events. 67

Figure 5.12 Error distribution of BTBB locations of class A and class B events 68

Figure 5.13 Event classification scheme based on location quality evaluation 69

Figure 6.1 Temporal distribution of events in new catalogue 2014-2017. 71

Figure 6.2 New catalogue 2014-2017. 72

Figure 6.3 Gutenberg-Richter's b-value variability 73

Part III

Figure 8.1 Illustration of criteria to distinguish between the multiplets and repeater 83

Figure 9.1 K means basic principle 85

Figure 9.2 Results of cluster analysis of highest quality events of new catalogue 2014-2017. 87

Figure 9.3 Temporal distribution of seismic activity for A and B class events 88

Figure 10.1 Example of a doublet identified in a dataset of Fuveau 91

Figure 10.2 Frequency content of a microseismic event recorded on station Fuveau 92

Figure 10.3 Spatio-temporal distribution of 100 identified Fuveau multiplet families. 93

Figure 10.4 Location of events of 100 multiplet families in period 2010-2017. 94

Figure 10.5 Spatial distribution of events of Fuveau families in period 2014 -2017 95

Figure 10.6 Cumulative number of events of multiplet families 96

Figure 10.7 Spatio temporal distribution of reconstructed families 97

Figure 11.1 The correlation matrix with the final CC values. 99

Figure 11.2 An example of multiplet family 101

Figure 11.3 Location of events of main multiplet families with more than 3 events 102

Figure 11.4 Spatio temporal distribution of multiplet families 104

Figure 12.1 The estimates of a) means stress drop and b) source radii for multiplet families 106

Figure 12.2 Figure shows events of central clusters families and corresponding source radii, depending on three different assumed stress drops 107

Figure 12.3 Figure shows events of northern clusters families and corresponding source radii, depending on three different assumed stress drops. 108

Figure 12.4 Illustration of the principle of interevent coherence for evaluating the corner frequencies and defining the seismic repeater occurrences 110

Figure 12.5 Frequency-dependent cross-correlation of 21 family groups 111

Part IV

Figure 14.1 Fourteen strong events recorded during 2019/2020 117

Figure 14.2 Determined location of 14 events and location uncertainties 120

Figure 14.3 2D representation of radiation patter of P waves and its polarity observations on seismic records accordingly, for different mechanism 121

Figure 15.1 Temporal distribution of seismic activity for A and B class events. 125

Figure 15.2 Spatio-temporal distribution of seismicity within two periods. 127

Figure 16.1 Temporal distribution of seismic activity compared with water levels 129

Figure 16.2 Possible triggering mechanisms of seismic activity in the study area 130

Figure 16.3 Illustration of mine water extraction 131

Figure 16.4 Secondary, driving mechanism behind clustering and multiplet families' sequences. 132

Figure 16.5 Local pore pressure on a fault patch (asperity). 133

Figure 16.6 Seismicity and proposed mechanisms behind triggering and clustering/repetitive behaviour 134

Figure 16.7 Dissimilarity of strongest (M> 1) events of clusters 3. 138

Annex

Figure A1. 1 Geological section of mining basin 169

Figure A1. 2 Timeline of important events in the study area of Gardanne mine, and available data. 170

Figure A1. 3 Microseismic networks and piezometric measurements in Gardanne mine 171

Figure A2. 1 Illustration of an equal differential time (TDE) surface in a homogeneous velocity model 179

Figure A2. 2 Examples of imaging functions 180

Figure A2. 3 Logarithm of amplitude ratios without frequency-dependent terms 185

Figure A3. 1 Elbow method used to determine the optimal number of clusters (k). The procedure described in the text. 197

Figure A3. 2 Station configuration change during periods of three seismic crises and its influence on spatio-temporal migration. 199

Figure A3. 3 Finding optimal cross-correlation value. The number of multiplet groups and a total number of events depending on the $\boldsymbol{CC}$ value 200

Figure A3. 4 Corner frequency and moment magnitude estimation for 21 main families 202

Figure A4. 1 Dominance of negative P waves polarities on the waveforms of 14 events. 206

Figure A4. 2 Simulation of direction of first motion (or polarity) of P waves 207

Figure A4. 3 Theoretical and observed S/P waves ratio values. 208

Figure A4. 4 Results of focal mechanisms for the 14 high quality events of 2019, presented in the form of a beachball, as well as the 25 best solutions obtained by inversion (gray circles within the beachballs). 209

Tables

Table 1 All arguments pro- /con- listed for each hypothesis based on seismic data analysis..... 123
Table A2. 1 STA and LTA windows lengths..... 182
Table A2. 2 Seismic data catalogue 2014-2017. A class events 186

Glossary

Abbreviations	Description
Ineris	Institut national de l'environnement industriel et des risques, France
BRGM	Bureau de Recherches Géologiques et Minières, France
BTBB	BackTrackBB method
P	compressional wave
S	shear wave
SH	shear wave horizontally polarized
SV	shear wave vertically polarized
SNR	signal to noise ratio
SHS	strain-hardening/softenin model
PWS methods	partial waveform stacking methods
FWI methods	full-waveform inversion methods
TRI methods	time reverse imaging methods
WT methods	wavefront tomography methods
FWI methods	full waveform inversion methods
STA/LTA	the short-term average over the long-term average
CF	characteristic function
TDE	time-delay function estimate
RMS	root-mean-square error, root-mean-square value between the theoretical and observed time delay estimates
MaxStack	the maximum value of 3D likelihood source location
MBF	multiband filter
MAA	the maximum value of absolute STA/LTA CF amplitude
MRMS	the maximum value of root-mean-square STA/LTA CF
PDF / pdf	probability density function
CC	cross correlation
EDT	equal differential time
DC	double-couple

Symbols: quantitiy	[unit]	Description
M	-	Gutenberg-Richter magnitude
M_c	-	magnitude of completeness
M_L	-	local magnitude
M_w	-	moment magnitude
M_0	Nm	seismic moment

σ_n	MPa	applied normal stress
σ_V	MPa	vertical stress
σ_H	MPa	horizontal stress
p	MPa	pore pressure in the fault zone
v_P	ms^{-1}	P-wave velocity
v_S	ms^{-1}	S-wave velocity
f	Hz	frequency
f_c	Hz	corner frequency
λ	m	wavelength
$\Delta\sigma$	MPa	stress drop
δ	°	fault dip
ψ	°	friction angle
MASL	m	meters above sea level
MBSL	m	meters below sea level
NGF	m	nivellement général de la France / general leveling of France
r_0	m	source radii
τ	MPa	shear stress required for failure
μ	-	coefficient of internal friction

PART I
General introduction: post-mining seismicity and Gardanne mine case study

Introduction

Many countries worldwide have had long mining traditions, including France, where over 4000 sites were mined (Didier *et al.* 2008). While mining progresses from one area to another, there also is a rapid increase of the number of abandoned mines. Return experience of many post-mining sites has revealed that mines may pose significant environmental problems, potentially severe and long-lasting, in the period after closure. Nowadays the wide range of potential post-mining consequences is generally known, but their manifestations are very specific to each site. Apart from the underground water flow circulation changes, underground water contamination, emission or discharge of potentially dangerous chemicals or toxic gases into the environment or health hazard from the dust of old waste disposal sites (Van Zyl *et al.* 2002, Didier *et al.* 2008), socio-environmental problems related to ground stability that are often observed can affect public safety and the sustainable development of post-mining regions.

When mines are abandoned, groundwater pumping is usually stopped, allowing the water to progressively fill the residual voids. Such water intrusion may affect the mechanical stability of the underground structures and perturb the local state of stress, which may lead to different forms of mining collapses. Especially observed in shallow underground mines, such collapses can provoke significant damage at the surface, involving sinkhole formations and rapid or slow ground subsidence. The geomechanical trigger and conditions generating these events and the implied hazard have been massively examined in several case studies. The Lorraine region in France has been particularly affected in the 90's by such phenomena (Didier *et al.* 2009). Based on this return of experience, several regulation guidelines, as well as risk management and assessment techniques, have been devised in recent years, establishing the procedure for the proper abandonment and flooding of the underground mines.

A poorly known hazard in flooded post-mining districts, non-considered in most post-mine risk procedures, is related to dynamic ground motions (shaking, vibrations) generated by seismic waves emitted from induced seismic sources. Compared to major natural events (that may reach a magnitude of M>6), seismic events in these environments are expected to be of smaller magnitude (typically M<4) but their impact on the surface may be more intense, mainly due to their comparatively shallow source depth. Such events may generally accompany the underground collapses itself and/or result from the reactivation of pre-existing fault structures next to the mining district (A. Miller *et al.* 1988, Wetmiller *et al.* 1993, Ogasawara *et al.* 2002, Senfaute *et al.* 2008, Goldbach 2009a). Nonetheless, seismic hazard assessment of these events remains very challenging, as triggering depends on many complexly interacting factors, such as the local geological setting, the mine geometry, its long-term mechanical alteration, the presence of pre-existing fault structures and in-situ stress state and very importantly the hydrological (flooding) condition being controlled by anthropogenic pumping regime and meteorological factors.

To gain experience in this respect, this thesis focuses on the case study of a flooded coal mine at Gardanne in the Provence region, South France, which was abandoned in 2007, and has been continuously affected by significant seismic activity during the last decade. The strongest seismic events reached magnitudes close to 2 and have been several times felt by the close living population, raising concern in terms of local seismic hazard assessment. The seismic events reoccur periodically, mainly in form of seismic swarms

which seem to be linked to the flooding level in the undermined areas which corresponds to the seasonal meteorological changes. Previous investigations have shown that most of these events seem to be related to the reactivation of a network of pre-existing fault structures located below the mine. Considering the fact that the Gardanne region is known to be tectonically active (M 4 events in the past), it seems of fundamental importance to examine and understand the local natural and post-mining seismic risk and how to determine it in the abandoned flooded mining conditions.

In Part 1 of this thesis, the reader is first reminded briefly of the main factors as well as mechanisms governing ground and surface failures in post-mining environments, as well as the role of seismic monitoring (objective, design, challenges) in this context. The mechanisms related to induced seismicity known in other post-mining sites and other relevant case-study related to anthropogenic/induced seismicity are then further introduced. The Gardanne site as a case study of this thesis is introduced in the following Chapter 2 proceeding the motivation, objectives, strategy and structure of the thesis presented in Chapter 3.

1 State of the art regarding seismicity in post-mining conditions

1.1 Post mining hazards: ground failures and surface consequences

In former underground mine districts, prior mining activity caused irreversible effects on the rock mass equilibrium. Hence, the stability of the ground, and surface and subsurface infrastructure can be affected by different forms of mine collapses and the risk of ground instability remains long after the mine closure.

To consider the potential impacts of underground mining on overlying structures in the study area of this thesis, the next sections describe surface and subsurface phenomena that can occur in the post-mining period, factors governing them as well as the causes and the mechanisms behind them.

1.1.1 Factors that affect rock mass stability in post-mining conditions

The nature of potential disturbances which can be expected during the post-mining period are related to several factors known to affect stability and govern underground and surface deformation and their specific configurations.

Particularly, the mining method has a strong impact on underground and surface deformation. In terms of expected failures around mining works, mining methods are typically classified in two categories: complete extraction methods, ensuring integral exploitation of the ore (i.e. longwall, sublevel stoping with backfilling...), and partial extraction methods, allowing the persistence of ore pillars after closure (i.e. abandoned room and pillar, dissolution cavities). Each technique can affect the surrounding rock in a different way. It has been observed that long-term impact on the ground surface is generally more significant in partial extraction mines with residual pillars leftover after mine closure than in complete extraction mines such as longwall, provided their voids are treated after extraction, for example with backfilling. This is especially the case for the room-and-pillar method, which is considered to be potentially the riskiest, from the perspective of long-term consequences (Schuchová & Lenart 2020). Impact of mining technique on the surrounding rock is governed by a combination of factors such as cavity geometry (e.g. height to width ratio of room, e.g., Bell & Genske 2001), the total volume of extracted material and/or pillar layout (F.T. Lee and F. Abel Jr. 1983, Didier *et al.* 2008). Over time, pillars may be affected by deterioration and weakening. For example, environmental factors such as flooding of mining works can induce degradation of mechanical properties of rock material (e.g., rock strength, rock stiffness) (Y. Yu *et al.* 2018). Furthermore, the stability of pillars depends considerably on their design (size and shape), which is based on the nature of the extracted material and its depth (Karfakis 1993). Decreased stability of pillars that are left underground to support the overburden impacts considerably the stability of the entire mine. Depth on mining excavation may represent a significant factor of impact on surface and subsurface deformation as well, especially in room-and-pillar mines (F.T. Lee and F. Abel Jr. 1983). The greater the depth of extraction, the longer it takes for rock deformation to reach the surface, which means that the shallower coal mines experience surface deformation earlier than deeper mines.

Therefore, old abandoned coal mines exploited by rooms and pillars often present a potential hazard as pillars collapse or voids migration to the surface, especially for mines at shallow depth.

The next section provides a description of typical failures such as subsidence or mining collapse of underground structures which can be expected in abandoned mines, with particular focus on mines exploited by the technique of rooms and pillars

1.1.2 Typical failures modes of abandoned underground mines

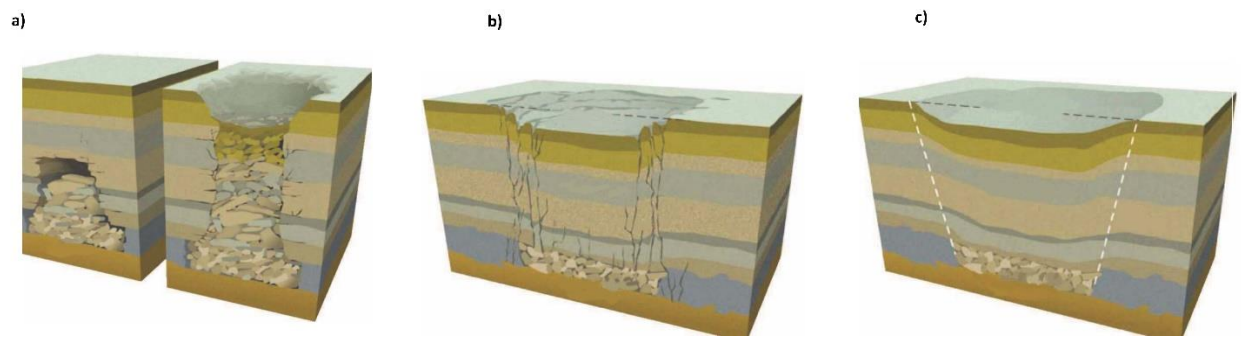

Figure 1.1 Typical failures in abandoned underground mines. a) localized collapse - sinkhole, b) generalized collapse c) progressive subsidence. Adapted from Salmon *et al.* (2019)

Localized collapse

A localized collapse (Figure 1.1a) is characterized by the sudden appearance of a collapsing crater at the surface. The horizontal extension of this phenomena generally varies between a few meters to a few tens of meters in diameter, while the crater depth depends mainly on the depth and dimensions of mine voids at its origin. The dimensions of the disorder and the brutality of its manifestation on the surface makes it potentially dangerous if it appears in the proximity of urbanized areas.

Depending on the initiating mechanism of the disorder they may take the forms of:

- **Sinkhole**

  It refers to disorder created by the rupture of the roof of a gallery and the gradual ascent of a chimney that reaches the surface, following an initial cave-in within an underground excavation (i.e room), Appearance or this disorder is very frequent and observed in shallow mining works up to 50 m of depth;

- **Rupture of the isolated pillar (s)**

  It refers to the collapse of one (or a few) pillar (s) that can lead to a collapse at the surface when the depth of the work and the thickness and stiffness of the overburden are up to 50 m.

Generalized collapse

Generalized collapses (Figure 1.1b), are manifested by the rupture, often dynamic (within a few seconds), of all or part of the underground mining works, thus affecting the stability of surface terrain. It can extend over areas up to several hectares. The depth of collapsed surface affecting the central part can reach several meters, or even several tens of meters in the case of a cavity collapse of saline dissolution (Franck *et al.* 2019). This is a rare phenomenon with consequences potentially very damaging to people and properties located on the surface. They may also be accompanied by earthquakes and blast effects which can project the materials through galleries and open wells to great distances. The main mechanisms or initiating scenarios are following:

- **The abrupt collapse of abandoned pillars resulting from a ruptured roof**

In underground mines with high extraction rates, large voids, undersized pillars or multi-level operations, where overburden consists of one (or more) stiff horizon(s) that may break suddenly. This creates a sudden overload on the pillars which break simultaneously. It is characterized by a sudden rupture of the overburden, in only a few seconds.

- **Cascade-like failure of pillars**

Pillars of an underground mine having reached the limit strength, affected by modification or development of a trigger. Overburden collapses following the underground cave-in front. It is a less brutal phenomenon than the previous one (a few minutes to a few hours), but potentially remains dangerous and can endanger the safety of people. Pillars of an underground mine having reached the limit strength, affected by modification or development of a trigger.

Both of these phenomena can be initiated several years or decades after the closure of a mine. The required configurations cause this phenomenon to be rather rare.

Subsidence

- **Progressive subsidence**

Progressive or continuous subsidence (Figure 1.1c) refers to the collapse of underground cavities that manifests itself on the surface with a “bowl-shaped” topographical depression without major failure, and it is characterized by a usually slow (progressively over several days or months, or even years), smooth and flexible readjustment of the surface.

Predisposition for this type of event concerns large-scale exploitations carried out at depths of several hundred meters and with significant horizontal extensions as well as a significant amount of residuals voids left after extraction. In the case of partial-exploitation type of mines (but not limited to), the main mechanism is described as delayed rupture of one or more supporting elements of the underground mining works (pillars, interlayers, roof, wall). The magnitude of phenomena is directly proportional to the opening of underground works, depending in particular on the depth of the work and the nature of methods of operation and treatment of voids (caving-in, backfilling, etc.). In the majority of cases, the

maximum deflection observed at the centre of the “bowl”, during or after an operation, are decimetric to metric. Surface infrastructures are not so much affected by vertical movements but rather by the deformations of the ground (horizontal differential displacements, flexions, toppling…). The effects on the surface are weaker as exploitation is deeper. The effect on the surface can extend to larger areas than for mining works collapses. This phenomenon can be initiated several years or decades after the closure of the mine and is observed very often, depending on the size of the opening of the underground mining works, the exploitation technique, the extraction rate, the depth and the width of the exploited layer, the nature of overburden, the dip of layers, the surface topography, presence of faults, etc.

- **Brittle subsidence**

Brittle or discontinuous subsidence refers to a phenomenon that requires the following conditions: partially exploited mining works (by rooms and pillars in particular) located at depths of a few hundred meters, the existence of significant residual voids in the mining works and overburden mostly rigid and brittle throughout. It involves roof failure due to shearing along the support pillars of certain partial exploitations in very specific conditions. The pillars collapse due to overloading, followed by movement of the roof as well as the entire overburden all the way to the surface.

Characteristics of the brittle subsidence which differ from progressive subsidence include the possible development of a network of crevices along the periphery of the concerned panel, which can present structural risks for buildings located within the subsidence zone and promote much faster kinetics of the phenomenon.

Although the beginning of disorder underground generally lasts several days (fracturing and crushing of the pillars, preliminary fracturing of the roof), the manifestation on the surface can be sudden (rupture of a fragile roof) and accompanied by one or more seismic tremors.

1.2 The role and challenges of microseismic monitoring in post-mining period

As described in the previous Chapter, managing the abandoned mining sites often involves mitigation of the long-term risk of potential ground movements and instabilities.

As the mining works in post-mining period are often inaccessible due to flooding or bad conditions, surveillance of potential disorders is no longer possible with standard deformation measurements or seismic monitoring installed within the mine works (as is the case in active mining). Therefore, seismic monitoring devices are installed on the surface or in the sub-surface (Bennani *et al.* 2003). Even though microseismic monitoring has been used as a tool in active mining sites for almost a century, one of the first tests to adapt it to abandoned mining sites with risk of ground failures was done in the Lorraine iron basin by Ineris (Bennani *et al.* 2003 and references within).

Since then, microseismic monitoring plays an important role in post-mining risk mitigation. Nowadays, real-time microseismic monitoring is often applied to highly hazardous zones where remediation is not possible and risk cannot be reduced forever with other options such as backfilling due to its high cost (Couffin *et al.* 2003, Contrucci *et al.* 2008, 2011, 2019, Didier *et al.* 2008). In these cases, monitoring is used for the detection of precursory seismic events, e.g., failure initiation in rocks and expected ground instabilities. Additionally, seismic monitoring is one of the key tools in surveying the long-term hazard evolution in post-mining environments, which depends on several complexly interrelated factors (e.g., evolving meteorological and climatic conditions, mechanical degradation of the mine workings) that are difficult to take into account in geomechanical forecast approaches.

However, reliable hazard assessment and mapping often face challenges as mining areas can be large, which makes it difficult or in some cases impossible to forecast the location of potential failures, especially above older mines for which even the mine layout is not precisely known anymore (e.g., in Lorraine region in France, Bennani *et al.* 2003, Contrucci *et al.* 2019). For this reason, the determination of zones that should be prioritized for seismic monitoring can be difficult.

For economic reasons, seismic networks are generally rather sparse and very often consist of only a single antenna, such as borehole sensors, positioned at a place identified as having the highest risk. These single station networks do not have high performance in terms of seismic event location accuracy and are clearly focused on event detection. When seismicity appears in any part of these large mining areas, complementary temporal mobile seismic monitoring networks (such as surface stations) may be installed to improve location accuracy and better understand the origin of seismic sources. Due to the generally limited station number, the implementation of automatic processing routines (e.g., event location and classification) remains challenging. Locating of events is therefore mostly done manually, which requires longer processing time at the cost of real-time monitoring capacity.

Apart from a well-designed monitoring network setup, the performance of its data processing system makes another important difference, as mislocated events may lead to severe interpretation problems and communication of results toward the public.

In the case of seismic monitoring networks of limited station coverage, especially the ones composed of one-component geophones, an automatic detection and location method would lead to improvement of

the detection performance of weak seismic signals, more accurate locations, magnitudes, and source parameters. This would be of great value especially in emergency situations where real-time operational monitoring is required.

1.3 Seismicity in post-mining districts

Earthquakes were for the first time associated with human activity in 1894 in Johannesburg (McDonald 1982) and were attributed to the Witwatersrand gold production mining production processes (Simpson 1986, McGarr *et al.* 2002 and references therein). Ever since, seismicity resulting from human activity (i.e., anthropogenic seismic activity) has been monitored and observed in numerous other mining settings, as well as in many other industrial operations.

As opposed to natural earthquakes, these anthropogenic earthquakes are referred to as induced or triggered. Mcgarr (1991) and Mcgarr & Simpson (1997) define seismic events as “induced” if they are resulting from an activity that causes a stress change that is comparable in magnitude to the ambient shear stress acting on a fault to cause a slip, whereas the term "triggered" is used if the stress change is only a small fraction of the ambient level. However, due to variety of different types of human activity which is connected to seismicity, there is a broad range of possible mechanism of earthquakes. In mining environments, seismic events may result from mining operations, and are generally recognized depending on the responsible mechanism as (Gibowicz 1990):

I) induced, if they are related to redistribution of stresses in the proximity of created voids in the rockmass, often in form of the creation of fractures, rupture of pillars, roof falls or rock mass failure.

II) triggered, if they are related to the reactivation of critically stressed preexisting faults. The stress perturbations, although often quite small, frequently result in the generation of seismicity because near-failure conditions are common in both active and stable tectonic environments (Gibowicz & Lasocki 2002)

In post-mining environments, seismicity and its governing mechanisms are generally seen to be similar to those observed in active mining regions. However, there are two main differences compared to active mining:

I) induced seismicity in post-mining cases does not result from active excavation, but rather from the degradation of abandoned mine workings (e. g. weakening of mechanical properties of rock) leading to failures (as described in previous section 1.1), often accompanied by significant seismic activity. Seismic activity in flooded post-mining has been also linked to the partial underground collapses, fluid-induced redistribution of the environmental stresses, and the reactivation of pre-existing fault structures next to the mining district of the mining environment (A. Miller *et al.* 1988, 1989, Wetmiller *et al.* 1993, Ogasawara *et al.* 2002, Goldbach 2009a, Kinscher *et al.* 2015).

II) apart from accelerating the degradation or remobilization of mine workings leading to seismicity described under I), flooding of the mines can lead to perturbation in the stress state and pore pressure in rocks and hence lead to fluid-triggering of seismic events in preexisting fault zones, joints or

geological interfaces in the proximity of mining area or initiate aseismic slip. In general, fluids are known to play an important role in triggering local earthquakes and reactivating faults, and many examples of either natural or man-made triggering exist (e.g., Mcgarr & Simpson 1997, Saar & Manga 2003, Costain & Bollinger 2010, Foulger *et al.* 2018).

Triggering of the earthquakes at geological discontinuities is most commonly explained by the application of the Mohr-Coulomb theory of shear failure. The basic principles of this theory are well understood: increase of the pore fluid pressure reduces the effective normal stress and thus can bring the fault to failure and start the nucleation of an earthquake. Earthquakes then release stored elastic strain energy during slip on geological faults. The shear stress required for failure τ is defined as:

$$\tau = \tau_0 + \mu(\sigma_n - p) \qquad 1.1$$

where μ represents the coefficient of friction, σ_n the applied normal stress and p the pore pressure in the fault zone. The Mohr-Coulomb failure criterion is commonly represented by the linear envelope that is on a plot of the shear strength of a material versus the applied normal stress (Figure 1.2)

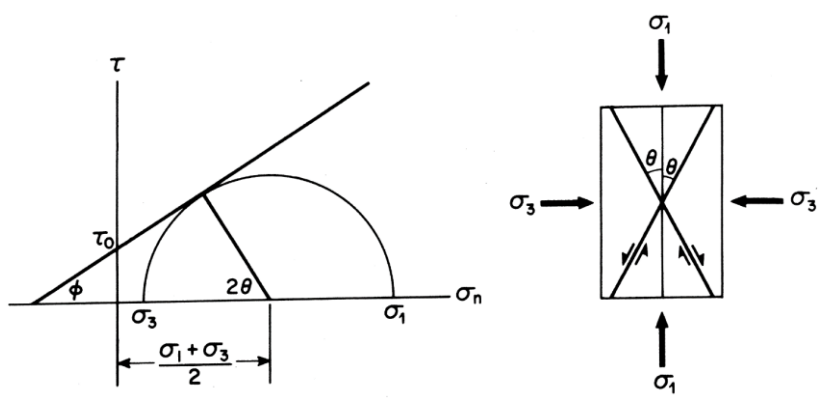

Figure 1.2 Illustration of the Coulomb fracture criterion by means of a Mohr diagram (left). On the right is shown the angular relationship between fracture planes and the principal stresses. From Scholz (2002a)

A large number of studies have shown that many different triggering mechanisms and factors can influence the nucleation of earthquakes (e.g., Figure 1.3). For example, faults can be brought closer to failure by the loss or gain of overlying mass, the introduction of fluid into a fault zone which changes the pore pressures in rock, or the imposition of vertical and/or horizontal stress by other means, e.g., stress transfer from nearby earthquakes (e.g., Mcgarr & Simpson 1997, McGarr *et al.* 2002, Foulger *et al.* 2018).

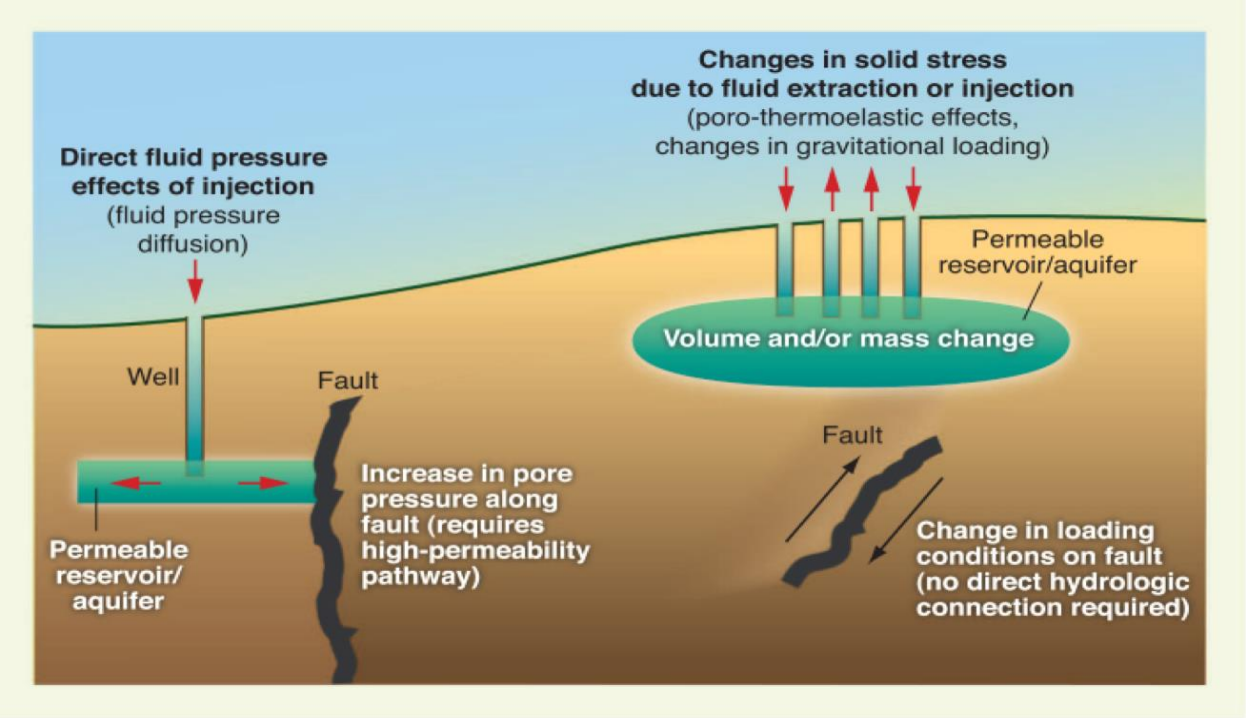

Figure 1.3 Schematic diagram of mechanisms for inducing earthquakes. Earthquakes can be induced by increasing the pore pressure acting on the faults (left) or by changing the shear and normal stress acting on the fault (right). From Ellsworth (2013).

The next sections provide insight into several case studies of abandoned mines where seismicity has been observed in different settings and due to different inducing/triggering mechanisms.

1.3.1 Seismicity associated with failures related to mining

Collapsing related seismicity was observed in the abandoned mine in Salsigne in France in 2011, where a seismic event of magnitude 2.5 was recorded (Dominique *et al.* 2012). Al Heib (2012) suggested that the weakness of the mine working played a role in triggering seismicity during the flooding, and the origin of the event was attributed to the rupture of several underground pillars, as a consequence of fault reactivations located at the mining site .

During a flooding experiment of an abandoned underground iron mine in Lorraine, significant microseismic activity (134 events, magnitude < 0) was recorded (Senfaute *et al.* 2008). The correlation between the water level and the seismic activity indicated that seismic activity has been triggered by the effective stress modification induced by the water filling the cavity. Two kinds of seismic events have been observed: a) seismic events regrouped in multiplet families which were triggered by an elastic response to the cavity loading affecting directly the sectors with pre-existing fractures; b) seismic events which are not regrouped in multiplets and probably result from complex interactions between an elastic stress increase, the cumulative effects of increased pore pressure and the initial stress field.

In a high-risk area of an old abandoned flooded underground mine in Queensland, Australia (Shen *et al.* 2017), microseismic monitoring was set up following the observed subsidence. The increased seismic

activity lasted 3 years following the subsidence. Afterwards, the number drastically dropped which was interpreted as the reach of mechanical equilibrium.

The collapse in Teutschenthal potash mine, Germany, in 1996 involved failure of 700 long pillars over an area of 2.5 km^2 and collapse of 620 to 770 m of overburden in approximately 2 seconds with consequences of the 4.8 magnitude seismic event and 0.5 m of surface subsidence (Whyatt & Varley 2008). Further seismic analysis showed the detection of negative first onsets of P-phase waves at all azimuths. The source radiation pattern showed significant non-double couple components. Both of these observations are consistent with implosive source, pillar bursts and a vertical closure of the mining cavities (Cesca *et al.* 2012).

At Cerville - Buissoncourt site in Lorraine region in France, mined with solution mining technique, the microseismic analysis revealed local caving and collapsing mechanisms linked to pre-existing fault structures. Locations of significant microseismic activity, recorded days before the final surface collapse, were widely related to cavity roof deformation processes, while major roof collapses were controlled by the reactivation of pre-existing structures and characterized by distinct spatio-temporal epicentre migration trends, which highlighted progressive cavity roof failures and dynamic propagations of mechanical instabilities. It was concluded that the creation of the cavity structure significantly reduced the vertical stresses in the overburden what lead to thrust faulting on the preexisting structures (Kinscher *et al.* 2015, 2016).

❖❖❖

In general, the number of research studies on seismicity in the post-mining environment available from literature is very limited, especially compared to research of seismicity in active mining, or research covering other cases of anthropogenically induced seismicity.

This may be related to the fact that mine abandonment and flooding has only intensified in the last 10 to 20 years. Another thing to take into consideration for the possible lack of post-mining seismicity case studies is the lack of recorded seismic events in monitoring sites. Consequently, the mechanism of induced/triggered seismicity in flooded abandoned mines is not very well understood.

Case histories of induced and triggered seismicity presented here provide evidence that post-mining induced seismicity can be associated with a wide range of potential mechanisms.

One of the main findings is the possibility of the interplay between fluid pore pressure and aseismic fault slip which can lead to dynamic ruptures along seismic asperities (evident by the occurrence of repeaters) and result in major seismic events (e.g., Cornet 2016).

The results raise thus questions about the performance of seismic monitoring as a tool for proper risk assessment.

1.3.2 Increase in pore pressure leading to fault reactivation

Fluid-related trigger mechanisms following the flooding in abandoned mines were evident in several examples.

In one of the deep mines of South Africa, seismicity was monitored over 5 years during flooding (Goldbach 2009b). The major seismic activity started appearing in the year 2000, with a delay of 14 months after flooding started (Figure 1.4). The largest seismic event that was recorded in the flooding area was magnitude 3.3. The strong correlation between the rising of water level and seismicity provided evidence that events are fluid-induced, and authors suggested that seismic activity was related to the reactivation of faults due to pore pressure increase in fault interfaces.

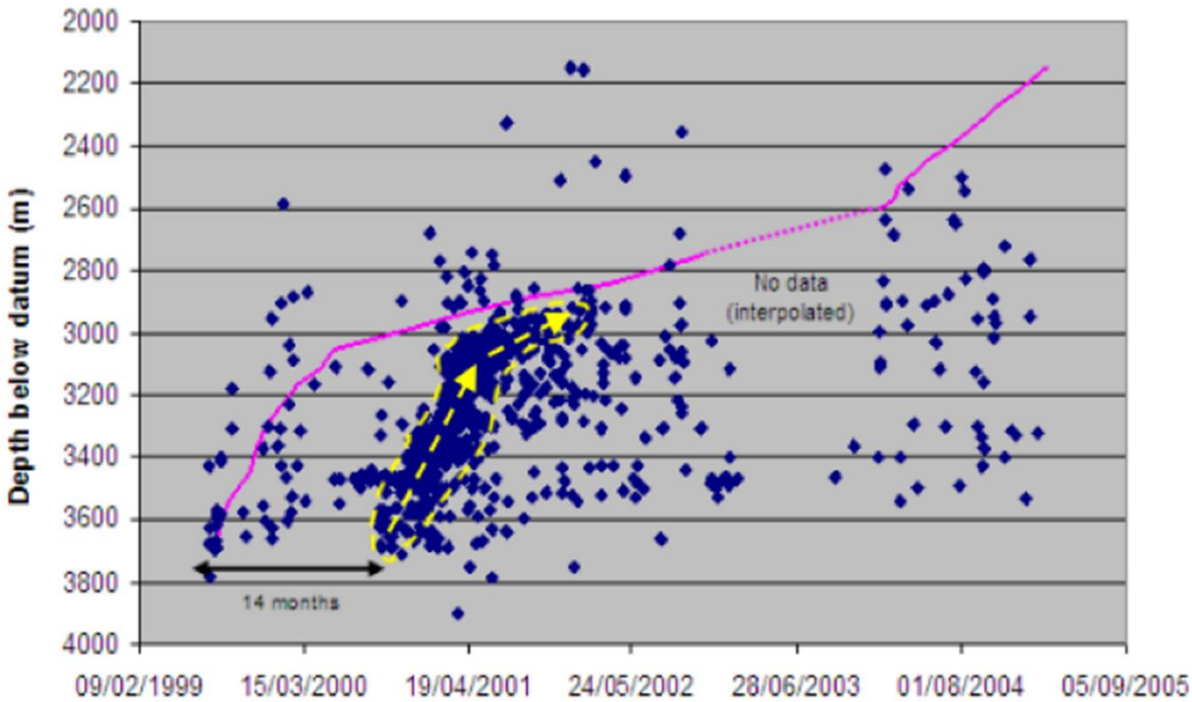

Figure 1.4 Elevation of water level (solid line) and depth of seismic event locations (diamonds) in the flooding area. Note the upwards migration of a cluster of seismic events (dashed line) between September 2000 and February 2002. From Goldbach (2009a)

In the Schlema-Alberoda uranium mine (Schütz & Konietzky 2016), the controlled flooding process which lasted 22 years after mine closure, was continuously monitored with a seismic network. Observed seismic events during this period were localized mainly below the mining site, connected to existing faults in the granitic rock formation. The maximum local magnitude of events was $M_L = 1.8$. Authors presented clear relation between triggered seismicity and the flooding process.

Triggering of earthquakes due to changes in the hydrological cycle such as seasonal groundwater recharges and precipitation has also been observed, in both natural and anthropogenic environments (e.g.,

Saar & Manga 2003, Hainzl *et al.* 2006) where it was demonstrated that faults can be very close to failure so that even tiny pressure variations associated with precipitation can trigger earthquakes at depths of few kilometres.

In the post-mining environment, such examples are scarce, however, an example of rainfall-induced seismicity comes from the flooded Ikuno mine in Japan, a vertical ore vein that extends to a depth of 1km (Ogasawara *et al.* 2002), where authors observed a relationship between the seismicity and heavy rainfall. Monitoring over 5 years showed that the highest seismic activities occur in two different areas. The first one was the area where 2 faults offset the ore veins, while the second one was near or along the faults substantially deeper than the excavated veins. Seismicity was linked to water level elevation. Water was drained by pumps in the case it reached a relatively high level. Larger events were associated with heavy rainfall that caused rapid elevation of the water level, although observed with significant delay. Maximum magnitude events were M=0. Authors suggested to regard the water system that floods the ore veins as a huge reservoir, with input from rainfall and output by pumping. Generally, delay of seismicity is observed from the onset of heavy rainfall, however, seismicity continues to be high when significant water level changes stop. The observed response of the system was faster for shallower hypocenters. The seismicity triggering mechanism was therefore interpreted as a diffusion process rather than the elastic response of the ground due to the water load.

1.3.3 Examples from non-mining settings: reservoir loading and depletion

In order to allow a better understanding of the mechanism of the seismic activity observed at Gardanne mine, several case studies of anthropogenic seismicity from reservoir induced seismicity are explored in the following sections, which could potentially be equivalent in terms of seismicity triggering mechanism of post-mining seismicity in Gardanne.

Flooding of mining voids can be regarded as a filling of an underground water reservoir. In general, the earthquake triggering mechanism by large reservoirs is more complex than most other types of triggered seismicity, with two different potential responses: either a rapid response related to instantaneous elastic response of the rock mass or a delayed response related to fluid diffusion (Simons *et al.* 1988). The fault zones on which the triggered activity occurs is in some cases remote or isolated from the reservoir.

Studies have shown that withdrawal (extraction) of large volumes of fluid or gas from a reservoir or creation of void space in a mine may modify the state of stress sufficiently to trigger seismic activity as well. It has been widely observed that even a produced small stress changes in the order of 0.01 MPa due to volume changes (e.g. changes in the water level) can be sufficient to reactivate fault segments (McGarr *et al.* 2002).

Potential mechanisms that may play a role in seismicity triggering may be related to poroelastic stressing, i.e. mechanism associated with volumetric contraction of the reservoir rocks responsible for induced seismicity associated with fluid extraction, that has been observed in the case of anthropogenic water reservoirs and exploited gas fields (Simons 1986, McGarr 1991).

Pore pressure decrease in case of fluid extraction from a reservoir can reach tens of MPa. The declining pore pressure causes a large contraction of the reservoir, inducing stress changes in the surrounding rock (Segall 1989), i.e., increasing horizontal stresses above and below the reservoir that could lead to reverse faulting. These volume contraction mechanisms in reservoirs from fluid withdrawal can cause earthquakes up to M=5.0 (Grasso 1992).

Induced seismicity was observed in the natural gas extraction field in the Netherlands (Van Eijs *et al.* 2006). In their study, authors suggest the three most important factors for seismicity triggering: the pore pressure drop from pumping, the density of existing faults in the overburden of the gas field, and the contrast in rock stiffness between the reservoir rock and the surrounding rock.

Lacq gas field in southwestern France presents one of the most known examples of induced seismicity associated with pore pressure decrease due to fluid extraction. Production in this gas field started in 1957, with a highly overpressured reservoir. The seismic activity started following the pore pressure decrease by around 30 MPa. When pore pressure dropped by an additional 50 MPa in the early 80s, around 800 seismic events with magnitude up to M=4.2 had been recorded (Figure 1.5). Segall (1989) suggested that poroelastic stressing, associated with volumetric contraction of the reservoir rocks, is responsible for induced seismicity associated with fluid extraction. Analysis of the stress changes above and below the reservoir indicates that the induced seismicity is consistent with a thrust fault regime, and the calculated maximum shear stress change was about 0.1 MPa for a pressure drop of 30 MPa suggesting that the in-situ stress prior to production was close to causing frictional failure of the faults (Segall 1989, Grasso 1992, Segall *et al.* 1994, Segall & Fitzgerald 1998).

Another proposed mechanism for initiating slip on preexisting faults is linked to the reduction of the vertical stress on the layers underlying the reservoir from which a large mass of hydrocarbons or rock has been extracted (McGarr 1991). An example is a recent strong earthquake in France in Le Theil (November 11th 2019, Mw 4.9), where a shallow hypocenter and its proximity to a large limestone quarry raised the question of the possible relationship between the mass of rock extracted and the triggering of the earthquake (e.g. Ampuero *et al.* 2020)

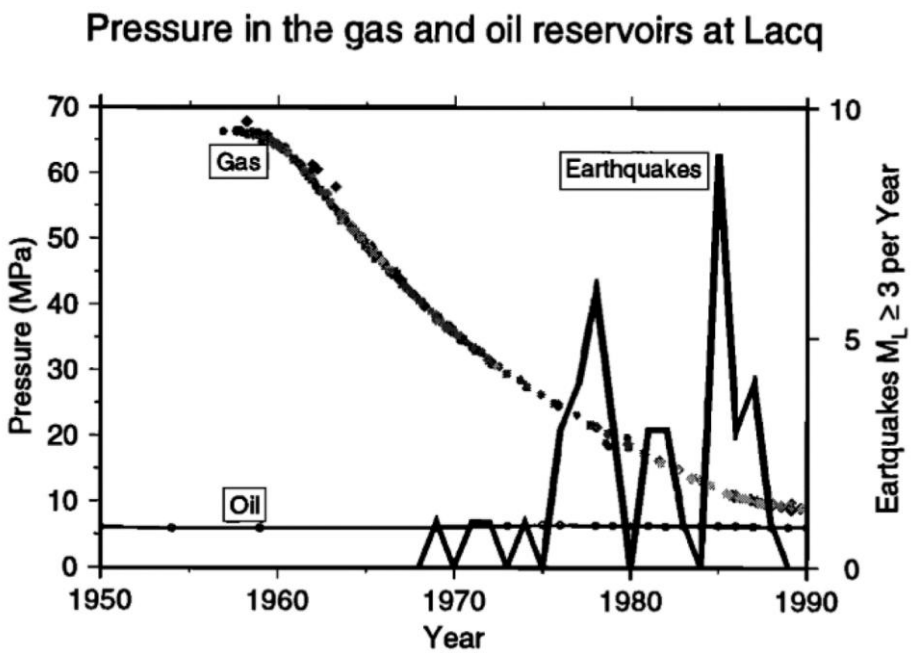

Figure 1.5 Pressure history within the Lacq oil and gas fields. Left scale: oil and gas field pressure, right scale: histogram of earthquakes located within the field with magnitudes greater than 3.0. Gas pressures in various monitoring wells are shown with different symbols. From Segall et al. *(1994)*

1.3.4 Thermal stressing

Thermal stressing, as another mechanism that may potentially play role in abandoned mines, refers to the rockmass expansion (due to heating) or shrinking (due to cooling) due to fluid-induced temperature changes. Such phenomena could be partially observed in geothermal exploration in particularly hot reservoirs (> 200°) such as the Geysers and Larderello sites (Batini *et al.* 1985, Martínez-Garzón *et al.* 2013), or the sites where the contrast in temperature between injected fluid and reservoir was particularly high. It is not easy to estimate if such a mechanism plays a significant role in post-mining environments, which would probably require the flooding of very deep mine workings, as high-temperature sources are usually found at depths below 2.5 km, which are the usual depths of Enhanced Geothermal Systems (ESG).

1.3.5 Aseismic slip movements (fault creep)

Aseismic movement in abandoned mines

Even though the development of surface and subsurface instabilities is commonly evidenced by seismic events as precursors, there is evidence that such processes can involve aseismic movements as well, potentially due to their relatively slow evolution.

A clear lack of microseismicity during almost 20 years of seismic monitoring was observed in Angevillers (Contrucci *et al.* 2019), in the Lorraine region in France. Even though an area over 100 m^2 was affected by

subsidence, only a few microseismic events have been detected by the local microseismic monitoring station. The maximum vertical velocity of 2 cm/month was recorded during more than 12 months, indicating a slow and steady strain energy release; with an increase of up to 10 cm/month during several months which led to a slight increase in the number of detected seismic events. Even though the extensive faults system that intersects the overburden seems to be the cause of significant anelastic attenuation on the site, results supported the idea that the triggering mechanism of subsidence on the surface is mainly aseismic nature due to its slow evolution.

Pore pressure changes and aseismic movement observed in other settings

Several studies so far suggest that fluid pressure build-up can, apart from triggering earthquakes, also induce aseismic deformation on preexisting faults (i.e., creep or aseismic slip) and contribute to the reloading of stress on an asperity (locked patch on a fault area,e.g. Figure 1.6),

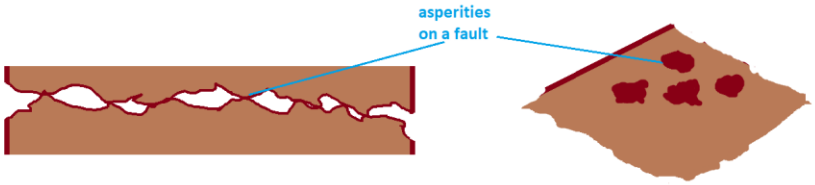

Figure 1.6 Illustration of asperities as contacting surfaces or locked patches on a fault. a) Section view along fault b) asperities along a fault plane

The presence of aseismic movements have been observed in many case studies on anthropogenic seismicity, especially fluid injection related scenario (e.g., Lengliné *et al.* 2017, Cappa *et al.* 2018).

It is generally suggested that the pore pressure increase due to the injected fluid reduces the normal stress on the fault plane, and tends to produce stable slip movement (e.g., Scholz 2002). This dominantly aseismic movement can itself cause significant stress changes which may potentially charge seismogenic structures or lead to dynamic ruptures along seismic asperities on the fault that has adequate initial stress and frictional instability conditions (e.g., F. H. Cornet *et al.* 1997, Bourouis & Bernard 2007, Guglielmi *et al.* 2015, Wei *et al.* 2015, François Henri Cornet 2016, Cappa *et al.* 2018, De Barros *et al.* 2018, 2020, Eyre *et al.* 2020)

One well-known case study to mention in this respect is the geothermal exploitation site at Soultz-sous-Forêts where aseismic movement have been evidenced from several observations, such as the comparison of the total slip and volume of seismic events to the observed slip in the local borehole and the size volume involving strong velocity changes in the reservoir following injection (Cornet 2016, Schmittbuhl *et al.* 2016).

2 Case study: Gardanne mine

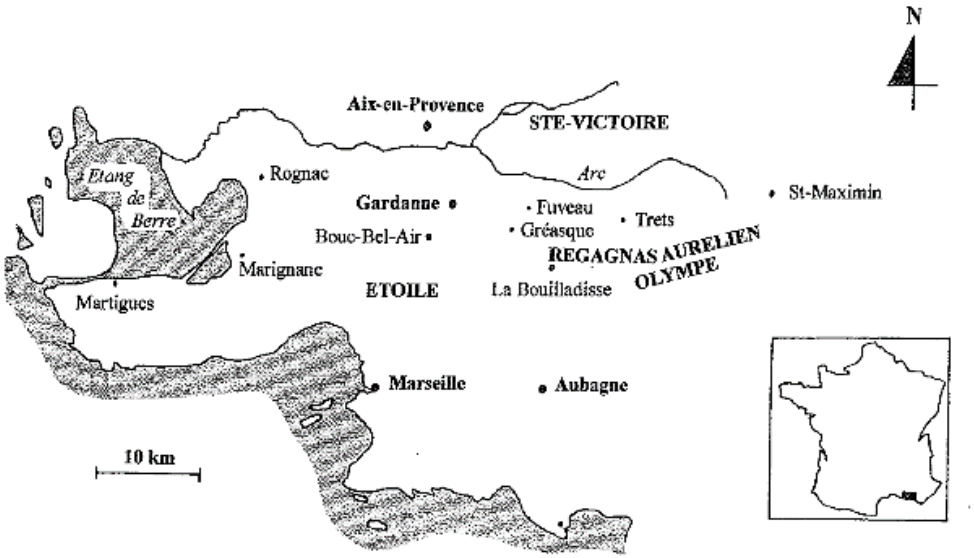

Figure 2.1 Geographical situation of Gardanne mining basin. After Chalumeau (2000)

2.1 A brief history of the mine and general context

The Gardanne coal mine is located in Provence region in south-eastern France. Geologically, it is situated in the large syncline unit called the Arc basin, which spans between the towns of Aix-en-Provence and Marseille (Figure 2.1). The formation of the basin is a result of a complex tectonic history (including faulting, folding, thrusting), most active from the Cretaceous, but especially throughout the Tertiary period. Basin is framed by the Sainte-Victoire mountain on the north and the thrust sheet of the “Massif de l’Etoile” (also called “Lambeau Charrié”) on the south. The stratigraphic series comprises the clayey rocks of the Valdonnien, surmounted by the Fuvélian limestone series, which are themselves covered by Begudian marls. Lignite (coal) was deposited in several layers of varying thicknesses interspersed within the Fuvélien limestone layer.

The extraction of coal (lignite) started in the 15th century. Initially, only outcrops in the eastern part (concentrated mainly in Regagnas and the Lambeau Charrié part) were exploited, as the coal seam was visible on the surface. Industrial exploitation began around 1850, which led to the development and modernization of production techniques, as well as the excavation towards the west.

The progress of the mine works followed the inclination of the axis of Arc basin synclinal and its lignite layers, from shallow east to the deeper west. In total, mining focused on the exploitation of lignite resources from four layers: Mauvaise Mine, 4 Pans, Gros Rocher and Grande mine. Only the Grande mine, deepest and thickest coal seam (thickness between 2 m and 5 m, but on average 3 m), was exploited throughout the entire mine, and the vast majority of total underground work was done within this layer.

The other 3 layers were mainly exploited at the Lambeau Charrié and the eastern parts of the autochthonous basin area.

Mine had two main parts (Figure 2.2):

I) part in autochthonous terrain, where Grande mine layer outcrops in the east and reaches the depth of 1400 m in the western part

II) part in thrust sheet Lambeau Charrié, almost perpendicular to the first part of mine

During the mining history, methods of exploitation have varied. Besides very old artisanal mining techniques used before 1850 near the outcrops, the main mining methods were (Figure 2.2):

I) “abandoned rooms and pillars” method, used until 1976 within different operating panels located in the eastern part of mine and Lambeau Charrié, for exploitation between 50 and 700 m of depth

II) “longwall” method was used after 1930 in the middle and the western part within a depth range from 400 to 1400 m

During the 20th century, eastern parts of the mine became less profitable and were gradually abandoned, while the western part of the mine became more important - especially since the 1980s, when two deep wells were opened allowing to reach depths of more than 1000 m for the first time: Yvon Morandat (Y well) 1105 m deep well, and Z well, 876 m deep.

However, exploitation gradually declined from the 1980s, until the final closure in 2003. In total, exploitation covered an area of approximately 60 km². It is estimated that over the entire mining period minimally 500 km of galleries were dug and 120-150 million tons of coal were extracted, corresponding to about 100 million cubic meters.

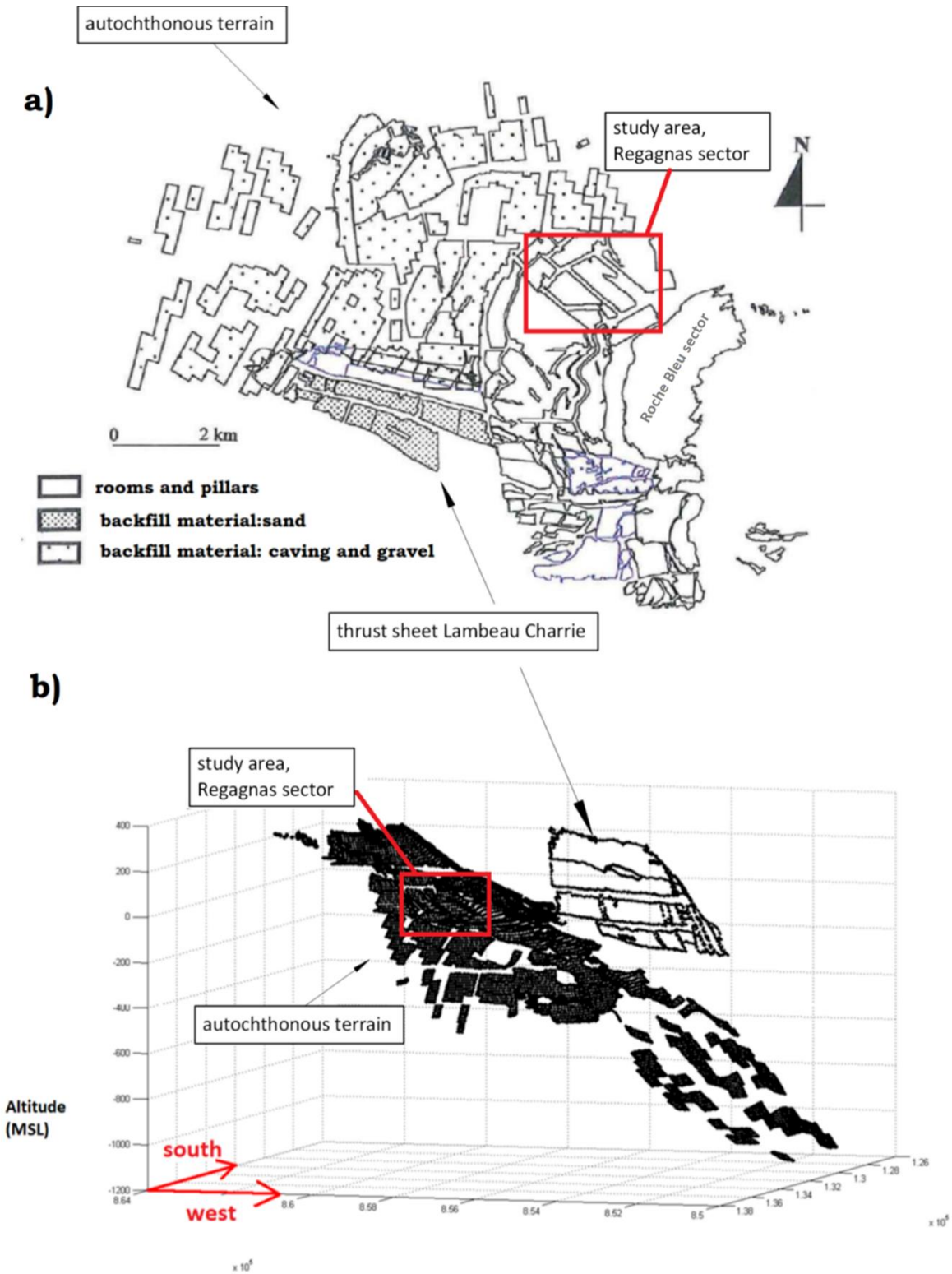

Figure 2.2 Gardanne mine exploitation methods and position Grande mine layer in space a) mining methods in Grande mine layer, adapted from Chalumeau (2000) b) Mine separated into two parts, see in text: autochthonous and Lambeau Charrié, adapted from Bosq (2013).

2.2 Mining disorders, rockbursts, induced and natural seismicity

In general, the Provence region is one of the most seismic areas in metropolitan France, with known major earthquakes in history (e.g., Lambesc earthquake in 1909, M_L = 6.2). The mining basin itself also contains several active faults that have generated strong earthquakes, such as the one that happened in the Mimet area on February 19, 1984, with determined magnitude M_w 4.3 (Nicolas *et al.* 1990) and M_L 4.5 (Haessler *et al.* 1985), that presents the strongest event in Provence since 1909 one.

Apart from seismicity due to slip of natural faults, mine exploitation can provoke disorders with movements in subsurface and surface, as well as induce seismic events. In the Gardanne mine area, however, the evidence for such disorders are sparse, especially in the part excavated with rooms and pillars. The bibliographic searches undertaken by Didier *et al.* (2003) did not lead to the discovery of any ancient surface movements induced by the old work carried out by abandoned rooms and pillars. Only one large-scale movement was discovered, referring to a brutal collapse on the night of April 29th to 30th, 1879, in the area of Rocher Bleu where the mining work was carried out in the layer Grande Mine.

2.3 Groundwater management during mining period

In order to understand the main characteristics of water circulation in the flooded mine in the post-mining period, this section describes briefly the flooding problems and known water sources that infiltrated the mine during its operational years.

Initially, pre-mining, the circulation of groundwater in the Gardanne area was strongly influenced by the complexity of the geological environment: the waters that diffusely drained in the basin infiltrated either from the limestone mountains (Sainte-Victoire, Etoile, Régagnas), either from the permeable layers of the Arc Basin (to a lesser extent). The geological structure of the southern slope of Sainte-Victoire mountain has provided the possibility of direct contact or geographical proximity (with only a few meters of separation by marls) of Jurassic and Fuvelian limestones, thus allowing the limestone layers of the basin to be supplied with the effective rain of the mountain. However, the way of transfers of water between aquifers is not completely known.

During the mine exploitation period, the direction of the progress of mining works was affected not only by natural constraints, such as the nature of the pre-existing faults, it was also strongly affected by the flow of groundwater. One of the problems the miners were facing since the start of the exploitation was the infiltration of waters in the mining infrastructures.

The history of flooding issues is too complex to provide all the details, however, access to deeper works was always problematic due to water inflows and limited mechanical dewatering resources. Pumping devices were installed in 1830 in order to lower the water table sufficiently to allow the miners to access the mine and work in dry. However, despite pumping and the isolation efforts imposed by the method of exploitation, water infiltration was still a problem due to the permeable nature and fracturing of Fuvelian limestone, which allowed communication with neighbouring mining sections (Ledoux *et al.* 2003). The solution that allowed further progress to greater depths in the west was provided by the 14 km long tunnel

"Galerie de la Mer" that was dug in period 1890-1905 within Lambeau Charrié, between the Biver well and the port of Marseille. Once finished, this tunnel allowed the mine water to be discharged into the Mediterranean Sea as well as to transport the mining ore by wagons between the mine and the port of Marseille. Additionally, the gallery developed towards the east (towards the Roche Blue sector, shown in Figure 2.2) allowed gravity drainage of part of the water (Dheilly *et al.* 2013). The water that infiltrated the mine works had two main origins:

I) in the extensive zone, flooding was provoked when the mine workings e.g. excavations in the northeast part crossed the permeable karstic fault zones which provide direct hydrological connections to major aquifers, (the Jurassic aquifer) (Dheilly *et al.* 2013). The two most productive water sources, named Sources 90 and Ste-Victoire, north of Régagnas, represented 75% of the volume of water pumped out and exhaled in the direction of the Galerie de la Mer. Inflow was rather constant at around 250 to 300 m3/h

II) the rainwater infiltrating rapidly through the Fuvelian outcrops both in the autochthonous zone of Roche Bleu and thrust zones of Lambeau Charrié. Works closer to the surface that were particularly vulnerable to water infiltration were quickly abandoned. One of the last major flooding incidences happened after an extremely rainy week (241 mm in seven days) in January 1978, which resulted in a production stop for 3 days in the eastern part of mine (Ineris 1995). This source could produce a flow rate from 0 to over 1000 m3/h, depending on the rainfall in the Mediterranean region. Additionally, during the mining operation, it was observed that the impact of these infiltrations on dewatering flows also depended if the subsoil and/or the works of the Roche Bleu were already saturated by previous precipitation (Dheilly *et al.* 2013, Kinscher *et al.* 2021).

On average, pumping rates during the exploitation period were around 800 m3/h. Additionally, in-situ measurements (quantitatively from the mining works and qualitatively by microtectonic surveys) showed that morphostructural anomaly of Gouste-Soulet divided the mining area into two zones. To the east of the anomaly, in the eastern part of the mine, Fuvelian limestones are characterized as highly permeable due to numerous open fractures (up to few decimeters) and karstified, while to the west fractures are closed or filled with clay and of low permeability and therefore limit the flow of water underground (Chalumeau 2000, Didier *et al.* 2003, Ledoux *et al.* 2003).

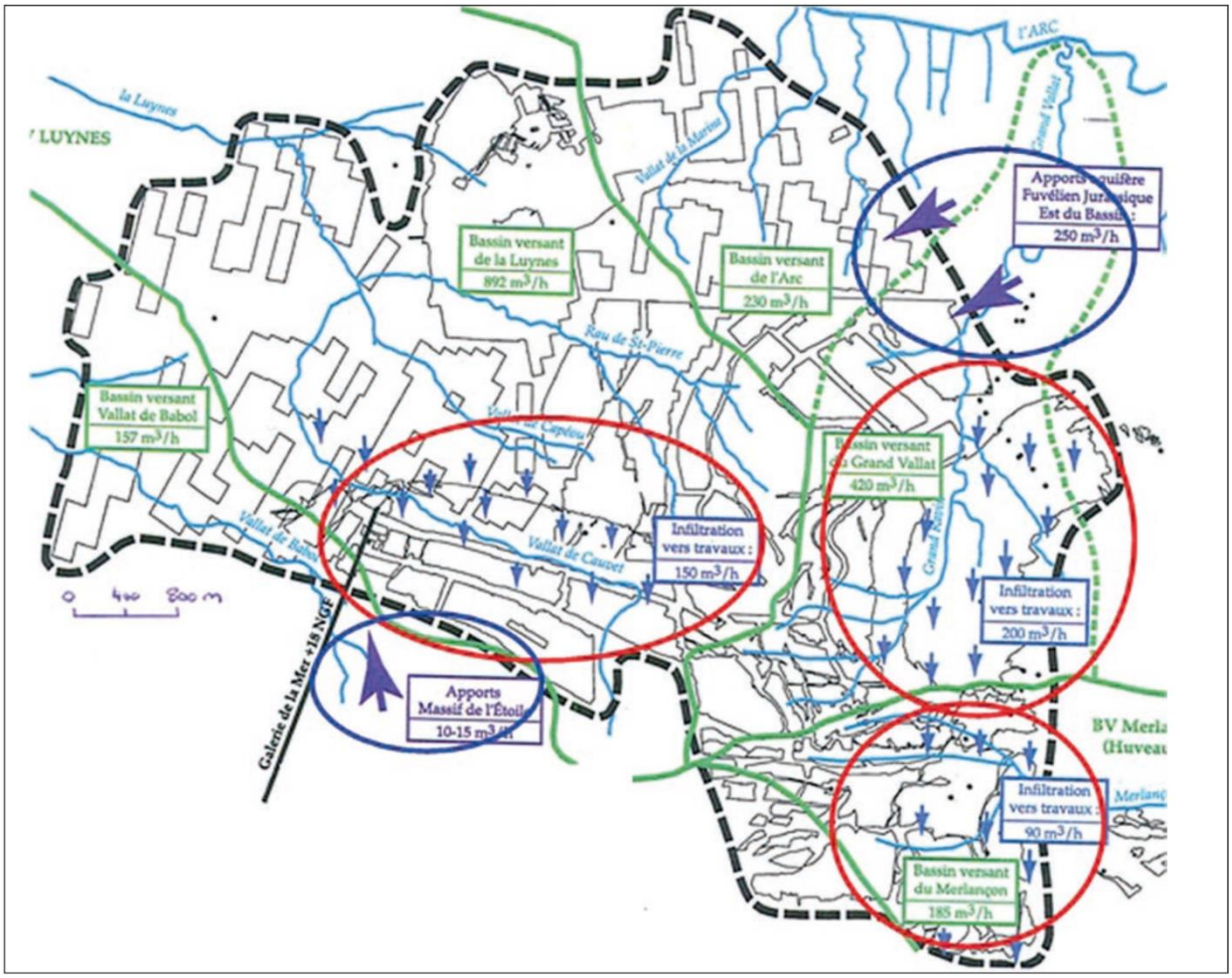

Figure 2.3 Localization of the main sources of water in mining works (after CESAME 2002)

2.4 Post-mining period

2.4.1 Water management

After the mine closure, a decision was made to stop the pumping. The progressive rise of underground water level led to the gradual filling of the mine reservoir: the leftover mining voids and fractures played a role in the creation of a new, mining aquifer (Cesame 2003).

Water level raised from -1100 MBSL to -14 MBSL, flooding first the western deeper part of mine and later the eastern shallower part. It is estimated that 15 and 45 million of cubic meters of mining voids were filled by water.

With the objective to avoid any overflow of mineralized water at the surface, pumping activity managed by BRGM was restarted again in 2010, by pumps installed in a former mine shaft Gérard well. Pumped out water is discharged to the Mediterranean via the canal of the Galerie de la Mer. Since then, the water

level is kept relatively stable by pumping, at a level of around -10 m MBSL, with annual fluctuations of the order about twenty meters (Dominique 2016a).

However, pumping itself needed to be reevaluated and readjusted on several occasions. The initial pumping rate was set to 600 m3/h. This proved to be under-estimated as the water level still continued to rise. Pumping was increased the same year, first to 800 then 1000 m3/h, which was still insufficient. Numerical modelling, as well as analytical and mathematical approaches, were combined to understand the water inflow into the reservoir (Dheilly & Brigati 2015). Reasons for the increase of the inflow rates seemed to be the augmentation of water flow from the Jurassic aquifer, due to a shutting down of pumping activity of the Arc shaft to the north of the mine in 2013, which was pumping out Jurassic aquifer at rates between 1500 and 2 000 m3/h. Additionally, after the mine shut down, a period without pumping from 2003 to 2010 allowed the creation of additional stocks of water in the room-and-pillar workings of the eastern part of the mine (Dheilly 2013). Since 2010, pumping was stopped for repairs or upgraded on several occasions (Dheilly & Brigati 2015). In the summer of 2016, the installation of additional pumping equipment allowed a further increase of the pumping rate to 1200 m3/h.

Piezometric measurements reaching the mining works depths continued in Gerard well, Y and Z wells. Rainfall data upon request from Meteo France, which has a meteorological station at Gréasque, are available as well.

To improve the hydrogeological model of the basin and to better understand the circulation of water in the old mining works as well as the interaction between groundwater flow and seismicity, additional piezometers were installed by Ineris: one in 2018 in wells Gréasque, and two in 2020 in wells Champisse and Huillier. The study was undertaken in 2020 (Kinscher *et al.* 2021).

However, due to complex circulation during the operational period (mining geometry, different excavations methods, different depths, water infiltrations problems, pumping, etc.), as well as only a few hydrogeological measurements available nowadays, the water circulation in the mine today is still not completely understood. Due to the lack of measurements directly in the study area, we lack the data of water levels directly in the seismically active sector.

2.4.2 Hazard identification and permanent microseismic monitoring

The progressive rise of groundwater level since the end of the intensive pumping raised concerns of increased risk for buildings on the surface above the areas exploited by rooms and pillars. Hence, several studies have been carried out to determine the zones of risk of surface instabilities following the mine flooding (Didier *et al.* 2003, Dominique 2014 and references within). The finally identified zones of risk (Figure 2.4) corresponds to areas characterized by:

I) presence of former operations of the Grande Mine layer in rooms and pillars not backfilled and with a high extraction rate, at a depth between 50 and 250 m;

II) high building density above the affected mining works

Even though pillars were evaluated to be in the state of equilibrium with the overburden (made of Fuvelian limestones), and the overburden is resistant and not very deformable, it is evaluated that the

equilibrium phase could end with the ruptures of pillars and the roof leading to evolution until the surface with mechanisms of either progressive subsidence, with low potential of substantial damage on buildings or brittle subsidence, with potential destructive impact on the surface. Depending on the character of the phenomena, expected seismic precursors (Driad-Lebeau 2010) are:

I) isolated events or evolving continuous activity forming seismic clouds, indicating instabilities at the level of pillars and roof; or

II) progressive seismic activity which increases in frequency (>100 Hz) and energy, with events located in the overburden. Calming of activity could be observed before the appearance of the phenomena on the surface.

In order to mitigate risk in these areas, the BRGM-DPSM has assigned Ineris to install and operate a permanent microseismic monitoring network of five stations (Figure 2.4), in the municipalities of Gardanne (zone 1), Fuveau (zone 2), Saint-Savournin, Cadolive and Peypin (zone 3). Antennas were installed in the period between the end of 2006 and the end of 2008, made up of several sensors positioned at different depths, monitoring microseismic activity within a radius of 400 m around the antennas.

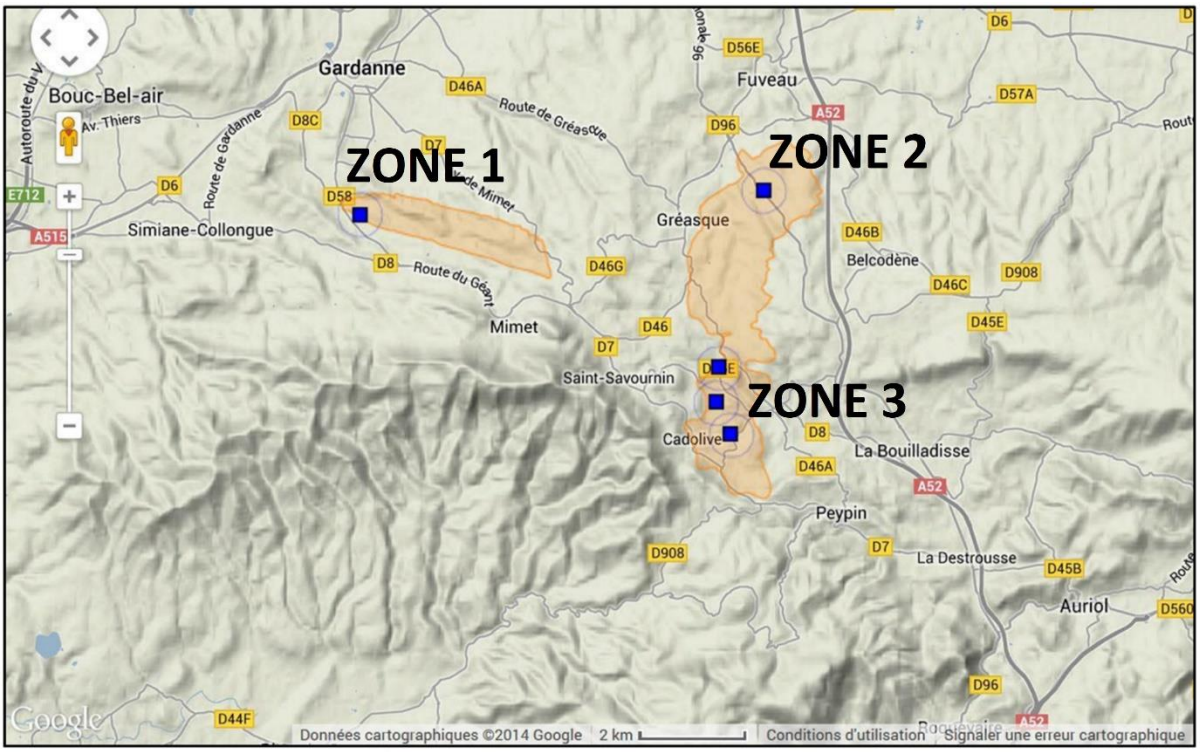

Figure 2.4 Initially identified zones of high seismic risk (orange) monitored by Ineris permanent monitoring network (blue squares) in the perimeter of 400 m

2.5 Post mining seismicity – the seismic swarm of Fuveau in Regagnas sector

The evolution of flooding, which was rising from the west, filling the mining voids of deepest parts, towards the shallower works on the east, was followed by the first occurrence of microseismic activity in the sector west of Fuveau (Figure 2.5). Seismic activity was significant and unexpectedly localized outside of identified high-risk zones of ground instabilities. Due to location outside of monitoring zones, approximately 2 km west of the Ineris station at Fuveau, it is named "the seismic swarm of Fuveau". Since then, seismic activity has been re-appearing periodically in the same area approximately every two years (2010, 2012, 2014, 2017). The strongest events with a local magnitude close to 2 are occasionally felt by the local population, which has led to new concerns regarding seismic hazard and risk (Matrullo *et al.* 2015, Dominique 2016a, Kinscher 2017)

After the strong seismicity in November 2012, a temporary seismic network of 4 surface stations was installed by BRGM during 2013-2014 in the sector, for research purposes to study this seismicity more precisely, as the Ineris monitoring network is not optimized for detecting all events in this area due to distance (Contrucci & Bennani 2013, Dominique 2016b). More details of the BRGM seismic network is provided in Annex- Part I.

2.5.1 Previous seismic data analysis in the post-mining period

Prior seismic data analysis mostly focused on the area of Fuveau, where the strongest seismic activity was recorded.

The first analysis of data recorded by the BRGM network between June 2013 and February 2014 already highlighted a correlation between seismic activity and the variation of water level in the mining works, locating the events below mining works (Dominique & Nédellec 2014).

It was observed that the first arrival of flooding front to mining works in the Gréasque and Regagnas sector, coincides temporally with the first appearance of the Fuveau seismic swarm in 2010 (Figure 2.5) and that in general, spatio-temporal distribution of the seismic activity seems to be controlled by the flooding front level in the mine. Furthermore, the main seismic crises are often preceded by intense rainfall events raising the level of the mining aquifer measured at Gerard well (Matrullo *et al.* 2015, Dominique 2016b, Kinscher 2017).

A more thorough analysis was done on a set of 140 events, recorded during seismic crises between December 1 and 28, 2014, carried out by Ineris (Matrullo *et al.* 2015) in collaboration with BRGM. Results have shown that events form a microseismic cluster which is located in the southern part of the Regagnas sector. The cluster shows NW-SE orientation (Figure 2.6a), which is consistent with the orientation of geological faults at depth. The determined depth of the events is between 500 m and 900 m, below mining works that are located at a depth of around 300 m (Figure 2.6b)

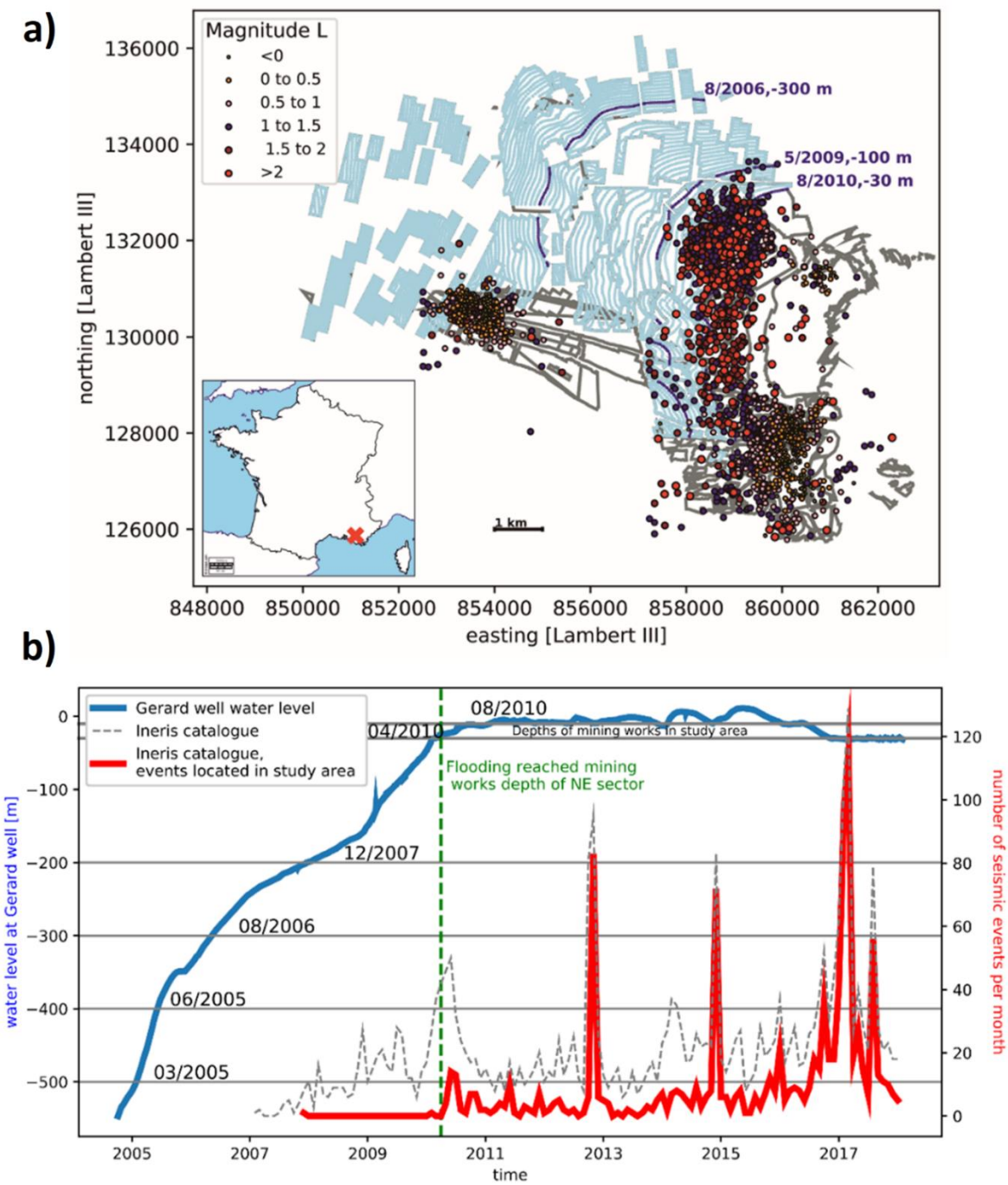

Figure 2.5. Flooded abandoned Gardanne mine with observed seismicity a) Flooded part of mine works shown in blue. Seismicity is shown as a function of magnitude by coloured dots, observed by the Ineris monitoring network in the period 2008-June 2020. Flooding front progress through mine works is indicated by dark blue lines and corresponding dates of arrival. b) Gradual flooding of mine works and first appearance of seismicity as flooding front reaches mine works level at the northeast area in 2010. The water level at Gérard well GW (blue line), corresponds to flooding front progress through mine works shown in a), together with time distribution of seismic events of Ineris catalogue in period 2008-2017 (all events shown as dotted line, events located in study area shown as full red line).

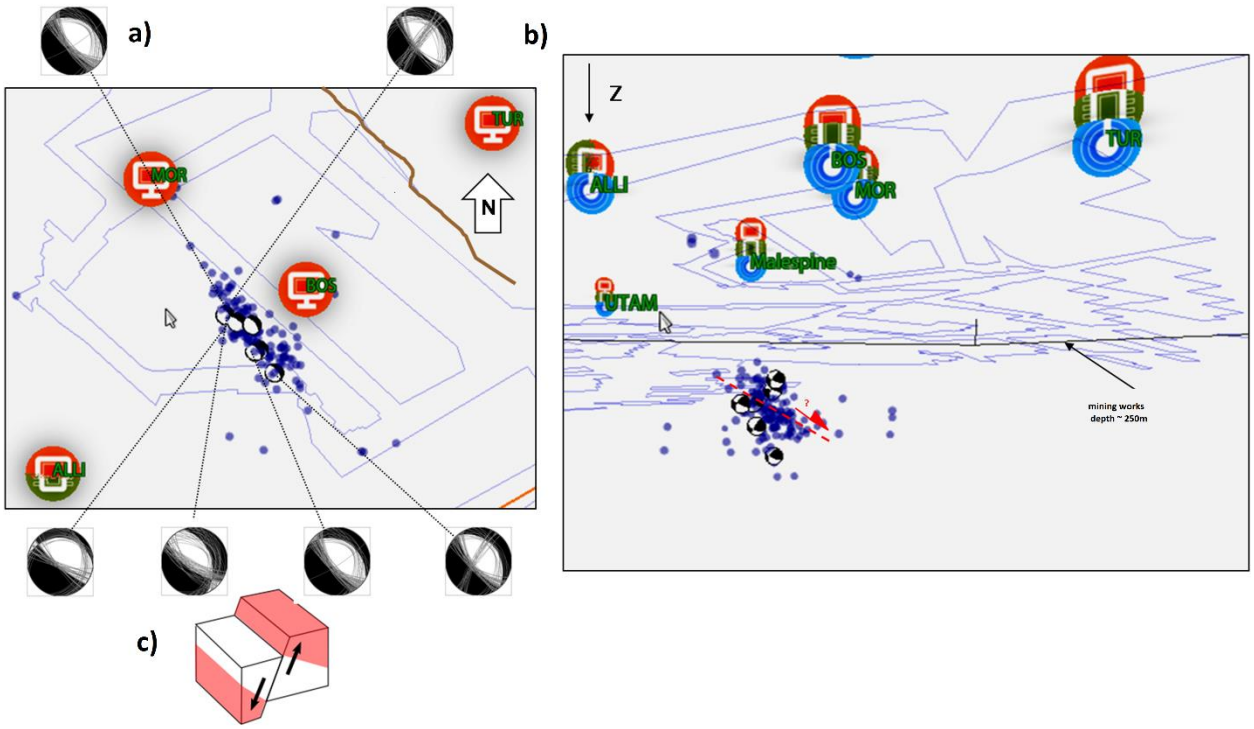

Figure 2.6 A Localizations of around 80 events of crisis 2014, recorded by BRGM seismic network 2014 (Matrullo *et al.*, 2015) together with source mechanism analysis results (Kinscher, 2017). Modified from Matrullo *et al.* (2015), Kinscher (2017) a) view from above b) profile W-E

Further analysis of events of the same crises was carried out by Ineris (Kinscher 2017) which showed that seismicity has typical characteristics of a seismic swarm (defined as a repetitive and spatio-temporally concentrated activity of a low-magnitude, with the absence of a stronger main event, Malone *et al.* 1975).

Additionally, the presence of at least three groups of multiplet families was found (Figure 2.7), comprising a number of events with similar waveforms of lower magnitudes. The source mechanism analysis was done with the classical source model, "double-couple", representing a shear along a fault. The choice of this model was justified by the presence of a significant energy fraction of SH (horizontally polarized S waves) waves relative to P and SV waves (vertically polarized S waves), which is a characteristic indicator of a mechanism in shear. Two methods were used – the simulation of waveforms and a composite method based on the P / S spectral ratio. Results indicated that the majority of the sources are related to NW-SE oriented normal faults, confirming consistency with the orientation of pre-existing geological faults. Based on source mechanism analysis, source radius was in the range of several tens of meters, with moment magnitude M_w in a range from -0.2 to 1.2.

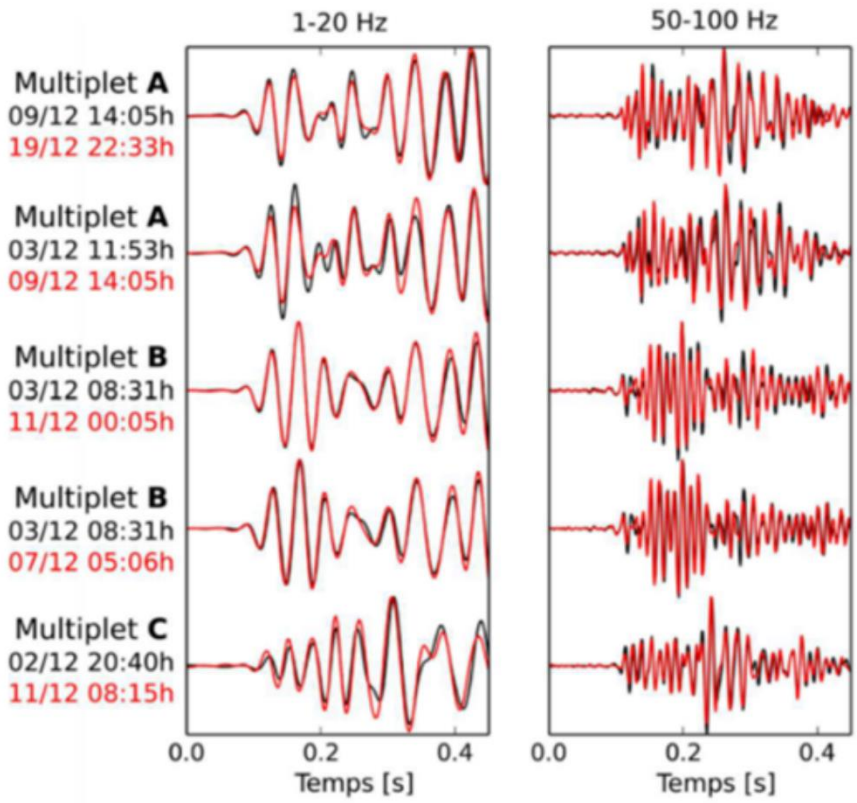

Figure 2.7 Waveforms of the events of the three multiplet groups observed at the S1 station, filtered at low (1-20 Hz) and high (50-100 Hz) frequency. From Kinscher (2017)

2.5.2 Study area in this thesis: the sector of Gréasque / Regagnas

Local geology, tectonics, exploitation history and observations

The zone of "Fuveau swarm", is located in the Gréasque / Regagnas sector of the mine, which lies in the North-East part of the mine, in the autochthonous part of the basin, where the dip of the layers is limited to about 5 degrees and regular, oriented to the West.

In this zone, the coal deposits were extracted exclusively from the Grande Mine layer. Located within the Fuvélien limestones, the depth of the Grande Mine varies between 300 m and 350 m (altitude MASL +30 to MBSL -60 m), with an average thickness of 2.4 m (Didier *et al.* 2003). The underlying Valdonian formation is made up of alternating limestone beds, marls and sandstones in its upper part, while the Bégudien formation in the overburden is made up of clayey-marly deposits interspersed with massive limestone beds.

Even though major documented faults in the mining basin have NE-SW and N-S orientations (Gaviglio 1980, 1985), the Fuvelian deposit northeast of the Regagnas zone is marked by faults trending N120°E to N150°E (Figure 2.8). This set is considered to be a system of normal faults created during the uplift of the dome of Regagnas, located to the south of the basin, and dated between 70 and 43 Ma.

Measurements of in-situ stress (Gaviglio 1980, 1985) at a depth of 390 m in the Sainte-Victoire sector to the north of Regagnas show that the major horizontal stress orientation is in agreement with NW-SE normal faulting. Hence, it seems that regional tectonic stress contributes significantly to the shear stress applied to the normal faults in the Regagnas sector, due to their favourable orientation.

Exploitation in this mining sector took place in the period between 1960 and 1975 (Chalumeau 2000). The mining technique was room and pillars without backfilling. The extraction ratio (ratio between the surface of galleries and total surface of galleries and pillars) has been estimated at 75% on average (Didier *et al.* 2003). The use of yielding pillars (i.e. pillars that yield in small amounts as a method to control and maintain the natural strength of the roof strata) avoids high-stress concentration in pillars.

2.5.3 The geotechnical state of mining works

Observed surface disturbances during the exploitation period

Surface disturbances had been reported in the Regagnas sector during the exploitation period, in particular during the years 1973 and 1974 (Figure 2.8). At the time, a geologist commissioned for an investigation concluded to the presence of a “ground collapse [….] in relation to a network of pre-existing natural fractures” (Didier, et al., 2003), while the direction of alignment of surface disturbances was comparable to the directions of known faults in the sector, oriented NW-SE (Chalumeau 2000).

Six months after the 1974 event, the geologist still observed the presence of vibratory phenomena and ground movements. He specified that these were small movements of settling in the area following the rockburst. Subsidence has hardly ever been observed in line with the works exploited by rooms and pillars (Didier *et al.* 2003).

At the time when the mine operation ended, in the eastern part of mine, several residents complained about disorders provoking cracked houses and the drying of a few wells, following the appearance of funnels of collapses and subsidence of more than 20 cm (Chalumeau 2000, Didier *et al.* 2003). The direction of alignment of surface disturbances was comparable to the directions of faults in this sector, oriented NW-SE (Figure 2.8) (Chalumeau 2000).

In-situ visits and borehole measurements

In order to check the state of mining works in this sector, visits were carried out in 1999. and 2000. by Ineris, from the Huillier well and to the NW of the Olympe sector (Didier *et al.* 2003).

Locations of the visited wells are indicated as a green dot in Figure 2.8. During these visits, a significant convergence of the roof was noted, with an opening reduced by 50% from ~ 2m to about ~ 1m. The pillars, strongly yielded, had undergone a significant increase in their width, which resulted in a reduction of the residual void volume, estimated between 20 and 25% compared to the 75% void volume initially left after the operation (Kinscher 2017). Based on observations of cracks and fractures made in situ, the crushing of the pillars would have occurred gradually under the weight of the overburden rather than abruptly.

These observations were then confirmed additionally by two boreholes located in the centre of the Regagnas sector (Didier *et al.* 2003), which showed that a residual void height of 1 to 1.50 m remained in the mining works in the Grande Mine layer. In addition, the authors specify that this important convergence is encountered rather at the centres of different sectors and galleries in Regagnas, while the pillars at the edges of the sectors still seem to be in good condition. Analysis of one of the core samples showed that the limestone beds that make up the roof of the Grande Mine layer were not very fractured, with a significant RDQ (Rock Quality Designation) fracturing index of around 80 to 100%. Field observations are consistent with these analyses as well, as there has been no presence of significant collapse or total closure of works in these areas.

Numerical modelling

To predict the occurrence of the surface effects of underground operations and any movements likely to affect surface land in the longer term, in line with old underground mining works, in particular those linked to old partial operations, geomechanical modelling was carried out (Didier *et al.* 2003). The model was calibrated using Information obtained from existing boreholes and site visits, as well as data obtained by miners. Simulations were carried out with UDEC, a two-dimensional numerical program, based on the Mohr-Coulomb failure criterion and an elastoplastic approach of the SHS type (Strain-Hardening / Softening model). A detailed description of this approach is given by Didier et al. (2003). Results of modelling in the Regagnas sector, for the mining works of depth greater than 250 m, showed that:

- significant convergence of 1 m of the galleries, observed in situ, can only be explained by a very significant plastic deformation of the overburden
- the large stiffness of the overburden effectively contributes to the transfer of stress to the firm edges (abutments) of the exploited area and thus “relieves” the pillars (Figure 2.9a)

when the lateral extension of mining works becomes too large while approaching a critical value, this "arch" effect of the roof no longer sufficiently reduces the vertical stress in the pillar, resulting from the weight of the overburden (Figure 2.9b). The pillars then gradually collapse, leading to a gradual flexion of rock layers in the overburden (Figure 2.9c). This is consistent with an increase of convergence at the firm edges around the exploited area, from 0 m to 1 m, observed during the visit.

Geomechanical numerical modelling has also revealed that the panels of rooms and pillars at great depth are in a "post-rupture" state. Calculations show that only major yielding of the overburden can produce a level of convergence as high as that observed in the underground workings (up to one meter), signifying that there is no more elastic energy stored in the pillars (crushed and in a state of post-rupture), nor in

the overburden (fractured and resting all its weight on the subjacent pillars), which means that any risk of sudden rupture of the overburden in the long term can be eliminated, however continuing (or further) smooth subsidence is still possible in the event of residual crushing of the collapsed pillars (Didier *et al.* 2003).

A risk of brittle and instantaneous remobilization to the surface is therefore unlikely in partial mining areas at depths of 250 m or greater. It is rather about a behaviour of the overburden which dissipates all the elastic energy "immediately" (after the extraction) in plastic deformation concentrated at the edges of the exploited zone, leading to a deflection inside the exploited zone (Figure 2.9c).

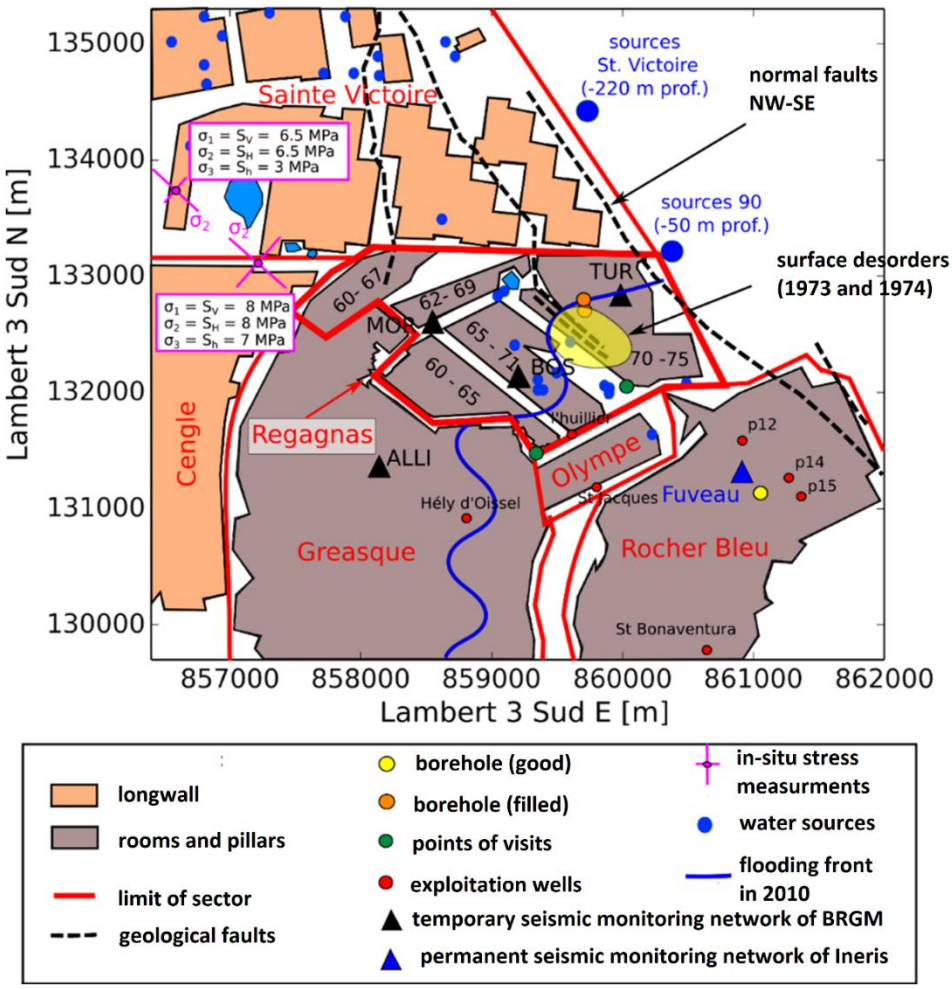

Figure 2.8 Map with information of sector Regagnas (study area), situated 2 km West of station Fuveau (blue triangle). Detailed view of mine plan showing faults geological observations in the field (Gaviglio 1980), the points of in situ constraints (Gaviglio *et al.* 1996), in situ and exploration visit points by drilling (Didier, et al., 2003), the locations of water inflows (Autran *et al.* 2013) and an area associated with surface and surface damage between 1973 and 1974 (surface are in yellow) (Chalumeau, 2000; Didier, et al., 2003).Modified after Kinscher (2017)

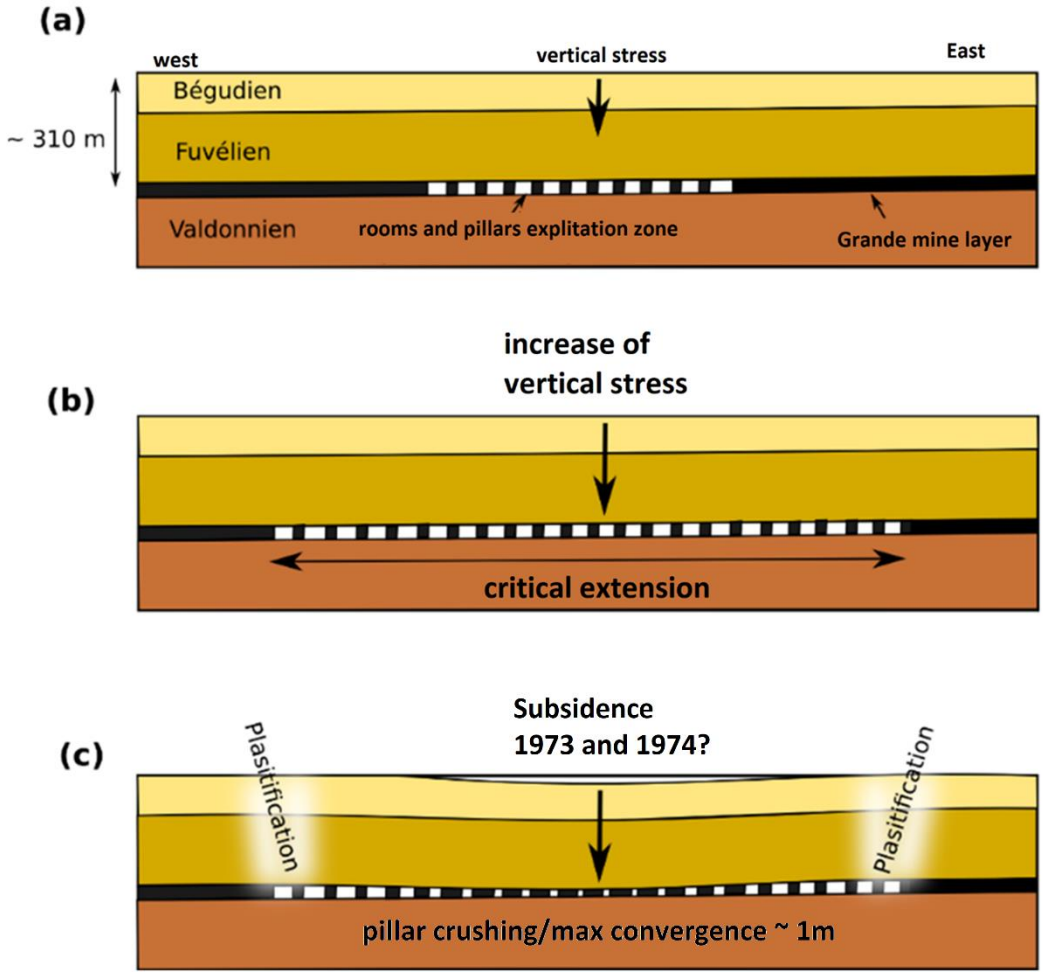

Figure 2.9 Illustration of the mechanical model of the chamber and pillar sector Regagnas (Didier, et al., 2003) describing significant convergence within the mining sectors. Qualitatively this model is consistent with subsidence observed on the surface following the blows of 1973 and 1974. See section **Numerical modelling** for details.

2.6 Discussion on the origin on seismicity and seismic hazard

As described earlier, in the abandoned mining areas, seismic events are commonly interpreted as a precursor of surface subsidence and/or collapse or as a consequence of the reactivation of preexisting fault in the proximity of the mining area.

Prior detailed seismic analysis carried on data recorded during the seismic crisis in 2014 in Gréasque and Regagnas sectors showed that the seismic sources seem to be mostly located below the mining works, between 550 m and 900 m of depth (e.g., Matrullo *et al.,* 2015, see section 2.5.1). Source mechanism indicated events related to a rupture mechanism along normal faults oriented NW-SE. These results are consistent with the documented normal faults by in situ geological observations further northeast of

Regagnas. Additionally, the presence of "multiplet" type events indicates the activity of segments which either gradually rupture over just a few days or could remain active for a few years (Kinscher 2017).

Even though seismic analysis contradicts an origin of the seismicity linked to collapses at the level of the exploited Grande mine layer, results of numerical modelling leave the possibility of reactivation of faults in the overburden, as well as the possibility of a reoccurrence of flexible and moderate subsidence linked to overburden of the overburden of collapsed works or in the event of residual crushing of the collapsed pillars (Didier *et al.* 2003).

However, the current lack of disorders on the surface is so far consistent with finally identified zones of risk (see section 2.4.2), which identified the sectors Gréasque and Regagnas as a low hazard area, based on the mining method and the depth of the mining works. Subsidence has not been observed in the post-mining period since the last occurrence in 1974.

Additionally, the observed temporal and spatial correlation of seismic activity with water level changes suggests that the flooding of mine works plays a role in the seismicity triggering mechanism.

Despite the strong indications that the majority of seismic events does not appear to be related to the occurrence of deformations in mining works but rather that the origin of the seismic activity is linked to a network of faults, this still requires confirmation. In that regard, 2 hypotheses and their hazard implications are defined:

I) origin of the seismicity is related to ongoing deformation in the mining works and in the overburden, along the virgin borders of the panels, that may lead to surface consequences and/or rupture of pre-existing faults in the Fuvelian layer (Figure 2.10a).

   These phenomena are often explained by an increase in the pore pressure induced by flooding at the level of mining works, thus modifying the stress field (decrease in the effective normal stress), which results in movements along weakness planes (cracks, pre-existing fractures) (McGarr *et al.* 2002).

   In this case, seismic activity is likely to stop when the mine collapses eventually reach equilibrium as the final stage. The expected maximum magnitude M_{max} of the seismic events will depend on the size of the mine area affected by the collapses.

II) origin of the seismicity is related to the reactivation of deeper faults located below the mining works (Figure 2.10b).

   This can be explained either by an increase in the vertical stress due to the increase in height of the water column, which causes the resistance of the pre-existing faults to be exceeded, or the diffusion of water at depth, leading to an increase in the pore pressure reducing the effective normal stress along pre-existing planes of weakness;

   The estimate of the hazard, in this case, would be completely different than for the first hypothesis, both in terms of the persistence of the long-term seismicity as well as in terms of the expected maximum magnitude M_{max}, which in this case depends on the size of the active fault segment.

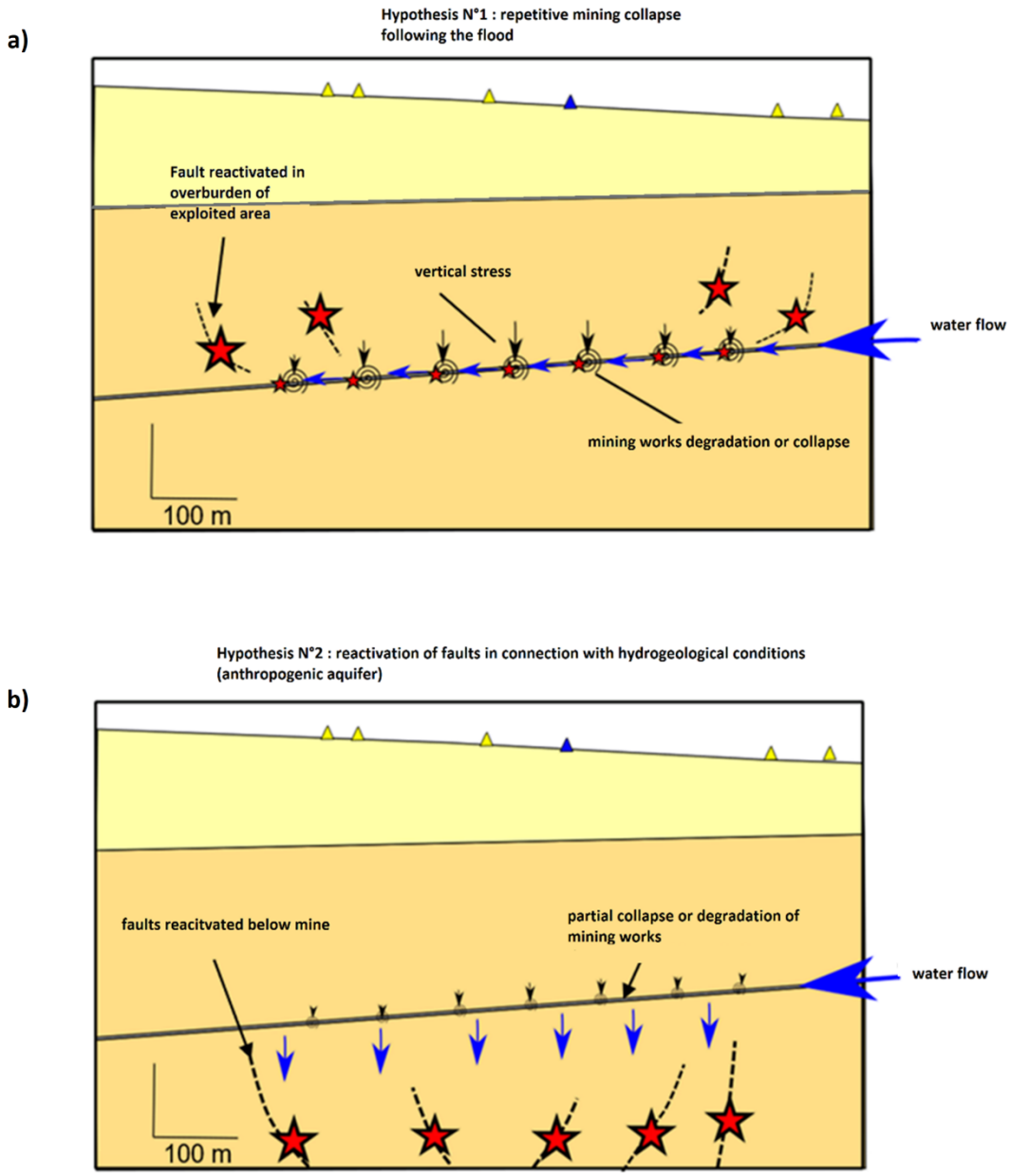

Figure 2.10 Illustration of the two hypotheses that could explain the origin of the seismicity observed at Gardanne in the study area (the Fuveau swarm). See section 2.6 for details. Modified after Kinscher (2021)

3 Thesis motivation and objectives

3.1 Motivation

The knowledge on the origin and the triggering mechanisms of the seismic activity in the Gréasque and Regagnas sector is the key for seismic hazard assessment of the entire Gardanne basin.

As presented in the previous Chapter, two hypotheses were raised about the origin of seismicity, one relating it to ongoing deformation in the mining works and in the overburden that may lead to surface consequences and/or rupture of pre-existing faults in the Fuvelian layer, while other relates it to the reactivation of deeper faults located below the mining works.

Previous results are inconclusive on origin as well as mechanisms of observed seismicity and its connection to the hydrogeological state (see section 2.5.1). Difficulties underlined as limitations in the previous studies include factors such as:

- existence of previously unknown faults and unknown potential of their reactivation, triggered by flooding and water level changes in mining works,
- unclear circulation of groundwater within the mining works after the mine closure and flooding
- the unknown water level in the mining works due to lack of measurements and lack of understanding of water circulation

Each of the two hypotheses on the origin of seismicity leads to different implications for hazard definition or risk management, therefore validation of one of them is crucial for the identification of potential consequences. The main motivation of this thesis work is therefore understanding the origin and the mechanisms that cause the seismicity.

The focus of thesis' work is the analysis of the data of the recorded seismic activity in the area of the Fuveau swarm, mainly in the period 2014-2017. This area is chosen as it has been the most seismically active area of Gardanne mine since mine flooding and closure, and therefore also is the best-instrumented area, monitored closely by 3-5 stations of the temporary seismic network of BRGM since 2013/2014, as well as by closest station Fuveau of Ineris permanent monitoring network since 2007.

More precisely, questions/tasks that are addressed in this thesis are:

- What is the seismic origin?
- What is the triggering mechanism of seismicity?
- What is the link between seismicity and water level variations?
- Improvement and development of new seismic monitoring methodologies.

3.2 Methodology and objectives

The thesis work is separated into four main units as follows:

PART I: General introduction

The objective of this part is to introduce all potential impacts of underground mining on overlying structures in the study area of this thesis as well as studies on seismicity in a post-mining environment. The role of seismic monitoring in this context is described. The mechanisms related to induced seismicity known in other post-mining sites and other relevant case-study related to anthropogenic/induced seismicity are also introduced. Further, the general context of the Gardanne case study is introduced, focusing on the post-mining period, results of previous geomechanical modelling and seismic analysis. Open questions regarding the origin of the seismicity are presented, and two hypotheses on the origin are introduced, that will be evaluated as a part of this thesis work.

PART II: Improvement in detection and location of microseismicity with a sparse network.

The objective of this part of the analysis is the improvement of the existing monitoring methodologies and the implementation of automatized methods of detection and location. The aim is building the seismic data catalogue by analysis of continuous seismic data recorded during the period of four years (2014-2017) by the temporary BRGM network, as having a more local seismic data catalogue and more detailed catalogue of the studied allows more detailed seismic data analysis area more accurate depiction of seismic activity in the area since the permanent monitoring network of Ineris does not permit it with such precision and detection limitations due to its distance.

Additionally, this part of the thesis work included the development of a new methodology for detection and location, concurrently automatization of the processing part of seismic data analysis, which directly contributes to the improvement of monitoring technologies - especially in networks with challenging configurations of few sensors. Even though analysis of the available dataset recorded by a sparse network is challenging, the application of new developed methods to the available dataset has led to improvement of the detection performance of weak seismic signals, more accurate locations, magnitudes, and source parameters.

Therefore, by tackling the challenges of seismic monitoring and analysis of a dataset of the sparse network, in order to build a seismic data catalogue, in this part of thesis work, one of the objectives was automatizing the detection and location processing.

PART III: Cluster and multiplet analysis

Multiple analyses are employed to identify and investigate seismically active structures and their spatio-temporal evolution. Multiplet occurrences analysis allowed to better understand the mechanism of the seismic event triggering in more detail.

PART IV: Seismicity origin and triggering mechanism

Seismicity linked to the fluctuations in the water table in the mine layer makes seismic hazard assessment in Gardanne mine very challenging; especially when faced with a lack of understanding of the origin of seismicity or the link between seismicity, hydrogeology and triggering mechanism.

This part of the thesis work implements additionally the results of additional seismic analysis undertaken in relation to this thesis, but not as part of it (Kinscher *et al.* 2021)

Complementary seismic analysis was done exploiting the newly enhanced seismic network of a total of 13 stations, as 8 additional temporary stations (4 stations of Ineris and 4 of BRGM) were installed since 2019 within the study area. This seismic data analysis focused on constraining the seismic source mechanism and better precision of the depth of the sources.

The objective is this part is to evaluate two hypotheses on the seismicity origin in the study area, as well as potential driving forces and triggering mechanisms behind the seismicity. Discussion is based on the results of this thesis' seismic data analysis presented in part II and part III of this manuscript, as well as results of undertaken complementary seismic analyses based on temporarily enhanced seismic monitoring by Ineris and BRGM.

PART II
Improvement in detection and location of microseismicity with a sparse network

Introduction

The focus of the next Chapters is on improvements of the current monitoring and processing techniques used for the analysis of seismic data recorded at Gardanne. The main objective is to produce a detailed seismic catalogue for the period 2014 -2017, based on the data of the temporary microseismic network of BRGM, by application and development of new processing tools for detection and location.

Located within the study area, and distributed at a small distance from each other around the Fuveau swarm cloud, stations of the BRGM temporary network are better suited to monitor the seismically active zone than the permanent network. Therefore, the local catalogue derived from its data would provide a higher magnitude of completeness (M_c) than the catalogue provided by the permanent seismic monitoring system by Ineris, and thus provide a more detailed insight into the seismic activity and its potential relation to water level variations within the mine.

Due to the large volume of data, usual time-consuming location procedures that included visual inspection and manual P and S phase picking operations are no longer feasible, automatization of processing is necessary. Therefore, the potential of the newest developments of automatic detection and location approaches is examined and proven.

State of the art (Chapter 4) introduces the full-waveform array coherency-based location methods, also called “locate and then pick methods” (Eaton 2018), which have been so far applied to different environments, such as microseismic monitoring in the oil and gas industry, volcanic tremor data, mining-induced seismicity, as well as to slow (tectonic tremor and low-frequency earthquakes) and regular earthquakes (e.g., Li *et al.* 2020, and references therein). The great benefit of these approaches, which find more and more application in microseismic monitoring, is that they do not require manual phase picking and are thus adapted for automatic processing.

In particular, the approach developed by Poiata *et al.* (2016), called Backtrack (BTBB), is tested in Chapter 5. This method is based on a kurtosis multifrequency band detection scheme and backprojection-based (source scanning by seismogram stacking) location principle. However, the application of an automatic processing tool to data from limited station numbers was challenging and required the development of new processing steps (Chapter 5) in order to reduce the number of false triggering of noise and to assess location quality. Results and evaluation of the developed approach are presented in Chapter 6, while interpretation and further of the results will be presented in the following parts of this manuscript.

The developed approach presented here offers a solution for automatizing detection and location in operational microseismic monitoring, especially, but not limited, to post-mining settings where sparse temporary monitoring networks with one-component geophones are very often the only available tool for hazard assessment, and where timely decisions based on accurate seismic event locations are of most importance.

The main parts of the developed methodology described here are recently published online in the international journal Pure and Applied Geophysics:

Namjesnik, D., Kinscher, J., Gunzburger, Y., Poiata, N., Dominique, P., Bernard, P., & Contrucci, I. (2021). Automatic Detection and Location of Microseismic Events from Sparse Network and Its Application to Post-mining Monitoring. *Pure and Applied Geophysics*, 1-29, DOI: 10.1007/s00024-021-02773-4

4 State of the art regarding detection and location of seismic events

4.1 Advantages of full-waveform and array coherency-based methods

In microseismic (operational, industrial) monitoring, conventional approaches for detection and location are generally adapted from global seismology. Still most commonly used (including the case of Gardanne mine), are the travel-time based methods based on modifications of the Geiger algorithm (Geiger 1912). These methods typically rely on manual or automatic picking of compressional (P-wave) and/or shear wave (S-wave) phases. The event location is determined in the iterative inversion process by minimizing the residuals between theoretical (i.e., predicted by an available earth model), and observed (relying on phase picking) travel times of the considered seismic phases. The analysis is also sometimes combined with the evaluation of polarization angles (Abdul-Wahed *et al.* 2001, Oye & Roth 2003, Contrucci *et al.* 2010).

As manual phase picking can be quite time demanding, not feasible and prone to human error, further developments in the last decades brought a large number of new algorithms for automatic phase picking (e.g. the Filter picker algorithm of Lomax *et al.* 2012 and Vassallo *et al.* 2012).

However, the performance of automatic pickers still remains limited. Even though automatic P phase onset picking can be quite accurate, the performance of picking of S-wave phase can be challenging and influenced by various factors that lead to significant errors, such as P-wave coda overlapping the S-wave, the presence of converted waves generated at different interfaces, the S-waves splitting caused by seismic velocity anisotropy (Crampin 1977, Amoroso *et al.* 2012, Grigoli *et al.* 2014).

Among the different detection and location methods developed throughout the last decades in the seismic and microseismic fields, as an alternative to the standard traveltime-based location methods (were main steps include picking of phases and location of the events though traveltime inversion method), new waveform-based methods, that emerged in recent years, bypass phases identification and picking, exploiting the information provided from the analysis of full-waveform records, as well as the coherency (and stacking) between the entire ensemble of full-waveform traces of all the stations within the network.

Adapted from migration or stacking techniques routinely used in exploration seismology, these methods have been rapidly gaining popularity due to their simplicity and minimal necessary a priori constraints (Cesca & Grigoli 2015). They have also proved to provide robust and effective source location results at various scales, allowing to detect and locate events with low signal to noise ratio (SNR) (L. Li *et al.* 2020).

With full-waveform methods and an increase in monitoring capacities, microseismic events have now become more easily detectable. These methods often show detection capacity improvement by a factor 10 or more, compared to standard triggering-based approaches (Poiata *et al.* 2016, López-Comino *et al.* 2017, Aden-Antóniow *et al.* 2020). The abundance of newly detected weak seismic events leads to the

lowering of the magnitude of completeness in seismic data catalogues and contributes to a more thorough analysis of seismicity worldwide.

To sum up, several advantageous factors have led to the conclusion that the analysis with a waveform-based detection and location method would present an important improvement compared to previously used methods to process Gardanne mine seismic data. Among the factors, the most important are:

- Potentially higher detection capacity (and thus more detailed seismic catalogue) compared to standard approaches based on station wise triggering;
- higher relative location precision (events of similar waveforms are located in the same manner), and thus more sensibility to detect seismic clusters;
- automatization of the processing, important due to large volumes of available data and time consuming manual seismic event location procedures;
- potential for implementation in a (near-) real-time processing being of interest in post-mining monitoring applications where decisions have to be taken rapidly.

4.2 Waveform-based detection and location methods: common basic principles

The basic principle of full waveform-based detection and location methods is the determination of the point where radiating energy refocuses (source location), with the use of imaging or migration operator (Figure 4.1). Following (L. Li *et al.* 2020), so far developed different methods can be categorized as following: partial waveform stacking (e.g., Poiata *et al.* 2016, Li *et al.* 2018) –i.e. PWS methods, time reverse imaging (e.g., Z. Li & van der Baan 2016)– i.e. TRI methods, wavefront tomography (e.g., Diekmann *et al.* 2019)– i.e. WT methods and full waveform inversion (e.g., Willacy *et al.* 2019) – i.e. FWI methods.

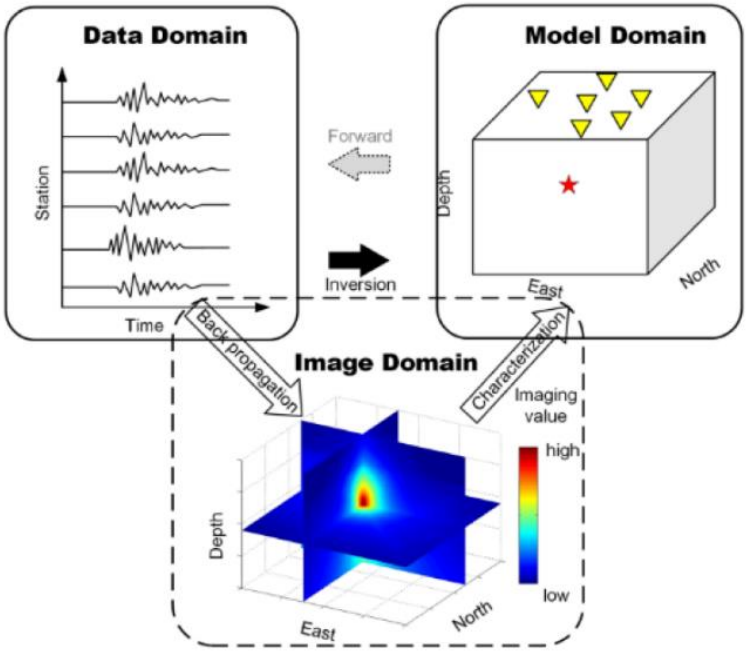

Figure 4.1 Scheme of waveform-based method processing. The seismic source is located through the backpropagation of seismic energy radiated by the source. From L. Li *et al.* (2020)

Out of these, the most widely used in local and regional scales are PWS methods. The basic idea of PWS methods follows the principle of diffraction stacking in exploration seismology combining arrival time predictions and grid search. Based on stacking types, they are classified as diffraction stacking or cross-correlation stacking methods. While diffraction stacking comprises stacking of signals from individual receivers along a theoretical travel time moveout curve (e.g., Kao & Shan 2004, Gajewski *et al.* 2007), cross-correlation stacking techniques correspond to stacking of cross-correlograms along differential travel time curves taking into account differential travel times on pairwise receivers for common events (e.g., Font *et al.* 2004, Poiata *et al.* 2016), following the idea analogue to travel-time based double-difference method (Waldhauser & Ellsworth 2000).

As a pre-processing step, regardless of stacking technique type, the PWS methods consists of input signal transformation to characteristic functions (CFs) designed to highlight body wave phase arrival times, among which most common examples are conversions to energy or envelope traces, the short-term average over long-term average (STA/LTA) traces or higher-order-statistics traces. Time-series of 3D spatial likelihood images are further created from spatial mapping and stacking functions and as a final step, the source location is determined from imaging function (Figure 4.2).

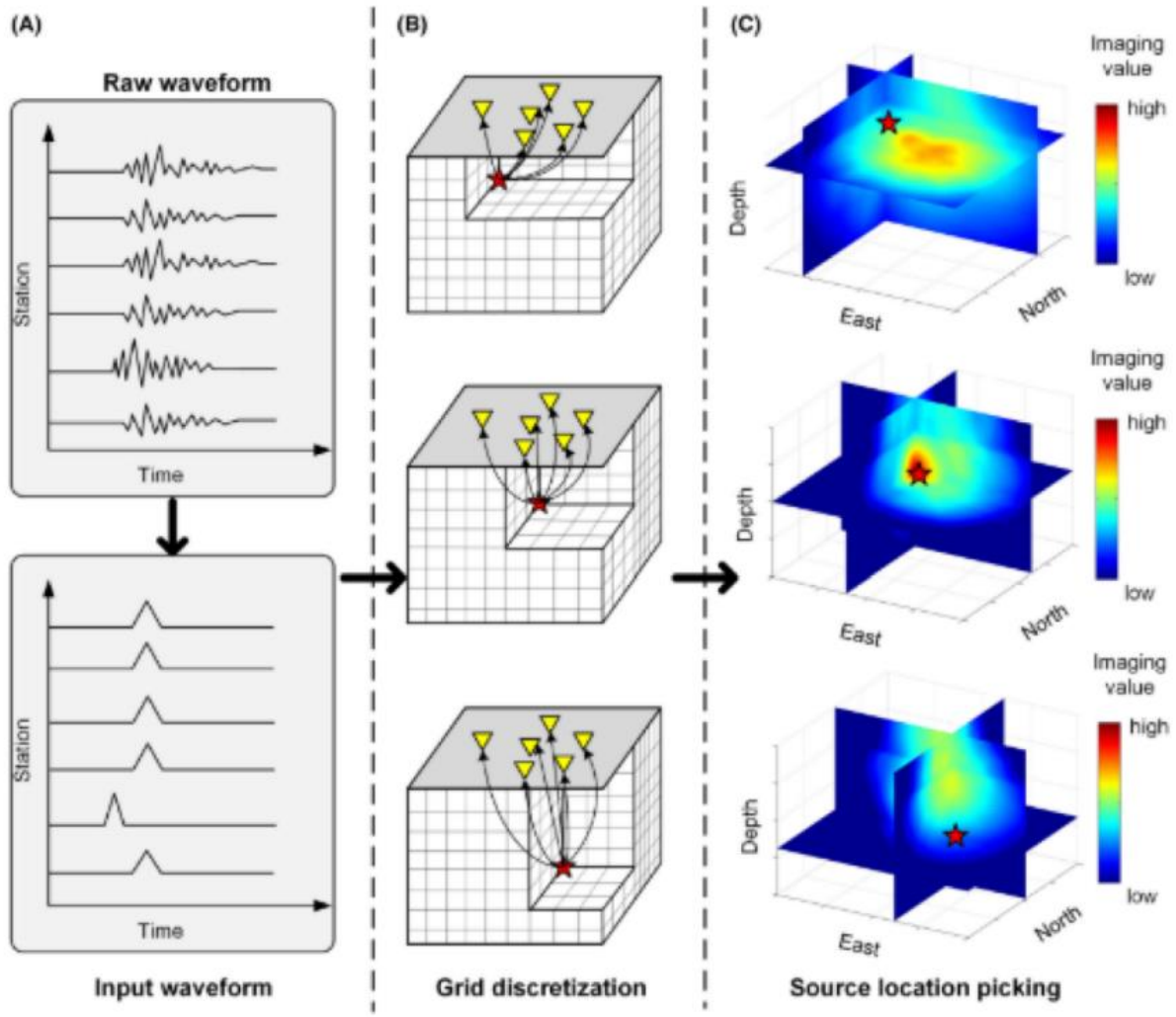

Figure 4.2 The simplified sketch presenting a general theory of migration and stacking process for PWS methods: a) raw data are processed to generate input waveforms, b) subsurface grid discretization: waveforms are stacked as imaging value of points of each potential grid, c) source location is determined by picking of grid points(s) with maximum imaging value. From L. Li et al. 2020

A more detailed overview of theoretical developments and principles of the full waveform-based detection and location methods, related challenges and recent applications can be found in S. Cesca & Grigoli (2015) and L. Li *et al.* (2020).

4.3 BackTrackBB (BTBB) method overview

Among the different methods available, BTBB methodology was chosen for application to our study area and recordings of the BRGM microseismic network. BTBB can be classified as PWS method, with cross-correlation stacking type. Compared to similar methods, the BTBB processing scheme was designed in a

particular manner to enhance coherent statistical features of the recorded wavefield, through multiscale, frequency-selective steps and the use of higher-order statistics.

It is adaptable to different environments through different choices in configuration and processing steps, which depend on the nature of the targeted signal. Initially developed for dense large-scale seismic networks and local antennas, it was first tested on data of dense network from Central Chile (22 stations). It has since proven to be successful in other challenging environments as well: from regular earthquakes and tectonic tremor in subduction zones in Chile and Japan (Poiata *et al.* 2016, 2018, Aden-Antóniow *et al.* 2020) to mining seismicity (Palgunadi *et al.* 2019), significantly improving detection and location performance.

Application in mining environments has presented strong potential, as demonstrated by the work of Palgunadi *et al.* (2019), where the main challenges were related to the presence of a wide range of seismic noise sources, connected to the ongoing mining activity, and a high sampling rate of recorded data (several kHz).

In general, the method is based on the assumption of the use of a single-phase, either P (earthquake location) or S (tremor location), using only vertical or horizontal components. Most recent developments include testing of the use of both P and S-phase arrivals at the same time, on the data of the Chile network (Aden-Antóniow *et al.* 2020), which is particularly important when considering event location outside the network zone.

Application of BTBB to Gardanne mine dataset presents one of the first application of a waveform method to data of post-mining monitoring with the sparse seismic network.

In the following section, only the main steps of the BTBB processing scheme are presented, in a very concise manner.

4.3.1 The BTBB processing scheme

The workflow of the method follows the common principle of full-waveform methods, as earlier introduced. It can be separated into 2 parts:

I) statistical signal analysis i.e. building of time-series of characteristic functions (CFs) from the seismograms recorded on stations in the network and the coherency analysis

II) detection and location, which consist of:

- creation of station-pair time-delay functions estimations (TDEs)
- spatial mapping and stacking of TDEs on a 3D grid
- determination of source location from time-series of 3D spatial likelihood images

The quality of the results and distinction between false and true event detection are measured by two BTBB detection parameters: MaxStack, which is the maximum value of 3D likelihood source location and RMS, which presents root-mean-square value between the theoretical and observed time delay estimates.

More details about the method processing are presented in the Annex – Part II (BTBB principle), however for the full overview of possible applications and detailed derivation of each step, readers are referred to Poiata *et al.* (2016).

5 New development for detection and location of events of sparse networks in the case of Gardanne

Data used in this part are continuous data of the BRGM temporary microseismic network recorded in the period 2014-2017 (see Annex Part I for details). Before any seismological analysis, the raw continuous ground motion signals recorded by the network(s) needed to be preprocessed. Data preparatory phase is described in Annex Part II.

5.1 Testing BTBB parametrization and limitations

In a first step, BTBB was tested to the training dataset in order to calibrate parametrization and to evaluate the performance in terms of detection and location quality and identify the potential limitation of the method. Used data for this part are continuous seismic data of December 2014. During this period, four stations have been operational, namely S1, S2, S3, S4. The choice of this dataset was related to the fact that it covers a period of increased seismic activity which was widely analyzed in terms of location, magnitude and source characteristics by several previous studies (Matrullo *et al.* 2015, Dominique 2016a, 2016b Kinscher 2017).

BRGM catalogue comprises for this period 213 events located within the study area.

For testing the BTBB method, a frequency range between 1 – 100 Hz was considered as it represents the main frequency content of the recorded seismic signal. CFs were calculated based on the stack of a total of 50 logarithmically spaced frequency bands covering the determined frequency range. An example of the CF of a signal is shown in Figure 5.1. The theoretical P-wave travel times necessary for the second detection and location step are calculated using the Grid2Time routine of the NonLinLoc program (Lomax 2005, 2008), over the grid covering the study area. Spacing between grid points (potential sources), was set to 10 m, and depths up to 1.5 km, with a constant homogeneous velocity model $v_P = 4.1\ kms^{-1}$(Kinscher, 2017). A minimum value of the MaxStack parameter is set to 0.7, which presents the detection threshold criteria. To run BTBB, time-series of 12s length were prepared as input data, as well as configuration files for each 12s widow.

For the largest events, clearly visible on all four stations, BTBB showed satisfying results in detection and location (e.g., Figure 5.2). However, by comparing the final catalogue, produced by the application of BTBB, with the BRGM catalogue it was noted that a significant number of false triggers and noise sources. Indeed, as shown in Figure 5.3a, by using the BTBB event triggering criteria MaxStack and RMS alone (defined in section 4.3.1) it seems impossible to distinguish between the seismic event (especially smaller ones) and noise events, which is most likely related to the limited station number. Indeed, as shown in an example in Figure 5.3b the MaxStack value, i.e., the stack quality for all station pairs with respect to the optimal source location, was observed to be as equally high for a particular noise source as for the seismic event.

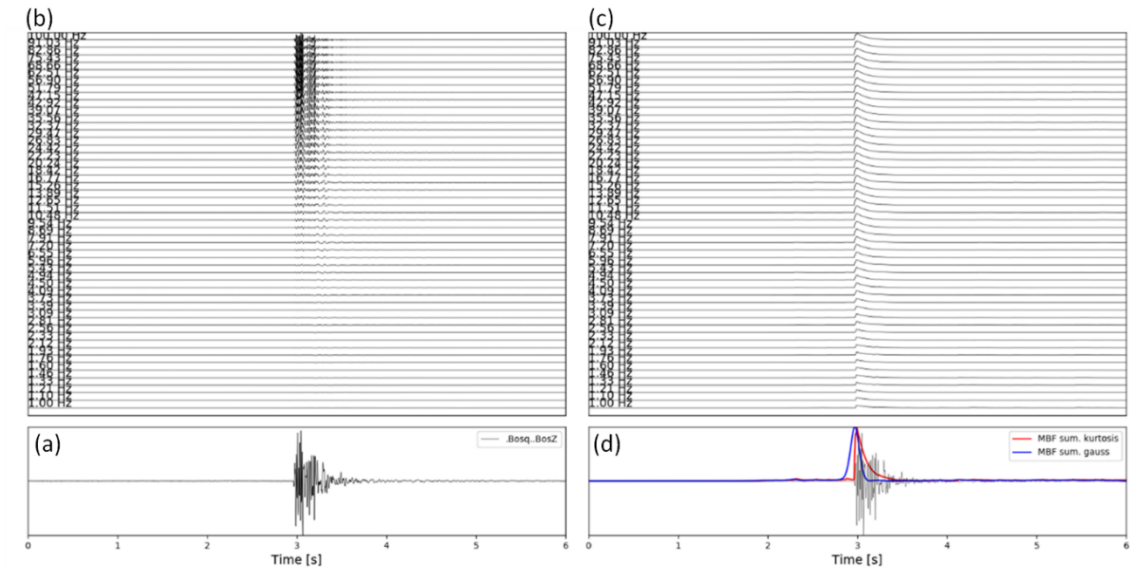

Figure 5.1 Example of the characteristic function of signal resulted in the first part of BTBB analysis. MBF filter is applied in frequency spectra from 1Hz to 100 Hz, in 50 bands on a logarithmic scale. a) raw signal of station Bosq, vertical component, b) MBF analysis applied to raw signal c) application of kurtosis to each frequency band d) sum of MBF kurtosis in red, and convolution of the positive derivation of CF with Gaussian function to reduce time uncertainties (blue)

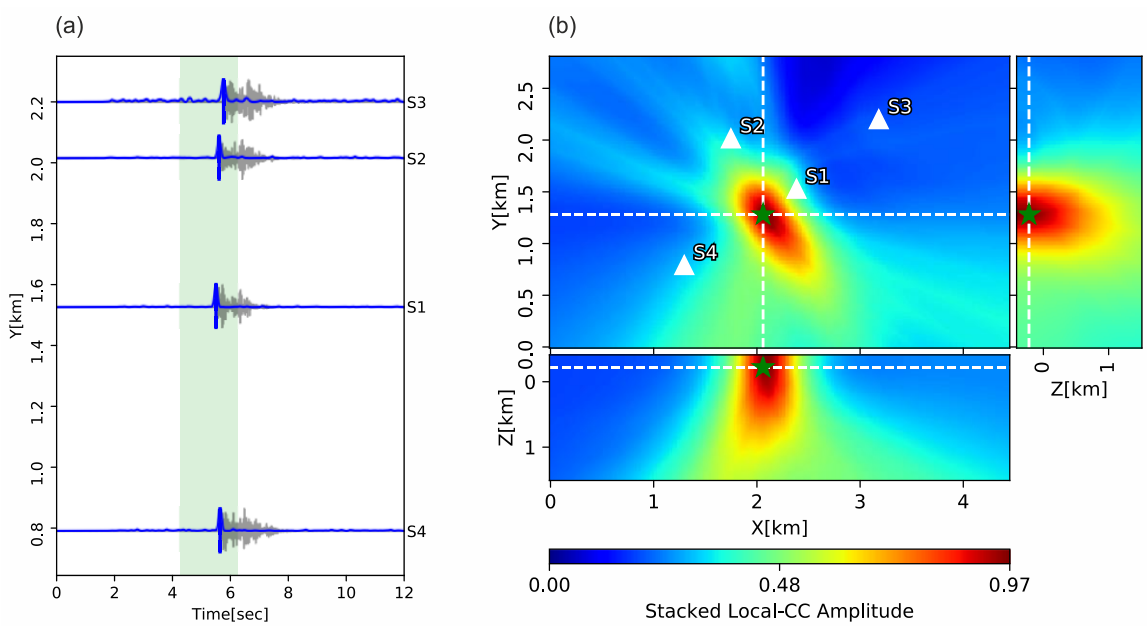

Figure 5.2 Example of successful detection and location of the seismic event as a result of the application of BTBB on extracted 12 seconds windows of vertical components of four available stations in the study area, containing a seismic event a) available traces (grey line) with final broad-band multi-band frequency characteristic functions (blue lines). Vertical blue bars indicate theoretical P-wave arrival times from estimated location b) A horizontal and two vertical sections thorough the maximum of imaging function

corresponding to determined location (green star) of an earthquake identified in the BRGM catalogue. White triangles correspond to station locations

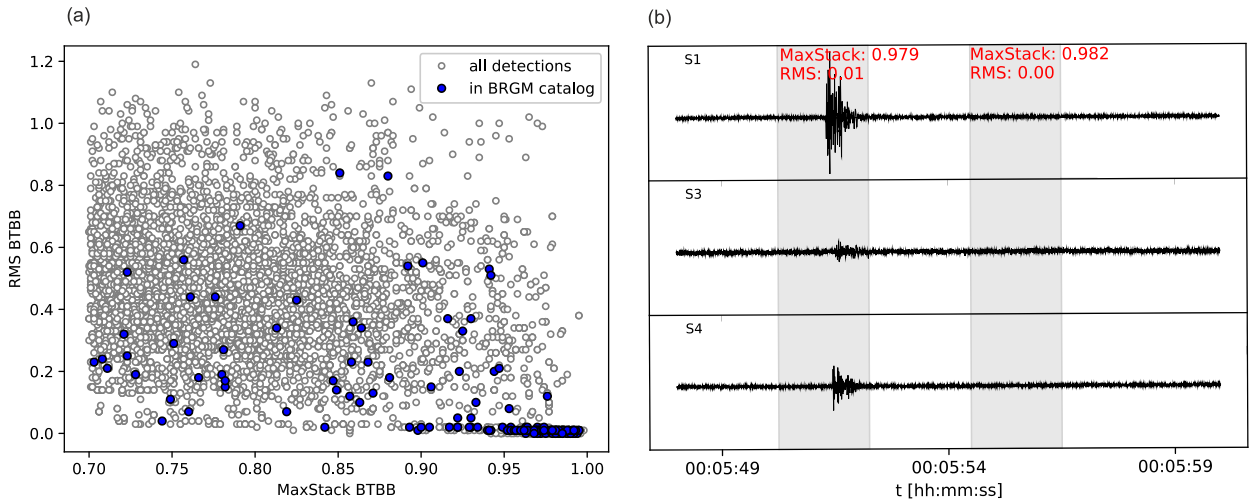

Figure 5.3 Challenges of discriminating between detected coherent noise and detected events when applying BTBB directly to continuous data of December 2014 testing dataset of 4 active stations, a) parameters MaxStack vs RMS of all detections (white dots) and seismic events identified from BRGM catalogue (blue dots). b) extracted 12 seconds window of vertical component recordings for three available stations, corresponding to the detections shown in a) with similar values of parameters in detection windows (grey areas), for seismic event and noise.

In order to exploit the benefits of the BTBB method automatic processing and refine the location accuracy, pre-processing detection and location steps with implemented noise removal criteria were developed, focused on reduction of noise in the data and minimizing the number of false detections. As shown in, the processing scheme is divided into detection and location steps, followed by a quality assessment scheme. This methodology follows a principle similar to the two-folded approach presented by Palgunadi *et al.* (2019).

The first step comprises a noise-robust, modified STA/LTA detection, applied directly to the time-continuous data in a moving time window. The second, location step consists of an amplitude-ratio based location algorithm, followed by a relocation with the BTBB method. An additional gain of this approach, besides noise-minimized detection and location of pre-BTBB processing, is the reduction of a large volume of continuous data to a more manageable data volume. Lastly, a classification scheme based on event location quality assessment was designed allowing to distinguish between high- and low-quality events and locations, consequently simplifying the interpretation of results. The final catalogue comprises the epicentral location, the local magnitude, the seismic moment and moment magnitude as well as a class assigned to each event based on an assessed quality of location. Steps are described more in detail in the following sections.

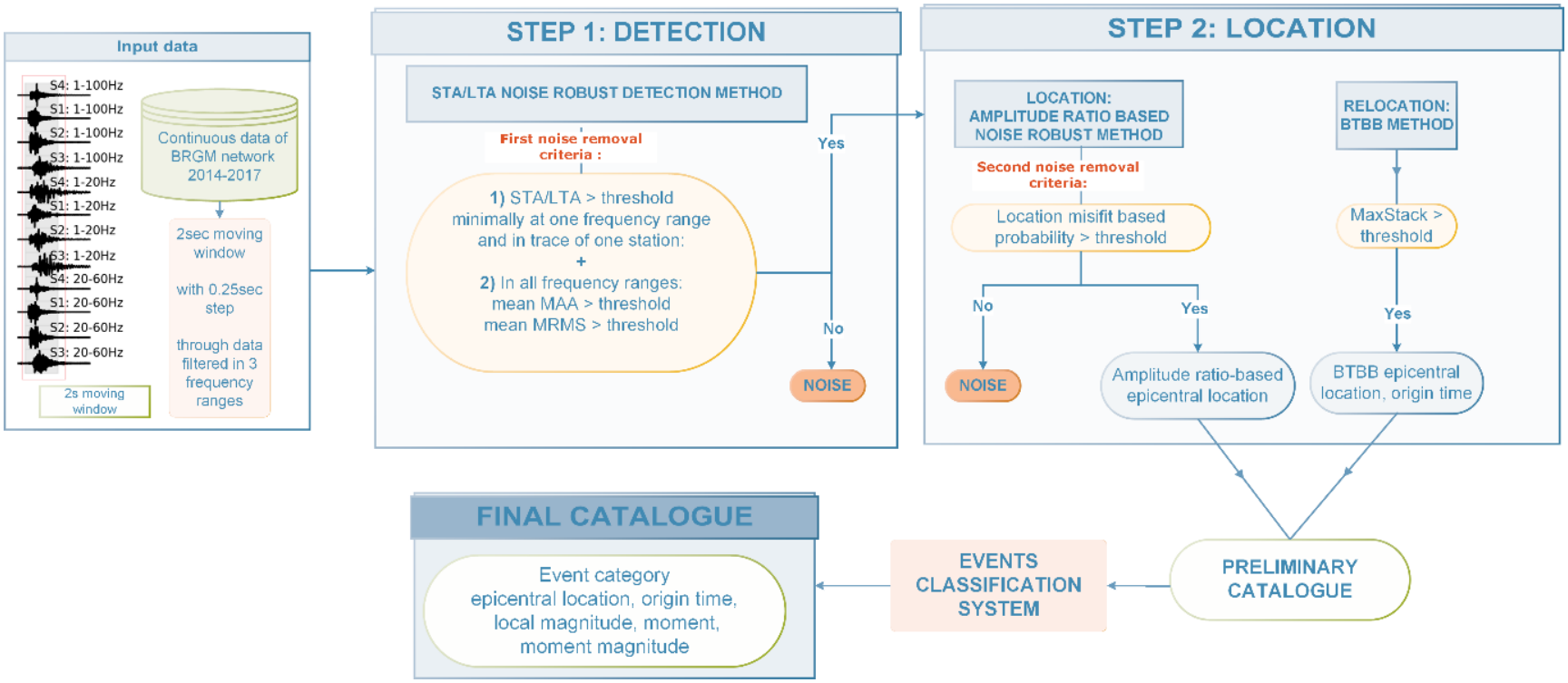

Figure 5.4 Scheme of detection and location methodology developed in this study. Main steps are detection (step 1) and location (steps 2), and event classification system based on location accuracy assessment. Final outcome is seismic data catalogue.

5.2 Step 1: Detection and first noise removal criteria using STA/LTA approach

In step 1, with the objective to detect potential events in the continuous dataset while simultaneously minimizing false detections, new parameters that are used to define noise removal criteria are introduced, within standardly used for triggering signal characterization method known as "short term average over long term average trigger" (STA/LTA) (Allen 1982, Withers *et al.* 1998).

Only the vertical components have been used in the analysis, allowing a wider application of the developed approach to other post-mining environments to the temporary monitoring networks consisting of one-component geophones.

By visually inspecting the spectral content of known events in the training data set, the dominant frequency range of the targeted events was identified. Correspondingly, further analysis was divided into three frequency bands: 1-20 Hz, 20-60 Hz and 1-100 Hz. The use of the multiple frequency bands allows a similar detection capacity for events with differences in spectral content due to the source size and location.

The filtered records (Figure 5.5a) are transformed into the characteristic function (CF) in each frequency band separately, using a recursive short-term average over long-term average (STA/LTA) algorithm (Withers et al., 1998) (Figure 5.5b). Both STA and LTA windows lengths are adjusted based on the frequency range. More details on STA/LTA recursive scheme used can be found in Annex Part II.

To declare that an event is recorded on at least one station within the moving time window, it is necessary that the maximum of STA/LTA of at least one signal of any station in one of the frequency bands is reaching the predetermined STA/LTA trigger value. The decision on the trigger value of the STA/LTA CF is based on testing several different STA/LTA trigger levels over the entire training dataset, taking into consideration the number of events of the BRGM catalogue that were triggered versus a total number of triggers. As it can be observed in the example in Figure 5.5b, this condition is reached in two different moving time windows, for both noise source and event source.

To reduce the false triggers, and further examine signal characteristics, two additional parameters are introduced: the maximum value of absolute STA/LTA CF amplitude (MAA) and the maximum value of root-mean-square STA/LTA CF (MRMS). The values of these parameters are calculated in 2 seconds moving time-window for CFs of each station, in all 3 frequency bands f_i separately. In general, the moving time-window length needs to be chosen based on the largest distance between the stations in the network to account for the maximum expected time delay between the signals of all stations. Choice of window length corresponds to approximately 1.5 times of the estimated maximum expected time delay of the farthest station pair in the seismic network (S3 and S4, with a distance of approximately 2.3 km between them) for S wave velocity of 1.8 kms^{-1}.

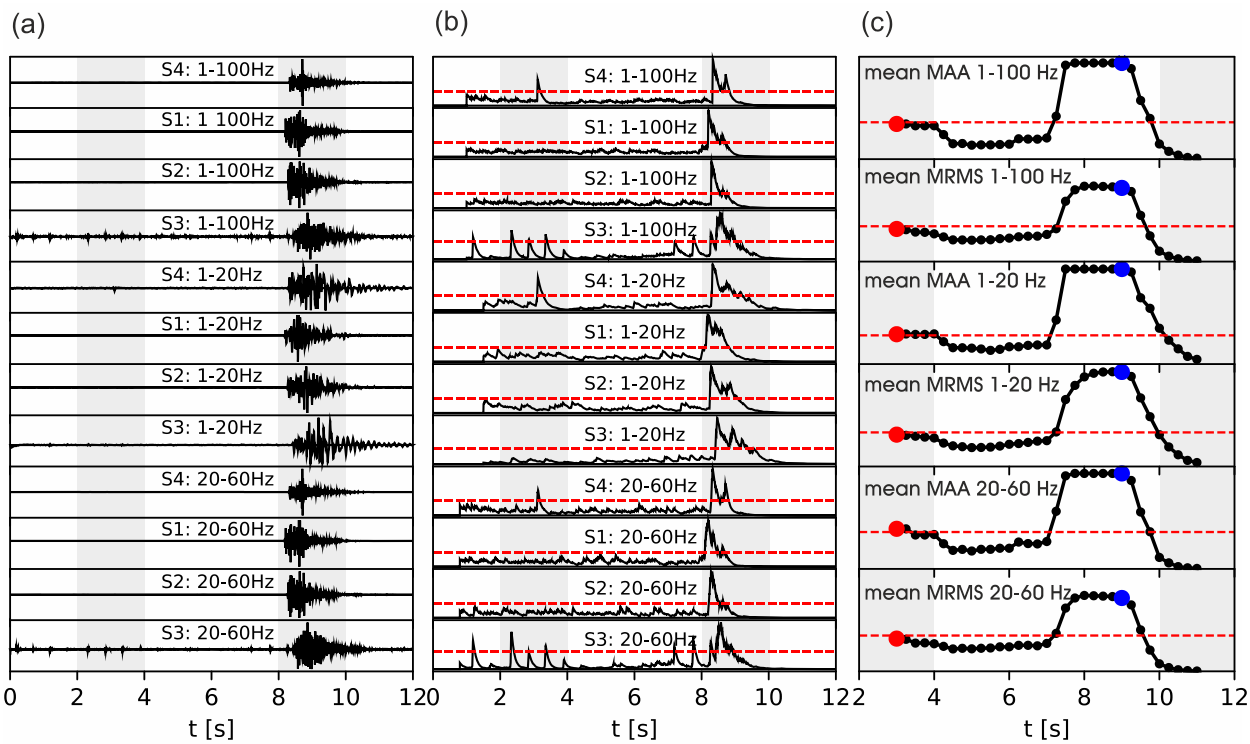

Figure 5.5 Example of step 1 processing for extracted 12 s window containing an identified seismic event from BRGM catalogue. a) Vertical traces for each station filtered in three frequency bands. b) STA/LTA CF of each filtered trace. The Red line indicates pre-set triggering threshold level. The threshold is reached for noise (window 2 – 4 s) and for the earthquake (window 8 – 10 s). c) Noise removal criteria parameters calculated in 2 s moving window (black dots, red and blue dots) with set threshold values (red dashed line). Noise check for windows whose CF was above threshold in b): values below the threshold for noise (window 2 - 4 s, red dot), values above the threshold for earthquake (window 8 – 10 s, blue dot)

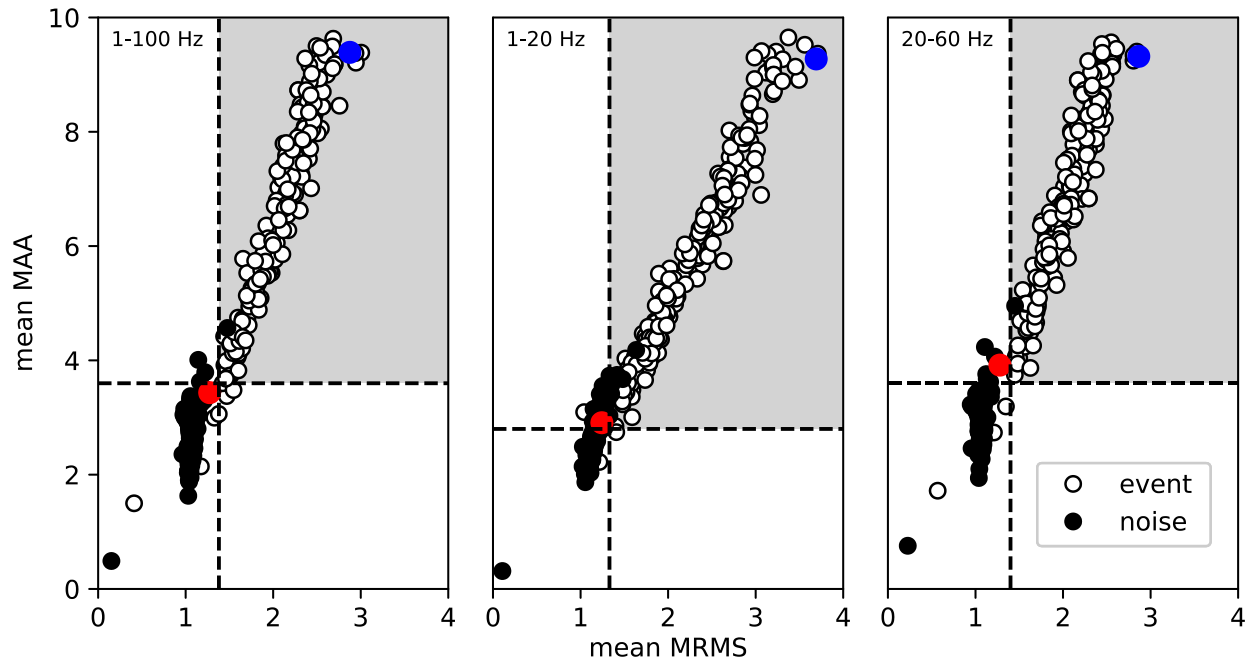

Figure 5.6 Setting threshold values in each frequency band for first noise removal criteria based on comparison of MAA and MRMS parameters of seismic events identified from BRGM catalogue and surrounding noise. Blue and red dots correspond to detections marked by blue and red dots in Figure 5.5c

Finally, the criteria parameters to separate noise and event are derived as mean values across all stations and for each frequency range separately:

$$mean\ MAA\ (f_i) = \frac{1}{n} \sum_{stations} \max \left| \frac{STA(f_i)}{LTA(f_i)} \right| \qquad [\ 5.1]$$

$$mean\ MRMS\ (f_i) = \frac{1}{n} \sum_{stations} \max \left(RMS \left(\frac{STA(f_i)}{LTA(f_i)} \right) \right) \qquad [\ 5.2\ ]$$

Choice of parameters MAA and MRMS for the noise removal criteria is based on the observation that seismic events in most cases have higher energy and a longer duration recorded at multiple stations compared to noise, implying that the RMS envelope of STA/LTA function and the maximum of STA/LTA function also have distinctly high values for events, compared to the values for noise. It can be observed in the example in Figure 5.5c, where points present values of parameters in equations [5.1] and [5.2], calculated for each moving time window.

Threshold values of parameters defined in equations [5.1] and [5.2], for each frequency band f_i separately, are determined based on the values calculated separately for all previously known events of the training dataset, already in the BRGM catalogue (213 events), and for preceding noise time windows. As it can be seen in Figure 5.6, in each frequency band, a representative range of values for both noise

and events can be distinguished. Nevertheless, due to the existing significant overlap in parameter values, the decision on threshold selection is subjectively adjusted based on the desired outcome (similarly to the setting of the STA/LTA trigger threshold, which can be either a more noise-free dataset but with the potential loss of weaker seismic events, or a dataset where the loss of seismic events is prevented but a higher number of false triggers remains).

The analysis of triggered 2 s time windows in multiple frequency bands indirectly enables the assessment of its spectral content. As the seismic events tend to have a wider spectral content compared to the more monochromatic noise sources, the trigger is declared as an event if values of parameters [5.1] and [5.2] reach the thresholds in all three frequency bands. Triggers are assessed as noise in case of a narrow-band detection and an inability to reach a threshold in all 3 frequency bands and are, therefore, removed from the dataset.

Values of parameters [5.1] and [5.2] for selected examples of detected noise and event (shown in Figure 5.5 and Figure 5.6) confirm the accuracy of our noise removal criteria.

Further applying the described noise-robust detection procedure to our testing dataset (one month of continuous data of December 2014) resulted in 603 potential event detections, with 94% of previously known events of the BRGM catalogue being correctly identified. Due to roughly three more times of detections in this step, compared to the 213 events in the BRGM catalogue within the observed area for the same period, as well as due to the unlikely possibility that such increase results from previously undetected events (even if some detected but non located events, due to low magnitude (Dominique 2016b) or human error during manual processing), a visual inspection of corresponding waveforms was performed which confirmed suspicions that the detection still contains some unwanted triggers. Therefore, detections are further de-noised and a preliminary seismic catalogue is created in the next step, by introducing a second noise removal criteria based on the amplitude-ratio based location approach

5.3 Step 2: Location and second noise removal criteria using the amplitude-based approach

Amplitude-ratio based location approaches, derived from attenuation law (Battaglia & Aki 2003), allow estimation of event location by determining the amplitude ratio of station pairs (Taisne *et al.* 2011) and minimizing the error between expected and observed values. The importance of this location approach, which is part of our methodology, is that it provides the means to recognize and remove the remaining triggered noise in the dataset resulting from the previous step.

The main idea behind the noise removal criteria that is introduced here is a significant difference in the values between the interstation amplitude ratios related to occurrences of noise and seismic events. These two types of signals manifest different attenuation behaviour due to differences in the source location, as seismic events are located at depth and often not in direct proximity to one particular station, on contrary to noise sources which are mostly at the surface and close to one station only. Consequently,

the noise sources will result in significantly higher amplitude ratio values between the closest station and the other stations, compared to amplitude ratio values of seismic event sources.

To determine the location of events, ideas of amplitude ratio-based location method previously applied to studies of salt solution mining microseismicity (Kinscher *et al.* 2015, 2016), and mining-induced microseismicity (Palgunadi *et al.* 2019) are followed. However, differences in the environment of the present study allowed us to introduce modifications and somewhat simplify the approach, following (Kinscher *et al.* 2015). More details on the approach used here can be found in Annex – Part II (Amplitude-ratio based method).

In the approach applied here, the attenuation law is described exclusively with a geometrical spreading, ignoring contributions from anelastic attenuation:

$$\log_{10}\frac{A_i}{A_j} = n\log_{10}\frac{r_j}{r_i} \qquad [5.3]$$

where A_i and A_j are the maximum amplitudes of signals at stations i and j, r_i and r_j are the source-station distances of the same station pair. Assumption of a body wave geometric spreading behaviour with $n = 2$ (Lay & Wallace 1995) provided a good fit for observed amplitude ratios as a function of the distance ratios obtained from manual location of the BRGM catalogue (Figure A2. 3 in Annex - Part II)

Indeed, it was confirmed that the fit is equally good for all frequency bands, justifying the choice of the frequency-independent attenuation model.

The location of a detected potential event is determined based on the L1 norm misfit between observed amplitude ratios and theoretical amplitude ratios of each station pair and at the potential source point l on the defined grid.

Following expression [5.3], the theoretical (expected) values of amplitude ratios $\boldsymbol{A_{i,j,l_{theortical}}}$ for each station pair are estimated as a function of the inverse ratio of hypocentral distances, on a grid of predetermined (potential) sources:

$$\boldsymbol{A_{i,j,l_{theortical}}} = 2\cdot\log_{10}\frac{r_{jl}}{r_{il}}\ for\ station\ pair\ (i,j)\ at\ grid\ point\ l \qquad [5.4]$$

The grid of potential sources of each station pair is simplified and presented as a 2D plane fixed to the mine layer depths, while stations are distributed on the surface. The size of the grid was set to 4440 m (in E-W direction) x 2770 m (in N-S direction), which frames the area of expected locations, based on locations of events in the BRGM catalogue. Spacing between grid points (potential sources) was set to 50 m, which represents the horizontal resolution of this location method. An illustration of the grid is presented in Figure 5.7.

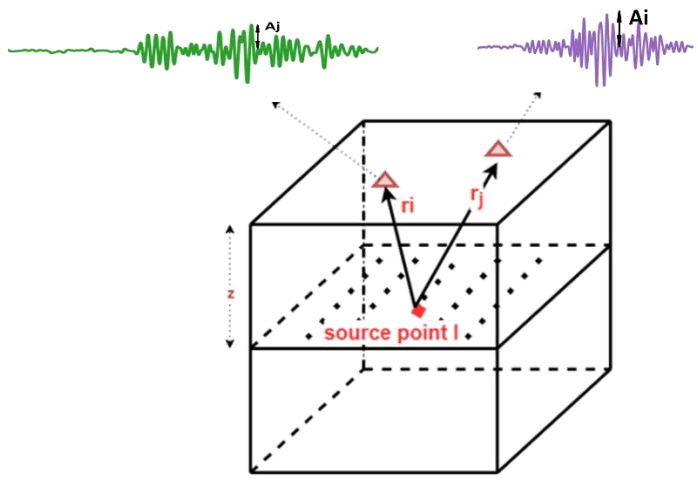

Figure 5.7 Illustration of a grid of one station pair and potential sources in a 2D plane at a depth z. Theoretical amplitude ratios are calculated in each potential source point based on the inverse ratio of their distances. Each station pair requires the calculation of the corresponding grid, i.e. the 2D plane of theoretical amplitude ratios at each potential source point

The observed amplitude ratio $A_{i,j_{observed}}(f_k)$ of a potential event for station pair (i, j) is determined as a ratio of the maximum absolute amplitudes, recorded at station i and j respectively, and filtered in the frequency band f_k:

$$A_{i,j_{observed}}(f_k) = \log_{10}\frac{\max|A_i(f_k)|}{\max|A_j(f_k)|}, for\ station\ pair\ (i,j) \qquad [5.5]$$

Observed amplitude ratios (equation [5.5]) for each station pair i and j are determined in a 2-sec time window corresponding to the trigger of the previous step.

For every point l on a defined grid of potential sources, the misfit between observed amplitude ratios and theoretical amplitude ratios of each station pair is determined, expressed in a form of a PDF, for a mean of the values observed over all station pairs, summing over the three frequency bands:

$$P(l) = \frac{1}{n}\sum_{f_k}\sum_{\substack{stat\\ pairs\ i,j}} e^{-\left|A_{i,j,l_{theortical}} - A_{i,j_{observed}}(f_k)\right|/2}, at\ grid\ point\ l \qquad [5.6]$$

where n represents the number of station pairs. The location of the event is determined as the grid point l with the maximum value of $P(l)$. An example of event and noise time-window located with this approach is shown in Figure 5.8

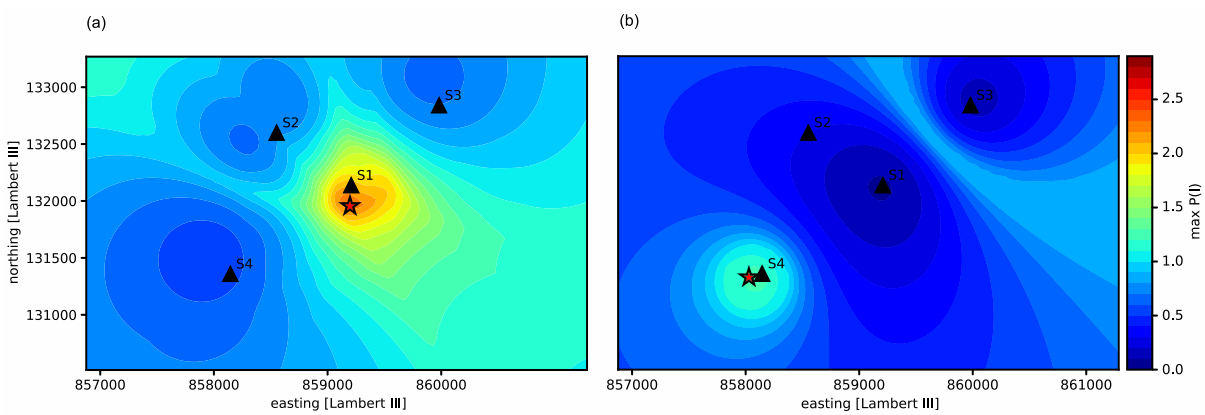

Figure 5.8 Example of amplitude ratio-based location method applied to the two detections passing first noise removal criteria. a) determined location of the event with P(l) value above second noise removal criteria threshold b) determined location of noise with P(l) value below second noise removal criteria threshold

The described amplitude-ratio based location approach was applied to all triggered time windows from December 2014 that passed the detection procedure with noise removal criteria in the first step.

As expected, due to differences in amplitude ratio values for noise and events, the histogram plot of maximum values of $P(l)$ for all triggers (Figure 5.9) reveals the bi-modal distribution of values, interpreted as two normal distributions: the one on the left, with lower probability values, corresponding to a distribution of noise and the one on the right, with higher probability values, corresponding to the distribution of seismic events, confirmed also by identifying the maximum of $P(l)$ values for events from BRGM catalogue, as shown in Figure 5.9. This observation is exploited to define the second noise removal criteria, by identifying the threshold value of $P(l)$ between events and noise. The threshold value in this case was determined as $P(l) = 2$ (black vertical line in Figure 5.9) which allowed the elimination of the remaining false triggers from the dataset.

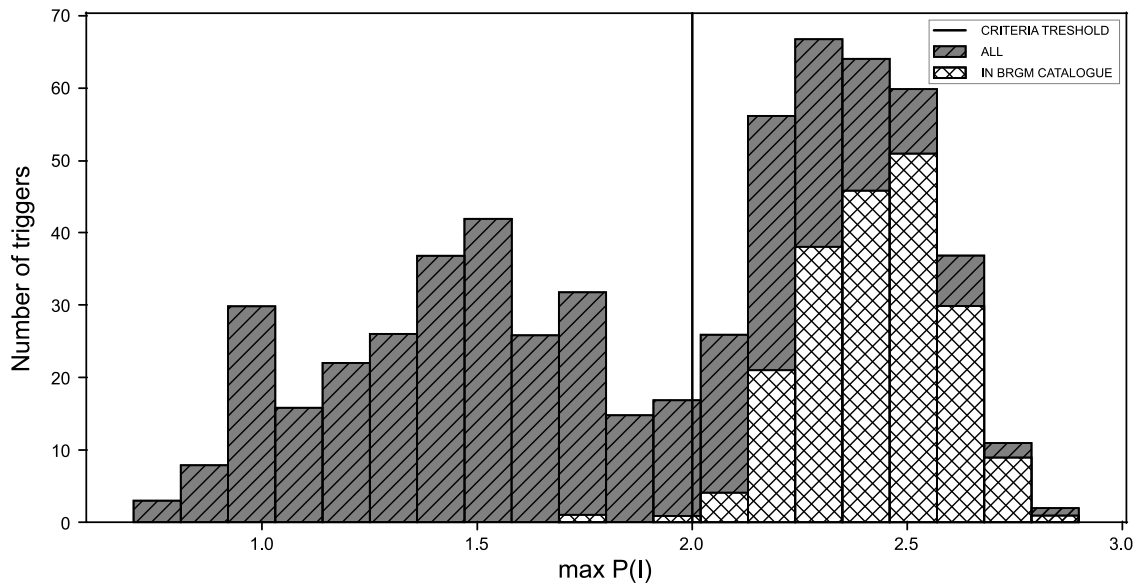

Figure 5.9 Bi-modal distribution of misfit probability $\boldsymbol{P(l)}$ values between observed and theoretical amplitude ratios, for all detections during December 2014 that passed first noise removal criteria and are located by amplitude ratio-based method (grey bars). $\boldsymbol{P(l)}$ values of seismic events from BRGM catalogue (white bars) allow setting a threshold value for second noise removal criteria (black vertical line at $\boldsymbol{P(l) = 2}$).

5.4 BTBB location

Events passing the second noise criteria were further relocated by BTBB.

BTBB was configured to calculate CFs in 50 logarithmically-spaced frequency bands covering the same frequency range from 1Hz to 100 Hz as in part 1 of our analysis. The theoretical P-wave travel times necessary for the second detection and location step are calculated using the Grid2Time routine of NonLinLoc program (Lomax 2005, 2008), over the grid covering the same horizontal extent as that for the amplitude ratio location approach, however, with a denser, 10 m, spacing and depths up to 1.5 km, with a constant homogeneous velocity model V_P =4.1 kms $^{-1}$ (Kinscher, 2017). The minimum value of the MaxStack parameter was set to 0.7, as a detection threshold criteria.

Even though BTBB determines location based on a 3D likelihood map, preliminary tests showed large errors in depth estimation, in comparison to the BRGM catalogue. Due to the low number of stations, all placed on the surface, dependence on the assumed velocity model and use of only P-phases, the depth resolution is not satisfying. Therefore, depth estimations were disregarded and the catalogue is limited to epicentral location.

5.4.1 Performance of detection and location scheme

Comparison of the events that were detected and located with our pre-BTBB steps, with the events of the BRGM catalogue for the period of December 2014, results in:

- a total of 314 events were detected and located in pre-BTBB processing (location by the amplitude ratio-based method), out of which 200 are BRGM catalogued events, while 114 events represent new detections.
- BTBB successfully relocated 177 events, 166 of which are in the BRGM catalogue. The number of relocated events is somewhat reduced, not only due to noise in the data but also due to the data availability that was limited sometimes to only 2 stations. Relocated with BTBB events have additional information of origin time.
- 94% of the BRGM catalogued events were detected and passed the first criteria, and within those, 93% passed the second noise removal criteria. As expected, a small number of events from the BRGM catalogue was left undetected (13 out of 213), due to values of their noise removal criteria parameters below the chosen threshold (due to high noise and/or low visibility), as can be seen in Figure 5.5 and Figure 5.6, or due to their origin outside of the defined grid.

5.5 Local magnitude determination

To complete the information in the new catalogue, a local magnitude, moment and moment magnitude were determined for each detected event as well.

The local magnitude was determined as a product of the absolute amplitude of an event in the frequency range 1-20 Hz, considering all events listed in the new catalogue, and source-station distance r averaged over a number of the available stations.

To calculate the source-station distance, the BTBB location is taken for events successfully relocated, otherwise it is taken as the amplitude ratio-based location. The local magnitude is expressed as follows:

$$M_L = \log_{10}(mean\,[(max|A| \times r]), \qquad [5.7]$$

and the determined values are in the range -1.38 to 1.7.

The relationship between moment magnitude Mw and local magnitude M_L (equation [5.7]) for the study region was investigated and estimated empirically, based on the data of 48 events of December 2014 for which values of Mw were available from a precedent study, while M_L determined in this study based on equation [5.7].

$$M_w = 0.68 \times M_L + 0.57 \qquad [5.8]$$

This expression was further applied to calculate the moment magnitude for all detected events. The seismic moment M_0 was determined based on the relation (Hanks & Kanamori 1979), where moment M_0 is expressed in N·m (Bormann & Giacomo 2010, Bormann *et al.* 2013), identical with the IASPEI (2005 and 2013) accepted standard form of writing the moment magnitude formula:

$$M_w = \frac{2}{3}\log M_0 - 6.1 \qquad [5.9]$$

5.6 Event classification and location quality assessment

To assess the quality of the new seismic catalogue in terms of location accuracy, the resulting location of 398 events in the period 2014-2015, common to the BRGM catalogue, are compared to the BRGM location, using it as a reference. During this period, our catalogue contains a total of 2154 detections, out of which 1691 are new events, not appearing in the BRGM catalogue. Within the same period, the BRGM catalogue overall comprises 677 events, out of which 143 are undetected with our approach.

As it can be observed in Figure 5.10, the BTBB location shows qualitatively a better consistency with the BRGM catalogue (especially for stronger events) than the amplitude-ratio based locations, which are more spread out.

As shown in Poiata *et al.* (2016), BTBB requires at minimum three stations to determine the event location (see Annex part II – BTBB principle), meaning that, in this case, a minimum of three records need to have visible P-phase arrival, with high enough signal to noise ratio. Even though all the detections have records of a minimum of 3 stations, events are often buried in noise and not visible on every available record, which can lead to false locations.

To identify these low-quality events, event visibility criteria were defined with STA/LTA function and threshold of 2 and further applied to all available records for each potential event.

Further, as shown in Figure 5.11, we determine location errors as a function of event visibility. The location errors are based on the comparison of both amplitude-based location and BTBB location with matching locations of the BRMG catalogue and defined as the Euclidean distance between them.

As expected, BTBB location error increases for low visibility events, (Figure 5.11a) while it provides better accuracy for events visible on a minimum of 3 stations, compared to amplitude-ratio based location (Figure 5.11b). Amplitude-ratio based location, as expected, provides more robust location quality for events visible on 2 stations only.

Events visible on a minimum of 3 stations are defined as events of A and B class, with high-quality BTBB locations. Events that are visible on less than 3 stations (n=26) are defined as C class events, and amplitude ratio location is assigned to them, as a better quality of location.

The location quality of BTBB for high-quality events visible on 3 or 4 stations (A and B class) was further assessed, as a function of local magnitude and visibility, as shown in Figure 5.12. This allowed discrimination between the highest quality events visible on a minimum of 4 stations with local

magnitudes equal or higher than zero, here defined as class A events (n=60), and events of somewhat less accurate location, therefore defined as class B events. (n=372). Based on the described observations, an event classification scheme was designed, shown in Figure 5.13.

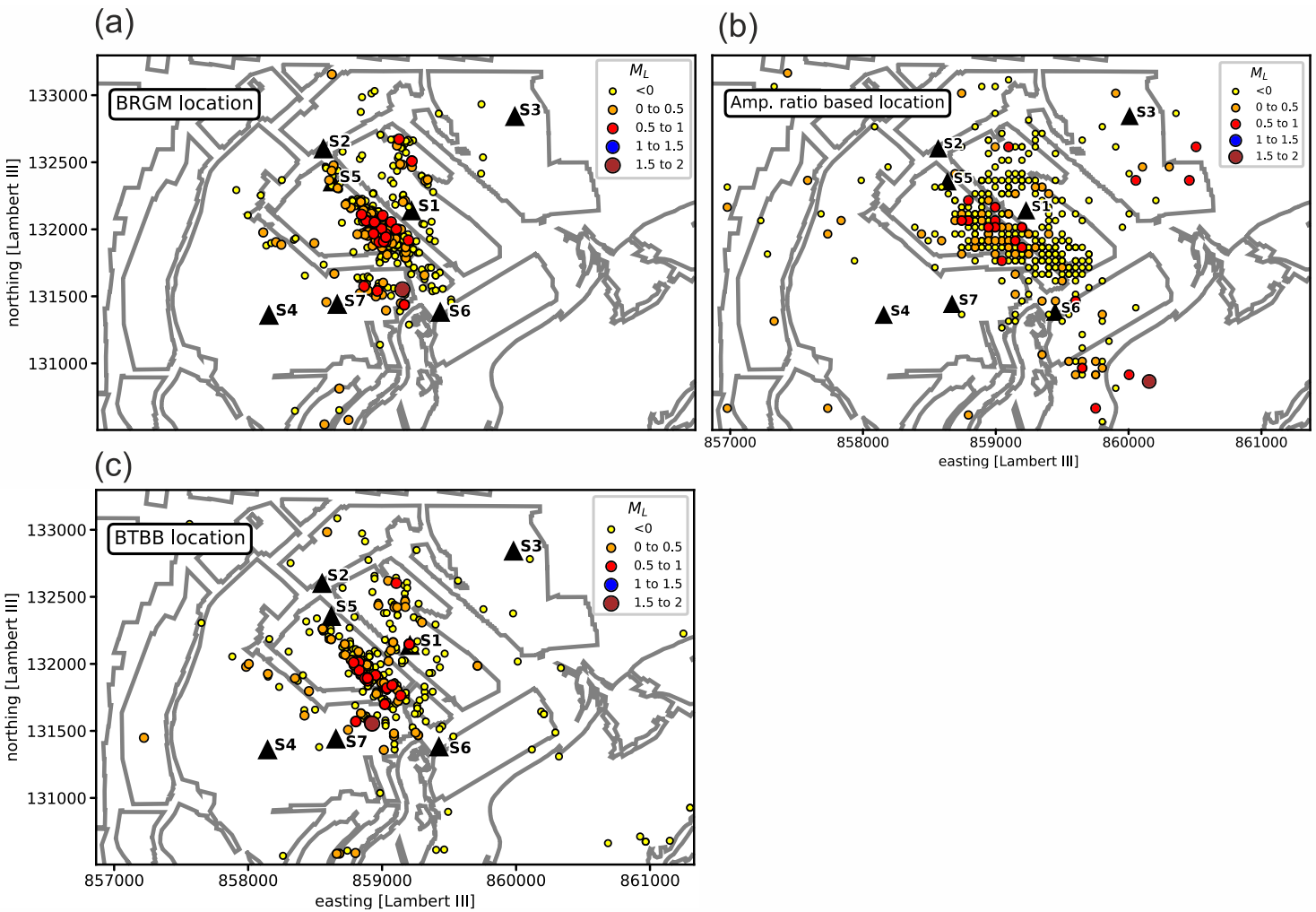

Figure 5.10 Comparison of locations determined in this study with 372 matching seismic event locations identified in BRGM catalogue during period of 2014-2015. a) BRGM location b) Matching events located by amplitude ratio-based method and c) Matching events relocated with BTBB

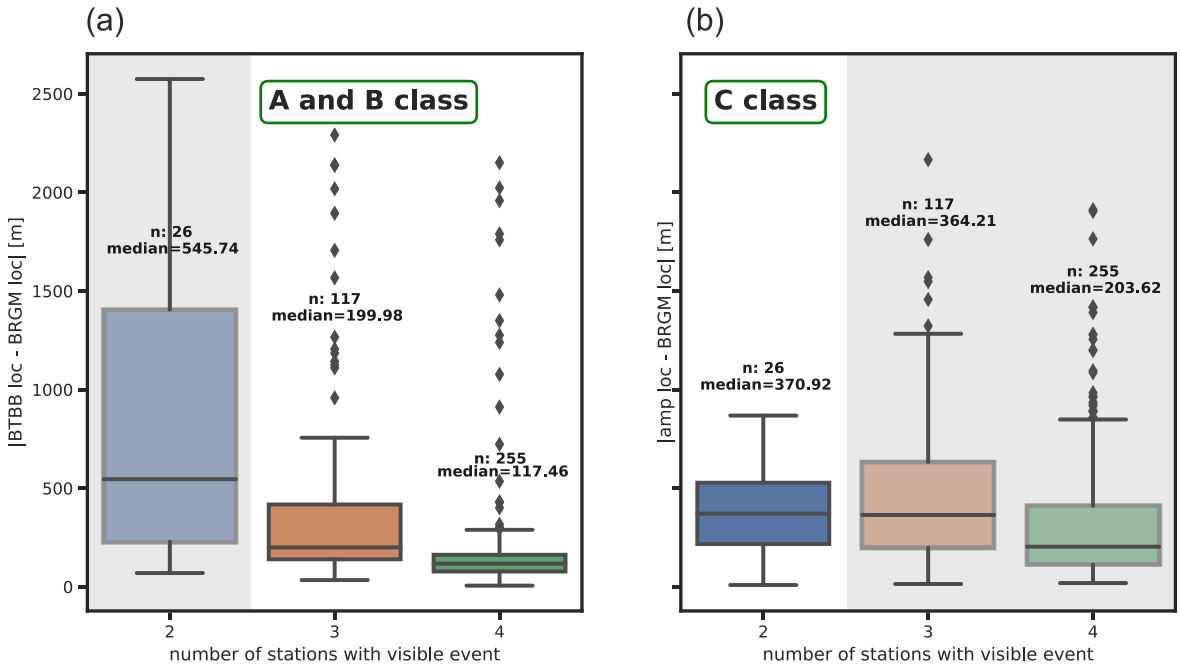

Figure 5.11 Identification of highest quality events based on location error as a function of event visibility. a) Error of BTBB locations, b) Error of amplitude ratio-based locations. Events with high visibility (minimum 3 stations) are classified as A and B class with BTBB location providing better quality than amplitude ratio-based method (white area in a) and the grey area in b)). For events with lower visibility (C class events), BTBB error distribution exceeds 2.5 km in some cases (grey area in a), while amplitude ratio-based location quality is more robust (white area in b). The box shows the distance between the quartiles, with the median marked as a line, and the `whiskers' show the extremes. Outliers, shown in the graph as separate points (diamonds), are the observations whose distance from the edge of the box (i.e. the quartile) is more than 1.5 times the length of the interquartile range. For each box, the median and number of events in the corresponding category (n) are shown.

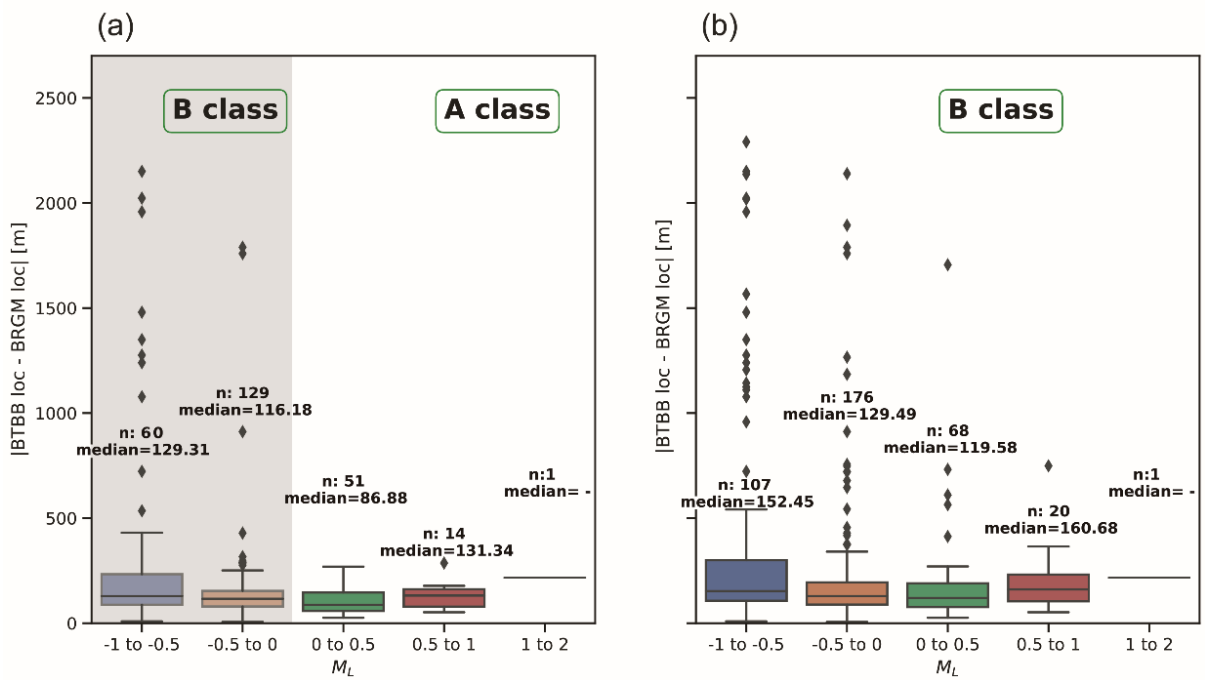

Figure 5.12 Error distribution of BTBB locations of class A and class B events as a function of event visibility and local magnitude distribution. a) error distribution for events visible on a minimum of 4 stations b) error distribution for events visible on a minimum of three stations. Highest quality events (class A) are determined as events with visibility on a minimum of 4 stations and local magnitude equal to or above zero. The remaining events (grey area in a) and white area in b) are classified as B class. The box shows the distance between the quartiles, with the median marked as a line, and the `whiskers' show the extremes. Outliers, shown in the graph as separate points (diamonds), are the observations whose distance from the edge of the box (i.e. the quartile) is more than 1.5 times the length of the interquartile range. For each box, the median and number of events in the corresponding category (n) are shown.

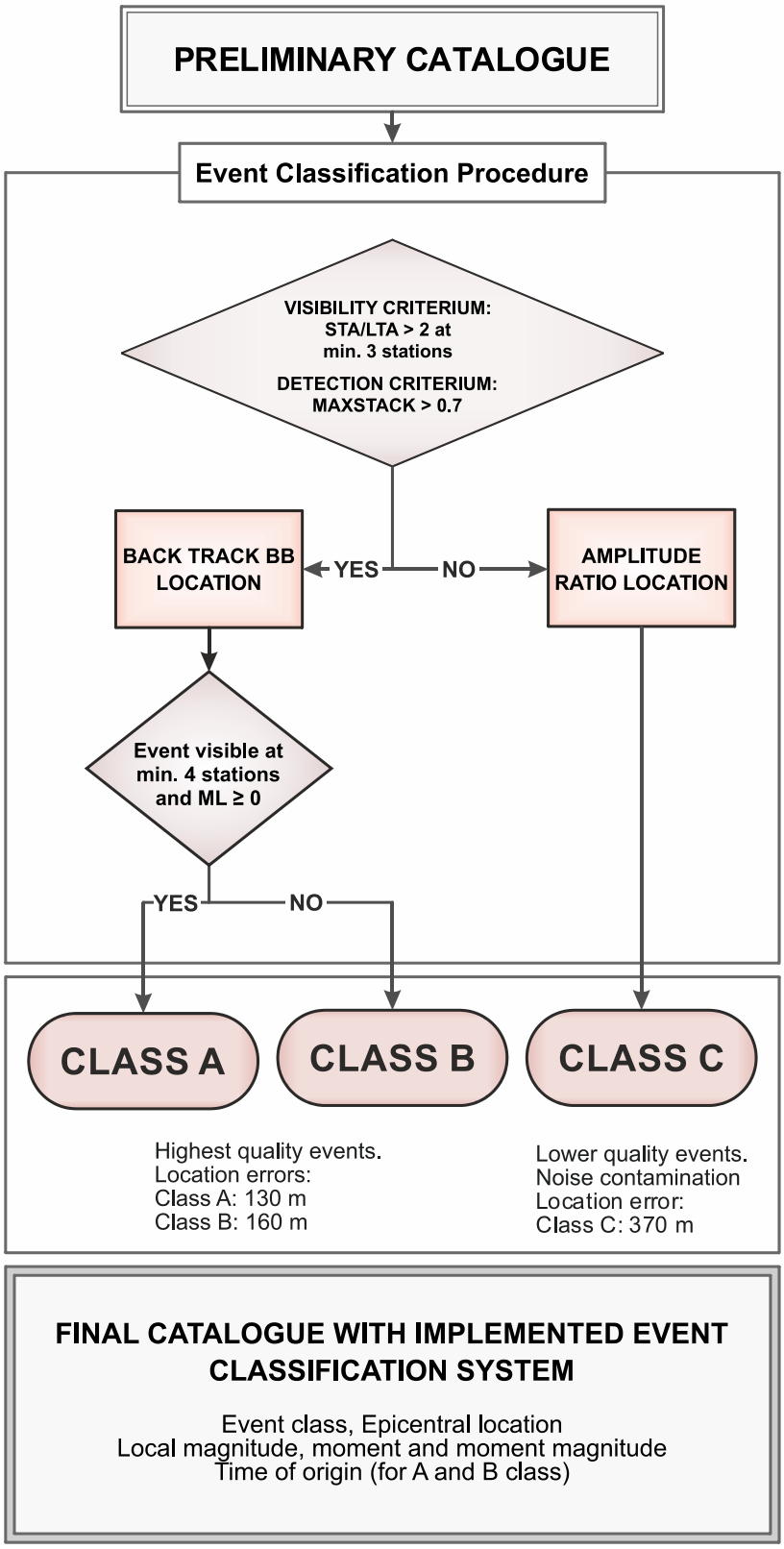

Figure 5.13 Event classification scheme based on location quality evaluation, applied to located events form a new catalogue of 2014-2017

6 Results – new catalogue of 2014-2017

6.1 Application of the new processing scheme to the 2014-2017 dataset

Following the earlier described steps, the new developed methodology was further applied to the entire training dataset, i.e. the continuous data of 2014-2017. Before analysis of the available continuous dataset, as a first step, data are preprocessed as described in Annex Part II – Data preparation.

Parametrization of step 1 and step 2 (such as threshold values, sliding window size, criteria values, grid size etc.) were kept the same as applied to the testing dataset of December 2014, BTBB configuration remained unchanged as well. Only changes compared to the testing dataset are changes of network configuration, which varies in time as well as space during these 4 years and, depending on the observed period, consists of 2 to 5 stations, distributed over 7 different locations. Hence for each event, it was necessary to update the configuration of the current network status, which was also automatized within the processing.

Local magnitudes, moment magnitudes and seismic moments were calculated as well for every detected event.

6.1.1 Comparison of catalogues

The developed classification scheme allowed the classification of all events in a new catalogue of 4-year (2014 – 2017) based on location quality. Out of 4705 events, 364 were classified as A class events, 1624 as B class events and 2717 as C class events.

To evaluate the method performance, the temporal distributions and the number of detected events of the new catalogue were compared with previously available catalogues: the BRGM catalogue, available for the period 2014-2015 and comprising 606 events within the studied area, and the Ineris catalogue for the entire period 2014-2017, comprising 790 events within the studied area.

As it can be seen in Figure 6.1, for the two periods of increased seismic activity (late 2014 and late 2016 to early 2017) all catalogues are consistent, and the high-quality A and B class events of the new catalogue provide a good match with both Ineris and BRGM catalogues while indicating an increased number of detections. However, low-quality C class events of the new catalogue indicate two additional seismically active periods (middle of 2014 and middle of 2015). As these apparent increases of seismic activity have not been previously observed, it broadly implies that C class events correspond to a mixture of small magnitude earthquakes just above the noise level with strong uncertainties in location as well as some remaining noise sources.

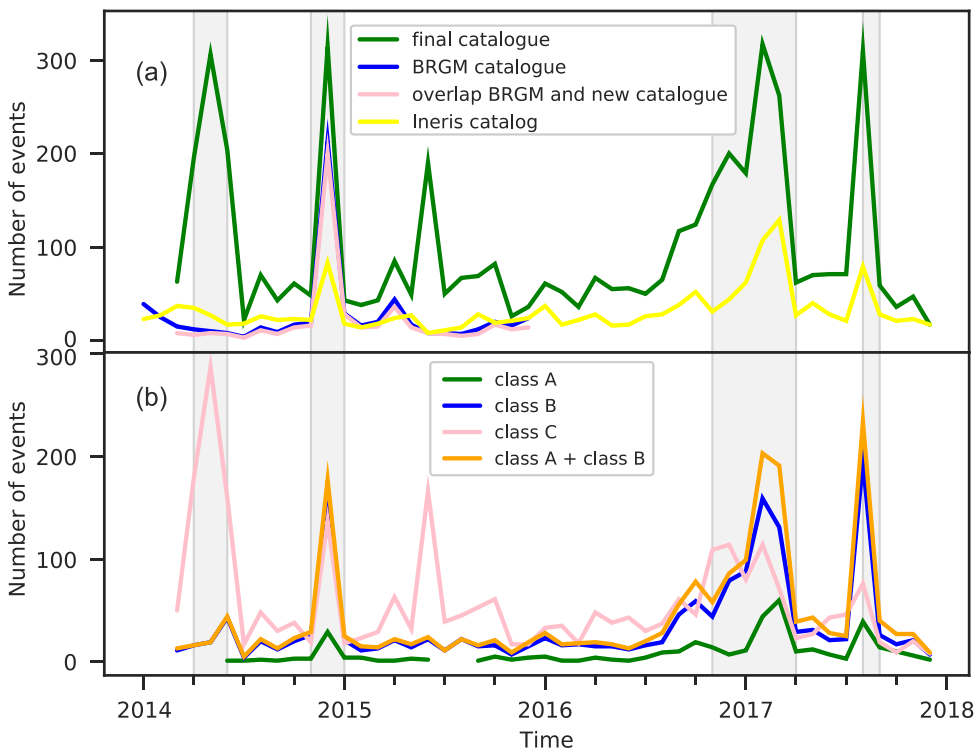

Figure 6.1 Temporal distribution of events in new catalogue 2014-2017 a) comparison with temporal distribution of events in BRGM catalogue, available for period 2014-2015, and events of Ineris catalogue for period 2014-2017, both limited to study area boundaries. b) temporal distribution of events of the new catalogue, separated into classes based on a developed classification scheme.

6.2 Classification scheme

The spatial distribution of events of the new catalogue of 2014-2017, separately for each class, is shown in Figure 6.2. As it can be seen, a clustering of the highest quality events of class A is clearly visible. The class B events, even though showing a somewhat more diffuse image, also indicate clustering. The spatial distribution of the C events is very diffused. These observations confirm the good functioning of estimated location errors and the classification approach. With this newly developed classification system, reliable assessment of the quality of the detected events is possible and it can be used as the basis of subsequent interpretation of the new seismic catalogue, which will be presented in further parts of this manuscript (Part III and Part IV).

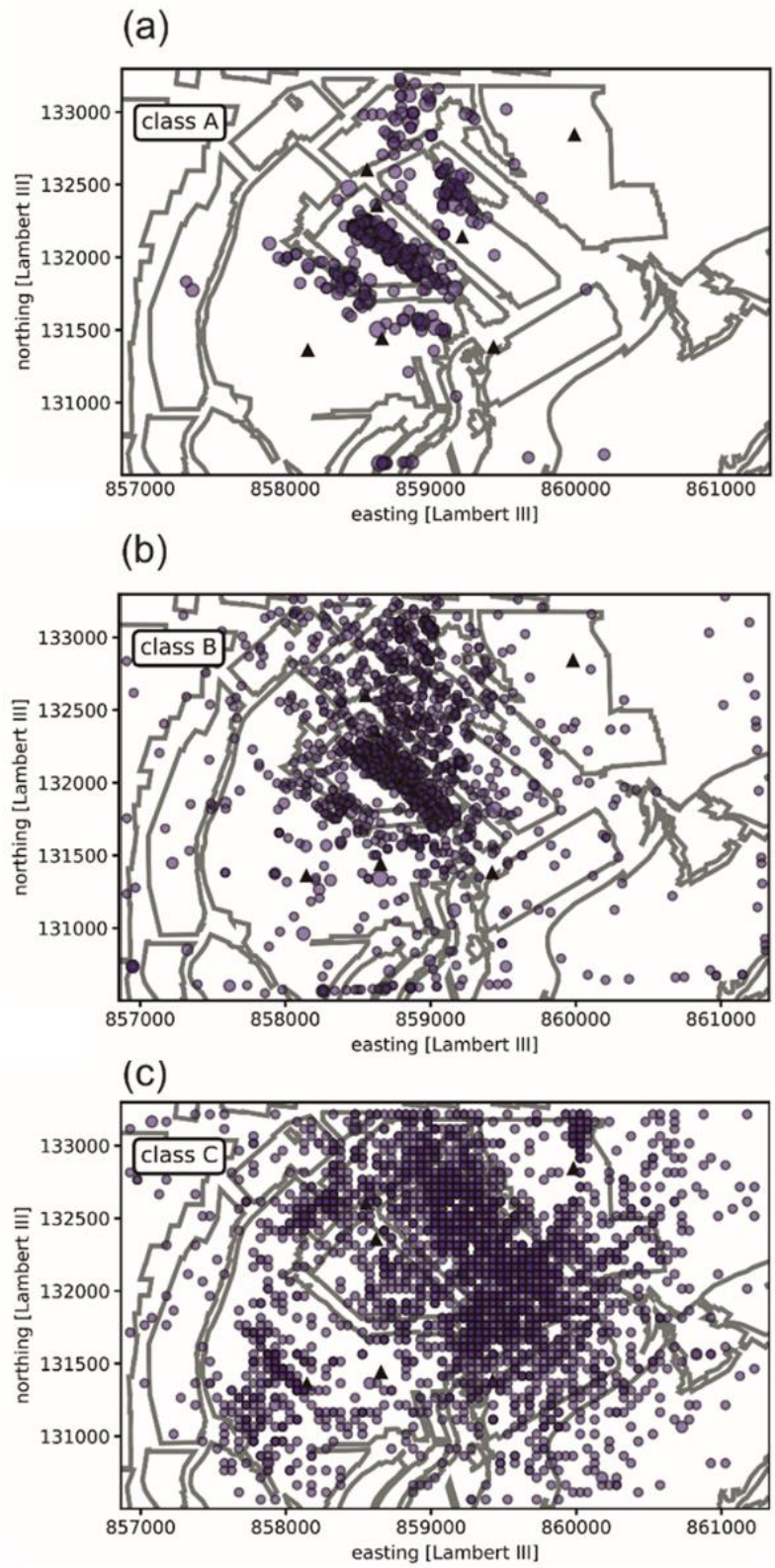

Figure 6.2 New catalogue 2014-2017 with events categorized and separated based on developed location quality-based classification scheme a) class A, 364 events, b) class B, 1624 events and c) class C, 2717 potential events**.**

6.3 b −value estimation and magnitude of completeness

To assess the reliability of the produced seismic catalogue and to estimate the magnitude of completeness (M_c), the well-known Gutenberg Richter relationship was used (Gutenberg & Richter 1949), which states that the logarithm of the number of seismic events N with magnitudes greater or equal to M depends on $\log_{10}(N) = a - b\,M$, where a characterizes the seismic rate, while the b-value describes the relative proportion between smaller and larger magnitude events which is usually around 1 (in natural tectonic environments).

Figure 6.3 shows the Gutenberg-Richter relation, moment magnitude vs events frequency distribution for the catalogue of A and B quality events (a) and all A, B, C events together (b). Furthermore, b -values were estimated by using the maximum likelihood approach by Aki (1965) and assuming different M_c as suggested by (Wiemer & Wyss 2000) (Figure 6.3 c and d). The final b-value was estimated by choosing M_c from which stability in b-value estimation is observed (gray shaded area in Figure 6.3d).

The determined b-values are very similar for both analyzed magnitude-frequency distributions and it is close to 1.5, for the Mc of around 0.2. The similarity between both distributions in b-value indicates that most of the detected C classes are likely true events. Indeed, in the case of dominance of noise events in the dataset one would potentially observe very unusual b-values as e.g., demonstrated by (Palgunadi *et al.* 2019).

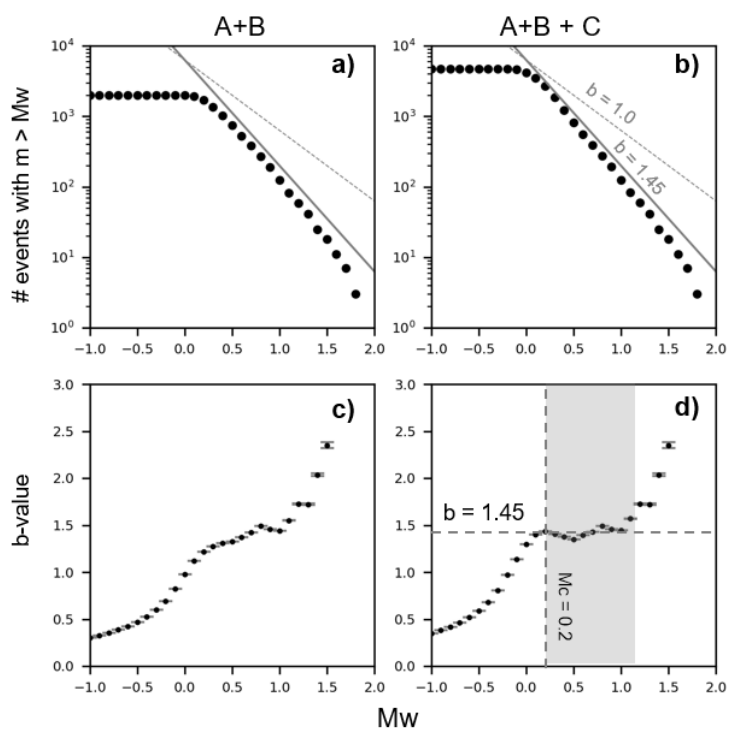

Figure 6.3 Gutenberg-Richter's b-value variability and uncertainty for seismic catalogues of A and B (a) and A, B, C events (b). b-values are estimated using the maximum-likelihood approach by Aki (1965), for

different assumed M_c, while standard deviations (grey error bars) are estimated following Shi & Bolt (1982)

7 Conclusion

The methodology described in Chapter 5 presents a new methodology for detection and location of events registered by a sparse network, developed as a part of this thesis. It represents the first application of a BTBB method, initially developed for larger-scale dense seismic networks, to the continuous data recorded by a sparse seismic network in the post-mining setting of the Gardanne mine. A new noise removal approach was developed to overcome the difficulties of station number limitations.

This approach enabled the analysis of 4 years records of seismic continuous data. Results show that the new methodology provides robust noise analysis and an increased number of detected microseismic events, allowing in next steps improved statistical analysis of seismicity and a better understanding of seismicity triggering mechanisms. Comparing the locations of new catalogues with both BRGM and Ineris catalogues (where location is determined with travel-time based methods), new methodology results in increased location accuracy, allowing more detailed identification of seismically active structures. Processing is automatized which enabled the processing of large volumes of data.

For the events that could not be relocated with BTBB due to low visibility, the amplitude ratio method provides successfully first order locations even for events with low SNR. The downside is higher location error, as maximum amplitudes on stations where events are buried within noise can be misrepresented. However, the primary objective of the amplitude ratio method is recognition and removal of noise as a part of pre-processing the large amount of data was reached. Events that passed visibility criteria were relocated with the BTBB method.

Hence, the quality of the results i.e. location accuracy is related to several factors:

- the number of stations used
- SNR (i.e. event visibility)
- knowledge of the velocity model
- configuration choices such as the size of the grid of potential sources.

Finer location requires a finer grid (i.e., a larger number of potential sources), however, this leads to an increase of the computation time.

As it is usual with the waveform-based location methods (e.g., Grigoli *et al.* 2014), BTBB is more computationally expensive compared to travel-time methods.

The developed approach has a potential for implementation as (near) real-time operational seismic monitoring in the Gardanne site, as well as in others sites with sparse networks. It can be particularly useful when a monitoring network comprises only one-component instruments, as is often is the case for the mobile or temporary deployments of task-force missions during the periods of stronger seismic activity.

Location quality-based event classification system allowed distinguishing of high-quality events (higher magnitude and/or higher SNR which allowed visibility at minimum 3 stations) from events buried in noise, which led to the identification of seismically active structures, and allows more detailed analysis of seismic characteristics as well as the connection of seismic activity with the hydrogeological conditions.

PART III
Cluster and multiplet analysis

Introduction

In this part, previously observed multiplet phenomena (Part I) and spatial event clustering (Part II) is analyzed in more detail in space, time and energy. Multiplet and cluster analysis aims at the identification and characterization of the underlying mechanisms and processes generating seismicity, which are discussed in Part IV. For the analysis, the seismic events of the new seismic data catalogue of 2014 – 2017 are mainly used, completed by data and seismic catalogue of the permanent network to obtain information on the period prior to 2014.

More precisely, the analysis is presented as follows:

First, Chapter 8 provides background, state of the art and definitions on different phenomena related to seismic clustering and particular phenomena known as multiplets and seismic repeaters (partly introduced in Part I). Chapter 9 focuses on the identification and spatio-temporal distribution of clusters of new catalogue 2014-2017 by applying the K-means approach. To reconstruct cluster activity back to 2008, a multiplet clustering approach is applied, as explained in Chapter 10. Chapter 11 and Chapter 12 present a more detailed analysis of the most important multiplet groups using more local stations of the temporary network (2014-2017) as their spatial proximity, temporal recurrence mode and potential interaction with the objective to characterize the underlying triggering mechanisms as later discussed in Part IV.

8 State of the art regarding clustering and multiplets

8.1 Clustering and underlying physical phenomena and mechanisms

Seismic clusters can be generally seen as a group of seismic events of similar type and magnitude concentrated in space and time. Clustering behaviour has been observed in the case of aftershock sequences (Dietz & Ellsworth 1990, King *et al.* 1995, Toda *et al.* 1998), that occur usually in the vicinity of preceding main shock events, as well as during seismic swarms which represent seismic activities of small to moderate magnitude events without any true main shock events (Hainzl & Ogata 2005, Dahm *et al.* 2012, Hainzl *et al.* 2012).

Swarming is often linked to the presence and migration of fluids in the subsurface, activated due to local concentration of high stress in a multitude of cracks or small faults, where the lack of a distinct major active fault limits the maximum magnitude potential, as well as the spatial extent (Kapetanidis *et al.* 2015). Examples where swarming has been documented include:

- a natural hydrofracturation or hydrostimulation process (e.g., Hainzl & Fischer 2002)
- fluid pressure fluctuations (Ake 2005)
- creep or aseismic slip of faults with induced ruptures on single asperities (Bourouis & Bernard 2007)
- the interplay of aseismic slip and fluid diffusion (De Barros *et al.* 2020).

Classical aftershock type events are most commonly interpreted as the result of stress transfer between neighbored faults (Stein *et al.* 1992, King *et al.* 1995, Stein 1999) associated with a weakening rate- and state-dependent friction behaviour (J. H. Dieterich 1994, J. Dieterich *et al.* 2000), induced by the direct effect of seismic stress change produced by the mainshock (post-seismic relaxation). Apart from the model of Dietrich, a variety of mechanisms of stress transfers have been proposed for triggering of earthquakes aftershock sequences, some of them also explaining sometimes observed delay in triggering. They include:

- aftershocks driven by fluid-driven from pore pressure diffusion (Nur & Booker 1972, Bosl & Nur 2002, Ross *et al.* 2017), where fracture that redistributes shear stress in a porous medium produces local fluid pore pressure changes. Decay of this pore pressure due to flow causes strain or generally involvement of high fluid pressure (Richard H. Sibson 1996, Streit & Cox 2001, S. A. Miller *et al.* 2004, Micklethwaite & Cox 2006). Most recently, Miller (2020) proposed a new model of long-duration aftershock sequences that are predominantly fluid-driven, numerically demonstrating that aftershock decay rates can reflect the tectonic ability to re-seal the co- and post-seismically generated fracture networks. In his model, fracture healing through time suppresses subsequent fluid flow and thus aftershock production, while the duration of aftershock sequences are dependent on tectonic ability to close the fracture networks (which is reduced in extension zones).

- aftershocks as sequential failures (secondary aftershocks) with triggered earthquakes promoting new earthquakes on nearby faults (e.g., Felzer 2003)
- aftershock due to postseismic stress changes which include viscous relaxation (e.g., Pollitz 2002) poroelastic rebound when excess fluid pressures recover to their pre-quake state (e.g., Peltzer *et al.* 1998)
- afterslip where the unrelieved accumulated strain on the fault causes aseismic slip along the fault surrounding the coseismic slip patch (e.g., Hearn 2002).

8.2 Multiplets and repeaters

The presence of multiplet events is often observed within events of spatially clustered seismicity, characterized as a group of earthquakes with similar waveforms that occur in close proximity from each other, at different times (e.g., Geller & Mueller 1980, Poupinet *et al.* 1984).

If there is evidence that multiplet events are co-located and share the same slip area then they are generally referred to as seismic repeaters (e.g., Uchida & Bürgmann 2019).

In practice, the classification of both multiplets and repeaters as well as their distinction is not straightforward and is still part of ongoing scientific debates (e.g., Uchida 2019). The most common and here used criteria to distinguish between the multiplets and repeater is to estimate the amount of overlap between two sources by comparing their relative location and source radii (Figure 8.1 a,b,c). Seismic repeating events, i.e. events occurring in the same seismic source (e.g., asperity), thus refer to the case when the source radii of each event cover the hypocenter of the other repeating events (Figure 8.1 a). Event groups showing partial source overlap are generally referred to as multiplets (Figure 8.1 b), while neighbored events without overlap are here referred to as aftershock type events (Figure 8.1 c).

Seismic repeaters are commonly interpreted with the asperity model, as repetitive rupture on seismic asperity (i.e. locked fault patch) surrounded by slowly (aseismically, creeping) slipping fault plane, as shown in Figure 8.1 e, where loading and rupturing of asperity depends on the surrounding creep rate. Here creep refers to aseismic motion on faults associated with a velocity-strengthening behaviour, i.e. the increase of friction with increasing slip velocity (e.g. Marone *et al.* 1991).

Seismic repeaters have been documented in different environments as e.g.

- in creeping portions of main tectonic faults (e.g., Vidale *et al.* 1994, Robert M Nadeau & Johnson 1998, R. M. Nadeau & McEvilly 1999, 2004, Rubin *et al.* 1999, Schaff *et al.* 2002, Waldhauser & Ellsworth 2002, Naoki Uchida *et al.* 2003, Waldhauser & Schaff 2008, Weston & Shirzaei 2016, Schmittbuhl *et al.* 2016)
- in aftershock sequences, related to afterslip (e.g., Papadimitriou *et al.* 2017, Yao *et al.* 2017, Wennerberg & Sharp 1997, Schaff *et al.* 1998)

- from fluid-induced creep in injection experiments (Bourouis & Bernard 2007) and natural environments (e.g Godano *et al.* 2014, Lambotte *et al.* 2014, Duverger *et al.* 2015)
- in mining environment (e.g., Naoi, Nakatani, Igarashi, *et al.* 2015, Naoi, Nakatani, Kgarume, *et al.* 2015, Yamaguchi *et al.* 2018, Kinscher *et al.* 2020).

In this study, multiplet events are referred to as a transition class between aftershock events and repeaters and are thus generated from cross-triggering mechanisms which can involve stress transfer, creep and fluid pressure changes. The interaction of these different driving forces may lead to partial repeat rupture on the same and/or neighbored asperities on the same fault segment as well as a subsequent rupture on neighbouring interacting faults. A good example of such a complex interaction of different driven forces causing multiplet occurrences with partially more repeater like and partially more aftershock like attributes have been studied in the rift of the Corinth region (e.g., Duverger *et al.* 2018).

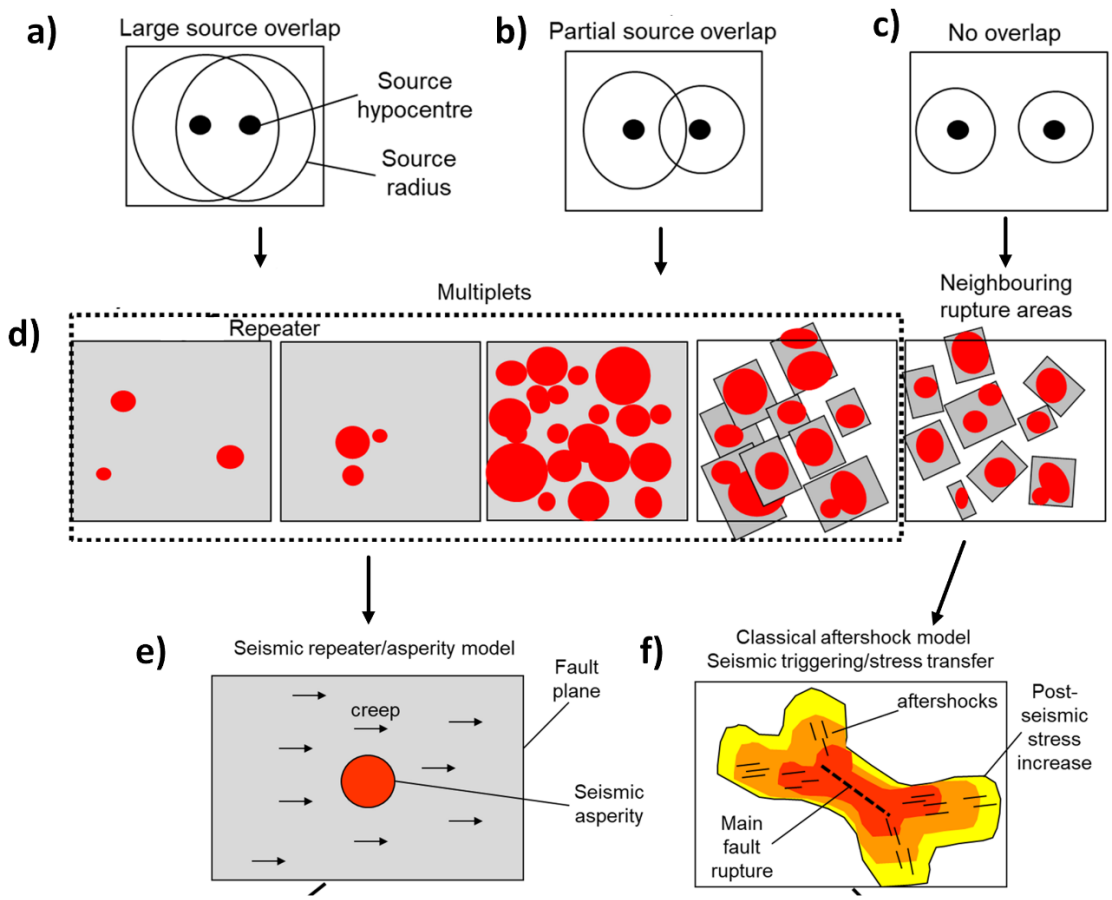

Figure 8.1 Illustration of criteria to distinguish between the multiplets and repeater by estimating the amount of overlap between two sources by comparing their relative location and source radii a) seismic repeating events b) multiplets, c) aftershock type events d) events on faults/faults segments e) model of

asperity with the surrounding creep f) mainshock-aftershock model. Adapted from Bourouis & Bernard (2007), Bernard (2014), Kinscher *et al.* (2020)

8.3 Repeat/Recurrence time

Classical aftershock pattern in time generally follows the well known Omori power law (Omori 1894) which refers to the characteristic 1/t decay rate of the number of earthquakes over time. The prediction of duration and rate of the Omori pattern (and their distribution in space) is still part of the current scientific debate and do generally depend on the involved processes.

Seismic repeaters can vary be generally classified into two main groups:

I) Long-lasting (or continuous type), which is usually observed at tectonic plate margin associated with periodic recurrence interval. Probably continuously creeping fault around the same mechanical asperity "proportional" to static tectonic loading; where recurrence rate depends on loading rate (e.g. (Nadeau & Johnson 1998, Mesimeri & Karakostas 2018)

II) Short-term (or burst type), linked to transient driving forces, such as afterslip, fluid pressure changes and volume changes (excavation) and occur during periods ranging from days to years

In some cases, short-term repeaters are characterized by Omori type repeat rates, which is often interpreted as the creeping behaviour (velocity strengthening friction behaviour) of the fault (Marone *et al.* 1991) loading the seismic asperity (Schaff *et al.* 1998, Bourouis & Bernard 2007, Kinscher *et al.* 2020).

9 Spatial cluster analysis

9.1 K-means clustering method

As seen in Figure 6.2 presented in Part II, clear space clustering behaviour of events from the new catalogue can be easily observed, particularly for the highest quality events of class A. To avoid subjectivity due to the difficulty of accurately assigning events to clusters "by eye", and due to the absence of other information on the seismic source such as focal mechanism, faults locations etc., an automatic clustering method was applied to A and B class events of new catalogue 2014-2017 to discriminate between clusters in an objective manner.

K-means method was chosen as it is a simple unsupervised machine learning algorithm that groups data into a pre-specified number of clusters (k). Developed by Hartigan (1975), Hartigan & Wong (1979), it is a clustering algorithm with Euclidean square distance metric, based on a central point (centroid), where M points are assigned to K clusters while each point is allocated to only one particular cluster. The principle of the algorithm is shown in Figure 9.1: k centroids are first randomly initiated (Figure 9.1a), followed by the step where the data are initially randomly partitioned into k clusters and iterative process where the mean position of each group calculated, and then the data re-partitioned by allocating each event to its nearest mean cluster position presenting new centroid (i.e. expectation-maximization steps, Figure 9.1b). Final results where iterative process converges is shown in (Figure 9.1c) (Weatherill & Burton 2009, VanderPlas 2016).

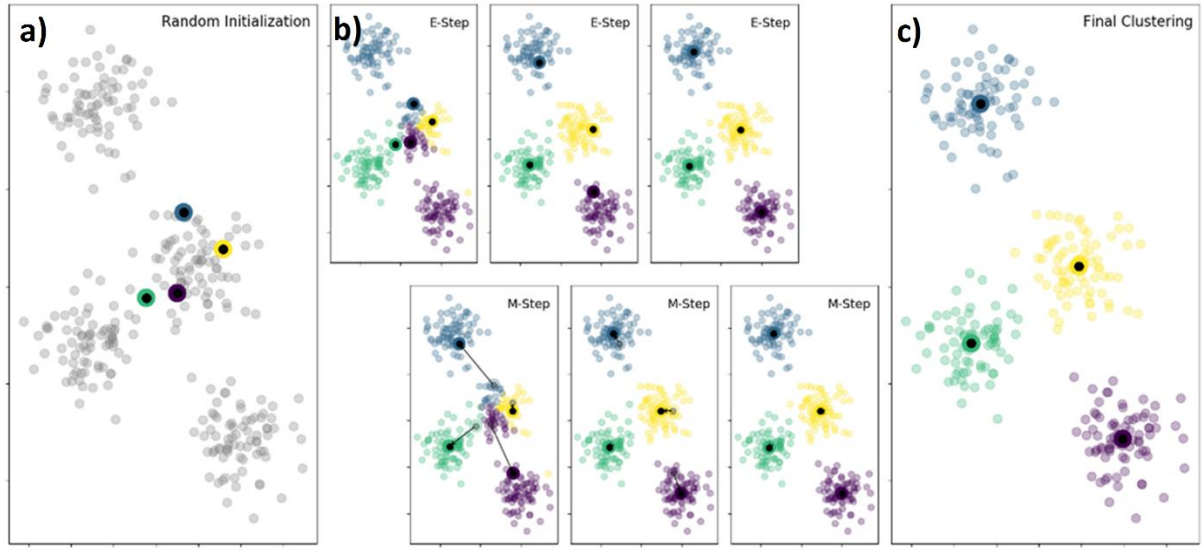

Figure 9.1 K means basic principle: Example of a dataset containing four distinct clusters. a) random initiation of cluster centroids b) iteration Expectation–maximization. c) Final clustering. Code source for the figure taken from Python Data Science Handbook, https://jakevdp.github.io/PythonDataScienceHandbook/05.11-k-means.html#K-Means-Algorithm:-Expectation-Maximization (Accessed: 18/02/2021)

The optimal clustering which represents the basis of the k-means model is based on two assumptions:

- The "cluster centroid" is the arithmetic mean of all the points belonging to the cluster;
- Each point in a cluster is closer to its own cluster centroid than to other cluster centroids.

K-means has been most widely used for cluster analysis in data mining and analysis field as an unsupervised machine learning technique, but has several recent applications on earthquake data as well (e.g., Weatherill & Burton 2009, Rehman *et al.* 2014, Novianti *et al.* 2017).

9.2 Clustering of events of new catalogue 2014-2017

K-means algorithm was applied to the dataset of A and B class events. Fitting the model of the K-means algorithm to data i.e., search for an optimal number of clusters is shown in Annex-Part III. Results of clustering analysis are shown in Figure 9.2, where events are assigned to six distinct clusters (shown in different colours) together with corresponding cluster centroids, demonstrating the successful application of the clustering method.

Formed clusters enabled further focus on their individual spatio-temporal analysis. As it can be observed in Figure 9.2a, clusters of A class events are well defined. However, the limitation of the K-means method has manifested for more diffused B class events (Figure 9.2b), which have also higher location error. Due to the inability to regulate at which maximum distance from centroid event needs to be considered as a part of the closest cluster, even events that are too far or scattered (meaning they should not be considered as a part of the same seismologically active structure) are also assigned the to the closest cluster.

In Figure 9.3a, clusters' temporal distribution is shown, while Figure 9.3b shows the time distribution of events' magnitudes, together with the cumulative number of events per each cluster. Even though moderate seismic activity can be observed throughout the entire period of 4 years, seismic crises of December 2014, end 2016-early 2017 and August 2017 are clearly visible as the number of events rapidly increase in a short time during these periods. According to Bath law (Båth 1965), the largest aftershock is usually about 1 magnitude unit smaller than the mainshock, independent of the mainshock magnitude. In this case, no clear mainshock-aftershock sequences are visible, which indicate that the activity of each cluster can be characterized as a seismic swarm. Colours in Figure 9.3 correspond to clusters' colours in Figure 9.2. Seismic activity throughout 4 years is either contained within the dimensions of the original cluster or breaks through multiple clusters.

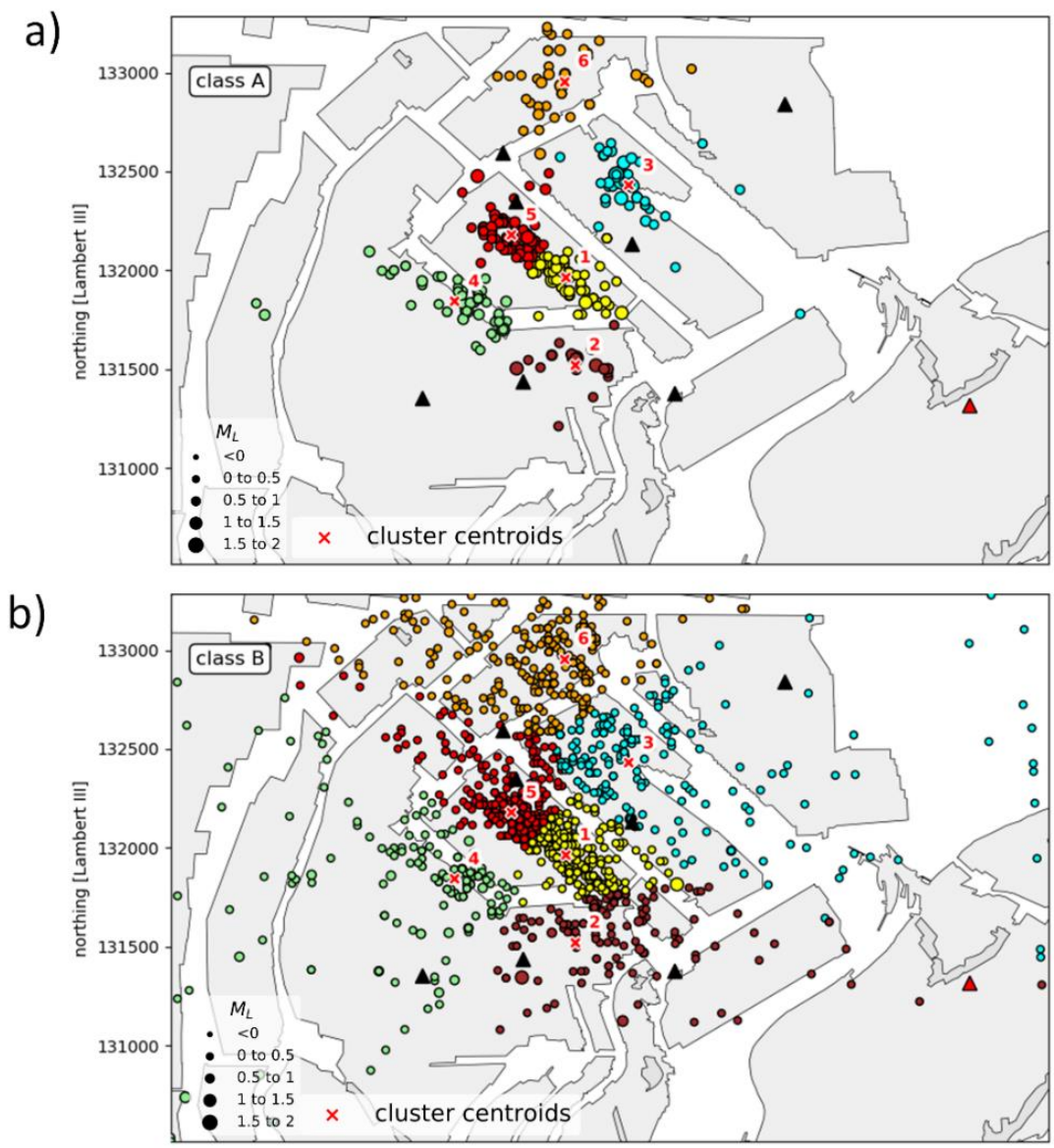

Figure 9.2 results of cluster analysis of highest quality events of new catalogue 2014-2017. Events of each cluster are presented in a different colour. Cluster centroid are marked as well: a) K-means applied to A class events b) class B events assigned to same clusters based on the minimal distance to cluster centroids.

During crises of December 2014, the most active clusters are 1, 2 and 3 (yellow, purple and blue, accordingly). The total number of events is highest in cluster 1, which is also the only cluster where earthquakes reach magnitude M_L=1, while the magnitude of events in other areas remains below 1, closer to 0.

When looking at the sequence of end 2016-early 2017, seismic activity can be separated into two phases. In the first phase, clusters with the strongest activity are 3 and 4. Magnitude evolving and increase compared to the previous crisis is observed in most clusters, as magnitude reach over M_L=1, strongest in

cluster 3 (M_L = 1.7). In the second phase, there is a clear order of activation/migration from southeast to northwest, when the seismic activity of cluster 1 breaks through cluster 5, while the activity of cluster 3 has calmed. Cluster 4 and 6 show moderate activity throughout both phases.

The seismic activity of cluster 6 is strongest during the crises of August 2017 when its activity dominates, compared to other clusters, with maximum magnitude observed M_L =1.3. The magnitude of events in other clusters during August 2017 is in decline compared to the crisis of late 2016-early 2017.

Looking at the seismic activity throughout 4 years period, the highest magnitude event is observed in cluster 3, while the cumulative number of events reveals that the most active clusters are 1, 5 and 6.

Potential bias of locations due to stations configuration changes within these 4 years is examined with the conclusion that the network configuration does not affect observed spatio temporal migration between clusters 1 and 5. Details are presented in Annex – Part III.

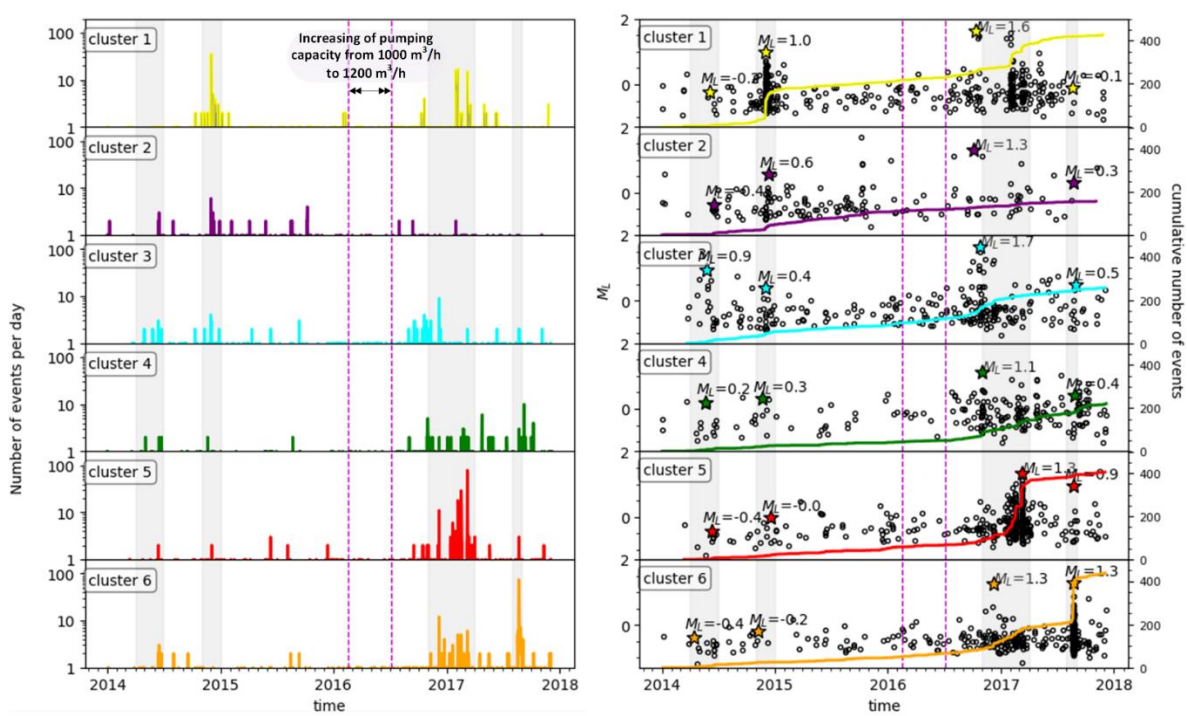

Figure 9.3 Temporal distribution of seismic activity for A and B class events. a) total seismic activity per day (top), and each cluster separately (figures below), compared with water levels at Fuveau Regagnas well, presenting efficient rainfall (blue line). b) the local magnitude of corresponding events with the cumulative number of events

10 Multiplets and cluster activity 2010-2017

As shown in the previous chapter, seismic activity in the study area shows spatio-temporal clustering behaviour in the period 2014-2017. Clustering is in agreement with the observation of multiplet families as observed from previous studies for the crisis in 2014 (Kinscher 2017). The evolution of both clusters and multiplets is further analyzed in detail in this Chapter to characterize the underlying trigger mechanisms (driving forces) in space and time.

The following multiplet analysis presented in this chapter focuses on a dataset recorded on station Fuveau of the Ineris permanent network. As it is installed in 2008, this is the only operational station for the entire post-mining monitoring period, hence covering the flooding history as well. Multiplet analysis provides two main elements: i) the classification of different multiplet families over space and time and ii) the reconstruction of the main spatial cluster until 2010. Note that station Fuveau is relatively far from the study area (> 2 km), which allows only the identification of the largest multiplet families (in terms of magnitude).

More detailed analysis of the multiplets, in terms of relative location and source dimensions (and potential repeater occurrences), following for the 2014-2017 period and dataset of the more local station of temporary BRGM microseismic network is presented in chapters 11 and 12.

10.1 Cross-correlation technique

In theory, repeating events will have identical waveforms due to identical source mechanisms, ray paths, and receiver response. Real seismograms, however, may exhibit small variations in the shape of the signals that reflect changes in the source, path, receiver characteristics, and/or noise (Waldhauser & Ellsworth 2002).

In general, the similarity of two waveforms can be assessed by cross-correlation (CC) of normalized waveforms and finding maximum CC coefficient between events as defined by:

$$CC_{xy}(\tau) = \frac{\sum_{i=1}^{N} x(t_i)y(t_i+\tau)}{\sqrt{\sum_{i=1}^{n} x(t_i)^2}\sqrt{\sum_{i=1}^{n} y(t_i)^2}} \qquad [10.1]$$

where $x(t_i)$ and $y(t_i)$ represent two waveforms (i.e. time series) of two earthquakes with N discrete samples and the lag time τ between them (Uchida 2019). Function [10.1] returns values in range of [-1,1], where value 1 means that waveforms are identical.

The differences between two earthquakes are reflected in the CC value, which generally depends on several factors: frequency content of cross-correlated waveforms, hypocenter separations Δr between earthquake sources, the effect of the propagation path R between an event source and station. The dependence of CC value on each of them is not trivial.

Nevertheless, several studies explore the change of CC values between two earthquakes and describe its tendencies in a relation to some of these factors (e.g., Nakahara 2004, Akuhara & Mochizuki 2014).

Hypocentral distances between earthquakes with very high CC values are considered to be small, indicating a similar source mechanism (Baisch *et al.* 2008). Path R contributes to decrease of CC coefficient value with increasing hypocentral separation, effect is increased in highly heterogeneous medium. CC value also drops with increasing distance Δr between the two events, and value can change depending on the frequency content of correlated waveforms as well (Nakahara 2004, Uchida 2019).

Separation of events Δr within families can be evaluated based on the generally used "quarter wavelength rule" for waveform similarity, defined by Geller & Mueller (1980). The rule states that two events located within a quarter of a wavelength from each other cannot be separated based on waveform similarity. In other words, the high similarity of waveforms indicates that the events are no farther apart than about one-quarter of the wavelength. (Baisch *et al.* 2008) has shown however that this rule is not always as restrictive and depends on the frequency of the waveforms. Reducing the signal to the low-frequency range reduces waveform complexity at larger distances. Limitation to higher frequency can be affected by the smallest differences that distinguish two event sources. Therefore, the selection of proper frequency range is important not only to reduce the noise but also to make CC or coherency values more informative, depending on the aim of the study. Generally, too low frequencies do not have enough resolution to distinguish nearby overlapping or non-overlapping events (Uchida 2019). The analysis presented in this Chapter does not require such high resolution.

10.2 Identification of multiplet families using Fuveau station

Fuveau station is equipped with a 3D geophone 40Hz located in a borehole at depth of 109 m, at a hypocentral distance of approximately 2 km (location shown in Figure A1. 3, Annex- Part I). For multiplet analysis, a total of 1179 events was used, recorded in the period from 27/2/2007 10:10:12 to 12/3/2018 11:18:28, which leads to a total of 694 431 event pairs. Before cross-correlation, waveforms of events were first downsampled to 500 Hz, de-meaned and band-pass filtered to the frequency range of 1-20 Hz. CC coefficient is determined separately across all 3 components (vertical, N-S, E-W) for all event pairs.

Identification of multiplet families was based on the equivalence class (EC) algorithm (Aster & Scott 1993) which follows the principle that: if two couples of events (A, B) and (B, C), both exceeding set CC threshold, share a common event B, than all three events can be merged into one family (A, B, C) even if the correlation between (A, C) is below threshold (Aster & Scott 1993, Cattaneo *et al.* 1999).

A wide range of CC thresholds was tested as shown in Appendix III – Finding the optimal value of the crosscorrelation function. A threshold of 0.75 was finally chosen, which resulted in 470 events grouped into 100 multiplet families (which will be referred to also as Fuveau families in further text). The threshold was found to provide good visually similarity in waveforms (e.g., Figure 10.1) and provide the maximum number of identified multiplet families.

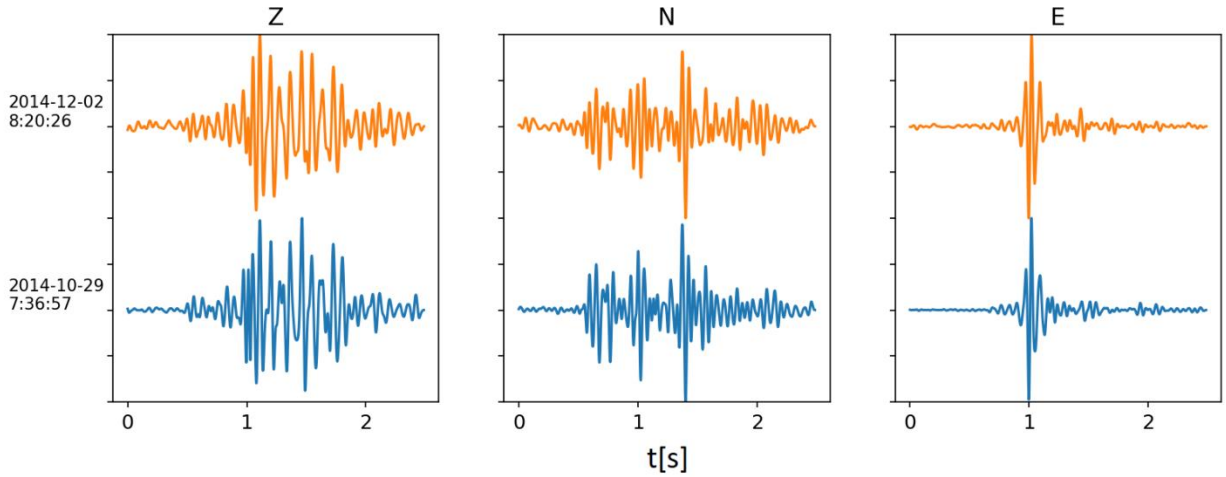

Figure 10.1 Example of a doublet identified in a dataset of Fuveau

10.3 The spatial resolution of multiplet analysis

As event locations from the permanent network are related to very high location errors (~ 1 km) and therefore their use is considered beyond the spatial resolution of the multiplet approach, the maximum interevent-distance for events grouped into the same multiplet family are estimated based on "the quarter wavelength rule", to obtain the spatial resolution of the multiplet analysis.

As mentioned above, waveform similarity was estimated for a frequency band 1-20 Hz, which corresponds to the dominant frequency of the recorded seismic signals at station Fuveau (Figure 10.2). As described in Section10.1, limitation towards higher frequency (due to attenuation) limits the capacity to distinguish between certain neighbored sources by the multiplet approach, meaning that their waveform similarity and CC coefficient is high even though their source radii do not overlap.

Hence, considering that waveforms of events have dominant frequency content between 10 Hz and 20 Hz (Figure 10.2), it means that the corresponding wavelength in the homogeneous model with P-wave velocity $v_P = 4.1\ \mathrm{kms}^{-1}$, is between 205 m (for $f = 20\ Hz$) and 410m (for $f = 10\ Hz$), and between 90 m ($f = 20\ Hz$) and 180 m ($f = 10\ Hz$) for S-wave velocity $v_S =\ 1.8\ kms^{-1}$, respectively (after $v = f\lambda$ equation). Quarter-wavelenght rule indicates that the distance between highly similar events in the multiplet family is in the order of 50 m - 105 m (P waves) and 22 m– 45 m (S waves). These distances imply that events in each Fuveau multiplet family are close enough to be considered as a part of the same seismic cloud (cluster).

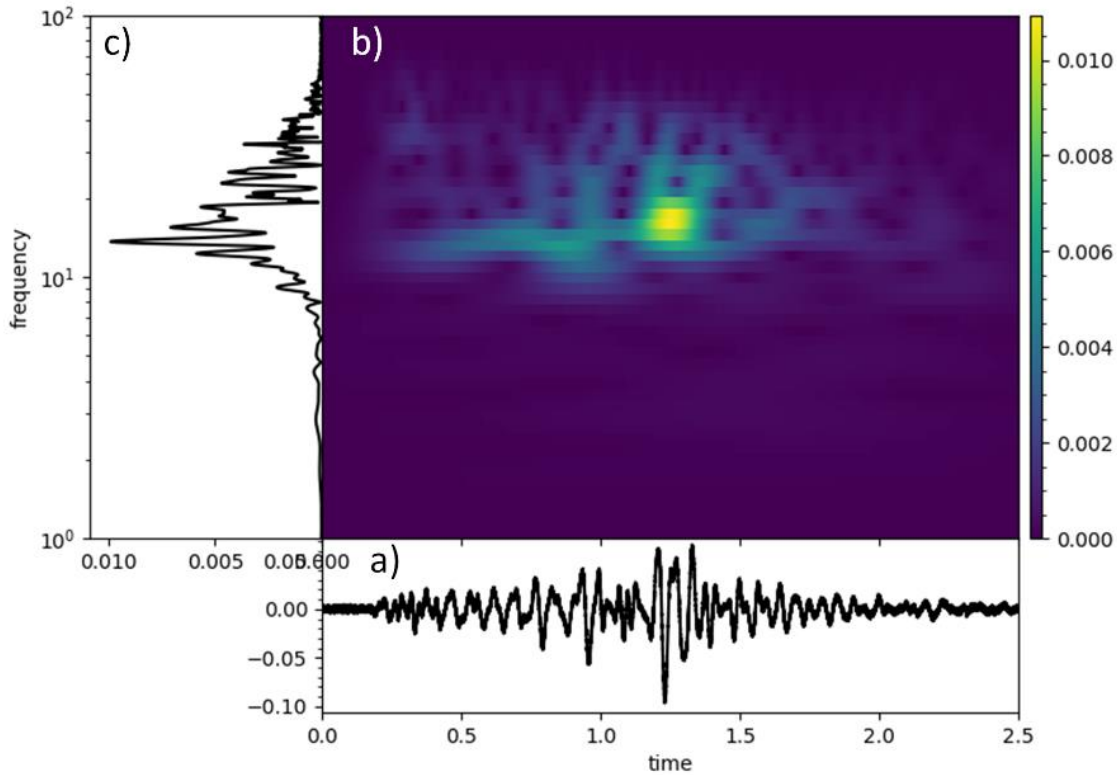

Figure 10.2 Frequency content of a microseismic event recorded on station Fuveau 28th May 2010, at 16:21:13h a) Z component of the signal, b) spectrum of the signal shown in a) with respect to energy (shown in colorbar) and c) time-frequency content representation of a). Note that the dominant frequencies are widely around 15 Hz. Missing spectral content below 10 Hz can be explained by instrumental damping towards the low frequencies.

10.4 Spatio-temporal distribution of multiplet families

10.4.1 Multiplets 2010-2017

Figure 10.3 shows the time distribution of 100 identified Fuveau multiplet families as a function of the mean of northing components of events per each family, while Figure 10.4 shows the spatial distribution of events in families, in corresponding colours. The mean position of each family, determined as a mean of northing and mean of easting components of events in each family are shown as well in Figure 10.4, as the black-bounded dots in corresponding colours.

Results reveal that most multiplet families are located within the study area, in the zone of the Fueveau swarm. Interestingly, several multiplet occurrences can be also found south of the study area where also continuously seismicity is recorded by the permanent network (e.g., as shown in Figure 2.5a) Multiplet

activity in both areas (i.e. in the Fuveau swarm and to the south) is observed since the time flooding front arrival in 2010 (Figure 2.5). Some families appear to last several years while others occur as rather short transients for periods of several months. Multiplet occurrences and their recurrence rates seem to be intensified during the periods of seismic crisis, while moderate activity can be found in between the crisis as well. Another interesting observation is seismic activity in mid-2017 when the multiplet families initiate in the north which did not seem to appear before.

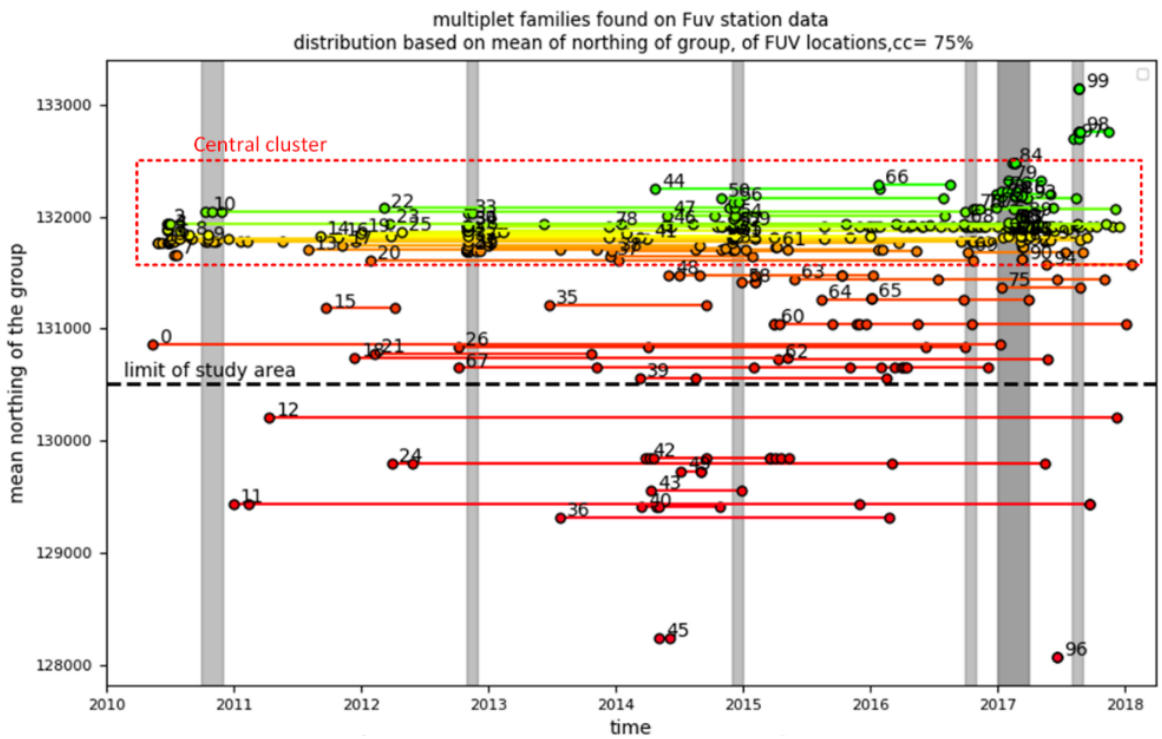

Figure 10.3 Spatio-temporal distribution of 100 identified Fuveau multiplet families.

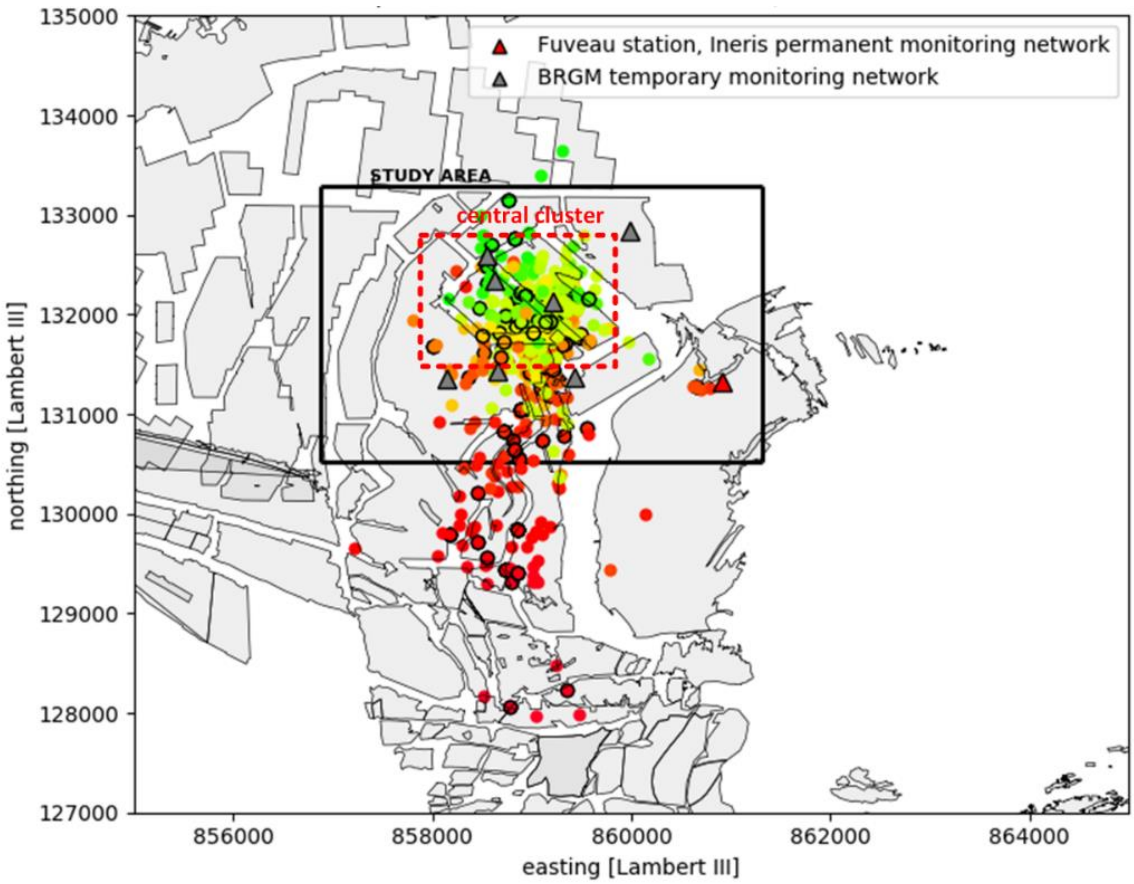

Figure 10.4 Location of events of 100 multiplet families in period 2010-2017 based on data of Fuveau station, together with the mean location of each family (black bounded circles).

10.5 Main multiplet families in the Fuveau swarm (study area)

Spatio-temporal distribution of multiplets in the study area is illustrated by Figure 10.5 and Figure 10.6. To improve visibility, only multiplet families with more than 3 events are shown here. To provide a more detailed picture of multiplet distribution in space, only multiplet events that have been also located with the temporary network and thus are part of catalogue 2014-2017 (Part II) are shown.

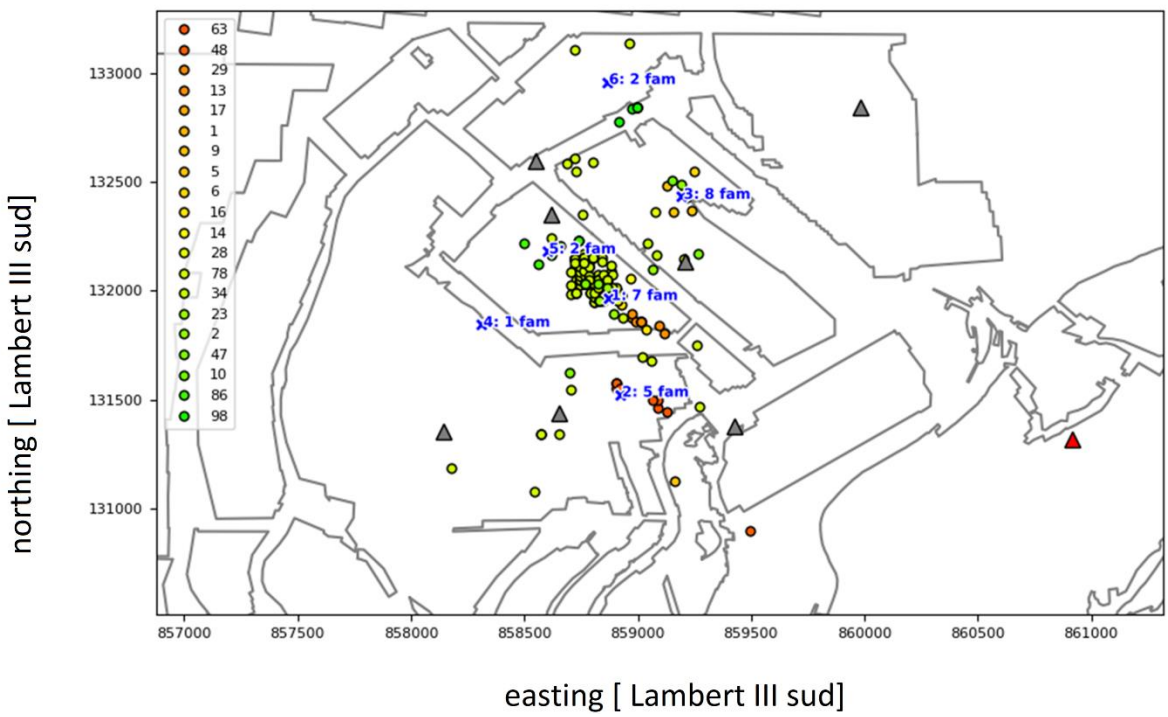

Figure 10.5 Spatial distribution of events of Fuveau families in period 2014 -2017, location-based on new catalogue 2014-2017. Only families with more than 3 events in this period have been shown. The number of families per each cluster in the corresponding period is indicated as well

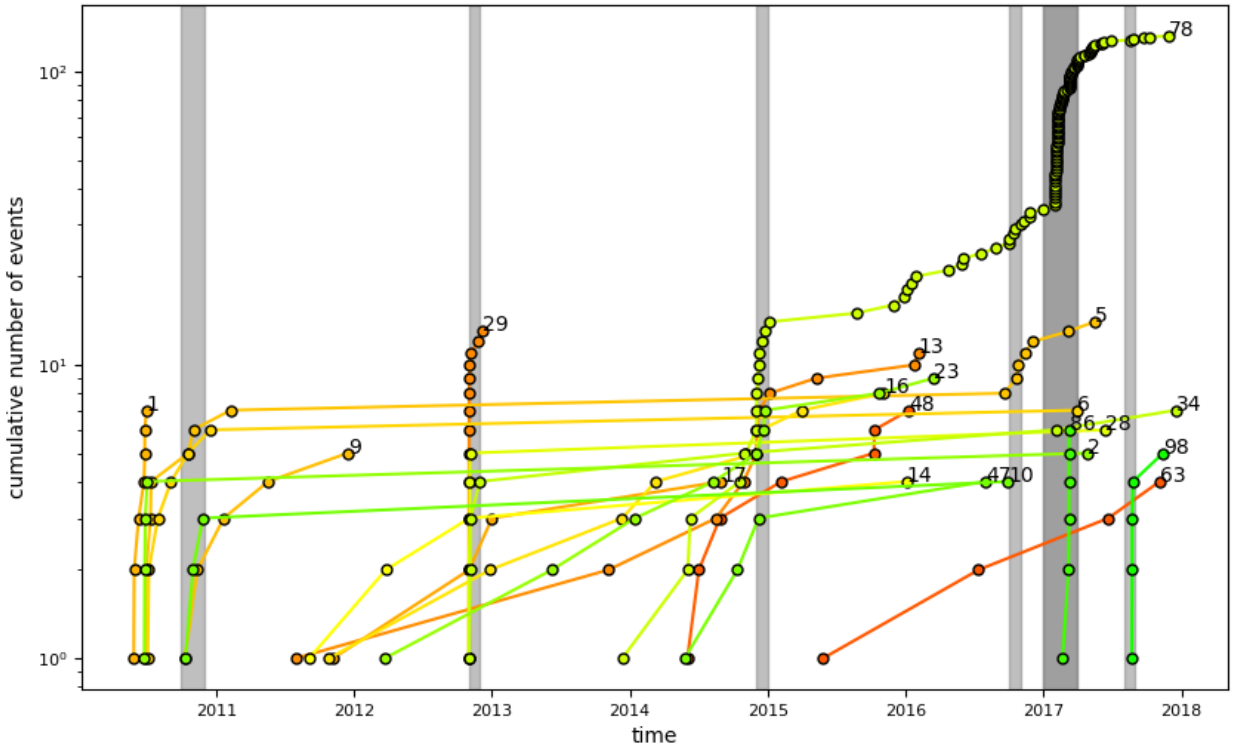

Figure 10.6 Cumulative number of events of multiplet families. Only groups with a minimum of 3 events with the CC threshold of 0.75 are shown

As it can be observed in Figure 10.6, consistent with the previous observation (Figure 10.3), some families are active over a longer period of several years - for example families, 2, 6, and 34 are active from 2010 to 2017, while some groups seem to be active only during one seismic crisis – for example family 29 active during December 2012. Family 78 is a particular case as it seems to be evolving through seismic crises of December 2014 and again in early 2017 and is concentrated in the main central cluster (clusters 1 and 5). Visual inspection on waveforms reveals that probably more families seem to have been merged, which cannot be distinguished due to the limited spatial resolution of the multiplet approach. Family 5 shows similar behaviour, first active in 2010 and further reactivated during crises of late 2016 and early 2017.

The decay of seismicity rates for some families seems to follow the Omori decay law. We can also observe that interevent times appear much smaller for families whose activity is limited to one crisis only, and the cumulative number of events for these families during crises increases more rapidly compared to longer-lasting families. The latter seems to have a generally smaller number of events and larger interevent times however their activity is not limited only to seismic crises periods and they remain active during periods between crises as well.

10.6 Reconstruction of cluster activity before 2014

Even though location errors from the temporary microseismic network compared to the ones of Fuveau station of Ineris network are much lower, one shortcoming from the new catalogue 2014-2017 is its temporal limitation. However, along with the multiplet families identified from Fuveau station, a partial reconstruction of the activity of the main clusters (Figure 9.2) beyond 2014 was achieved.

Locations of events in Fuveau families based new catalogue 2014-2017 allowed to locate the families within the clusters, while the spatial resolution of the multiplets of the permanent network (section 10.3) in the period prior to 2014 allowed to associate the events of the same families to the clusters as well. As a result, the activity of each multiplet family having at least one multiplet event (re)located (with sufficient quality A and B) by the temporary network can be reconstructed

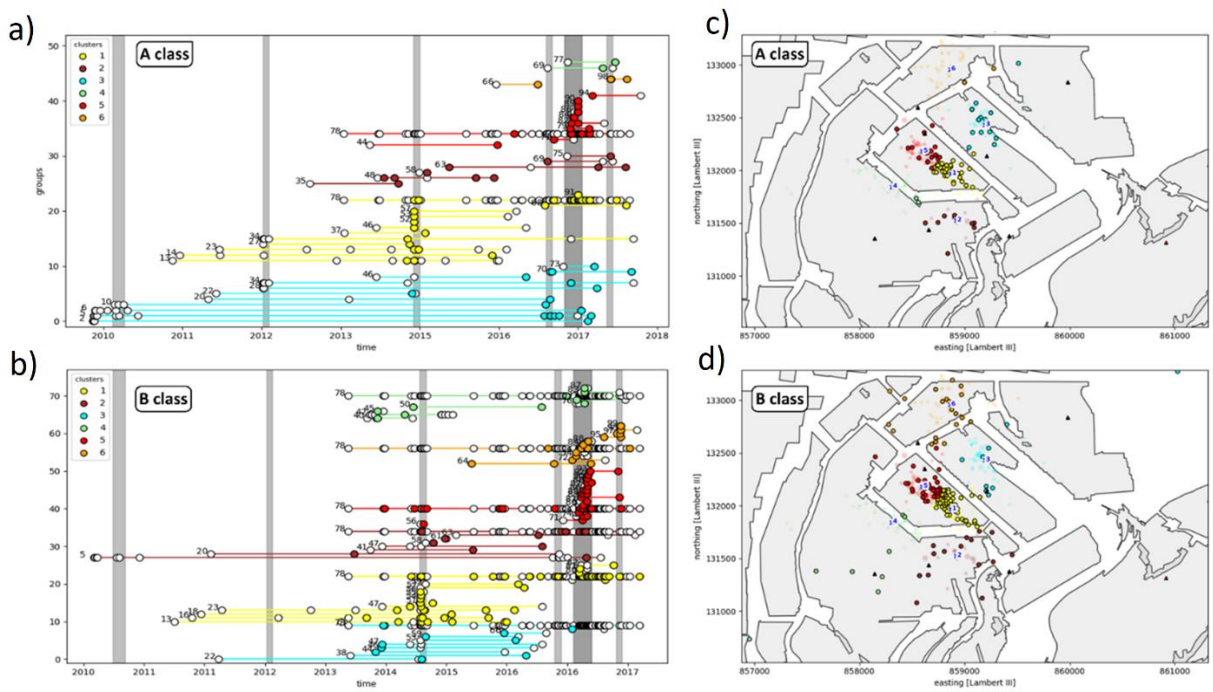

Figure 10.7 Spatio temporal distribution of reconstructed families. a), b) shows temporal distribution of class A and class B events, correspondingly. Each line presents the temporal range of a family, while points present events. Filled circles are events with the corresponding location in the new catalogue 2014-2017. c, d) shows the location of events of a), b) relocated based on the new catalogue

Temporal reconstruction of the main cluster (Figure 10.7 a,b) demonstrates that the first family emerges in 2010, located within cluster 3, where families are reactivated in each following crisis together with the emergence of the new families as well. Together with cluster 3, cluster 2 has been active since 2010. During crises of late 2012, only clusters 3 and 1 appear to be active. The high seismic activity of cluster 1 characterizes crises of late 2014. Cluster 1 remains active during the next crisis of late 2016-early 2017, however during this period highest active cluster is cluster 5, indicating seismicity migration towards the northwest.

These findings are in accordance with previous results (Figure 9.3) and underline the strong correlation of seismicity in space and time in form of clusters since 2010. It seems thus that some clusters have been repeatedly active during a period of a minimum of 8 years.

11 Detailed multiplet analysis 2014-2017

In the following, a similar multiplet analysis as in the preceding Chapter is performed on local, high-frequency waveform records from 2014-2017, recorded on the S1 station of the temporary network. This analysis aims to provide a more detailed picture of the spatio-temporal characteristics of multiplet families.

11.1 Multiplet families in new catalogue 2014-2017

Detailed multiplet analysis was performed on all A and B class events of the new catalogue 2014-2017. Events were extracted from continuous recordings of station S1. A total of 1986 events were analysed by following the crosscorrelation approach described in Chapter 10, applied to waveforms on all 3 components filtered in the range 1 – 100Hz.

The correlation matrix in Figure 11.1 shows the final CC values, calculated as a mean value across all 3 components, for each event-pair (a) and their relative time difference measured relative to the first detected event of the catalogue (b).

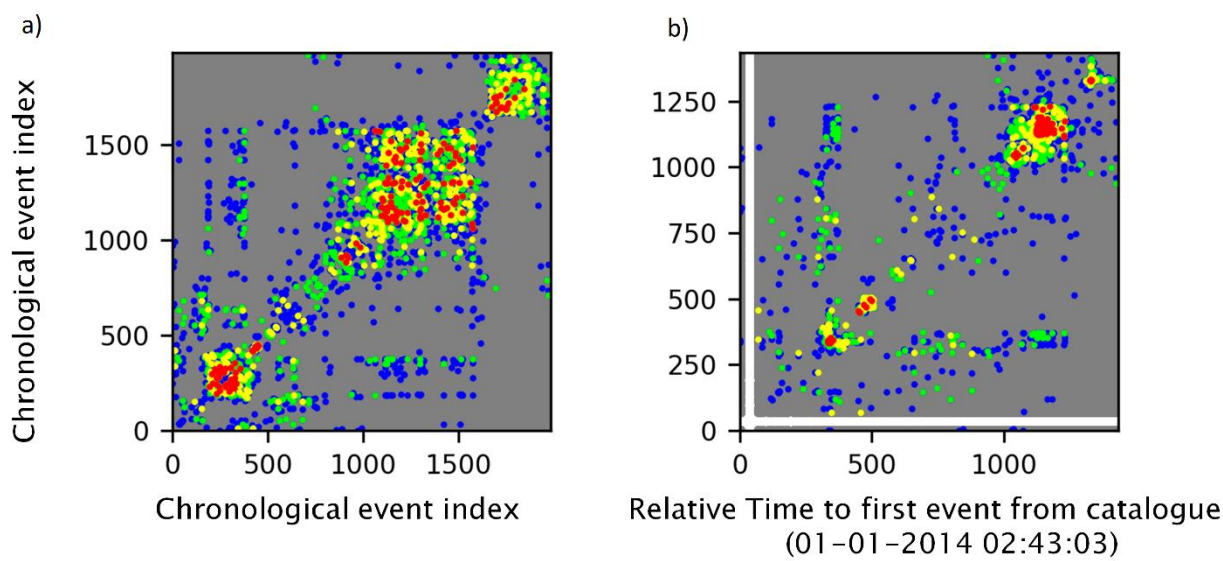

Figure 11.1 The correlation matrix with the final CC values, calculated as a mean value across all 3 components, for each event-pair (a) and their relative time difference measured relative to the first detected event of the catalogue (b). Colors are based on CC value as following grey: <0.6 ; blue: 0.6-0.7; green: 0.7-0.8; yellow: 0.8-0.9; red > 0.9.

The correlation matrix reveals the presence of three larger clusters (Figure 11.1 a) which seem to correspond to the three main seismic crises: December 2014, late 2016-early 2017 and August 2017. The figure also demonstrates the connection of the clusters of the first two crises, as the waveform similarity

between them corresponds to CC value 0.7 (blue). It means they are at small enough inter-event distances and most likely both located at the central cluster (within clusters 1 and 5, correspondingly). The final cluster shows low waveform similarity with the preceding clusters, thus most likely involving multiplets located in the most northern cluster 6.

Identification of the multiplet families was performed following the same approach as described in section 10.2. The CC threshold was here set to 0.8. This value was chosen as the optimal value, the best compromise between $CC = 0.7$, where events are not sufficiently similar and groups get excessively large (602 events within 170 multiplet families, and one family containing over 70 events corresponding to the main cluster) and 0.9 (where 122 events are grouped into 51 groups, however only 4 groups contain more than 3 events). CC threshold 0.8 is also most often chosen as criteria in other similar studies (e.g., Chen *et al.* 2008, W. Yu *et al.* 2013, Uchida 2019 and references within).

Results reveal in total 342 out of 1986 events are identified as multiplets, grouped into 121 multiplet families. The multiplet family with the highest number of events is shown in Figure 11.2, confirming the high similarity of waveforms and consequently justifying the choice of the CC threshold.

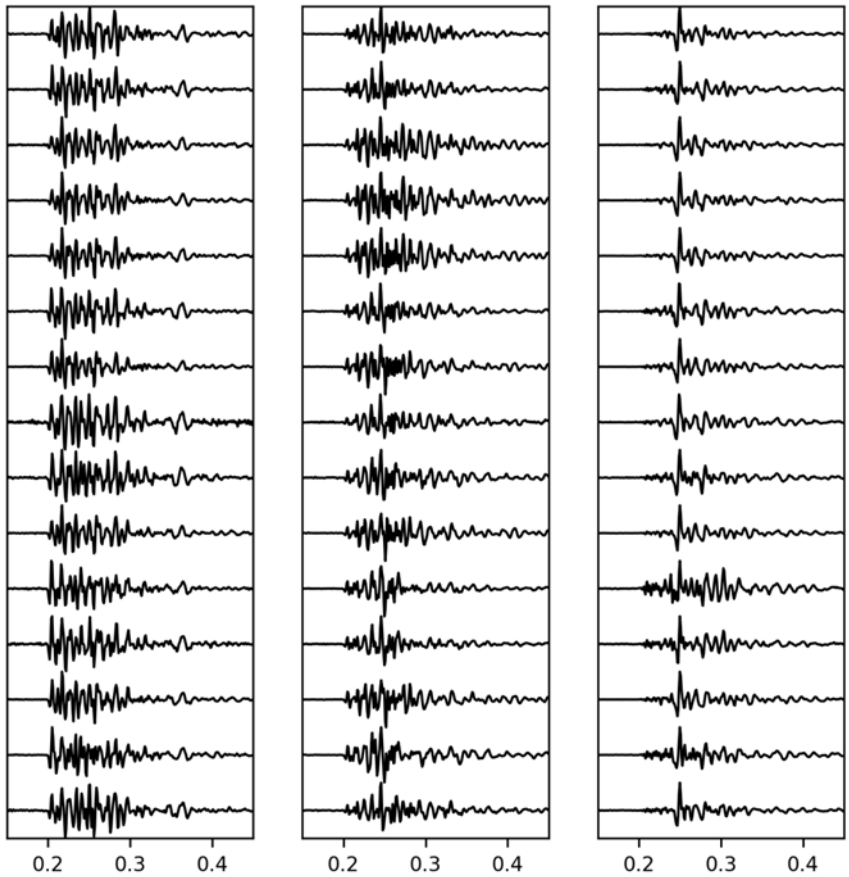

Figure 11.2 An example of multiplet family, with the highest number of events, based on data of station S1 of temporary BRGM network and new catalogue 2014-2017

11.2 Spatio temporal distribution of multiplets

For further analysis, only the main 21 families with a minimum of 4 events were chosen. To assure better location accuracy, as the BTBB method uses only P waves events of chosen families were relocated using probabilistic approach following Contrucci *et al.* (2010), which is implemented into Ineris SYTMIS Software for real-time microseismic monitoring. The method is based on a probabilistic approach that solves the inverse problem of (Moser *et al.* 1992) Tarantola & Valette (1982) and works by maximizing the probability density function (pdf) of the hypocenter at a given point using the equal differential time (EDT) or Euclidean (L2) norm, by minimizing the misfit between observed and calculated arrival times. Misfit between observed and calculated polarization angles can also be considered but in this case, only P and S waves were used. The hypocenter with the maximum likelihood is determined by using the Oct-Tree nonlinear method of Lomax & Curtis (2001).

For calculation on event location, P- and S-wave phases were manually picked from 3 component waveforms, recorded on all available stations of BRGM temporary microseismic network, with constant

uncertainty for P and S picks 0.05 s and 0.2 s respectively, identified from seismogram inspection. The assumed velocity model is homogeneous with P wave velocity $v_p = 4.1\ kms^{-1}$ and S wave velocity $v_s = 1.8\ kms - 1$ (Kinscher 2017, Kinscher *et al.* 2021). Event location search was limited to grid corresponding to Lambert III coordinates from 857000 m to 861000 m in easting direction, from 130500 m to 133500 m in northing direction, both with 10 m in resolution and vertically limited from the depth of -1000 NGF [m] to surface at 300 NGF [m] with a resolution of 100 m.

A total of 109 events were relocated, 6 of which are A class events and 103 B class events.

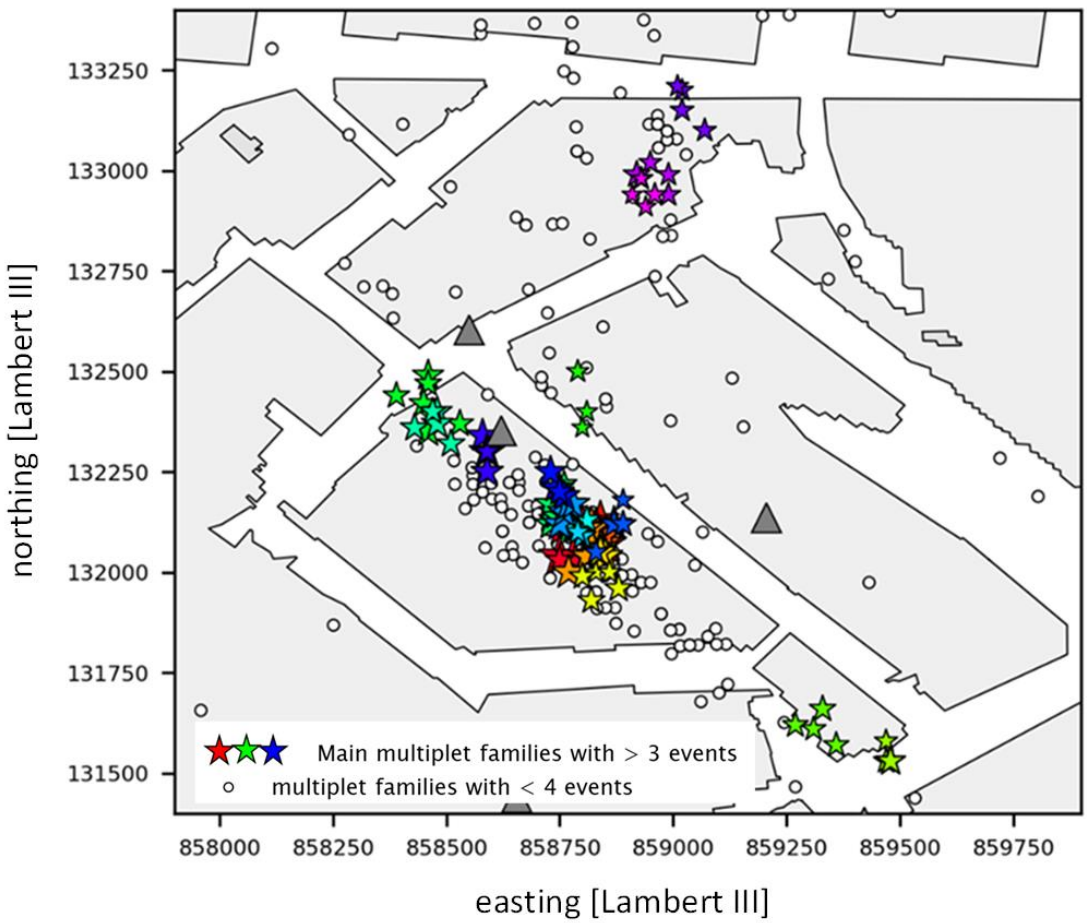

Figure 11.3 Location of events of main multiplet families with more than 3 events

Figure 11.3 shows event location results, where stars with the same colour correspond to events in the same family. Multiplet families with < 4 events are shown as white points. Multiplet families seem mostly present in the central cluster (clusters 1 and 5), where they appear to group into two separate seismically active areas. The largest number of families appear to be centred southeast, located within cluster 1. Their activity is initiated either during the crisis of December 2014 or during the crisis of late 2016-early 2017. Several families are located to the northwest, in the area of cluster 5, active during late 2016-early 2017.

Some families can be also found in a northern cluster (6), which is most seismically active during the seismic crises of August 2017. Interestingly, no multiplet families seem to be related to clusters 2, 3 and 4.

The temporal distribution of the multiplet families is qualitatively analysed and presented in Figure 11.4 a). The colours of each family match the colours in Figure 11.3 for main families with more than 3 events, while families with 3 or fewer are marked with white circles. Grey stars represent larger events associated with $M_w > 1$.

The behaviour of these families is similar to what was observed previously for Fuveau families in section 3.5. As it can be seen in Figure 11.4 a), multiplet families mostly occurs in form of transients - with temporary, relatively short-lived activity, which can cover periods from weeks to months before disappearing. Most of them appear for the first time during the period of seismic crises, and consequential events in the family appear within short interevent times during the same crisis. Some families are however continuously active or appearing for the first time during inter-seismic crises periods as well.

Families are in some cases showing Omori decay power-law type behaviour, however, some families present rather periodic recurrence times. The latter is the case for some longer family sequences which are active over years with rather a periodic recurrence.

However, some are active only for a short period, usually during a single swarm, and then disappear, which indicate that the same asperity never breaks again.

Spatial distribution of detected families between the period of different seismic crises, shows slight changes of locations when looking at the seismic activity in regards to easting Figure 11.4 b) and northing Figure 11.4 c) components, indicating possible evolution or migration trends, as shown by arrows and numbers. As visible in Figure 11.4 b), relative to the crises of December 2014, seismic activity in the next two crises has appeared more to the west (①), where crises of August 2017 is even more spatially constrained relative to the easting component of crises of late 2016-2017 (②). In Figure 11.4 c, changes with the northing component can be observed. We can see that seismic activity appeared stronger and denser towards the north during the late 2016-early 2017 compared to the prior crises of December 2014(③,④), migrating more to the north in the crisis of August 2017 (⑤).

Observations are consistent with previous results, indicating the most active central cluster (1 and 5) during crises of December 2014 and late 2016-early 2017, and migration trend between the two, while cluster 6 is almost only active during August 2017.

The further section focuses on analysis and interpretation of whether these multiplet families could be true repeaters or not.

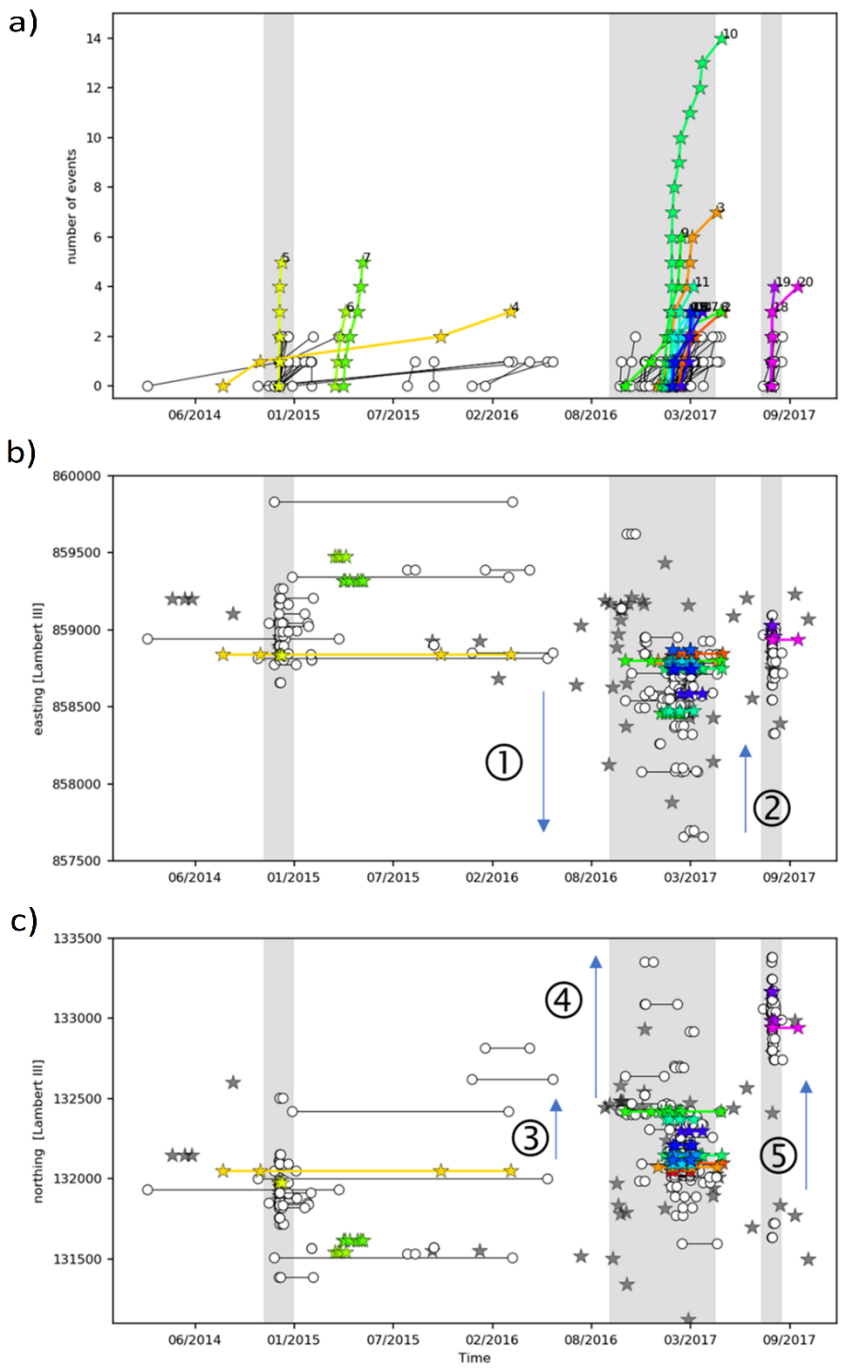

Figure 11.4 Spatio temporal distribution of multiplet families, corresponding to a) temporal distribution of events per each family b) distribution of families with regards to mean easting component c) distribution of families with regards to mean northing component. Families are the same as shown in Figure 11.3

12 Repeaters or multiplets?

Multiplets are studied more in detail by determination of source parameters (spectral analysis to determine moments, corner frequencies to characterize source sizes and stress drops), to examine source overlaps of multiplet families (see Figure 8.1, section 8.2) following Bourouis & Bernard (2007) and Kinscher *et al.* (2020).

The main goal of this analysis is to understand if similar multiplet events present nearby interacting fault segments or eventually repetitive rupture on identical segments (seismic repeaters) resulting from surrounding aseismic creep. Thus, source radii are calculated and discussed in section 12.1 and compared relative locations of the multiplet (section 12.2). Estimates on source radii (corner frequencies) are then further discussed with the dependency of the multiplet internal waveform fit with frequency (section 12.3).

The focus of the analysis remains on the main 21 multiplet families with more than 3 events.

12.1 Source parameters determination

A source spectrum fit method was applied to determine moment magnitudes and source radii (from corner frequency f_c) of the stacked source spectrum of each of the 21 main families. Stacking is generally justified by high spectral similarity in the multiplet spectra, as notably the stable corner frequency (Figure A3. 4, Annex – Part III). The approach is constrained to data of one single station S1 (station of highest SNR ratio) and thus provides only first-order estimation on source radii.

Source spectrum inversion was performed by using the methodology proposed by Kinscher (2015), following the SourceSpec approach (Satriano 2020), implemented in Ineris SYTMIS software. The main particularities of the method are the presentation of source spectra in moment magnitudes and the consideration of anelastic attenuation in the inversion by varying the Q factor. Details of the analysis can be found in Annex – Part III - Corner frequency estimation for families.

Source radius r_0 was determined for each family from corner frequency (f_c), computed with the S-wave spectra, and considering the circular source model of Madariaga (1976) which assumes singular crack radially expanding at a constant speed with constant $K_c = 0.32$, for S-waves:

$$r_0 = K_c V_s / f_c \qquad [12.1]$$

where $v_s = 1.8\ \mathrm{km s^{-1}}$ is the S wave velocity (Kinscher 2017). In addition, stress drops $\Delta\sigma$ are calculated using Eshelby (1957):

$$\Delta\sigma = \frac{7}{16}\frac{M_0}{r_0^3} \qquad [12.2]$$

To evaluate results, the estimates of means stress drop and source radii for multiplet families in the present study have been compared with the previously determined values for all events associated with the crises of December 2014 (Kinscher 2017). Comparison of results of two studies is shown in Figure 12.1 and shows that they are in good agreement. Stress drop of multiplet families seems to be in the typical range between 0.1 and 10 MPa, with a mean value around 1 MPa, while source radii are in the range from meters to some ten of meters.

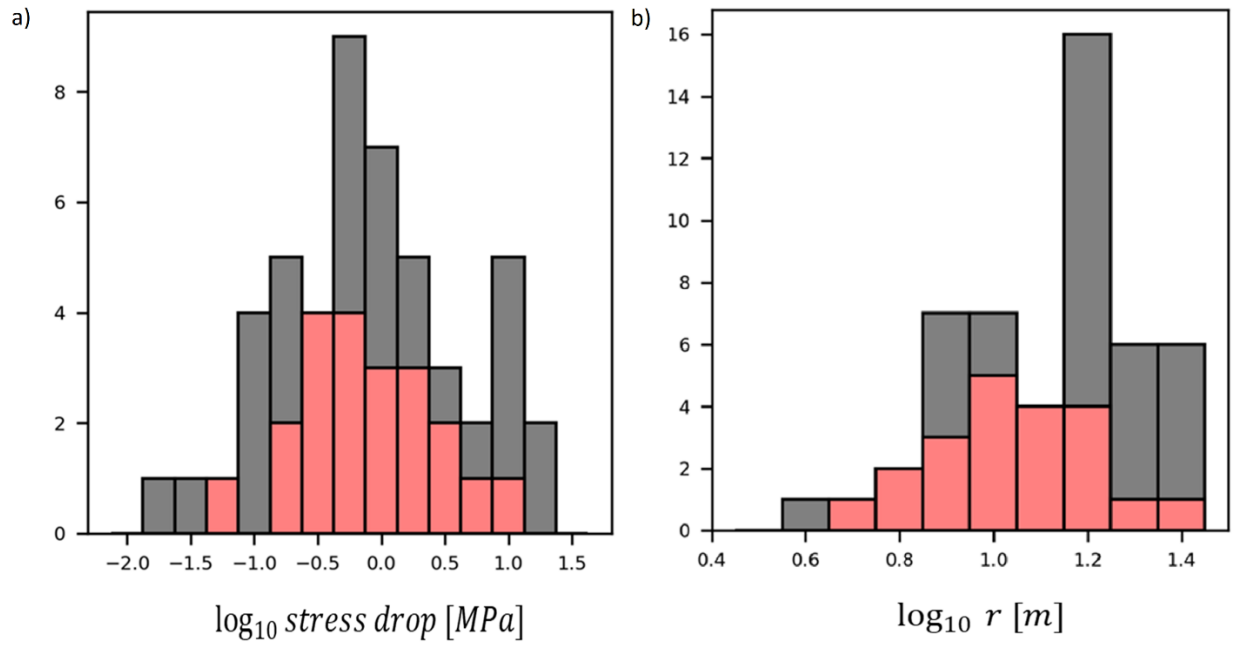

Figure 12.1 The estimates of a) means stress drop and b) source radii for multiplet families in the present study (red) and for all events associated with the crises of December 2014 (Kinscher 2017)(grey)

12.2 First repeater identification method: seismic source overlap

To study source overlap for events of each multiplet family and in between different multiplet families, source radii were calculated for each event by assuming constant stress-drops, namely a 0.1 MPa, 1 MPa and 10 MPa, as suggested from the previous section and Figure 12.1. To evaluate overlap, the radii are shown together with source location separately for the central cluster and the northern cluster in Figure 12.2 and Figure 12.3 Figure shows events of northern clusters families and corresponding source radii, depending on three different assumed stress drops: a) stress drop of 0.1 MPa, b) stress drop of 1 MPa and c) stress drop of 10 MPa. Colours of events in each family match colours in Figure 11.3 and Figure 11.4., respectively.

In the central cluster, source overlaps for events within families can be observed in some cases, particularly considering stress drops of 0.1 and 10 MPa, which indicates the presence of true repeaters.

Even though the observed time range of activity of each family is limited and does appear to span longer than one crisis (as observed in section 11.2, Figure 11.4), families within each cluster appear very close to each other. Apparent overlap of source radii between families can be observed often. However, due to lack of depth resolution interpretation remains limited.

In general, considering a higher stress drop, the source radii decreases with the inverse cube law accordingly, which results in lower rates of overlapped families. Hence, for a stress drop of 10 MPa, almost no true repeaters can be observed.

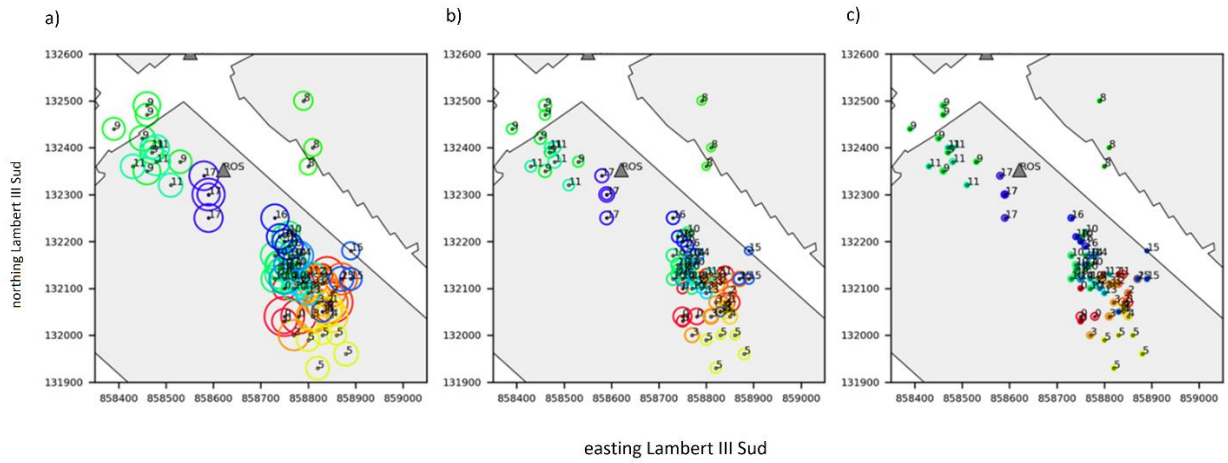

Figure 12.2 Figure shows events of central clusters families and corresponding source radii, depending on three different assumed stress drops: a) stress drop of 0.1 MPa, b) stress drop of 1 MPa and c) stress drop of 10 MPa. Colours of events in each family match colours in Figure 11.3 and Figure 11.4.

Consistent with observations in the central cluster, families in the northwest quadrant of the study area, which belong to cluster 6, do not appear to have overlapping sources when the highest stress drop is considered (Figure 12.3c). For lower stress drops, however, source radii are increased and overlaps of source area within some families can be observed (e.g. families 18, 29). Source radii overlap between the families can be observed as well, indicating the possibility of nearby interacting repeating sequences.

However, it is necessary to keep in mind that events in this area are generally affected by a higher location uncertainty due to distance from the BRGM microseismic network, compared to the central cluster which is surrounded by seismic stations. Lack of depth resolution remains a limitation.

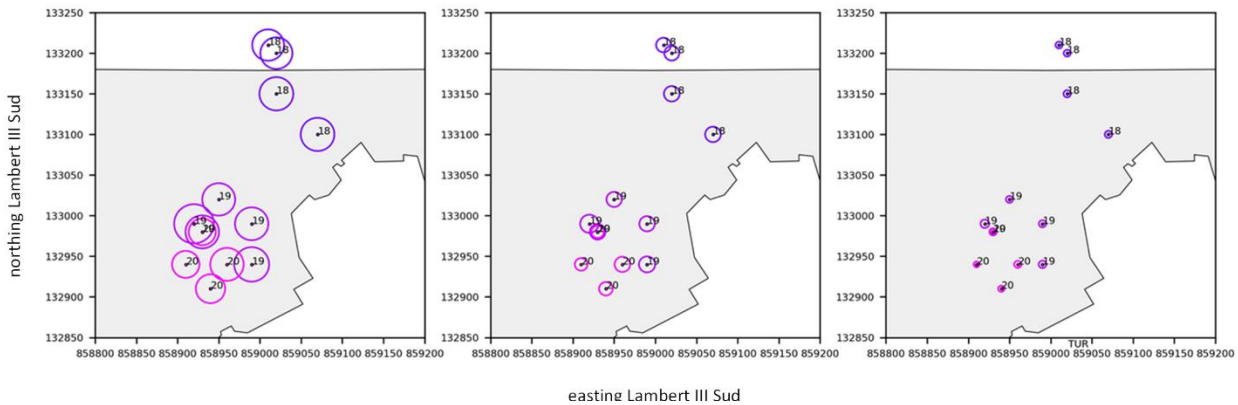

Figure 12.3 Figure shows events of northern clusters families and corresponding source radii, depending on three different assumed stress drops: a) stress drop of 0.1 MPa, b) stress drop of 1 MPa and c) stress drop of 10 MPa. Colours of events in each family match colours in Figure 11.3 and Figure 11.4.

As a conclusion, given the uncertainties, results for both central and northern clusters are inconclusive. Despite high waveform similarity and similar locations, it remains difficult to interpret the nature of multiplet families and distinguish neighbouring events from co-located (repeating).

Unfortunately, due to the low number of records available per each event due to a low number of stations, (which is occasionally reduced more due to high noise), the application of relative location methods to improve both the location and depth resolution remains unattainable.

However, both, multiplets and repeaters appear to be present under assumptions of stress drop in the range 0.1-1 MPa.

12.3 Second repeater identification method: coherency analysis

Another approach that could indicate re-rupture of the same area by events within families is investigated in regards to the crosscorrelation function between events, as a function of their corner frequencies fc, following Uchida (2019) and Kinscher *et al.* (2020).

Uchida describes the relationship between inter-event distance and coherence (which is defined very similar to cross-correlation, as a cross-spectrum between earthquakes rather than waveform correlation). He suggested that coherence decreases significantly when the pairs are not true repeaters when the analysis is done in the frequency range near the corner frequency. On the other hand, in the low-frequency range, a drop in the coherence is not significant for non-overlapping events, and the coherence can remain high even for them, which implies that a high coherence threshold is not sufficient for identifying the overlapping events in the lower frequency range. As an appropriate lower limit of the frequency range for selecting repeaters, dependent on the source size, he refers to the “quarter wavelength rule” (introduced in section 10.1) as one possibility. The higher frequency content can allow

distinguishing the overlapping sources easier, however, the upper limit of the appropriate frequency range also exist. Variability of the rupture processes within the slip area, which can differ for repeating earthquakes even when sharing the same source area, reflecting the heterogeneous stress and strength within the patch, can lead to the variability of high-frequency content and therefore influence the change of waveforms which is reflected in the coherency of events.

Similarly to Uchida (2019), Kinscher *et al.* (2020) refer the behaviour of repeaters with regards to coherence function, which they define as the average waveform cross-correlation coefficient for all event pairs of each family, averaged at each station over multiple frequency bands. The principle of the approach is illustrated in detail in frequency Figure 12.4(a)–(c). At low frequencies, authors assume identical Green functions for each event pair of the same family and therefore source mechanism correspondingly. At higher frequencies, however, a much complex source process can be expected, different for each event, resulting in a significant decrease in the coherence for frequencies beyond the corner frequency (Figure 12.4c). On the contrary, a smooth decrease in coherence after the corner frequencies are an indication of the same complexity in the high-frequency spectrum which therefore implies repetitive signal at the same source (Figure 12.4d).

This approach is applied to the same set of 21 main multiplet families observed in the study area, analyzed in previous sections. Estimated coherencies for each family are shown by Figure 12.5, in comparison to the corner frequencies estimated from source spectra and corner, frequency ranges estimated from the range of potential stress drops. In this approach, it is assumed that all events within a family have identical corner frequency, and coherence is determined as a cross-correlation coefficient for all event pairs of each family averaged for one station over multiple frequency bands.

In Figure 12.5 it can be observed that coherencies for some families decrease beyond the estimated corner frequencies, however, for certain families (e.g., 12, 13, 16, 17, 19) decrease in coherence after the corner frequency is rather smooth and could indicate repeating rupture of the same source.

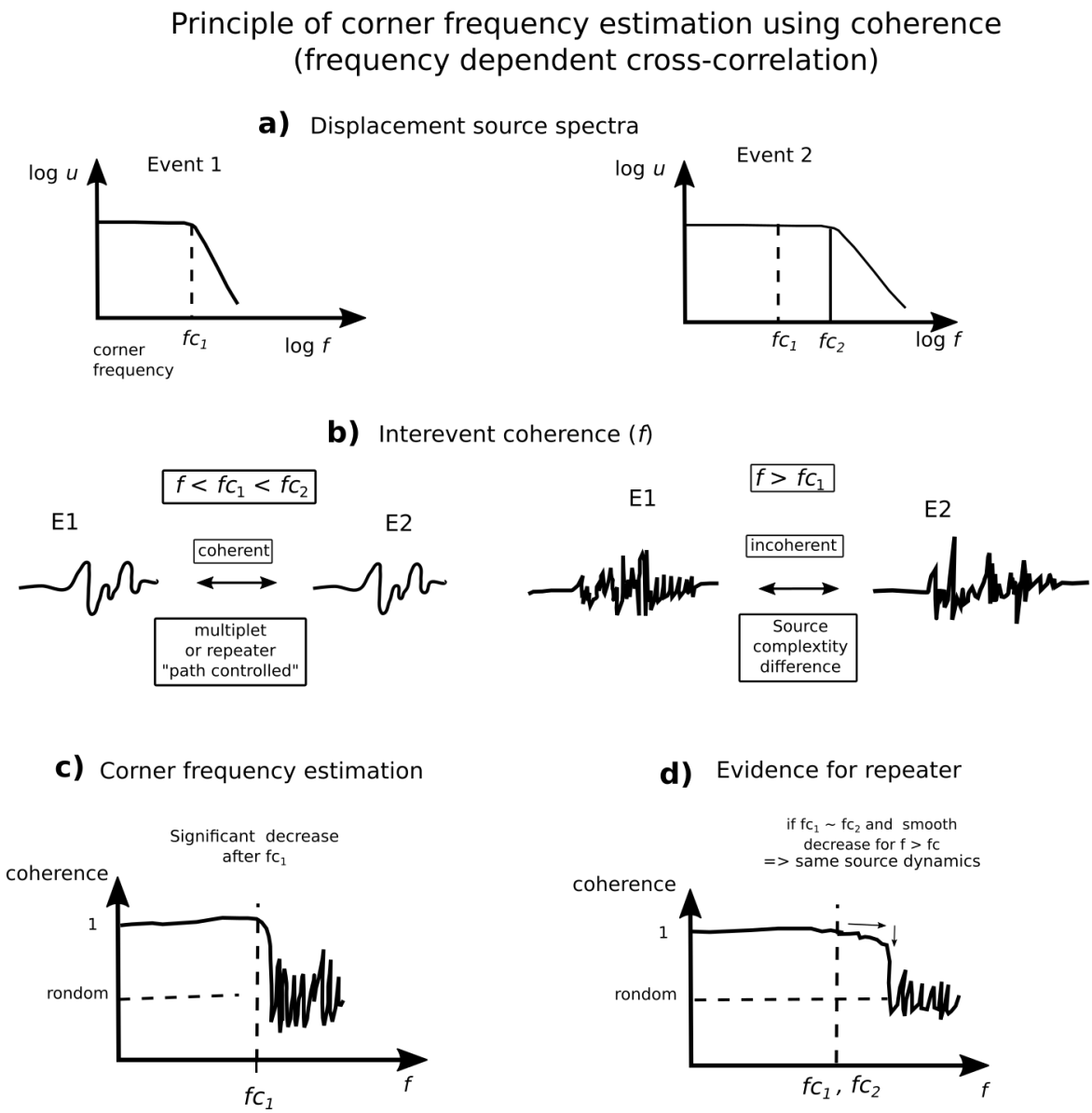

Figure 12.4 Illustration of the principle of interevent coherence for evaluating the corner frequencies and defining the seismic repeater occurrences (see text). From Kinscher (2020)

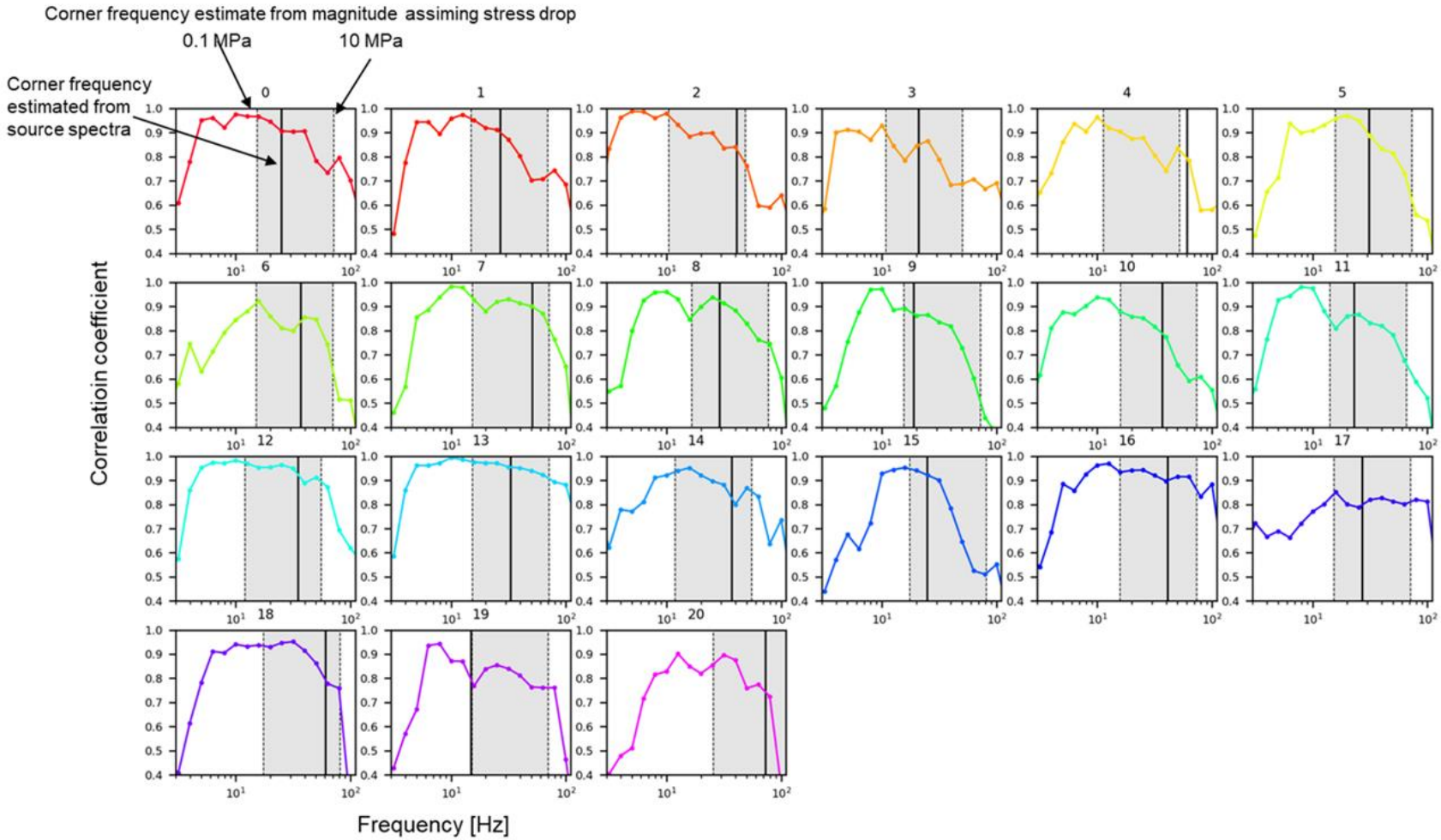

Figure 12.5 Frequency-dependent cross-correlation of 21 family groups and defining the seismic repeater occurrences

13 Summary of main observations

Several clustering and multiplet/repeater analyses have been applied leading to the following main observation:

Clustering analysis showed the presence of 6 main clusters in the Fuveau swarm area. Most of these clusters have been active since 2010 and show constant background activity with temporary varying increases in the number of events during the main crises. It seems that particularly clusters located more to North-West have been more active during the last crisis in 2017.

Multiplet analysis on a broader scale (using Fuveau station) showed that multiplet families occur since the beginning of the flooding of the central basin area in 2010. Some of the families are located southwards of the Fuveau swarm area, however, most of the multiplets are observed within the central cluster of the Fuveau swarm. During microseismic crises, multiplets occur in form of short-term transients (weeks to months), partly following the Omori decay pattern but also in form of long-term sequences with a partially period recurrence rate in the order of months over a period of several years.

More detailed multiplet analysis (using S1 station) from the new seismic catalogue of events (2014-2017) confirmed these observations. Likewise, it is observed that most multiplet families occur in the central cluster. Particularly, spatio-temporal migration trends seem to be visible. Multiplet families can be observed in the most northern cluster which was mainly active during the last crisis in August 2017. Interestingly, almost no multiplet families are observed within clusters 2, 3 and 5.

Discrimination between multiplets and repeaters has been investigated by analyzing source overlap based on a comparison of i) source radii event location and ii) frequency-dependent waveform similarity. Both approaches showed evidence for potential source overlaps which imply repeater occurrences. However, due to strong uncertainty in absolute event location (due to limited station number), a detailed quantification of source overlap and related classification of repeater/multiplet family is unfortunately not possible.

PART IV
Seismicity origin and triggering mechanism

Introduction

Two hypotheses on the seismicity origin in the study area of Gardanne mine have been brought up: i) seismicity related to a collapse of the mining works following the flooding, and ii) the (re-) activation of nearby faults. Both lead to very different consequences in terms of seismic hazard and hence very different decisions regarding the mitigation of the possible consequences (Part I). The objective of this part of the thesis work was to combine the results of the thesis work and complementary approaches undertaken in relation to this thesis (additional seismic analysis and geomechanical modelling), as well as their interpretation in order to get a comprehensive understanding of the origin of the seismicity in the study area and the triggering mechanism(s) behind it.

In the following, Chapter 14 presents a pro-contra discussion regarding the mechanism behind seismicity being either related to mine collapse or reactivation of faults located below the mine layer. Discussion is based on the results of this thesis' seismic data analysis presented in Part II and Part III of this manuscript, as well as results of undertaken complementary seismic analyses based on temporarily enhanced seismic network by Ineris and BRGM. This complimentary analysis focused on constraining the depths of seismically active clusters and source mechanism analysis.

Chapter 15 combines the newly obtained seismic catalogue 2014-2017 and hydrological datasets to further constrain and understand the link between water level fluctuation in the mine layer and the generation of seismicity.

In Chapter 16 potential triggering mechanisms and driving forces which could explain the apparent hydrogeology-seismicity correlation and seismic rates of multiplet families are discussed, by referring to results from i) complementary geomechanical modelling and ii) clustering and multiplet/repeater analysis from part III.

14 Origin of seismicity

14.1 The repetitive long term seismic activity

As shown by the results from Part III, the seismic activity in the period 2014-2017 is spatially constrained to 6 main spatial clusters. Moreover, similarity analysis and discovery of multiplets in the seismic recordings of Ineris' Fuveau station provided evidence of seismic activity in clusters since the year 2010.

Clusters were characterized by repetitive behaviour based on a more detailed analysis of the seismic data recorded station closest to central clusters (S1), which showed the existence of very close events in terms of source location and source parameter. The possible existence of repeaters was found (i.e., same fault patch rupturing repeatedly).

The repetitive nature of the seismicity, where each identified multiplet family indicates repetitive stress release in the same geological seismogenic structure, with the same failure mechanism, seems not to be compatible with seismicity triggering by degradation of the mining work as a result of the flooding, which would rather show a progressive spatial evolution of seismicity typically seen in underground collapsing environments (e.g., Kinscher 2015). Indeed, contrary to the observed repetitive nature of seismic events, the type of instabilities or fracturing provoked within the mining works, related to a group of adjacent pillars, would be characterized by evolving progression of the rupture from one pillar to the next. Hence seismic activity related to the mining collapse would have variations in the mechanisms over time, due to rather progressive and significant changes in the local stress states associated with the collapse. Due to significant changes in the propagation conditions of seismic waves in the environment, the seismic signature would therefore be a priori dominated by spatial-temporal evolutions as well as various and evolutionary waveforms, contrary to observations.

Finally, as outlined by Didier *et al.* (2003), the mine working at Regagnas have been already in a "post-collapsing" state in 2003, as shown by the results of geomechanical modelling study and in-situ observations of neighbouring sectors (Part I). It seems thus highly unlikely that the flooding front arrival in 2010 would lead to collapsing processes and degradation of the remaining mine workings which last for more than 7 years (period of seismic activity).

Therefore, in favour of hypothesis N°2, we can assume that clusters of seismic events correspond to activated faults or fault segments. As observed in Part III, seismic activity either stay within the boundary of one cluster or progresses, indicating either separate segments rupturing (potentially clusters 2, 3, 4 and 6) or rupture progress connecting segments into one large fault line (potentially clusters 1 and 5)

14.2 Depth and source mechanism

This section focuses on describing and interpreting the results of seismic analysis done as complementary to the thesis (Kinscher *et al.* 2021).

The increase of the number of seismic stations in the study area from 5 to 13 when additional temporary stations were installed (4 of BRGM and 4 of Ineris) in 2019 enabled the analysis aiming to constrain the depth of seismic sources, as well as the focal mechanism, which are the key parameters in the understanding of the origin of seismicity and discriminating between two hypotheses.

Fourteen stronger $M_w > 1$ events recorded during 2019 and early 2020, identified from the catalogue of Ineris permanent monitoring network, were analyzed. They were recorded by the majority of stations (minimum 11) and had high SNR. Their location placed them within the same clusters as found and identified in the preceding period (Part II and Part III, Figure 14.1), providing further evidence of clusters enduring activity, consistent with results presented in Part III. Most importantly, due to comparable locations, the results of this analysis are considered representative of the characterization of each spatial (historical) cluster.

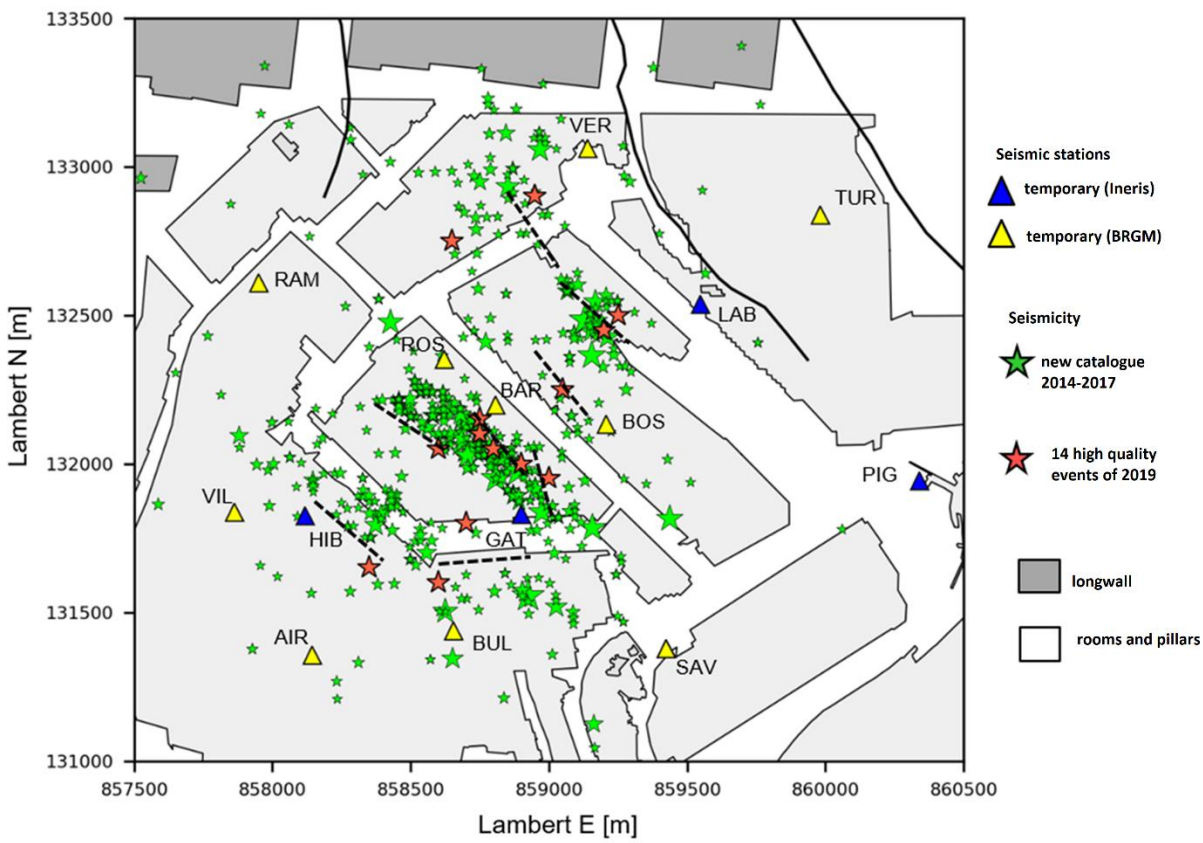

Figure 14.1 Fourteen strong events recorded during 2019/2020 chosen for analysis, located within clusters of new catalogues 2014-2017. Figure adapted from Ineris (2021)

Prior to the determination of the depth of events, the new enhanced network data were exploited to re-calibrate local velocity models. Results are in close agreement with prior analyses, (Dominique 2015, Kinscher 2017) and the velocity model used in Part II and III, namely: a single-layer model with velocities $v_P = 3900\, ms^{-1}$ and $v_s = 1950\ ms^{-1}$ (with $V_P/V_S = 2$).

Source depths of the events have been then estimated by taking into account the P and S wave picking by using the probabilistic approach as introduced in Part III, Chapter 11.2. Results indicate that depths of the 14 events (Figure 14.2a, events indexed from A to N) are mostly between 50 and 200 m below the mining works and only a few events appear to be closer to the mine work, but no events appear to be above (Figure 14.2b). Depth uncertainties are presented as cumulative probability contours of probability function (PDF) for each localization result, representing the probability that an event will be located at 68%, 95% and 99% chance in the area limited by these curves. As shown in Figure 14.2b, location uncertainties depend on the number of stations available around the source for different events, decreasing with the more stations available. For a 99% probability, uncertainty was estimated between 50 and 100 m for the epicentre and 100 to 200 m for the depth.

Seismic source mechanisms are commonly mathematically represented with the seismic moment tensor which comprises the generalized force couples. Natural tectonic earthquakes are expected to have only double couple (DC) components, which represent a pair of force-couples whose torques cancel each other (Gilbert 1971, Aki & Richards 2002). Fault rupture is associated with a shear failure. The equivalent radiation pattern of the P-wave of shear failure is four-lobed, resulting in alternating polarity (direction of the first motion) which can be recorded by seismic stations (Figure 14.3 a). Unlike tectonic earthquakes, the source mechanisms of mining-induced seismic events are usually driven by other types of dynamics resulting in other types of failures. Apart from DC components, in moment tensor decomposition often NON-DC components dominate (A. Miller *et al.* 1998, Julian *et al.* 1998, Cesca *et al.* 2012), more precisely implosive components, or a mix of implosive plus shear source mechanisms, rather than pure shear. Source signature of these events are additionally influenced by the complex interaction of the waves with the mining excavations and surrounding disturbed rockmass (Linzer *et al.* 2021). Case studies of collapses of mining galleries (e.g.: pillar failure, roof fall, etc.) usually observe dominant implosive component (Hudson *et al.* 1989, McGarr 1992a, b, Malovichko *et al.* 2012, Boettcher *et al.* 2015), which can be recognized in seismic recordings as the negative onset of P-waves on all stations regardless of azimuth (Figure 14.3 b). An example of such case, as presented in Part I, describes the collapse in Teutschenthal potash mine in Germany (Cesca *et al.* 2012).

For seismic events located in the study area of this thesis, the source mechanism was determined by (Kinscher 2017) for several events of a seismic crisis of December 2014, with recordings of the sparse network, based on the inversion of the waveforms and the analysis of the P and S amplitudes ratios. Analysis revealed a normal fault-type mechanism, also consistent with the faults documented within the Grande mine layer in the northern part of the study area. These results obtained from recordings of only 4 stations, are associated with high uncertainties and were therefore reevaluated (Kinscher *et al.* 2021) due to much better conditions of newly enhancement in the seismic network. The same 14 events priorly chosen for depth analysis were used. Several approaches were applied:

I) Analysis of the direction of first motion (or polarity) of P waves on each station;

II) P and S wave amplitude ratio analysis;

III) Full waveform moment tensor inversion method.

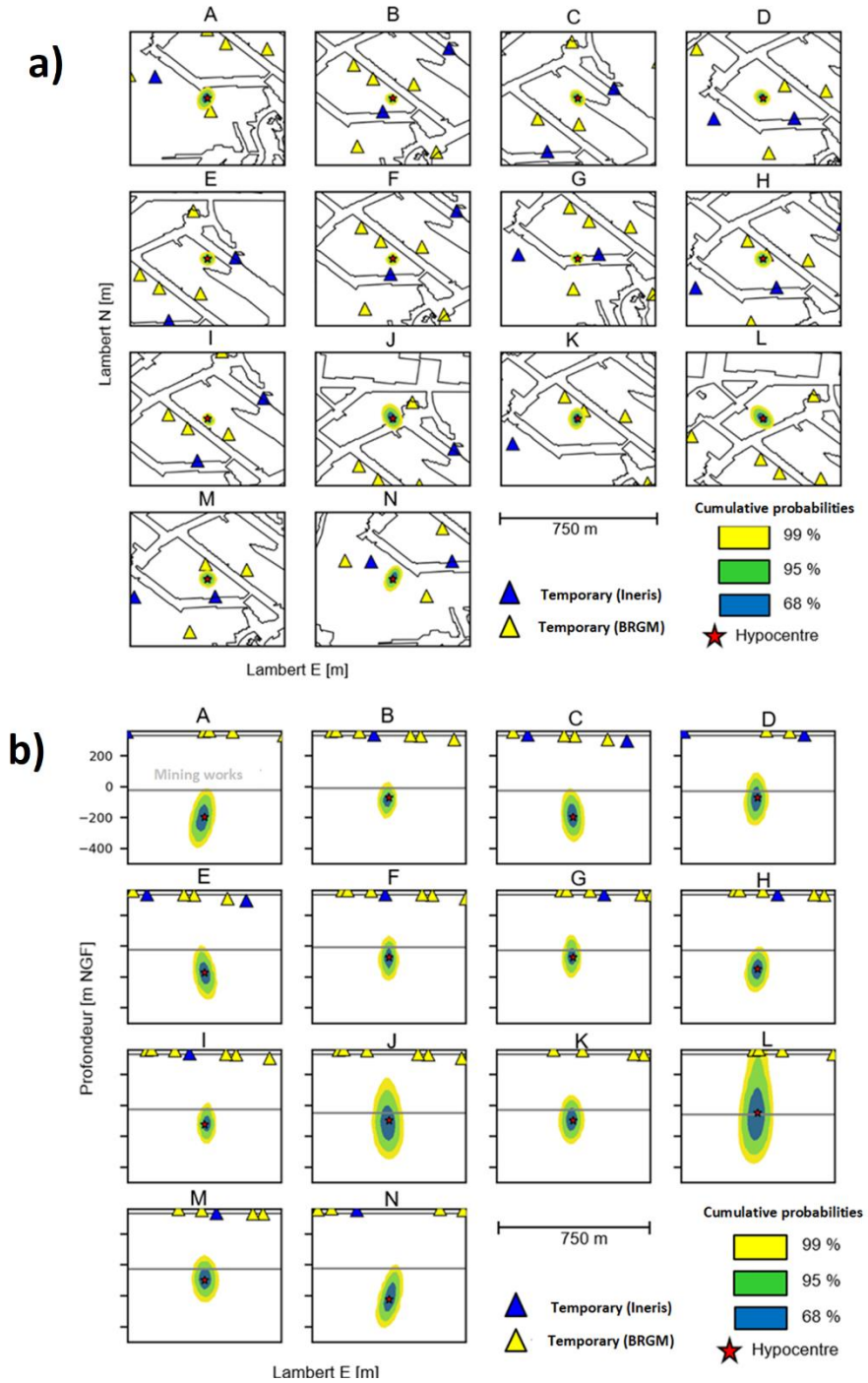

Figure 14.2 Determined location of 14 events and location uncertainties (see text). A) Epicentral location. The cumulative probability curves in the horizontal plane represent the epicentral localization uncertainties B) Depth estimates. The cumulative probability curves in the vertical plane represent the depth localization uncertainties. Figure adapted from Kinscher (2021).

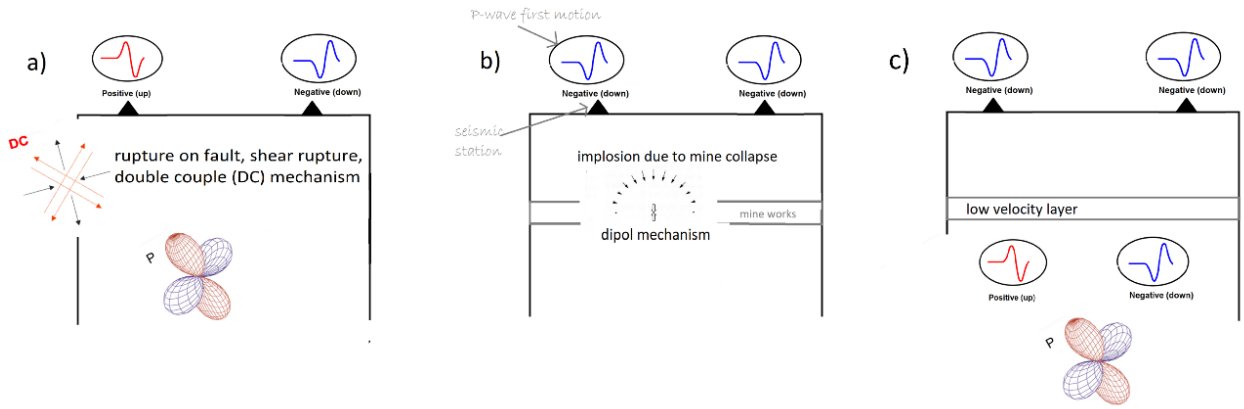

Figure 14.3 2D representation of radiation patter of P waves and its polarity observations on seismic records accordingly, for different mechanism a) general case of fault rupture – DC mechanism; b) in mining environment: mine collapse – implosion mechanism c) suggested polarity change due to low-velocity layer – DC mechanism (Kinscher et al. 2021) case of fault below mine layer with observed apparent implosion mechanism Figure with adaptations from Hasegawa et al. (1989) and Šílený & Milev (2008)

The first approach revealed a dominance of P waves negative polarities in all 14 events, which, as mentioned, is a characteristic of the implosive type rupture behaviour (Figure 14.3 b) and an indication of the collapse in mine. However, additional modelling with synthetic seismograms including the effect of a low-velocity layer provided an explanation of the observed negative polarities of the P waves, showing that this can be an effect of the mine layer and/or fluid in rock, which can result in changing of the wave polarity (Figure 14.3 c).

Considering that the characteristic indicator of the DC mechanism is the presence of a significant energy fraction of SH waves relative to P and SV, the observed implosion mechanism was additionally investigated with the second approach, analysis of the S and P wave relationships. The results show that SH and P ratios seem much more consistent with a shear failure than with a tensile failure mode as expected in the model of the mine collapse. These results agree with the previous study (Kinscher 2017).

Results from waveform-based inversion were of poor quality due to the complexity of the analyzed seismograms, which seems to be related to wave passing through the mine workings. So this analysis could unfortunately not provide reliable DC source mechanisms which would have allowed to relate seismic events to preexisting fault structures and to understand their sense of faulting. On the other hand, complexity in the waveform presents indirect evidence that events were located below the mine layer

For further details please see Annex IV -.

In conclusion, both source depth and source mechanism analysis consistently indicate source depths are below mine working and related to the shearing mechanism which is rather in agreement with hypothesis N°2.

14.3 Conclusion about source origin

To better understand the origin of the observed local seismicity and to evaluate the two main hypotheses, results of extensive seismic data analysis done as part of thesis work and study done by (Kinscher *et al.* 2021) are presented and interpreted in previous sections of this Chapter.

Combined, they provide a significant set of arguments to evaluate hypotheses of the origin of seismic events, which are summarized in Table 1.

Additionally, first attempts of geomechanical numerical modelling, which was done as a complementary to thesis performed to verify hypothesis N°2 according to which the post-mining seismicity could be linked to a shear movement of the faults present in the district of Régagnas. Results showed that reactivation of faults below the mine layer is from a geomechanical point of view a realistic scenario, under following conditions: faults are dipping at angles δ lower than 80°, the ratio between the minor horizontal stress σ_H and the vertical stress σ_V is lower than 0.6 and the friction angle ψ is below 30°. However, these parameters are highly uncertain and have not confirmed the observations completely, so the results of modelling are not completely conclusive (Kinscher *et al.* 2021)

In conclusion, all the indications are in favour of seismic sources origin on the fault below mine hypothesis 2 as a more valid conclusion of the origin of the seismicity.

Table 1 All arguments pro- /con- listed for each hypothesis based on seismic data analysis

Argument/results of the analysis	Hypothesis 1	Hypothesis 2
Depth: some events in mine layer + most events below mine (Kinscher *et al.* 2021)	PRO: a location of certain events in mining works cannot be ruled out CON: events mostly located below mine	PRO: Most events below mine CON: -
Spatially constrained clusters with a long period of activity (Same clusters active 2010-2020!) (thesis work)	PRO: Possible if faults in the overburden CON: pillar rupture does not take years	PRO: Possible CON: -
Repetitive activity in the same source (multiplets and repeaters) (thesis work)	PRO: Possible if faults in overburden (?) CON: ruptured pillar can not rupture repeatedly and in the same source	PRO: such observations usually connected to rupture of asperities on creeping faults CON: -
The identical polarity of first onsets of P-phase waves at all azimuths (Kinscher *et al.* 2021)	PRO: compatible with a mechanism of the implosion-type that would be expected in the case of a mining collapse CON: -	PRO: effect of the presence of a low-speed layer, such as mining work and/or the presence of water, on the P-wave waveform CON: not expected for a DC mechanism
The dominance of events with a significant energy fraction of SH waves relative to P and SV waves (Kinscher *et al.* 2021)	PRO: Indication of shear rupture mechanism (fault) possible if the fault in the overburden CON: not consistent with the previous argument of a tensile failure mode as expected in the model of mine collapse	PRO: Indication of shear rupture mechanism (fault) CON: -
Source mechanism DC (Kinscher 2017)	PRO: possible if a fault in overburden (?) CON: expected NON-DC components in case of mine collapse	Indication of shear rupture on a fault

15 Seismicity-hydrology connection

Even though the apparent connection of seismicity with hydrogeological conditions has been previously observed in the studied area of the mine (as presented in Part I section 2.5.1), the relationship between seismic activity and hydrology as well as the triggering mechanism is not well understood.

Circulation of the water in Gardanne mine in the period after the closure and the flooding is not well understood in the study area, mainly due to the complexities of the mining drainage systems and limited hydrogeological instrumentation (Part I section 2.4.1, Kinscher *et al.* 2021). Despite these complexities and shortcomings in hydrological data, we discuss the main trends visible by comparing the available hydrological data with the new seismic catalogue (2014-2017) produced in Part II.

15.1 Influence of the rainfall on the seismicity triggering

As noted already by Dominique (2015) for the seismic crises of June 2010, November 2012, and December 2014, an increase in seismic activity occurred after a delay of about ten days after the peak of the effective rain[1].

The influence of the rainfall on seismic activity separately of each cluster in the period 2014-2017 is explored in Figure 15.1. Temporal distribution of seismic activity of each cluster, identified as potential faults in the previous Chapter, are compared separately with the hydrological data recorded in the Fuveau Regagnas well. Hydrological data of this well are considered as a good indication of the amount of effective rain that reaches the mining aquifer due to the shallow depth of the well, which does not reach depths of mine works or known aquifers.

We can observe that the strongest seismic activity of most clusters correlates with the rainfall period, which is in the agreement with prior observations. The crisis which occurred late 2016-early 2017 followed the heavy rainfall period as well.

The strongest activity of cluster 6 in the northwest is however observed during a dry period in August 2017, indicating the involvement of the other factors in the triggering mechanism of seismicity.

[1] **effective rain** is the excess of water that can flow when the soil is completely saturated, either for a runoff to streams, either for a return to the water table. This rain or runoff is said to be "effective" because it alone contributes to the replenishment of water tables. It depends regionally on the type of soil and climate conditions (Dominique 2016a)

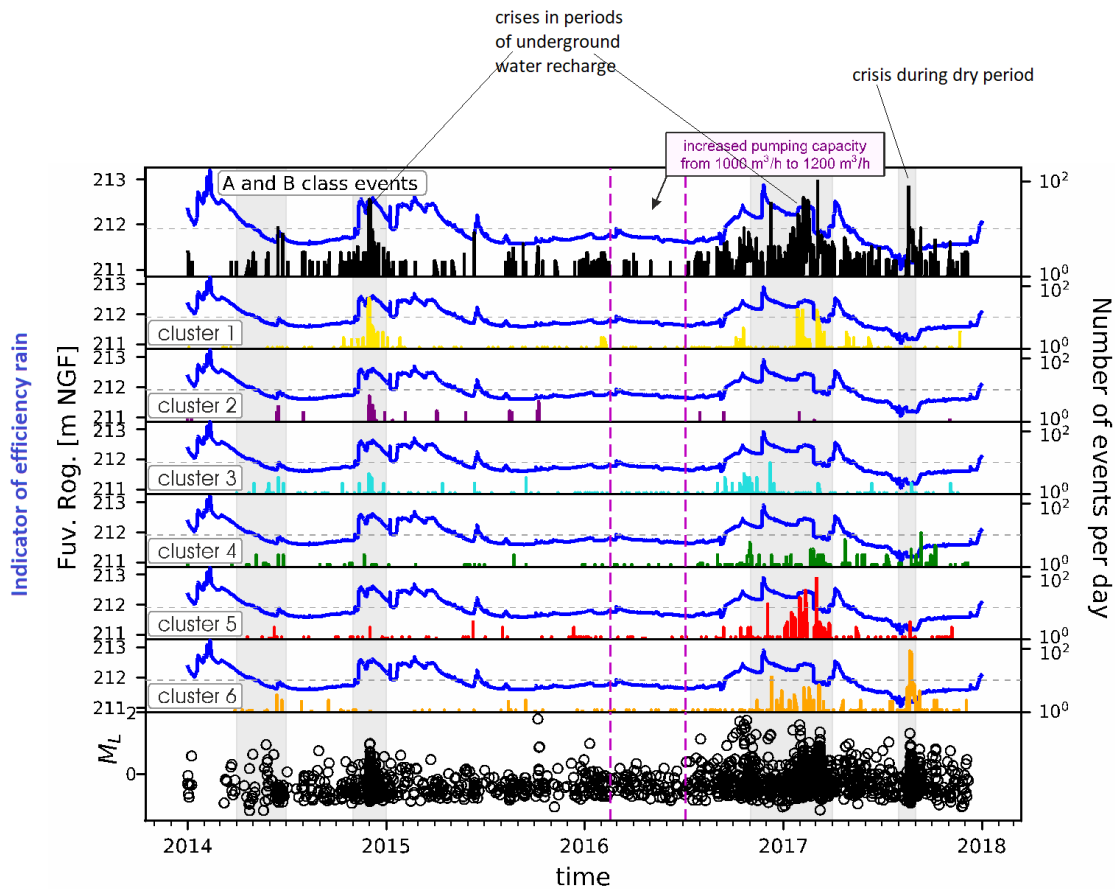

Figure 15.1 Temporal distribution of seismic activity for A and B class events per day (top figure), and each cluster separately and their magnitudes (figures below), compared with water levels at Fuveau Regagnas well (F on Figure in Annex- Part I - Seismic networks and data used) presenting effective rainfall (blue line).

15.2 Influence of the pumping on seismicity migration

Spatio-temporal migration of seismic sources has been clearly observed for events of the new catalogue 2014-2017, notably between clusters 1 and 5 (Part III, section 11.2). In this section, a correlation of this migration with the hydrogeological conditions in the mine is established.

Spatio-temporal distribution of seismicity is shown separately for two 2-year periods (2014-2015 and 2016-2017) in Figure 15.2 . Separation of these two periods allowed to observe differences in seismic distribution as a function of the flooding front position. The year 2016 is marked by an increase in pumping capacity at Gerard well from 1000 m3/h to 1200 m3/h. This led to a notable decrease in water levels in the mine, and the withdrawal of the flooding front in the study area in the period 2016-2017 (Figure 15.2 b) compared to the period 2014-2015 (Figure 15.2 a).

In the period 2014-2015 (Figure 15.2 a), water levels were higher and the flooding front fluctuations were confined to shallower depths of mine works, and the strongest seismic activity is observed in the

southeast (cluster 1, 2 and 3). During this period strongest seismic activity was during the seismic crises of December 2014 in cluster 1.

During the period of 2016-2017, clusters in the southeast remain seismically active, however, increased seismic activity can be observed in the northwest (clusters 4, 5 and 6). This period is marked by two seismic crises: first in late 2016-early 2017 and second during August of 2017.

As pumping capacity at the Gerard well increased, the variations of the water level were probably getting more intense during periods of strong water incomes (rainfall period in 2017-2016) and lead to fast increases and decreases and thus very strong pore pressure perturbation

Looking at the central cluster (clusters 1 and 5), the strongest seismic activity seems to follow the withdrawal of the flooding front from the southeast towards the northwest, due to an increase of pumping capacities.

The influence of the change in the pumping rate is furthermore visible by a change in the seismic signature. For example, certain long-term multiplet families seem to disappear when pumping started which suggest that pore-pressure was lower in certain fault segments.

Additionally, no new seismic crisis had been observed since the crisis of August 2017, which suggest that the water level is finally stabilized at a lower level and that the strong pore pressure increases due to flooding are impeded by the stronger dewatering rate in the mine layer.

Influence of the pumping on the seismicity triggering, based on the flooding front withdrawing is not easy to interpret, especially in central cluster, as cluster 5 was not active prior to crises of late 2016 – early 2017 even though same water levels and hence same pore pressure have been reached during previous periods as well, e.g. prior to the crisis of December 2014 and activity of the cluster 1. Hence, observed migration of seismic activity within the central cluster suggests an additional triggering mechanism than pore pressure.

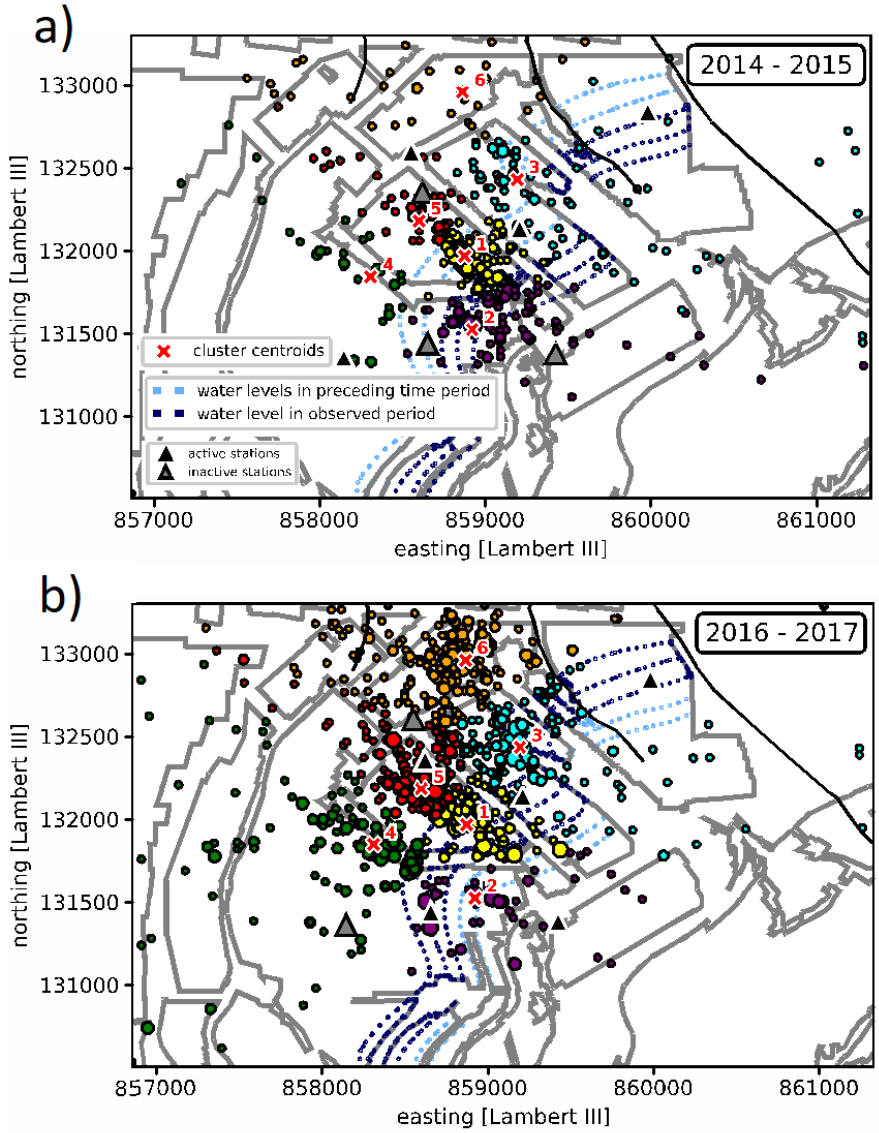

Figure 15.2 Spatio-temporal distribution of seismicity within two periods a) 2014-2015 b) 2016-2017. Station configuration changes are indicated: active stations within the observed period are shown with black triangles, while grey triangles correspond to non-active stations. Flooding front migration is shown with front position: a dark blue indicates levels in this sector in the observed period, while light blue indicates flood front position in the preceding period. The flooding front is presented based on a projection of the water level measured at the Gerard well.

15.3 Conclusion about the hydro-seismic connection

The previous observations demonstrate and confirm that water level changes in the mine layer, linked to rainfall and the dewatering pumping rate, influence the seismic rate of the Fuveau swarm.

Seismic crises of December 2014 and end 2016-early 2017 follow the water level periodic changes depending on the rainfall season and pumping. Rainfall seems to present a significant factor in the triggering and activation of faulting. Indeed, as presented in Part I (section 1.3.2) seismic triggering from precipitation is a phenomenon already observed in few other mining sites, interpreted as triggered by the pore pressure diffusion process (e.g., Ogasawara *et al.* 2002).

In contrast, the seismic crisis of August 2017 during the drought period disrupts this pattern, possibly affected by the increase of pumping rate, which consequently lowered the water level in the mine works. During this crisis, the level of the water table assumably reached a minimal level since the flooding front reached the study area, significantly decreasing the hydrostatic pore pressure.

Unfortunately, due to the lack of piezometric instrumentation in the study area, it is not possible to quantify the exact water level nor the amplitude of water level changes. Therefore, the order of magnitude of hydrostatic pressure in these mining areas remains unknown.

Even though the precise determination of the seismicity triggering mechanism requires more precise information on the range of variation of the water levels, the newly raised questions of the triggering mechanism of seismicity during the dry season as well as the triggering mechanism during the period of rain are addressed in the next Chapter.

16 Mechanics behind triggering and clustering of earthquakes

Previous Chapters showed that seismicity is likely related to rupture on faults located below the mine workings. As shown in section 15.1, seismic rates seem to increase during periods of intense rainfall, likely due to pore pressure increases at the faults interfaces. Hence, pore pressure increase seems to be one of the main triggers of seismicity. In addition, strong spatial clustering of seismicity on specific zones generally suggests that certain groups of faults are more sensitive to pore pressure changes than others. This may depend on the local state of stress, the fault mechanical properties and their hydrological connection to the mine layer. In contrast, other fault groups seem to be active during periods when pore pressures decrease, as indicated by the occurrence of the last seismic crisis during a dry period (Figure 15.1, Figure 16.1, suggesting that also volumetric effects such as decompression seem to play a role in triggering seismicity (e.g. Part I, section 1.3.3).

In the following sections, potential mechanisms generating seismicity are discussed more in detail by focusing on the spatiotemporal evolution of each cluster separately in terms of the occurrence of multiplet and repeater phenomena and their duration and recurrence rates as introduced in Part III. In the discussion, generating mechanisms are separated into two phases:

I) the main mechanism that generates stress changes (perturbations) that lead to the occurrence (initiation) of seismicity (section 16.1, Figure 16.2), similar to mechanisms discussed in Part I, section 1.3;

II) 'secondary' mechanisms, responsible for subsequent clustering and repetitive nature of seismicity in time and space after stress perturbations caused by one of the primary driving forces (section 16.2, Figure 16.4), as already partially introduced in Part III chapter 8.

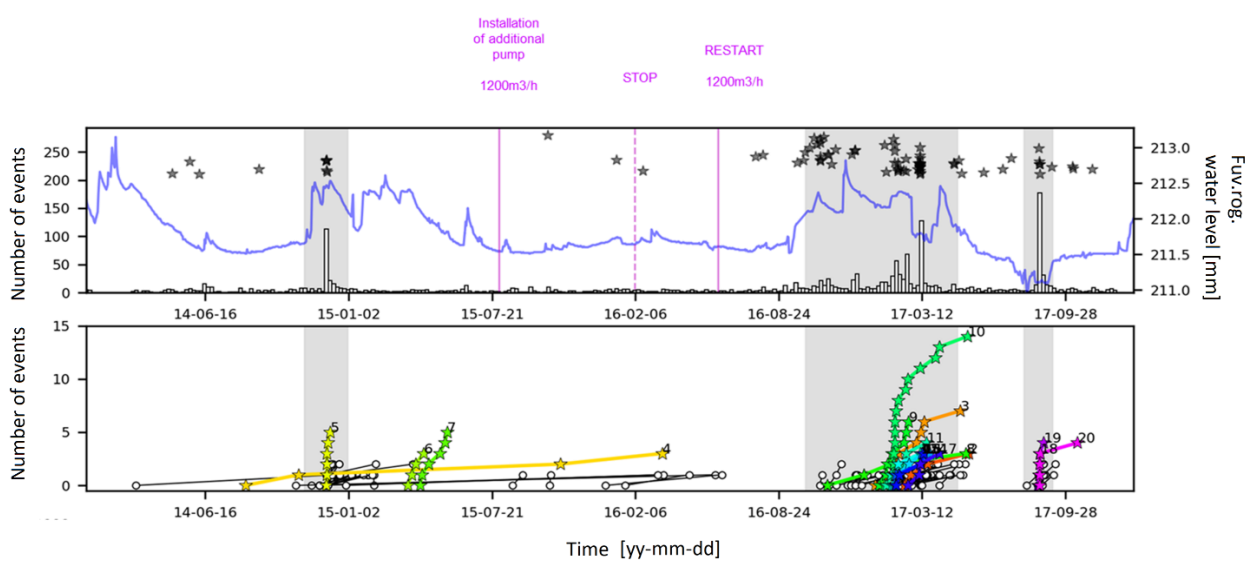

Figure 16.1 Temporal distribution of seismic activity compared with water levels at Fuveau Regagnas events in 21 main families (top figure), and time distribution of each family (figure)

16.1 Triggering mechanism of the seismic activity

The factors that are recognized as the main sources of stress changes responsible for the occurrence of seismicity at Gardanne are following (Figure 16.2):

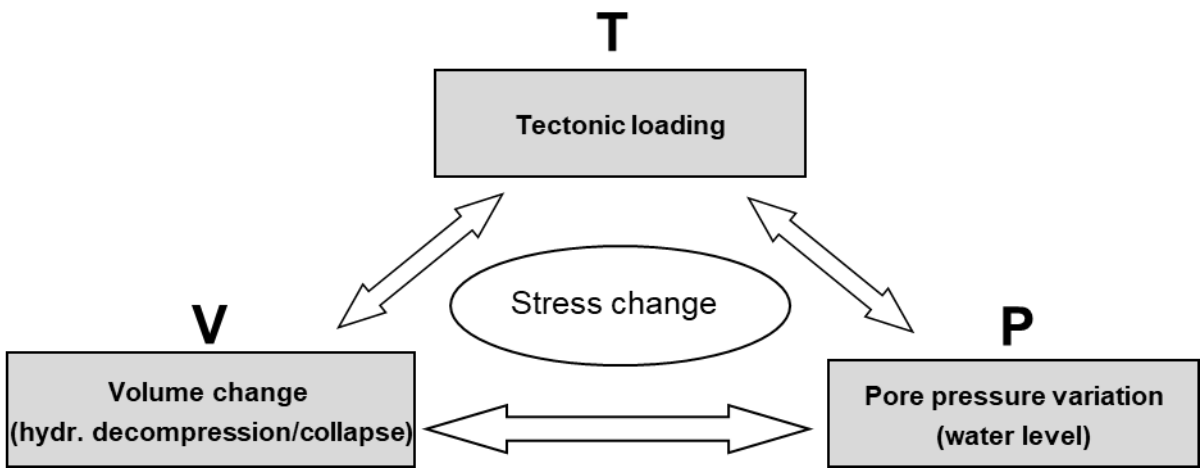

Figure 16.2 Possible triggering mechanisms of seismic activity in the study area: tectonic loading, volume change due to fluid extraction and/or pore pressure increase

Tectonic loading

(further referred to as **T**)

In any fault zone in the Earth's crust, under a constant rate of tectonic loading, the critical value of the stress on the fault will be reached at more or less regular intervals. This leads to sudden failure accompanied by the emittance of seismic waves and a local stress drop (earthquake), followed by a new phase of stress build-up (Brandes & Tanner 2020). The concept of periodic build-up and release of stress on a given fault is known as a seismic cycle (Convertito & Faenza 2014), was first presented by (Reid 1910), but redefined over the years (R H Sibson 1986, Richard H Sibson 1989, Di Toro *et al.* 2012).

As mentioned in Part I, (Chapter 2), the Gardanne mining basin is a known naturally seismic active region and known for the occurrences of moderate earthquakes (e.g., at Mimet on February 19, 1984).

Volume changes due to fluid extraction

(further referred to as **V**)

Mechanisms of seismicity induced due to fluid extraction were introduced in a part I, section 1.3.3. Several examples of reservoir induced seismicity were presented (e.g. Lacq gas field in France), where seismicity

is triggered by rock compaction (volume decrease) during pore fluid extraction, as often observed in reservoirs.

Similarly, flooded Gardanne mine workings can be interpreted as a water reservoir associated with volume changes due to, as observed, periodical water level changes.

Significant dewatering phases (e.g. caused dry periods and/or intensified pumping rate) of the mine are expected to cause compaction of the surrounding rock, and hence may lead to two possible mechanisms:

I) compaction in the overburden (roof of the mine), and thus may involve a collapse of mine workings, modifying the stress state near the mine workings and provoking seismicity.
II) inducing stress changes in the surrounding rock, that could lead to triggering of seismicity in preexisting faults (e.g., section 1.3.3).

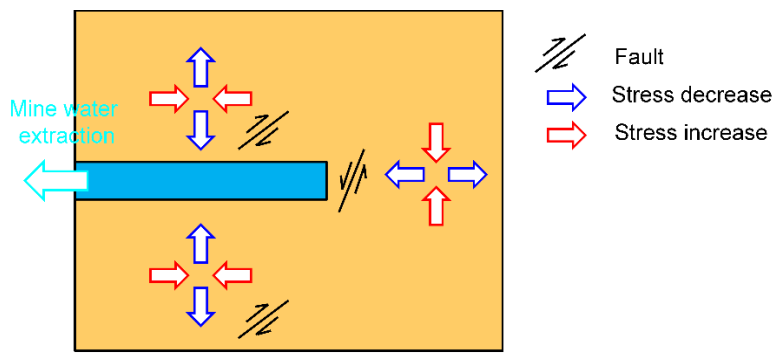

Figure 16.3 Illustration of mine water extraction

Pore pressure increase effect due to water level increase

(further referred to as **P**)

As mentioned earlier, pore pressure increases are likely to occur during wet periods, as also consistently observed in other flooded abandoned mine environments. As described in Part I, shear failure on fault as an effect of the increase of the pore fluid pressure can be explained by Mohr-Coulomb criteria, and may result from the reduction of effective normal stress on the fault.

16.2 The secondary, driving mechanism behind clustering and multiplet families' sequences

In the previous section, the possible initiation mechanism of the rupture on the fault(s) were presented, while in this section we focus on understanding of the mechanism behind clustering and repetitive behaviour. As described in part III (Chapter 8), the driving mechanism behind the formation of the spatial clusters, multiplets and repeater can be summarized as in Figure 16.4 Secondary, driving mechanism

behind clustering and multiplet families' sequences: creep, localized pore pressure effect or seismic stress transfer by fault slip:

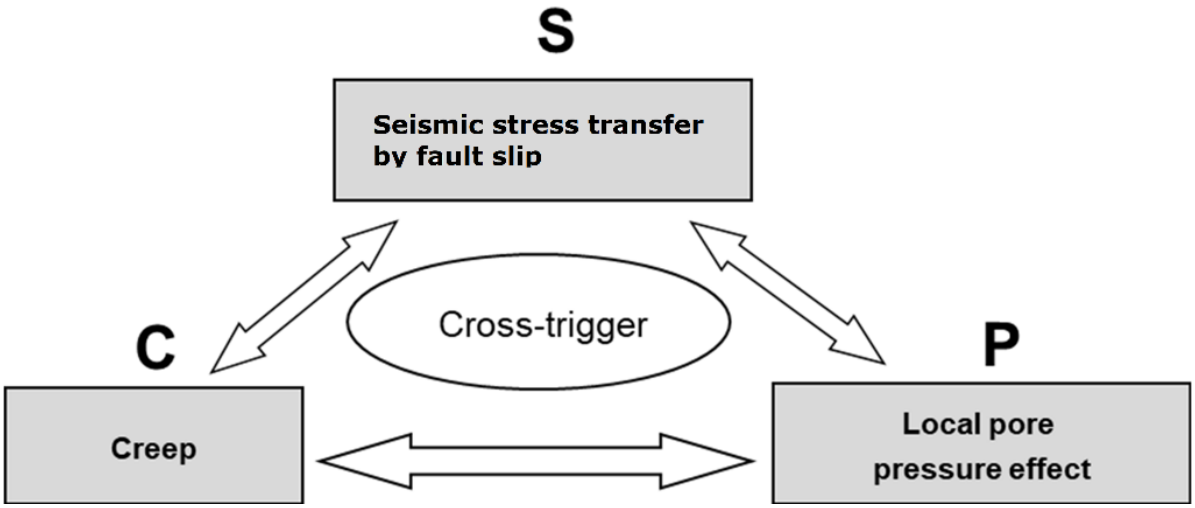

Figure 16.4 Secondary, driving mechanism behind clustering and multiplet families' sequences: creep, localized pore pressure effect or seismic stress transfer by fault slip.

Seismic stress transfer due to fault slip

(further referred to as **S**)

Each rupture/slip on a fault generates stress changes in its environments which itself may lead to rupture on the neighbouring fault segments. Such static stress transfer is often seen to be the main driving force of aftershock clusters, as described in Part III Chapter 8.

Creep

(further referred to as **C**)

Creep is often considered to be the main driving source of seismic repeaters (PART III Figure 8.1). The recurrence rate of repeaters reflects the repeated charging of a seismic asperity depending on the creeping behaviour of the fault, e.g. constant creep related to tectonic loading and/or afterslip after main fault rupture and/or fault creep due to pore pressure increase.

Local pore pressure effect

(further referred to as **P**)

In some case studies, it has been shown that transients of seismic repeaters and multiplet occurrences can be also sometimes related to the local pore pressure effect alone without fault creep (PARTIII, Bernard 2014, Duverger *et al.* 2018). Indeed, this particular case may occur when pore pressure increases very locally at certain fault patches, leading to acceleration of the loading cycle (i.e. tectonic shear loading

fastened by pore pressure). The recurrence rates of the multiplet would thus depend on the pore pressure evolution at that specific fault patch (Figure 16.5)

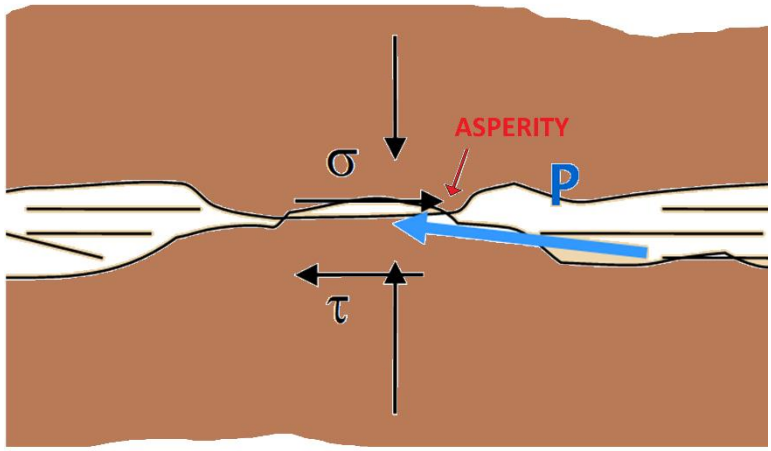

Figure 16.5 Local pore pressure on a fault patch (asperity)**.**

16.3 Interpretations of mechanism for each cluster

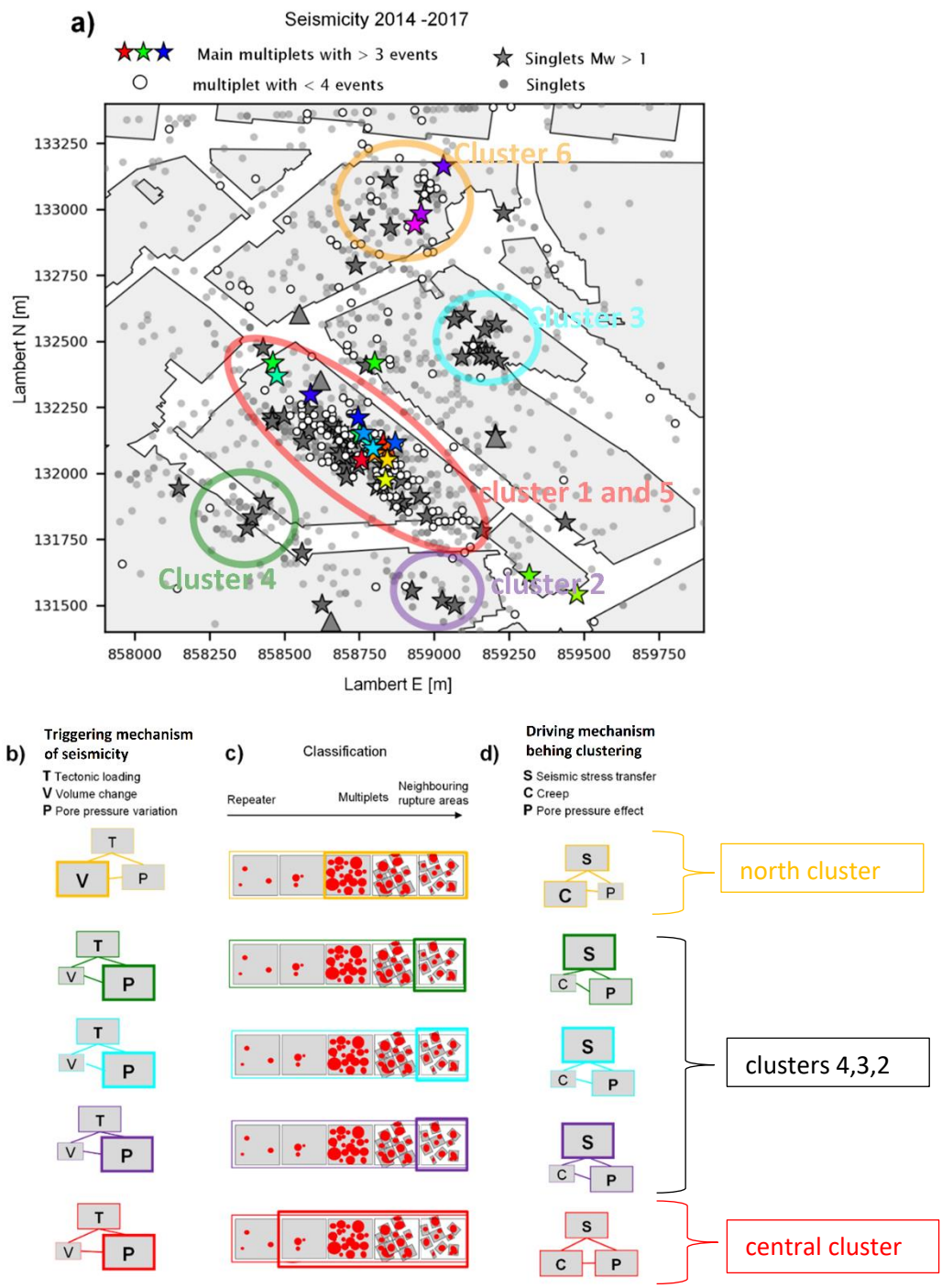

Figure 16.6 Seismicity and proposed mechanisms behind triggering and clustering/repetitive behaviour a) Location of clusters of multiplet families and/or strong events, and singlets b) Proposed triggering mechanisms of each cluster; colours match clusters in a), (see sections 16.1, 16.3 for details), c) Repeaters, multiplets and/or neighbouring rupture areas within the cluster (see sections 8.2, 16.3 and Figure 8.1 for details) d) driving mechanism behind the clustering/repetitive behaviour of each cluster (see sections 16.2, 16.3 for details)

16.3.1 Central Cluster (clusters 1 and 5)

Circled with red colour in Figure 16.7, the central cluster represents the seismically most active zone of the study area.

The estimated source dimensions (see Chapter 12) of these clusters suggest the presence of a dense network of faults with a dimension of some meters to some tens of meters, which partially cross-cut each other and partially form common rupture planes.

Triggering mechanism (in regards to section 16.1)

The main activity of this cluster during both crises of December 2014 and late 2016-early 2017, started following the start of strong rainfall periods and thus likely has been triggered by an effect of the increase of the pore fluid pressure (P) (figures 16.8 and 16.6b), which led to shear failure on fault(s).

As described in Part III (section 9.2, Figure 9.3), the activity of this cluster during crises late 2016-early 2017 can be separated into 2 phases. The period of the few weeks of delay between them may either reflect the time scale for the build-up of stress redistribution from one primary structure to the next activated one, finally reaching its failure strength (for instance elastic stress build-up due to the slow slip on a fault segment), or/and the time scale for decreasing the strength of the target structure (for instance through pore pressure diffusion and increase).

Repetitive behaviour and clustering (in regards section 16.2)

Cluster is characterized by the presence of numerous partially overlapping multiplet families and potentially repeaters (see PART III, Chapter 12, Figure 12.2, Figure 16.6c).

The observed decrease of seismic activity of short-term multiplets/repeaters (e.g, figure 16.1) can be characterized as (or similar to) Omori-law decay, which indicates the potential creep (C) mechanism, as repeaters are most commonly described by the creeping behaviour (velocity strengthening friction behaviour) of the fault, as described in section 8.3. However, seismic stress transfer (S) in classical aftershock pattern in time generally follows the well known Omori power law as well. Due to this complexity, it is very difficult to associate in detail the difference in the recurrence rate (rather periodic vs Omori-like), to specific driving forces.

However, in principle, Omori like pattern cannot be excluded regarding the mechanism (P) neither. Indeed one could imagine a pore pressure evolution at respective asperities, which increases sharply during intensified rainfall, followed by a dewatering phase of the mine layer similar to an Omori decay behaviour, as partly seen in the piezometric data.

- **Multiplet transients (i.e., short-term or burst type, section 8.3)**

Some multiplets' short-lasting duration can be interpreted by several processes. One is due to the pore pressure decreases (P) during the dewatering phase, while another possible mechanism is the locking of

faults due to faulting (dislocation) on intersecting faults. Indeed, the central cluster seems to be a rather complex cluster of intersecting faults as demonstrated by the number of multiplets and isolated events. A third somewhat similar mechanism is energy exhaustion by rather "large" slip potentially associated with the isolated M> 1 events, associated with the relatively large slip events which may potentially reduce the local loading stress acting on the neighbouring multiplets.

- **Longlasting multiplets (i.e, long-lasting or continuous type, section 8.3)**

Apart from multiplet transients, some long-lasting multiplet families are observed as well, partly characterized by rather periodic recurrence rates. Long-lasting periodic multiplets seem most likely to reflect accelerated loading of certain asperities due to local overpressure (P) and/or constantly creeping fault structures (C). Interestingly, most of these long-lasting multiplets seem to disappear after the increase of the pumping rate in 2016 (Figure 16.1). This generally suggests that the water level was generally higher before and the pore pressure apparently high enough to significantly accelerate the loading cycle / accelerate recurrence time. The end of the long term multiplets in 2016 corresponds to the pumping installation which likely decreased the pore pressure/water level and thus the shear loading rate

- **Isolated events**

The presence of the isolated events within the cluster is also observed, including larger M>1 events suggest that stress transfer by slip on neighbored fault segments (S) probably also contributes to spatio-temporal clustering of seismicity, as described in Chapter 8 (Figure 8.1).

. . .

As the pore pressure increase is not constant and depends on rainfall periods, the clustering sequence in the case of seismic repeaters is most likely related to the creep transients (C) triggered by pore pressure increase (P), while in the case of multiplets or aftershock sequence it is rather related to stress transfer (S) (interevent triggering) between neighbouring asperities and/or ruptures areas.

Local pore pressure increase (P) can be however excluded for the largest multiplet family 10 with around 15 events. Indeed the 15 events imply a stress release of around 15 MPa which would require an overpressure of around 25 MPa when assuming a standard friction coefficient $\mu = 0.6$, following Mohr-Coloumb criteria which would correspond to a water level rise of 250 m which can be generally excluded (Kinscher *et al.* 2021). However, a short-lasting multiplet with around 4-5 events would require overpressure of around 7-8 MPa, which remains in the potential range of water level rise in the target area from a hydrological point of view.

In conclusion, all three main driving forces as presented above (Figure 16.4, Figure 16.6d) seem to be involved in the main cluster formation and activity. Clustering behaviour (Figure 16.6 b),c) and d)) is characterized by duration and repeat rates of multiple and repeat transients, which are probably mainly controlled by local pore pressure evolution (P), and creep rates(C) of given faults, while isolated events could be caused by stress transfer by slip (S) on neighbored fault segments.

16.3.2 Cluster 2, 3 and 4

Triggering mechanism (in regards section 16.1)

As described in section 9.2, seismic activity in clusters 2, 3 and 4 (Figure 16.6, clusters marked with blue, green and purple) widely coincide with periods of increased rainfall and thus seems widely triggered by pore pressure increase (P) on critically stressed faults located/concentrated in the cluster areas (Figure 16.6.b) Interestingly, in all three of these clusters, almost no multiplet/repeater activity can be observed. In contrast, comparatively large events ($M_W < 1$) dominate. These events occur in a form of rather isolated events, with differently looking waveforms (Figure 16.).

Clustering behaviour (in regards section 16.2)

This absence of multiplets and repeaters generally indicates that stress transfer between neighbored faults (S) seems to be the main driving force for spatial and temporal cluster formation, comparable to aftershock patterns after main shock events (Chapter 8, Figure 8.1). In this case, however, no main shocks can be observed, but rather swarm episodes initialized by pore pressure perturbation and interevent triggering related to static stress transfer (Figure 16.6.d)

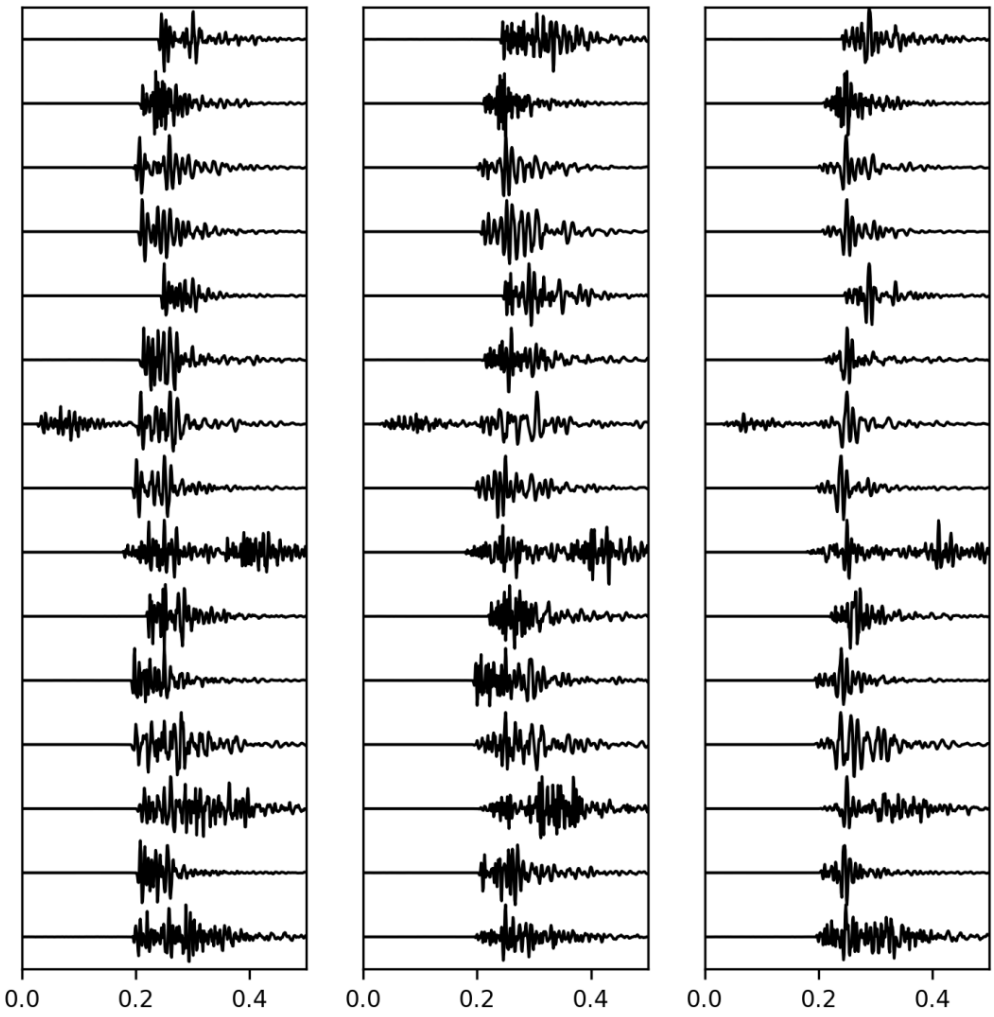

Figure 16.7 Dissimilarity of strongest (M> 1) events of clusters 3**.**

16.3.3 Cluster 6

Triggering mechanism (in regards to section 16.1)

Cluster 6, the most northern cluster (Figure 16.6 marked with the orange colour), is somewhat specific compared to the previous ones since it seems to be mainly active during an apparent dry period without rainfall and with a high pumping rate (Figure 15.1). The main driving forces of the last significant increase in activity in August 2017 is thus most likely linked to the compaction phase due to fluid extraction (V) (Figure 16.2).

Repetitive behaviour and clustering (in regards to section 16.2)

Compared to previously described clusters 2, 3 and 4, more multiplet/repeater families seem to be located within this cluster, occurring in form of short-term transients over weeks to some months. These transients may potentially represent two mechanisms (Figure 8.1., Figure 16.4): stress redistribution by fault slip on neighbored fault segments (S) and/or fault creep transients (C), both following the change of stresses (due to dewatering). Unfortunately, quantification of source overlap of multiplet families in Part III was ambiguous such that it remains impossible here to conclude which of the two mechanisms is dominant here.

16.4 Conclusion about triggering

Based on presented observations, there are strong indications that the primary triggering force for all the clusters except cluster 6 (orange) is the increase of the pore pressure, while the activity of cluster 6 appears to be triggered by significant fluid extraction from the mine layer, where the exact mechanism remains an open question. Most multiplet families, and potentially repeaters, occur in the central cluster and cluster 6. Multiplet events are likely related to both slowly slipping, creeping fault segments and/or accelerated loading cycles of seismogenic faults due to localized pressure increase at the faults interface (asperities). Few or no multiplet families are observed in clusters 2, 3, 4 which seem also more dominated by isolated stronger M> 1 events. The observed increases in seismic activity (temporal clustering) in each of these clusters most likely represent stress redistribution (relaxation) following pore pressure induced fault slip on neighbored slipping fault planes comparable to classical aftershock pattern, without any visible mainshock.

General conclusion and perspectives

Summary and conclusions

As the number of mine closures increases throughout the world, so does the concern for public security and the need to manage related issues, due to problems that can potentially arise from it. In this context, the subject of this thesis focuses on the problem of induced seismicity with the case study of the flooded coal mine of Gardanne, in southern France, where a reliable assessment of the induced seismicity hazard and awareness of the potential magnitude of surface seismic vibration in the area is of uppermost importance, due to significant post-mining seismicity problem. The seismic hazard in flooded post-mining districts, related to dynamic ground motions (shaking, vibrations) generated by seismic waves, is generally poorly known and very challenging to determine and to include in post-mine risk procedures.

***

Gardanne mine was closed in 2003. As a result of the shutdown of mining operations, the pumping was greatly reduced thus causing the flooding of a large part of the exploited areas. Since 2010, the coal basin has been periodically affected by significant seismic activity that is located both within as well as outside the areas identified as zones of high risk of ground instabilities, which are monitored by the Ineris permanent monitoring network. This seismicity appears to be related to the flooding of mine voids and the fluctuations in the water table caused by rainfall events.

Particularly active zone (the so-called “Fuveau swarm” zone) is in the Regagnas (and partly Gréasque) mining sector, where seismic events occur as “crises”, which reoccur periodically (2012, 2014, 2016-2017), mainly in form of seismic swarms. The most important seismic events recorded during these crises show magnitudes close to 2, which were felt locally by the local population. Gardanne mining basin is also known as a naturally seismic active region and associated with the occurrence of some moderate M~4 earthquakes (e.g., at Mimet, on February 19, 1984). The strong seismic activity led to the installation of a temporary seismic network by BRGM-DPSM in 2013.

Preliminary studies, mostly based on analyses of a seismic crisis in 2014, suggested that seismicity seems to be triggered by seasonal fluctuations of the water level in the mining works (Dominique 2015, Matrullo *et al.* 2015, Kinscher 2017). As a result, mining work has been identified as an effective “anthropogenic” aquifer with significant storage capacity, particularly in areas with numerous mine voids (rooms and pillar operations), thus significantly altering the natural hydrogeological system. Subsequent studies on the 2014 crisis showed that seismic sources seem to be mostly located 100-500 m below the mining works (~400 m MBSL). Source mechanism indicated events related to a rupture mechanism along normal faults-oriented NW-SE. In addition, several "multiplet" type events have been observed, i.e., events with highly similar waveforms, indicating the repeated rupture on same or neighboured fault segments over periods from days to a few years.

Based on these results, two hypotheses regarding the origin of the seismicity have been brought up:

Hypothesis N°1: the origin of the seismicity is related to ongoing deformation in the mining works and in the overburden, which may lead to surface consequences and/or rupture of pre-existing faults. In this

case, seismic activity is likely to stop when the mine collapses eventually reach equilibrium as the final stage. The expected maximum magnitude M_{max} of the seismic events will depend on the size of the mine area affected by the collapses. This hypothesis is in contradiction to the estimated source depths which have been related to strong uncertainties due to a limited station number in the seismic source location.

Hypothesis N°2: the origin of the seismicity is related to the reactivation of deeper faults located below the mining works. The estimate of the hazard, in this case, would be completely different than for the first hypothesis, both in terms of the persistence of the long-term seismicity as well as in terms of the expected maximum magnitude, which in this case depends on the size of the active fault segment.

Each hypothesis leads to different implications for hazard definition or risk management.

***

The motivation of this thesis was therefore based on three main questions:

- what is the seismic source origin, in regards to two hypotheses?
- what are the triggering mechanisms behind the seismicity, in regards to the relationship between the hydrological and seismic system?

More specifically, the thesis focused on seismic data analysis, recorded in the most seismically active area, namely the Fuveau swarm. The analysis covered the period of 4 years, 2014-2017, during which the seismicity has been monitored closely by 3-5 stations of a temporary microseismic network of BRGM. Seismic data of the closest station Fuveau of Ineris permanent monitoring network (2 km away) was partially used as well, covering the period 2010-2017.

Part I of this manuscript provides an overview of the main factors as well as mechanisms governing ground and surface failures in post-mining environments as well as the role of seismic monitoring in this context. The mechanisms related to induced seismicity known in other post-mining sites and other relevant case studies related to anthropogenic/induced seismicity are also introduced. Main aspects of the Gardanne mine in the post-mining period are introduced, as well as hypotheses on the origin of the seismicity.

In Part II, improvements of the current monitoring and processing techniques used for the analysis of seismic data recorded at Gardanne are presented. To produce a detailed seismic catalogue for the period 2014 -2017, based on the data of the temporary microseismic network of BRGM. Due to the large volume of available unprocessed data, the first focus was on the application and development of an automatic detection and location approach. In this respect, a new detection and location methodology has been designed, that implemented full-waveform coherency-based detection and location approach Backtrack BB by Poiata. The main challenge in the adaption of the BTBB method (initially designed for dense seismic networks and arrays) due to the limited number of stations and to deal with challenges related to the false triggering of noise. Results of the analysis on 4 years of continuous seismic data show that the new methodology provides robust noise analysis and an increased number of detected microseismic events. Benefits of the new catalogue are multiple:

- it enables further more detailed analysis of seismically active structures and seismic sources, allowing to reduce the gap in understanding of the origin of seismicity towards confirming one of two proposed hypotheses of the seismic origin

- it enables a more accurate comparison of the spatio-temporal evolution of seismic activity along with changes of flooding level in the mine, by comparison with available hydrological data, thus enabling better insight into the connection between them as well as evaluation of triggering mechanism.

Additionally, the developed approach offers a solution for automatizing detection and location in operational microseismic monitoring, especially, but not limited, to post-mining settings where sparse temporary microseismic networks with one-component geophones are very often the only available tool for hazard assessment, and where timely decisions based on accurate seismic event locations are of most importance.

In Part III, the focus was on clustering of seismic events and exploring previously observed multiplet phenomena in more detail in space and time. Multiplet and cluster analysis objective was the identification and characterization of the underlying mechanism and processes generating seismicity. For the analysis, the seismic events of the new seismic data catalogue of 2014 – 2017 are mainly used, completed by data and seismic catalogue of the permanent network to obtain information on the period before 2014. Several clustering and multiplet/repeater analyses have been applied leading to the following main observation:

Clustering analysis showed the presence of six main clusters in the Fuveau swarm area. Most of these clusters have been active since 2010 and show constant background activity with temporary varying increases during main crises. Main seismic activity is related to clusters in the central part of the study area, active during periods of crises of December 2014 and late 2016-early 2017. A particular activity of an isolated cluster was observed at the North-East of the study area during the final crisis in August 2017.

Multiplet analysis on a broader scale (using Fuveau station) showed that multiplet families occur since the beginning of the flooding of the central basin area in 2010 and are also located southwards of the Fuveau swarm area. Most multiplets are however observed in the area of the central cluster of the Fuveau swarm. Multiplets occur in form of short-term transients (weeks to months), partially following the Omori decay pattern, especially during occurrences of microseismic crisis. They also occur in a form of long-term sequences with a partially periodic recurrence rate in the order of weeks and months to several years.

More detailed multiplet analysis, based on the new seismic catalogue of events (2014-2017) and the dataset recorded on the station of the temporary network, confirmed these observations. Multiplet families are observed also in the most northern cluster, mainly active during the last crisis in August 2017. Interestingly, in three clusters out of six, almost no multiplet families have been observed. Source parameter analysis was applied to examine source overlap of neighboured multiplets and evaluate the eventual presence of seismic repeater, potentially triggered by creeping fault zones. However, apart from some rather qualitative evidence, a detailed quantification of source overlap and related classification of

repeater/multiplet family could not be achieved due to strong uncertainty in absolute event location (due to limited station number).

As the monitoring network in the study area has been enhanced since 2018 and 2019, now comprising a total of thirteen instruments, an additional study was performed by Ineris on the newly recorded data of 2019 to better constrain seismic source mechanisms and source depths of identified faults segments. To better understand the origin of the observed local seismicity and to evaluate the two main hypotheses, the study results of this study are presented and interpreted. Both source depth and source mechanism analysis consistently indicate source depths are below mine working and related to the shearing mechanism which is rather in agreement with hypothesis N°2.

Additionally, first attempts of geomechanical numerical modelling were presented within the same study, performed to verify hypothesis N°2 accordingly. Results provided conditions under which the post-mining seismicity could be linked to the reactivation of faults below the mine layer, from a geomechanical point of view.

Thesis results were also in favour of hypothesis N°2. The repetitive nature of the seismicity, where each identified multiplet family indicates repetitive stress release in the same geological seismogenic structure, with the same failure mechanism, seems not to be compatible with seismicity triggering by degradation of the mining work as a result of the flooding, which would show a rather progressive spatial evolution of seismicity as typically seen in underground collapsing environments (e.g., Kinscher *et al.* 2015). Seismic activity related to the mining collapse would have variations in the mechanisms over time due to significant changes in the propagation conditions of seismic waves in the environment, the seismic signature would therefore be a priori dominated by spatial-temporal evolutions as well as various and evolutionary waveforms, contrary to observations.

The combined results provide a significant set of arguments to evaluate hypotheses of the origin of seismic events. In conclusion, all the indications are in favour of seismic sources origin on the fault below the mine i.e., hypothesis N°2 seem to be a more valid conclusion of the origin of the seismicity. Therefore, we can assume that clusters of seismic events correspond to activated faults or fault segments.

Even though the apparent connection of seismicity with hydrogeological conditions has been previously observed in the studied area of the mine, the relationship between seismic activity and hydrology as well as the triggering mechanism is not well understood. The previous observations demonstrate and confirm that water level changes in the mine layer, linked to rainfall and the dewatering pumping rate, influence the seismic rate of the Fuveau swarm. Seismic triggering from precipitation is a phenomenon already observed in few other mining sites, interpreted as triggered by the pore pressure diffusion process (e.g., Ogasawara et al., 2002).

In Part IV, to evaluate the hypothesis of connection to the hydrogeological system, available hydrological data are compared with the new seismic catalogue (2014-2017). Main trends visible in relation to each cluster are discussed. Seismic crises of December 2014 and end 2016-early 2017 follow the water level periodic changes depending on the rainfall season and pumping. Particularly, spatio-temporal migration

trends seem to be visible. Rainfall seems to represent a significant factor in the triggering and activation of faulting. In contrast, the seismic crisis of August 2017 during the drought period disrupts this pattern, possibly affected by the increase of pumping rate, which consequently lowered the water level in the mine works. During this crisis, the level of the water table assumably reached a minimal level since the flooding front reached the study area, significantly decreasing the hydrostatic pore pressure. Unfortunately, due to the lack of piezometric instrumentation in the study area, it is not possible to quantify the exact water level nor the amplitude of water level changes. Therefore, the order of magnitude of hydrostatic pressure in these mining areas remains unknown.

The final focus was on the characterization of the triggering mechanism behind the observed seismicity. Even though the precise determination of the seismicity triggering mechanism requires more precise information on the range of variation of the water levels, the newly raised questions of the triggering mechanism of seismicity during the dry season as well as the triggering mechanism during the period of rain are further discussed.

Based on observations, there are strong indications that the primary driving force for all the clusters (i.e., clusters N°1-N°5), except for the crisis of August 2017 (i.e., cluster N°6), is the increase of the pore pressure. The seismic activity of this last crisis appears to be triggered by significant fluid extraction from the mine layer. Most multiplet families, and potentially repeaters, occur in the central cluster and cluster N have multiplet events, which are likely related to both, slowly slipping, creeping fault segments and/or accelerated loading cycles of seismogenic faults due to localized pressure increase at the faults interface (asperities). Clusters in which few or no multiplet families are observed seem more dominated by isolated stronger M>1 events. The observed increases in seismic activity (temporal clustering) in each of these clusters more likely represent stress redistribution (relaxation) following pore pressure induced fault slip on neighboured slipping fault planes comparable to classical aftershock pattern, without any visible mainshock.

In conclusion, despite the difficulties underlined as limitations in the previous studies (which include the existence of previously unknown faults and unknown potential of their reactivation, triggered by flooding and water level changes in mining works, unclear circulation of groundwater within the mining works after the mine closure and flooding and unknown water level in the mining works due to lack of measurements and lack of understanding of water), current understanding of the processes behind the triggering of seismic events allowed to draw some broad conclusions.

In terms of seismic hazard, it remains difficult to resolve whether the single fault structure can produce larger events M> 3. Based on current knowledge, it seems that this is not the case as it would require the fault segment of size >500m. Seismic activity is rather characterized by swarming meaning that stress release (caused by pore pressure increased) occurs rather along the several small-scaled structures instead of by one single larger event.

Perspectives

Determination of fault geometry and potential creeping behaviour

As shown so far, due to limitations regarding the lack of data, particularly the small number of stations in monitoring network and lack of knowledge of water levels in the mining levels of the study area, several aspects still remain unclear- including the faults' characteristics, discrimination between multiplets and repeaters, and more precise evaluation of triggering mechanism.

To improve on understanding of the seismicity in Gardanne mine and better define the characteristics of the faulting network, further analysis should be based on data of new reinforced seismic monitoring network. During 2019, both Ineris and BRGM have installed additional 4 temporary seismic stations within the study area, leading now to a total of 13 stations and allowing to improve on the resolution of the prior results.
To specify faulting mechanism more in detail, determine geometry and dimension of fault network, better results could be achieved with multiplet analysis, in particular:

- better precision of relative location
- determination of source parameters would be more robust. Better evaluation of the corner frequencies would allow re-examining the existence of repeaters and easier discriminate between them and multiplet families, whether by checking for the source overlaps or by coherency analysis, as presented in thesis work, as well as the check if there is potential for dynamic rupture via interaction of different segments. Based on the size of a slip on each patch, and cumulative slips of all events in a family as well as the activity pattern, one could potentially estimate the fault creeping behaviour.

Additionally, determination of the source mechanism would allow to estimate the geometry, and characteristics of fault, which is a crucial parameter in order to estimate the potential maximum magnitude. As preliminary source mechanism analysis was inconclusive, potentially a new approach needs to be found, and/or take into account the mining layer (i.e., low velocity) and potential non-DC components.

Understanding the seismo-hydrogeology and triggering mechanism

Due to the lack of hydrological data from the mine layer, as an alternative to water level measurements, a noise-correlation-based monitoring approach could be applied. Small velocity changes can be explained by the changes in water levels in the aquifer, providing the level is at a few hundred meters from the surface.
However, in order to better constrain the seismicity-hydrogeology connection in terms of a better understanding of the water circulation in the mine as well as the triggering mechanism, it is imperative to have direct water level measurements. Hence new instrumentations via boreholes in the study area are strongly advised.

Controlling the seismic hazard

Based on the following observations:

- influence of the pumping on seismic activity (presented in part IV);
- proposed seismicity triggering mechanism in the study area and its connections to water levels changes (high pore pressure of drought) (presented in apart IV);
- lack of seismic crisis in the period 2017 until today, when pumping has increased capacity;

controlling of the seismicity triggering and therefore reducing the seismic hazard seems potentially possible by the means of continuous pumping. There are strong indications that the water levels are nowadays stable, the water level at the central cluster area is lower and hence pore pressure is reduced well and does not reach the point of triggering of new seismic crises.
However, as high pore pressure due to the rise of water levels seem to be one of the main controlling factors in inducing the seismic activity in the study area, it is highly likely that reducing the pumping capacities and allowing of the water levels to rise in the future would lead to increase of seismicity. Therefore, it is strongly advised that the water pumps in the Gerard well are maintained active in order not to provoke another seismic crisis.

Valorization of developed detection and location methodology.

The new developed methodology for detection and location in sparse networks could be implemented into operational monitoring. Potential application of the approach in the context of sparse networks in induced seismicity settings could be imagined as well.

Bibliography

Abdul-Wahed, K.M., Senfaute, G., Piguet, J., Abdul-Wahed Mohamad Khir, Senfaute, G., Piguet, J. & Source, J.P. (2001) Source location estimation using single station three-component seismic date. *Int. Symp. Int. Soc. rock Mech. (EUROCK 2001). Espoo, Finl.* Retrieved from https://hal-ineris.archives-ouvertes.fr/ineris-00972215

Aden-Antóniow, F., Satriano, C., Bernard, P., Poiata, N., Aissaoui, E. -M., Vilotte, J. -P. & Frank, W.B. (2020) Statistical Analysis of the Preparatory Phase of the M w 8.1 Iquique Earthquake, Chile. *J. Geophys. Res. Solid Earth*, **125**, 1–14. doi:10.1029/2019JB019337

Ake, J. (2005) Deep-Injection and Closely Monitored Induced Seismicity at Paradox Valley, Colorado. *Bull. Seismol. Soc. Am.*, **95**, 664–683. doi:10.1785/0120040072

Aki, K. (1965) Maximum likelihood estimate of b in the formula log N= a-bM and its confidence limits. *Bull. Earthq. Res. Inst., Tokyo Univ.*, **43**, 237–239.

Aki, K. & Richards, P.G. (2002) *Quantitative seismology*, University Science Books.

Akuhara, T. & Mochizuki, K. (2014) Application of cluster analysis based on waveform cross-correlation coefficients to data recorded by ocean-bottom seismometers: results from off the Kii Peninsula. *Earth, Planets Sp.*, **66**, 80. doi:10.1186/1880-5981-66-80

Allen, R. (1982) Automatic phase pickers: Their present use and future prospects. *Bull. Seismol. Soc. Am.*, **72**, S225–S242.

Amoroso, O., Maercklin, N. & Zollo, A. (2012) S-wave identification by polarization filtering and waveform coherence analyses. *Bull. Seismol. Soc. Am.*, **102**, 854–861. doi:10.1785/0120110140

Ampuero, J.-P., Billant, J., Brenguier, F., Cavalié, O., Courboulex, F., Deschamps, A., Delouis, B., *et al.* (2020) The November 11 2019 Le Teil, France M5 earthquake: a triggered event in nuclear country. EGU General Assembly 2020, Online, 4–8 May 2020 EGU2020-18295. doi:https://doi.org/10.5194/egusphere-egu2020-18295

Aster, R. & Scott, J. (1993) Comprehensive characterization of waveform similarity in microearthquake data sets. *Bull. Seismol. Soc. Am.*, **83**, 1307–1314.

Autran, J., Lochard, T. & Monteau, R. (2013) L'exploitation dans le bassin minier de provence. Quarties puits et galeries., s.l.: Travaux de l'Observatoire Hommes-Milieux du Bassin minier de Provence (TOHM).

Baisch, S., Ceranna, L. & Harjes, H.-P. (2008) Earthquake Cluster: What Can We Learn from Waveform Similarity? *Bull. Seismol. Soc. Am.*, **98**, 2806–2814. doi:10.1785/0120080018

Barros, L. De, Cappa, F., Deschamps, A. & Dublanchet, P. (2020) Imbricated Aseismic Slip and Fluid Diffusion Drive a Seismic Swarm in the Corinth Gulf, Greece. *Geophys. Res. Lett.*, **47**. doi:10.1029/2020GL087142

Barros, L. De, Guglielmi, Y., Rivet, D., Cappa, F., Duboeuf, L. & Dé Ric Cappa, F. (2018) Seismicity and fault aseismic deformation caused by fluid injection in decametric in-situ experiments, **350**, 464–475, Elsevier Masson. doi:10.1016/j.crte.2018.08.002ï

Båth, M. (1965) Lateral inhomogeneities of the upper mantle. *Tectonophysics*, **2**, 483–514. doi:10.1016/0040-1951(65)90003-X

Batini, F., Console, R. & Luongo, G. (1985) Seismological study of Larderello — Travale geothermal area.

Geothermics, **14**, 255–272. doi:10.1016/0375-6505(85)90066-5

Battaglia, J. & Aki, K. (2003) Location of seismic events and eruptive fissures on the Piton de la Fournaise volcano using seismic amplitudes. *J. Geophys. Res.*, **108**, 2364. doi:10.1029/2002JB002193

Bell, F.G. & Genske, D.D. (2001) The influence of subsidence attributable to coal mining on the environment, development and restoration; some examples from Western Europe and South Africa. *Environ. \& Eng. Geosci.*, **7**, 81–99, Association of Environmental \& Engineering Geologists.

Bennani, M., Josien, J. & Bigarré, P. (2003) Surveillance des risques d ' effondrement dans l ' après mine , besoins , méthodes. *Colloq. Int. Après-mine 2003,Nancy, Fr.* Retrieved from https://hal-ineris.archives-ouvertes.fr/ineris-00972401

Bernard, P. (2014) Interaction and loading of non-repeating multiplets [Conference presentation]. *Earthquakes Nucleation, Triggering, Relationships With Aseismic Process. Cargèse, Corsica, Fr. 3–10 Novemb. 2014*.

Boettcher, M.S., Kane, D.L., McGarr, A., Johnston, M.J.S. & Reches, Z. (2015) Moment Tensors and Other Source Parameters of Mining-Induced Earthquakes in TauTona Mine, South Africa. *Bull. Seismol. Soc. Am.*, **105**, 1576–1593. doi:10.1785/0120140300

Bormann, P. & Giacomo, D. (2010) The moment magnitude and the energy magnitude : common roots and differences. *J. Seismol.*, **15**, 411–427, Springer Verlag. doi:10.1007/s10950-010-9219-2ï

Bormann, P., Wendt, S. & DiGiacomo, D. (2013) Seismic sources and source parameters. in *New Manual of Seismological Observatory Practice 2 (NMSOP2)*, pp. 1–259, Deutsches GeoForschungsZentrum GFZ.

Bosl, W.J. & Nur, A. (2002) Aftershocks and pore fluid diffusion following the 1992 Landers earthquake. *J. Geophys. Res. Solid Earth*, **107**, ESE 17-1-ESE 17-12. doi:10.1029/2001JB000155

Bosq, H. (2013) *Etude hydromécanique du bassin minier de Gardanne. Rapp. stage pour l'obtention du diplôme d'Ingénieur l'Ecole Obs. des Sci. la Terre l'Université Strasbg.*

Bossu, R. (1996) *Etude de la sismicité intraplaque de la région de Gazli (Ouzbékistan) et localisation de la déformation sismique,* Université Joseph-Fourier - Grenoble I. Retrieved from http://theses.fr/1996GRE10002

Bourouis, S. & Bernard, P. (2007) Evidence for coupled seismic and aseismic fault slip during water injection in the geothermal site of Soultz (France), and implications for seismogenic transients. *Geophys. J. Int.*, **169**, 723–732. doi:10.1111/j.1365-246X.2006.03325.x

Brandes, C. & Tanner, D.C. (2020) Fault mechanics and earthquakes. in *Understanding Faults*, pp. 11–80, Elsevier. doi:10.1016/B978-0-12-815985-9.00002-3

Brune, J.N. (1970) Tectonic stress and the spectra of seismic shear waves from earthquakes. *J. Geophys. Res.*, **75**, 4997–5009. doi:10.1029/JB075i026p04997

Cappa, F., Guglielmi, Y., Nussbaum, C. & Birkholzer, J. (2018) On the Relationship Between Fault Permeability Increases, Induced Stress Perturbation, and the Growth of Aseismic Slip During Fluid Injection. *Geophys. Res. Lett.*, **45**. doi:10.1029/2018GL080233

Cattaneo, M., Augliera, P., Spallarossa, D. & Lanza, V. (1999) A Waveform Similarity Approach to Investigate Seismicity Patterns. *Nat. Hazards*, 123–138.

doi:https://doi.org/10.1023/A:1008099705858

Cesame. (2003) Rapport. Etude hydrologique. Concessions minières de la région de Gardanne (13).

CESAME. (2002) *Étude hydrogéologique - Concessions minières de la région de gardanne (13). H.B.C.M., vol. 1 et 2*.

Cesca, S. & Grigoli, F. (2015) Full waveform seismological advances for microseismic monitoring. *Adv. Geophys.*, **56**, 169–228, Academic Press Inc. doi:10.1016/bs.agph.2014.12.002

Cesca, S., Rohr, A. & Dahm, T. (2012) Discrimination of induced seismicity by full moment tensor inversion and decomposition. *J. Seismol.*, **17**. doi:10.1007/s10950-012-9305-8

Chalumeau, A. (2000) *Fonctionnement hydrogéologique des exploitations de lignite du bassin de Fuveau (Bouches-du-Rhône, France).Thèse de Sciences de la terre, Université de Franche-Comté*.

Chen, K.H., Nadeau, R.M. & Rau, R.-J. (2008) Characteristic repeating earthquakes in an arc-continent collision boundary zone: The Chihshang fault of eastern Taiwan. *Earth Planet. Sci. Lett.*, **276**, 262–272. doi:10.1016/j.epsl.2008.09.021

Contrucci, I., Balland, C., Kinscher, J., Bennani, M., Bigarré, P. & Bernard, P. (2019) Aseismic Mining Subsidence in an Abandoned Mine: Influence Factors and Consequences for Post-Mining Risk Management. *Pure Appl. Geophys.*, **176**, 801–825. doi:10.1007/s00024-018-2015-6

Contrucci, I. & Bennani, M. (2013) Rapport INERIS DRS-13-136284-07432A. Détectabilité des réseaux de surveillance microsismique du bassin minier de Gardanne. *INERIS DRS-13-136284-07432A*.

Contrucci, I., Klein, E., Bigarré, P., Lizeur, A. & Lomax, A. (2008) Early-warning microseismic systems applied to the management of post-mining large-scale ground failures: calibration by a geophysical field experiment of blast swarms. *Geophys. Res. Abstr.*, Vol. 10.

Contrucci, I., Klein, E., Bigarré, P., Lizeur, A., Lomax, A. & Bennani, M. (2010) Management of Post-mining Large-scale Ground Failures: Blast Swarms Field Experiment for Calibration of Permanent Microseismic Early-warning Systems. *Pure Appl. Geophys.*, **167**, 43–62. doi:10.1007/s00024-009-0005-4

Contrucci, I., Klein, E., Cao, N.T., Daupley, X. & Bigarré, P. (2011) Multi-parameter monitoring of a solution mining cavern collapse: First insight of precursors. *Comptes Rendus Geosci.*, **343**, 1–10. doi:10.1016/j.crte.2010.10.007

Convertito, V. & Faenza, L. (2014) Earthquake Recurrence. in *Encyclopedia of Earthquake Engineering* eds. Beer, M., Kougioumtzoglou, I.A., Patelli, E. & Au, I.S.-K., pp. 1–21, Berlin, Heidelberg: Springer Berlin Heidelberg. doi:10.1007/978-3-642-36197-5_236-1

Cornet, F.H. (2016) Seismic and aseismic motions generated by fluid injections. *Geomech. Energy Environ.*, **5**, 42–54, Elsevier Ltd. doi:10.1016/j.gete.2015.12.003

Cornet, F.H., Helm, J., Poitrenaud, H. & Etchecopar, A. (1997) Seismic and Aseismic Slips Induced by Large-scale Fluid Injections. in *Seismicity Associated with Mines, Reservoirs and Fluid Injections*, pp. 563–583, Basel: Birkhäuser Basel. doi:10.1007/978-3-0348-8814-1_12

Costain, J.K. & Bollinger, G.A. (2010) Review: Research results in hydroseismicity from 1987 to 2009. *Bull. Seismol. Soc. Am.*, **100**, 1841–1858. doi:10.1785/0120090288

Couffin, S., Bigarré, P., Bennani, M. & Josien, J.-P. (2003) Permanent real time microseismic monitoring of abandoned mines for public safety. *Fields Meas. Geomech. (ed. Myrvoll)(Sweets Zeitlinger, Lisse 2003) pp*, 437–444.

Coutant, O. (1990) Programme de Simulation numerique AXITRA, Rapport LGIT, Universite Joseph Fourier, Grenoble, France.

Crampin, S. (1977) A review of the effects of anisotropic layering on the propagation of seismic waves. *Geophys. R. QStr. SOC*, Vol. 49. doi:10.1111/j.1365-246X.1977.tb03698.x

Dahm, T., Becker, D., Bischoff, M., Cesca, S., Dost, B., Fritschen, R., Hainzl, S., *et al.* (2012) Recommendation for the discrimination of human-related and natural seismicity. *J. Seismol.*, **17**, 197–202, Springer. doi:10.1007/s10950-012-9295-6

Dheilly, A. (2013) Compréhension des circulations d'eau souterraine dans l'ancienne mine de Gardanne (13) - Argumentaire pour l'implantation de 2 à 3 piézomètres dans le réservoir minier - Rapport final. BRGM/RP-62412-FR, 45 p., 36 ill.

Dheilly, A. & Brigati, B. (2015) Gestion du réservoir minier de Gardanne, Bouches du Rhône : Approches environnementales et hydrauliques du pompage et de son rejet dans la Mer Méditerranée. *Exploit. minières passées présentes Impacts environnementaux sociétaux* Collection EDYTEM, 71–84. Retrieved from https://hal-brgm.archives-ouvertes.fr/hal-01100951

Dheilly, A., Brigati, B., Nedellec, J.-L. & Nicolas, M. (2013) Mine water management in the former Gardanne lignite mine: towards sustainable uses of the mine aquifer. *Proc. Eighth Int. Semin. Mine Clos.*, pp. 135–148. doi:10.36487/ACG_rep/1352_12_Dheilly

Didier, C., Laouafa, F., Thoraval, T. & Tritsch, J. (2003) Bassin houiller de Provence. Etude des effets sur les terrains de surface des travaux miniers souterrains et de leur évolution prévisible dans le temps, s.l.: INERIS. DRS- 03-36460/R01.

Didier, C., Merwe, J.N. Van Der, Betournay, M., Mainz, M., Aydan, Song, W.K., Kotyrba, A., *et al.* (2009) +++. *ISRM Int. Symp. Rock Mech. SINOROCK 2009*.

Didier, C., Merwe, N. van der, Betournay, M., Mainz, M., Kotyrba, A., Oydan, O., Josien, J., *et al.* (2008) MINE CLOSURE AND POST-MINING MANAGEMENT INTERNATIONAL STATE-OF-THE-ART INTERNATIONAL COMMISSION ON MINE CLOSURE INTERNATIONAL SOCIETY FOR ROCK MECHANICS. doi:10.13140/2.1.3267.8407

Diekmann, L., Schwarz, B., Bauer, A. & Gajewski, D. (2019) Source localization and joint velocity model building using wavefront attributes. *Geophys. J. Int.* doi:10.1093/gji/ggz342

Dieterich, J., Cayol, V. & Okubo, P. (2000) The use of earthquake rate changes as a stress meter at Kilauea volcano. *Nature*, **408**, 457–460. doi:10.1038/35044054

Dieterich, J.H. (1994) A constitutive law for rate of earthquake production and its application to earthquake clustering. *J. Geophys. Res. Solid Earth*, **99**, 2601–2618. doi:10.1029/93JB02581

Dietz, L.D. & Ellsworth, W.L. (1990) The October 17, 1989, Loma Prieta, California, Earthquake and its aftershocks: Geometry of the sequence from high-resolution locations. *Geophys. Res. Lett.*, **17**, 1417–1420. doi:10.1029/GL017i009p01417

Dominique, P. (2014) Analyse préliminaire de la crise sismique de Fuveau (Bouches-du-Rhône).BRGM/RP-

635992-FR.

Dominique, P. (2015) Bassin houiller de Provence (13). La crise sismique de Fuveau de décembre 2014. Rapport BRGM/RP-65050-FR.

Dominique, P. (2016) Résultats issus du dispositif microsismique de surveillance complémentaire La crise de décembre 2014. Rapport BRGM/ RP-65561-FR.

Dominique, P. (2016) Bassin houiller de Provence (13). Bilan de l'activité sismique 2015 - Secteur de Fuveau ouest - Rapport BRGM/RP-66203-FR.

Dominique, P., Bendif, F. & Loher, M. Le. (2012) Instrumentation d'une petite crise sismique à Salsigne (Aude). *Journées Natl. Géotechnique Géologie l'Ingénieur*, p. 8, Bordeaux. Retrieved from https://hal-brgm.archives-ouvertes.fr/hal-00822447

Dominique, P. & Nédellec, J.L. (2014) Premiers résultats issus du dispositif de surveillance complémentaire.BRGM/ RP-63681-FR.

Driad-Lebeau, L. (2010) Geoderis rapport S-2010/29DE-10PAC3200 Procédure de surveillance microsismique des anciennes exploitations de houille en chambres pilliers.

Duverger, C., Lambotte, S., Bernard, P., Lyon-Caen, H., Deschamps, A. & Nercessian, A. (2018) Dynamics of microseismicity and its relationship with the active structures in the western Corinth Rift (Greece). *Geophys. J. Int.*, **215**, 196–221, OUP. doi:10.1093/gji/ggy264ï

Duverger, C., Lambotte, S., Bernard, P., Lyon-Caen, H., Deschamps, A. & Nercessian, A. (2018) Dynamics of microseismicity and its relationship with the active structures in the western Corinth Rift (Greece). *Geophys. J. Int.*, **215**, 196–221. doi:10.1093/gji/ggy264

Duverger, Clara, Godano, M., Bernard, P., Lyon-Caen, H. & Lambotte, S. (2015) The 2003–2004 seismic swarm in the western Corinth rift: Evidence for a multiscale pore pressure diffusion process along a permeable fault system. *Geophys. Res. Lett.*, **42**, 7374–7382. doi:10.1002/2015GL065298

Eaton, D.W. (2018) *Passive Seismic Monitoring of Induced Seismicity*, Cambridge University Press. doi:10.1017/9781316535547

Eijs, R.M.H.E. Van, Mulders, F.M.M., Nepveu, M., Kenter, C.J. & Scheffers, B.C. (2006) Correlation between hydrocarbon reservoir properties and induced seismicity in the Netherlands. *Eng. Geol.*, **84**, 99–111. doi:10.1016/j.enggeo.2006.01.002

Ellsworth, W. (2013) Injection-induced earthquakes. *Science (80-.).*, American Association for the Advancement of Science. doi:10.1126/science.1225942

Eshelby, J.D. (1957) The determination of the elastic field of an ellipsoidal inclusion, and related problems. *Proc. R. Soc. London. Ser. A. Math. Phys. Sci.*, **241**, 376–396. doi:10.1098/rspa.1957.0133

Eyre, T.S., Zecevic, M., Salvage, R.O. & Eaton, D.W. (2020) A long-lived swarm of hydraulic fracturing-induced seismicity provides evidence for aseismic slip. *Bull. Seismol. Soc. Am.*, **110**, 2205–2215. doi:10.1785/0120200107

F.T. Lee and F. Abel Jr. (1983) Subsidence from Underground Mining: Environmental Analysis and Planning Considerations GEOLOGICAL SURVEY CIRCULAR 876. Retrieved from https://pubs.usgs.gov/circ/1983/0876/report.pdf

Felzer, K.R. (2003) Secondary Aftershocks and Their Importance for Aftershock Forecasting. *Bull. Seismol. Soc. Am.*, **93**, 1433–1448. doi:10.1785/0120020229

Font, Y., Kao, H., Lallemand, S., Liu, C.-S. & Chiao, L.-Y. (2004) Hypocentre determination offshore of eastern Taiwan using the Maximum Intersection method. *Geophys. J. Int*, **158**, 655–675. doi:10.1111/j.1365-246X.2004.02317.x

Foulger, G.R., Wilson, M.P., Gluyas, J.G., Julian, B.R. & Davies, R.J. (2018) Global review of human-induced earthquakes. *Earth-Science Rev.*, **178**, 438–514, Elsevier B.V. doi:10.1016/j.earscirev.2017.07.008

Franck, C., Salmon, R., Didier, C., Paquette, Y. & Pokryszka, Z. (2019) Post-Mining Hazard Evaluation and Mapping in France. Ineris DRS-19-178745-02411A.

Gajewski, D., Anikiev, D., Kashtan, B., Tessmer, E. & Vanelle, C. (2007) Localization of seismic events by diffraction stacking. *SEG Tech. Progr. Expand. Abstr.*, **26**, 1287–1291. doi:10.1190/1.2792738

Gaviglio, P. (1980) La fracturation dans le gisement de lignite du bassin de 1'Arc. *Rev. Ind. Min.*, **62**, 93–99.

Gaviglio, P. (1985) A fault and stress field analysis in a coal mine Gardanne, Bouches Du Rhone, France. *Tectonophysics*, **113**, 349–366. doi:10.1016/0040-1951(85)90205-7

Gaviglio, P., Bigarré, P., Baroudi, H., Piguet, J.-P. & Monteau, R. (1996) Measurements of natural stresses in a Provence mine (Southern France). *Eng. Geol.*, **44**, 77–92. doi:10.1016/s0013-7952(96)00041-5

Geiger, L. (1912) Probability method for the determination of earthquake epicenters from the arrival time only. *Bull. St. Louis Univ.*, **8**, 60–71.

Geller, R.J. & Mueller, C.S. (1980) Four similar earthquakes in central California. *Geophys. Res. Lett.*, **7**, 821–824, John Wiley & Sons, Ltd. doi:10.1029/GL007i010p00821

Gibowicz, S.J. (1990) Seismicity Induced by Mining. *Adv. Geophys.*, **32**, 1–74, Elsevier. doi:10.1016/S0065-2687(08)60426-4

Gibowicz, S.J. & Lasocki, S. (2002) Seismicity induced by mining. *Publ. Inst. Geophys. Polish Acad. Sci. Ser. M Misc.*, **25**, 201–242.

Gilbert, F. (1971) Excitation of the Normal Modes of the Earth by Earthquake Sources. *Geophys. J. Int.*, **22**, 223–226. doi:10.1111/j.1365-246X.1971.tb03593.x

Godano, M., Deschamps, A., Lambotte, S., Lyon-Caen, H., Bernard, P. & Pacchiani, F. (2014) Focal mechanisms of earthquake multiplets in the western part of the Corinth Rift (Greece): influence of the velocity model and constraints on the geometry of the active faults. *Geophys. J. Int.*, **197**, 1660–1680. doi:10.1093/gji/ggu059

Goldbach, O.D. (2009) Seismic risks posed by mine flooding. *South. African Inst. Min. Metall. Hard Rock Safe Saf. Conf. 2009*, p. 26. Retrieved from http://hdl.handle.net/10204/3647

Goldbach, O.D. (2009) What is the seismic risk of mine flooding? *South. African Inst. Min. Metall. Hard Rock Safe Saf. Conf. 2009.*, pp. 1–26, Sun City, South Africa.

Grasso, J.R. (1992) Mechanics of seismic instabilities induced by the recovery of hydrocarbons. *Pure Appl. Geophys. PAGEOPH*, **139**, 507–534. doi:10.1007/BF00879949

Grigoli, F., Cesca, S., Amoroso, O., Emolo, A., Zollo, A. & Dahm, T. (2014) Automated seismic event location

by waveform coherence analysis. *Geophys. J. Int.*, **196**, 1742–1753, Oxford University Press. doi:10.1093/gji/ggt477

Guglielmi, Y., Cappa, F., Avouac, J.-P., Henry, P. & Elsworth, D. (2015) Seismicity triggered by fluid injection-induced aseismic slip. *Science (80-.).*, **348**, 1224–1226, American Association for the Advancement of Science. doi:10.1126/science.aab0476

Gutenberg, B. & Richter, C.F. (1949) Seismicity of the earth and associated phenomena. *Princet. Univ. Press. Princeton, New Jersey.*

Haessler, H., Hoang-Trong, P. & Legros, Y. (1985) L'Événement Sismique Du 19 Férier 1984 En Provence Occidentale: Seisme Tectonique Ou Coup De Terrain Minier? in *Seismic Activity in Western Europe*, pp. 223–232, Dordrecht: Springer Netherlands. doi:10.1007/978-94-009-5273-7_18

Hainzl, S. & Fischer, T. (2002) Indications for a successively triggered rupture growth underlying the 2000 earthquake swarm in Vogtland/NW Bohemia. *J. Geophys. Res. Solid Earth*, **107**, ESE 5-1-ESE 5-9. doi:10.1029/2002JB001865

Hainzl, S., Fischer, T. & Dahm, T. (2012) Seismicity-based estimation of the driving fluid pressure in the case of swarm activity in Western Bohemia. *Geophys. J. Int.*, **191**, 271–281. doi:10.1111/j.1365-246X.2012.05610.x

Hainzl, S., Kraft, T., Wassermann, J., Igel, H. & Schmedes, E. (2006) Evidence for rainfall-triggered earthquake activity. *Geophys. Res. Lett.*, **33**, L19303. doi:10.1029/2006GL027642

Hainzl, S. & Ogata, Y. (2005) Detecting fluid signals in seismicity data through statistical earthquake modeling. *J. Geophys. Res.*, **110**, B05S07. doi:10.1029/2004JB003247

Hanks, T.C. & Kanamori, H. (1979) A moment magnitude scale. *J. Geophys. Res.*, **84**, 2348. doi:10.1029/JB084iB05p02348

Hartigan, J.A. (1975) *Clustering algorithms*, John Wiley & Sons, Inc.

Hartigan, J.A. & Wong, M.A. (1979) Algorithm AS 136: A K-Means Clustering Algorithm. *Appl. Stat.*, **28**, 100, [Wiley, Royal Statistical Society]. doi:10.2307/2346830

Hearn, E.H. (2002) Dynamics of Izmit Earthquake Postseismic Deformation and Loading of the Duzce Earthquake Hypocenter. *Bull. Seismol. Soc. Am.*, **92**, 172–193. doi:10.1785/0120000832

Heib, M. Al. (2012) Mine d'or de Salsigne (Aude, Languedoc- Roussillon): Analyse préliminaire des causes de l'événement sismique du 15 novembre 2011. Rep., Ineris, DRS-12-130671- 09119A.

Hudson, J.A., Pearce, R.G. & Rogers, R.M. (1989) Source type plot for inversion of the moment tensor. *J. Geophys. Res.*, **94**, 765. doi:10.1029/JB094iB01p00765

Ineris. (1995) Synthèse Hydrogéologique du bassin minier de Gardanne-Fuveau.

Julian, B.R., Miller, A. & Foulger, G.R. (1998) Non-double-couple earthquakes 1. Theory. *Rev. Geophys.*, **36**, 525–549. doi:10.1029/98RG00716

Kao, H. & Shan, S.-J. (2004) The Source-Scanning Algorithm: mapping the distribution of seismic sources in time and space. *Geophys. J. Int.*, **157**, 589–594. doi:10.1111/j.1365-246X.2004.02276.x

Kapetanidis, V., Deschamps, A., Papadimitriou, P., Matrullo, E., Karakonstantis, A., Bozionelos, G., Kaviris, G., *et al.* (2015) The 2013 earthquake swarm in Helike, Greece: seismic activity at the root of old

normal faults. *Geophys. J. Int.*, **202**, 2044–2073. doi:10.1093/gji/ggv249

Karfakis, M.G. (1993) Residual subsidence over abandoned coal mines. *Compr. rock Eng. Vol. 5*, 451–476, Pergamon. doi:10.1016/b978-0-08-042068-4.50026-0

King, G.C.P., Stein, R.S. & Jian Lin. (1995) Static stress changes and the triggering of earthquakes. *Int. J. Rock Mech. Min. Sci. Geomech. Abstr.*, **32**, A50–A51. doi:10.1016/0148-9062(95)94484-2

Kinscher, J. (2015) *The analysis and interpretation of microseismicity induced by a collapsing solution mining cavity : A contribution for progress in hazard assessment of underground cavities*. Retrieved from http://www.theses.fr/2015LORR0022/document

Kinscher, J. (2017) Rapport INERIS DRS-17-164272-00556A. Origine de la sismicité après mine du bassin houiller de Gardanne Programme EAT-DRS06 - Rapport de fin d'opération 4 « sismicité induite par les activités industrielles et extractives ».

Kinscher, J., Bernard, P., Contrucci, I., Mangeney, A., Piguet, J.-P. & Bigarré, P. (2015) Location of microseismic swarms induced by salt solution mining. *Geophys. J. Int.*, **200**, 337–362. doi:10.1093/gji/ggu396

Kinscher, J., Cesca, S., Bernard, P., Contrucci, I., Mangeney, A., Piguet, J.-P. & Bigarré, P. (2016) Resolving source mechanisms of microseismic swarms induced by solution mining. *Geophys. J. Int.*, **206**, 696–715. doi:10.1093/gji/ggw163

Kinscher, J., Coccia, S., Daupley, X. & Bigarré, P. (2017) Microseismic monitoring of caving and collapsing events in solution mines. *9th Int. Symp. Rockbursts Seism. Mines*.

Kinscher, J., Gombert, P., Contrucci, I. & Thoraval, A. (2021) Rapport Ineris-201216-2215842. Origine de l'essaim sismique de Fuveau et son lien avec l'ennoyage des anciens travaux miniers du bassin de Gardanne : apport des analyses sismique, hydrogéologique et géomécanique.

Kinscher, J., Santis, F. De, Poiata, N., Bernard, P., Palgunadi, K.H. & Contrucci, I. (2020) Seismic repeaters linked to weak rock-mass creep in deep excavation mining. *Geophys. J. Int.*, **222**, 110–131. doi:10.1093/gji/ggaa150

Lambotte, S., Lyon-Caen, H., Bernard, P., Deschamps, A., Patau, G., Nercessian, A., Pacchiani, F., *et al.* (2014) Reassessment of the rifting process in the Western Corinth Rift from relocated seismicity. *Geophys. J. Int.*, **197**, 1822–1844. doi:10.1093/gji/ggu096

Lay, T. & Wallace, T.C. (1995) *Modern global seismology*. *Int. Geophys. Ser.*, Vol. 58, San Diego, CA: Elsevier.

Ledoux, E., Mudry, J., Takla, G. & Merwe, N. Van der. (2003) Expertise internationale du dossier d'arrêt définitif des travaux des concessions de Gardanne (13). Rapport GEODERIS 03 PACA-5001R03.

Lengliné, O., Boubacar, M. & Schmittbuhl, J. (2017) Seismicity related to the hydraulic stimulation of GRT1, Rittershoffen, France. *Geophys. J. Int.*, ggw490. doi:10.1093/gji/ggw490

Li, L., Becker, D., Chen, H., Wang, X. & Gajewski, D. (2018) A systematic analysis of correlation-based seismic location methods. *Geophys. J. Int.*, **212**, 659–678. doi:10.1093/gji/ggx436

Li, L., Tan, J., Schwarz, B., Staněk, F., Poiata, N., Shi, P., Diekmann, L., *et al.* (2020) Recent advances and challenges of waveform-based seismic location methods at multiple scales. *Rev. Geophys.*, 1–47. doi:10.1029/2019RG000667

Li, Z. & Baan, M. van der. (2016) Microseismic event localization by acoustic time reversal extrapolation. *GEOPHYSICS*, **81**, KS123–KS134. doi:10.1190/geo2015-0300.1

Linzer, L.M., Hildyard, M.W. & Wesseloo, J. (2021) Complexities of underground mining seismic sources. *Philos. Trans. R. Soc. A Math. Phys. Eng. Sci.*, **379**, 20200134. doi:10.1098/rsta.2020.0134

Lomax, A. (2005) A Reanalysis of the Hypocentral Location and Related Observations for the Great 1906 California Earthquake. *Bull. Seismol. Soc. Am.*, **95**, 861–877. doi:10.1785/0120040141

Lomax, A. (2008) Location of the Focus and Tectonics of the Focal Region of the California Earthquake of 18 April 1906. *Bull. Seismol. Soc. Am.*, **98**, 846–860, GeoScienceWorld.

Lomax, A. & Curtis, A. (2001) Fast, probabilistic earthquake location in 3D models using oct-tree importance sampling. *Geophys. Res. Abstr*.

Lomax, A., Satriano, C. & Vassallo, M. (2012) Automatic Picker Developments and Optimization: FilterPicker--a Robust, Broadband Picker for Real-Time Seismic Monitoring and Earthquake Early Warning. *Seismol. Res. Lett.*, **83**, 531–540. doi:10.1785/gssrl.83.3.531

López-Comino, J.A., Cesca, S., Heimann, S., Grigoli, F., Milkereit, C., Dahm, T. & Zang, A. (2017) Characterization of Hydraulic Fractures Growth During the Äspö Hard Rock Laboratory Experiment (Sweden). *Rock Mech. Rock Eng.*, **50**, 2985–3001. doi:10.1007/s00603-017-1285-0

Madariaga, R. (1976) DYNAMICS OF AN EXPANDING CIRCULAR FAULT. *Bull. Seismol. Soc. Am.*, Vol. 66.

Malone, S.D., Rothe, G.H. & Smith, S.W. (1975) Details of microearthquake swarms in the Columbia Basin, Washington. *Seismol. Soc. Am. Bull.*, **65**, 855–864, Bulletin of the Seismological Society of America.

Malovichko, D., Aswegen, G. van & Clark, R. (2012) Mechanisms of large seismic events in platinum mines of the Bushveld Complex (South Africa). *J. South. African Inst. Min. Metall.*, **112**, 419–429, scieloza. Retrieved from http://www.scielo.org.za/scielo.php?script=sci_arttext&pid=S2225-62532012000600005&nrm=iso

Marone, C.J., Scholtz, C.H. & Bilham, R. (1991) On the mechanics of earthquake afterslip. *J. Geophys. Res.*, **96**, 8441. doi:10.1029/91JB00275

Martínez-Garzón, P., Bohnhoff, M., Kwiatek, G. & Dresen, G. (2013) Stress tensor changes related to fluid injection at the Geysers geothermal field, California. *Geophys. Res. Lett.*, **40**, 2596–2601. doi:10.1002/grl.50438

Matrullo, E., Contrucci, I., Dominique, P., Bernard, P., Aochi, H. & Bennani, M. (2015) Induced micro-seismicity by flooding of the abandoned Gardanne coal field (Provence,France): analysis and interpretation, Rapport INERIS DRS-15-151231-10877A;Rapport BRGM/RP-65968-FR.

McDonald, A.J. (1982) *Seismicity of the Witwatersrand basin. M.Sc. Thesis*, University of the Witwatersrand, Johannesburg, South Africa.

McGarr, A. (1991) On a possible connection between three major earthquakes in California and oil production. *Bull. - Seismol. Soc. Am.*, **81**, 948–970. doi:10.1016/0148-9062(92)93678-d

McGarr, A. (1992) An implosive component in the seismic moment tensor of a mining-Induced tremor. *Geophys. Res. Lett.*, **19**, 1579–1582. doi:10.1029/92GL01581

McGarr, A. (1992) Moment tensors of ten witwatersrand mine tremors. *Pure Appl. Geophys. PAGEOPH*,

139, 781–800. doi:10.1007/BF00879963

Mcgarr, A. & Simons, M. (1997) Keynote lecture: a broad look at induced and triggered seismicity, "Rockbursts and seismicity in mines". *Gibowicz SJ, Lasocki S Proceeding 4th Int. Symp. rockbursts Seism. mines, Poland, 11–14 August 1997. A.A. Balkema, Rotterdam, pp 385–396*, Balkema.

McGarr, A., Simons, M. & Seeber, L. (2002) 40 Case histories of induced and triggered seismicity. in *International {Geophysics}*, Vol. 81, pp. 647–661, Elsevier. doi:10.1016/S0074-6142(02)80243-1

Mesimeri, M. & Karakostas, V. (2018) Repeating earthquakes in western Corinth Gulf (Greece): implications for aseismic slip near locked faults. *Geophys. J. Int.*, **215**, 659–676. doi:10.1093/gji/ggy301

Micklethwaite, S. & Cox, S. (2006) Progressive fault triggering and fluid flow in aftershock domains: Examples from mineralized Archaean fault systems. *Earth Planet. Sci. Lett.*, **250**, 318–330. doi:10.1016/j.epsl.2006.07.050

Miller, A., Foulger, G.R. & Julian, B.R. (1998) Non-double-couple earthquakes 2. Observations. *Rev. Geophys.*, **36**, 551–568. doi:10.1029/98RG00717

Miller, A., Richards, J.A. & McCann, D.M. (1988) Microseismic monitoring of the infill trial at Castlefields Mine, Dudley. *Geol. Soc. London, Eng. Geol. Spec. Publ.*, **5**, 319–324. doi:10.1144/GSL.ENG.1988.005.01.34

Miller, A., Richards, J.A., McCann, D.M., Browittt, C.W.A. & Jackson, P.D. (1989) Microseismic techniques for monitoring incipient hazardous collapse conditions above abandoned limestone mines. *Q. J. Eng. Geol. Hydrogeol.*, **22**, 1–18. doi:10.1144/GSL.QJEG.1989.022.01.01

Miller, S.A., Collettini, C., Chiaraluce, L., Cocco, M., Barchi, M. & Kaus, B.J.P. (2004) Aftershocks driven by a high-pressure CO2 source at depth. *Nature*, **427**, 724–727. doi:10.1038/nature02251

Moser, T.J., Eck, T. van & Nolet, G. (1992) Hypocenter determination in strongly heterogeneous Earth models using the shortest path method. *J. Geophys. Res.*, **97**, 6563, John Wiley & Sons, Ltd. doi:10.1029/91JB03176

Nadeau, R.M. & Johnson, L.R. (1998) Seismological Studies at Parkfield VI: Moment Release Rates and Estimates of Source Parameters for Small Repeating Earthquakes. *Bull. Seismol. Soc. Am.*, **88**, 790–814, Citeseer.

Nadeau, R.M. & McEvilly, T. V. (1999) Fault Slip Rates at Depth from Recurrence Intervals of Repeating Microearthquakes. *Science (80-.).*, **285**, 718–721. doi:10.1126/science.285.5428.718

Nadeau, R.M. & McEvilly, T. V. (2004) Periodic Pulsing of Characteristic Microearthquakes on the San Andreas Fault. *Science (80-.).*, **303**, 220–222. doi:10.1126/science.1090353

Nakahara. (2004) Correlation distance of waveforms for closely located events - I. Implication of the heterogeneus structure around the source region of the 1995 HYgo - Ken Nanbu, Japan earthquake. *Geophys. J. Int.*, 1255–1268.

Naoi, M., Nakatani, M., Igarashi, T., Otsuki, K., Yabe, Y., Kgarume, T., Murakami, O., *et al.* (2015) Unexpectedly frequent occurrence of very small repeating earthquakes ($-5.1 \leq M_w \leq -3.6$) in a South African gold mine: Implications for monitoring intraplate faults. *J. Geophys. Res. Solid Earth*, **120**, 8478–8493. doi:10.1002/2015JB012447

Naoi, M., Nakatani, M., Kgarume, T., Khambule, S., Masakale, T., Ribeiro, L., Philipp, J., *et al.* (2015) Quasi-static slip patch growth to 20 m on a geological fault inferred from acoustic emissions in a South African gold mine. *J. Geophys. Res. Solid Earth*, **120**, 1692–1707. doi:10.1002/2014JB011165

Nicolas, M., Santoire, J.P. & Delpech, P.Y. (1990) Intraplate seismicity: new seismotectonic data in Western Europe. *Tectonophysics*, **179**, 27–53, Elsevier. doi:10.1016/0040-1951(90)90354-B

Nur, A. & Booker, J.R. (1972) Aftershocks Caused by Pore Fluid Flow? *Science (80-.).*, **175**, 885–887. doi:10.1126/science.175.4024.885

O'Kane, D., Setyorini, D. & Rafflesia, U. (2017) K-means cluster analysis in earthquake epicenter clustering. *Int. J. Adv. Intell. Informatics*, **3**, 81–89. doi:10.26555/ijain.v3i2.100

Ogasawara, H., Fujimori, K., Koizumi, N., Hirano, N., Fujiwara, S., Otsuka, S., Nakao, S., *et al.* (2002) Microseismicity Induced by Heavy Rainfall Around Flooded Vertical Ore Veins. in *The Mechanism of Induced Seismicity*, Vol. 159, pp. 91–109, Basel: Birkhäuser Basel. doi:10.1007/978-3-0348-8179-1_4

Omori, F. (1894) On the after-shocks of earthquakes. *J. Coll. Sci., Imp. Univ., Japan*, **7**, 111–200.

Oye, V. & Roth, M. (2003) Automated seismic event location for hydrocarbon reservoirs. *Comput. Geosci.*, **29**, 851–863. doi:10.1016/S0098-3004(03)00088-8

Palgunadi, K.H., Poiata, N., Kinscher, J., Bernard, P., Santis, F. De & Contrucci, I. (2019) Methodology for full waveform near real-time automatic detection and localization of microseismic events using high (8 kHz) sampling rate records in mines: Application to the Garpenberg mine (Sweden). *Seismol. Res. Lett.*, **91**, 399–414, Seismological Society of America. doi:10.1785/0220190074

Papadimitriou, E., Karakostas, V., Mesimeri, M., Chouliaras, G. & Kourouklas, C. (2017) The Mw6.5 17 November 2015 Lefkada (Greece) Earthquake: Structural Interpretation by Means of the Aftershock Analysis. *Pure Appl. Geophys.*, **174**, 3869–3888. doi:10.1007/s00024-017-1601-3

Peltzer, G., Rosen, P., Rogez, F. & Hudnut, K. (1998) Poroelastic rebound along the Landers 1992 earthquake surface rupture. *J. Geophys. Res. Solid Earth*, **103**, 30131–30145. doi:10.1029/98JB02302

Poiata, N., Satriano, C., Vilotte, J.-P., Bernard, P. & Obara, K. (2016) Multiband array detection and location of seismic sources recorded by dense seismic networks. *Geophys. J. Int.*, **205**, 1548–1573, Oxford University Press. doi:10.1093/gji/ggw071

Poiata, N., Vilotte, J.-P., Bernard, P., Satriano, C. & Obara, K. (2018) Imaging different components of a tectonic tremor sequence in southwestern Japan using an automatic statistical detection and location method. *Geophys. J. Int.*, **213**, 2193–2213. doi:10.1093/gji/ggy070

Pollitz, F.F. (2002) Stress Triggering of the 1999 Hector Mine Earthquake by Transient Deformation Following the 1992 Landers Earthquake. *Bull. Seismol. Soc. Am.*, **92**, 1487–1496. doi:10.1785/0120000918

Poupinet, G., Ellsworth, W.L. & Frechet, J. (1984) Monitoring velocity variations in the crust using earthquake doublets: An application to the Calaveras Fault, California. *J. Geophys. Res. Solid Earth*, **89**, 5719–5731. doi:10.1029/JB089iB07p05719

Rehman, K., Burton, P.W. & Weatherill, G.A. (2014) K-means cluster analysis and seismicity partitioning for Pakistan. *J. Seismol.*, **18**, 401–419, Kluwer Academic Publishers. doi:10.1007/s10950-013-9415-y

Reid, H.F. (1910) The mechanics of the earthquake. *Calif. Earthq. April 18, 1906, Rep. State Earthq.*

Investig. Comm.

Ross, Z.E., Rollins, C., Cochran, E.S., Hauksson, E., Avouac, J.-P. & Ben-Zion, Y. (2017) Aftershocks driven by afterslip and fluid pressure sweeping through a fault-fracture mesh. *Geophys. Res. Lett.*, **44**, 8260–8267. doi:10.1002/2017GL074634

Rubin, A.M., Gillard, D. & Got, J.-L. (1999) Streaks of microearthquakes along creeping faults. *Nature*, **400**, 635–641. doi:10.1038/23196

Saar, M.O. & Manga, M. (2003) Seismicity induced by seasonal groundwater recharge at Mt. Hood, Oregon. *Earth Planet. Sci. Lett.*, **214**, 605–618, Elsevier B.V. doi:10.1016/S0012-821X(03)00418-7

Salmon, Franck, Lombard, Thiery & Hadadou. (2019) Rapport Ineris DRS-19-178745-02406A-Post Mining Risk Management in France.

Satriano, C. (2020) SourceSpec – Earthquake source parameters from S-wave displacement spectra. doi:10.5281/ZENODO.3688587

Schaff, D.P., Beroza, G.C. & Shaw, B.E. (1998) Postseismic response of repeating aftershocks. *Geophys. Res. Lett.*, **25**, 4549–4552, American Geophysical Union. doi:10.1029/1998GL900192

Schaff, D.P., Bokelmann, G.H.R., Beroza, G.C., Waldhauser, F. & Ellsworth, W.L. (2002) High-resolution image of Calaveras Fault seismicity. *J. Geophys. Res. Solid Earth*, **107**, ESE 5-1-ESE 5-16. doi:10.1029/2001JB000633

Schmittbuhl, J., Karabulut, H., Lengliné, O. & Bouchon, M. (2016) Long-lasting seismic repeaters in the Central Basin of the Main Marmara Fault. *Geophys. Res. Lett.*, **43**, 9527–9534. doi:10.1002/2016GL070505

Scholz, C. (2002) Brittle fracture of rock. in *The Mechanics of Earthquakes and Faulting*, pp. 1–52, Cambridge University Press. doi:10.1017/CBO9780511818516.003

Scholz, C. (2002) *The Mechanics of Earthquake Faulting*. doi:10.1017/CBO9780511818516

Schuchová, K. & Lenart, J. (2020) Geomorphology of old and abandoned underground mines: Review and future challenges. *Prog. Phys. Geogr. Earth Environ.*, **44**, 791–813, SAGE Publications Sage UK: London, England. doi:10.1177/030913332091731|4

Schütz, H. & Konietzky, H. (2016) Evaluation of flooding induced seismicity from the mining area Schlema/Alberoda (Germany). *Rock Mech. Rock Eng.*, **49**, 4125–4135. doi:10.1007/s00603-016-1032-y

Segall, P. (1989) Earthquakes triggered by fluid extraction. *Geology*, **17**, 942–946. doi:10.1130/0091-7613(1989)017<0942:ETBFE>2.3.CO;2

Segall, P. & Fitzgerald, S.D. (1998) A note on induced stress changes in hydrocarbon and geothermal reservoirs. *Tectonophysics*, **289**, 117–128. doi:10.1016/S0040-1951(97)00311-9

Segall, P., Grasso, J.R. & Mossop, A. (1994) Poroelastic stressing and induced seismicity near the Lacq gas field, southwestern France. *J. Geophys. Res.*, **99**. doi:10.1029/94jb00989

Senfaute, G., Wassermann, J. & Homand, F. (2008) Induced micro-seismicity and mechanical response during the experimental flooding of an iron ore mine. *Symp. Post-Mining 2008 ASGA. Vandoeuvre-les-Nancy*, p. 11.

Shen, B., Poulsen, B., Luo, X., Qin, J., Thiruvenkatachari, R. & Duan, Y. (2017) Remediation and monitoring of abandoned mines. *Int. J. Min. Sci. Technol.*, **27**, 803–811, China University of Mining and Technology. doi:10.1016/j.ijmst.2017.07.026

Shi, Y. & Bolt, B.A. (1982) The standard error of the magnitude-frequency b value. *Bull. Seismol. Soc. Am.*, **72**, 1677–1687.

Sibson, R H. (1986) Earthquakes and Rock Deformation in Crustal Fault Zones. *Annu. Rev. Earth Planet. Sci.*, **14**, 149–175. doi:10.1146/annurev.ea.14.050186.001053

Sibson, Richard H. (1996) Structural permeability of fluid-driven fault-fracture meshes. *J. Struct. Geol.*, **18**, 1031–1042. doi:10.1016/0191-8141(96)00032-6

Sibson, Richard H. (1989) Earthquake faulting as a structural process. *J. Struct. Geol.*, **11**, 1–14. doi:10.1016/0191-8141(89)90032-1

Šílený, J. & Milev, A. (2008) Source mechanism of mining induced seismic events — Resolution of double couple and non double couple models. *Tectonophysics*, **456**, 3–15. doi:10.1016/j.tecto.2006.09.021

Simons, M. (1986) Triggered Earthquakes. *Annu. Rev. Earth Planet. Sci.*, **14**, 21–42, Annual Reviews. doi:10.1146/annurev.ea.14.050186.000321

Simons, M., Leith, W.S. & Scholz, C.H. (1988) Two types of reservoir-induced seismicity. *Bull. Seismol. Soc. Am.*, **78**, 2025–2040.

Stein, R.S. (1999) The role of stress transfer in earthquake occurrence. *Nature*, Vol. 402. Retrieved from www.nature.com

Stein, R.S., King, G.C.P. & Lin, J. (1992) Change in failure stress on the San Andreas and surrounding faults caused by the 1992 M=7.4 Landers earthquake. *Science (80-.).*, **258**, 1328–1332.

Streit, J.E. & Cox, S.F. (2001) Fluid pressures at hypocenters of moderate to large earthquakes. *J. Geophys. Res. Solid Earth*, **106**, 2235–2243. doi:10.1029/2000JB900359

Taisne, B., Brenguier, F., Shapiro, N.M. & Ferrazzini, V. (2011) Imaging the dynamics of magma propagation using radiated seismic intensity. *Geophys. Res. Lett.*, **38**, 2–6. doi:10.1029/2010GL046068

Tarantola, A. & Valette, B. (1982) Generalized nonlinear inverse problems solved using the least squares criterion. *Rev. Geophys.*, **20**, 219. doi:10.1029/RG020i002p00219

Toda, S., Stein, R.S., Reasenberg, P.A., Dieterich, J.H. & Yoshida, A. (1998) Stress transferred by the 1995 M w = 6.9 Kobe, Japan, shock: Effect on aftershocks and future earthquake probabilities. *J. Geophys. Res. Solid Earth*, **103**, 24543–24565. doi:10.1029/98JB00765

Toro, G. Di, Mittempergher, S., Ferri, F., Mitchell, T.M. & Pennacchioni, G. (2012) The contribution of structural geology, experimental rock deformation and numerical modelling to an improved understanding of the seismic cycle. *J. Struct. Geol.*, **38**, 3–10. doi:10.1016/j.jsg.2012.01.025

Uchida, N. (2019) Detection of repeating earthquakes and their application in characterizing slow fault slip. *Prog. Earth Planet. Sci.*, **6**, 40. doi:10.1186/s40645-019-0284-z

Uchida, N. & Bürgmann, R. (2019) Repeating Earthquakes. *Annu. Rev. Earth Planet. Sci.*, **47**, 305–332. doi:10.1146/annurev-earth-053018-060119

Uchida, N., Matsuzawa, T., Hasegawa, A. & Igarashi, T. (2003) Interplate quasi-static slip off Sanriku, NE

Japan, estimated from repeating earthquakes. *Geophys. Res. Lett.*, **30**. doi:10.1029/2003GL017452

VanderPlas, J. (2016) *Python data science handbook: Essential tools for working with data*, ' O'Reilly Media, Inc.'

Vassallo, M., Satriano, C. & Lomax, A. (2012) Automatic Picker Developments and Optimization: A Strategy for Improving the Performances of Automatic Phase Pickers. *Seismol. Res. Lett.*, **83**, 541–554. doi:10.1785/gssrl.83.3.541

Vidale, J.E., Ellsworth, W.L., Cole, A. & Marone, C. (1994) Variations in rupture process with recurrence interval in a repeated small earthquake. *Nature*, **368**, 624–626. doi:10.1038/368624a0

Waldhauser, F. & Ellsworth, W.L. (2000) A Double-Difference Earthquake Location Algorithm: Method and Application to the Northern Hayward Fault, California. *Bull. Seismol. Soc. Am.*, **90**, 1353–1368. doi:10.1785/0120000006

Waldhauser, F. & Ellsworth, W.L. (2002) Fault structure and mechanics of the Hayward Fault, California, from double-difference earthquake locations. *J. Geophys. Res.*, **107**, 2054. doi:10.1029/2000JB000084

Waldhauser, F. & Schaff, D.P. (2008) Large-scale relocation of two decades of Northern California seismicity using cross-correlation and double-difference methods. *J. Geophys. Res. Solid Earth*, **113**. doi:10.1029/2007JB005479

Weatherill, G.A. & Burton, P.W. (2009) Delineation of shallow seismic source zones using K -means cluster analysis, with application to the Aegean region. *Geophys. J. Int.*, **176**, 565–588, Oxford Academic. doi:10.1111/j.1365-246X.2008.03997.x

Wei, S., Avouac, J.-P., Donnellan, A., Parker, J.W., Graves, R.W., Helmberger, D., Fielding, E., *et al.* (2015) The 2012 Brawley swarm triggered by injection-induced aseismic slip. *Earth Planet. Sci. Lett.*, **422**, 115–125, Elsevier. doi:10.1016/j.epsl.2015.03.054

Wennerberg, L. & Sharp, R. V. (1997) Bulk-friction modeling of afterslip and the modified Omori law. *Tectonophysics*, **277**, 109–136. doi:10.1016/S0040-1951(97)00081-4

Weston, J. & Shirzaei, M. (2016) Combining GPS and repeating earthquakes for a high resolution analysis of subduction zone coupling. *Tectonophysics*, **667**, 37–47. doi:10.1016/j.tecto.2015.11.009

Wetmiller, R.J., Galley, C.A. & Plouffe, M. (1993) Post-closure seismicity at a hard rock mine. *Rockbursts Seism. Mines*, **93**, 445–448, Balkema, Rotterdam.

Whyatt, J. & Varley, F. (2008) Catastrophic Failures of Underground Evaporite Mines. *Proc. 27th Int. Conf. Gr. Control Min.*, **1**, 113–122.

Wiemer, S. & Wyss, M. (2000) Minimum Magnitude of Completeness in Earthquake Catalogs: Examples from Alaska, the Western United States, and Japan. *Bull. Seismol. Soc. Am.*, **90**, 859–869. doi:10.1785/0119990114

Willacy, C., Dedem, E. van, Minisini, S., Li, J., Blokland, J.-W., Das, I. & Droujinine, A. (2019) Full-waveform event location and moment tensor inversion for induced seismicity. *GEOPHYSICS*, **84**, KS39–KS57. doi:10.1190/geo2018-0212.1

Withers, M., Aster, R., Young, C., Beiriger, J., Harris, M., Moore, S. & Trujillo, J. (1998) A comparison of select trigger algorithms for automated global seismic phase and event detection. *Bull. Seismol. Soc.*

Am., **88**, 95–106, The Seismological Society of America.

Yamaguchi, J., Naoi, M., Nakatani, M., Moriya, H., Igarashi, T., Murakami, O., Yabe, Y., *et al.* (2018) Emergence and disappearance of very small repeating earthquakes on a geological fault in a gold mine in South Africa. *Tectonophysics*, **747**–**748**, 318–326. doi:10.1016/j.tecto.2018.10.014

Yao, D., Walter, J.I., Meng, X., Hobbs, T.E., Peng, Z., Newman, A. V., Schwartz, S.Y., *et al.* (2017) Detailed spatiotemporal evolution of microseismicity and repeating earthquakes following the 2012 M w 7.6 Nicoya earthquake. *J. Geophys. Res. Solid Earth*, **122**, 524–542. doi:10.1002/2016JB013632

Yu, W., Song, T.-R.A. & Silver, P.G. (2013) Repeating aftershocks of the great 2004 Sumatra and 2005 Nias earthquakes. *J. Asian Earth Sci.*, **67**–**68**, 153–170. doi:10.1016/j.jseaes.2013.02.018

Yu, Y., Chen, S.E., Deng, K.Z., Wang, P. & Fan, H.D. (2018) Subsidence mechanism and stability assessment methods for partial extraction mines for sustainable development of mining cities-A review. *Sustain.*, **10**, 1–21. doi:10.3390/su10010113

Zyl, D. Van, Sassoon, M., Digby, C., Fleury, A.M., Kyeyune, S. & Mining, M. and S.D. (2002) Mining for the future. Appendix C: Abandoned Mines Working Paper. *Int. Inst. Environ. Dev. World Bus. Counc. Sustain. Dev.*

Annex Part I

Geological section

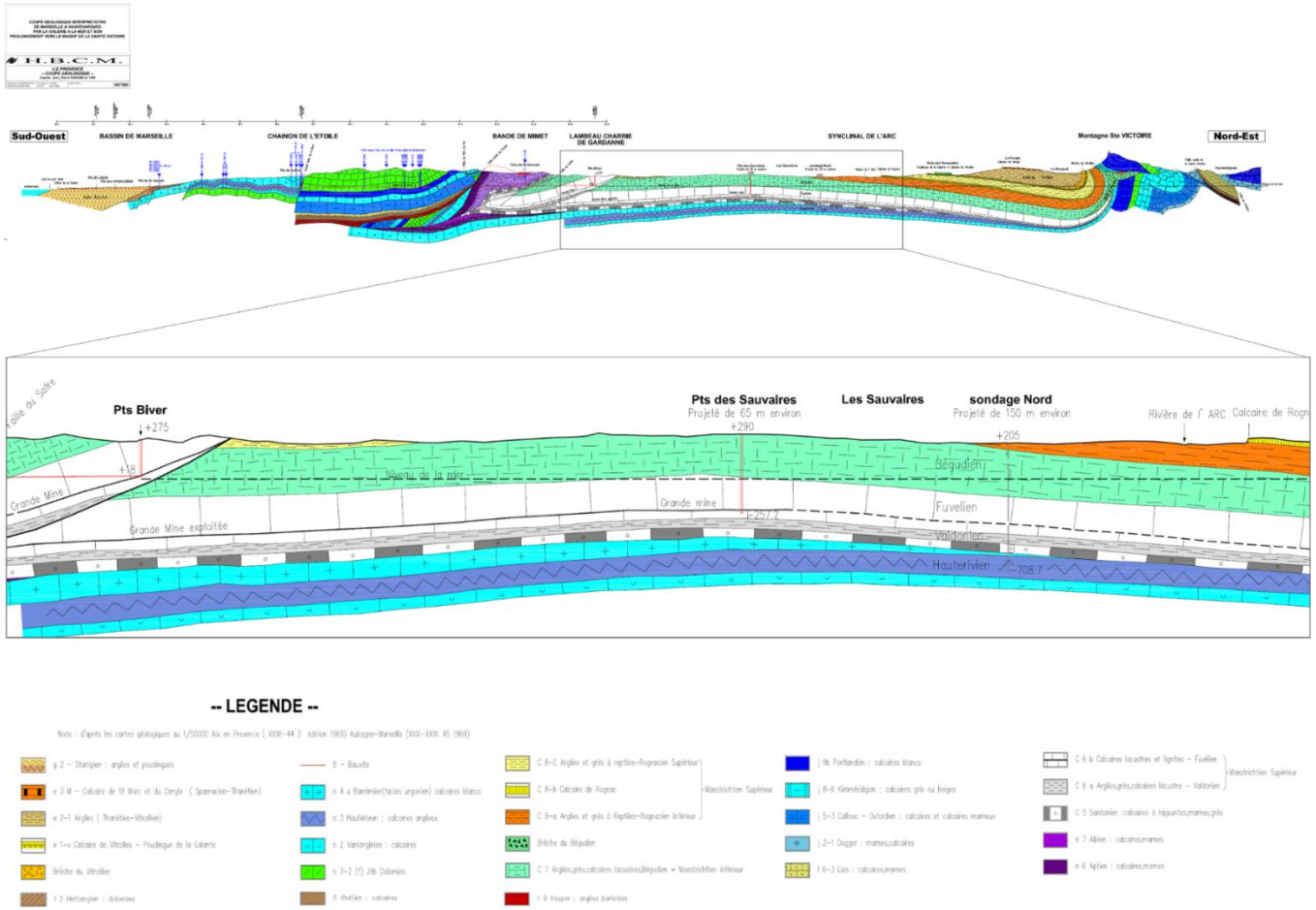

Figure A1. 1 Geological section of mining basin. Zoom in to Modified after http://www.lithotheque.ac-aix-marseille.fr/Affleurements_PACA/13_fuvelien/images_fuvelien_HD/coupe_geologique_sw_ne.pdf

Timeline of available data

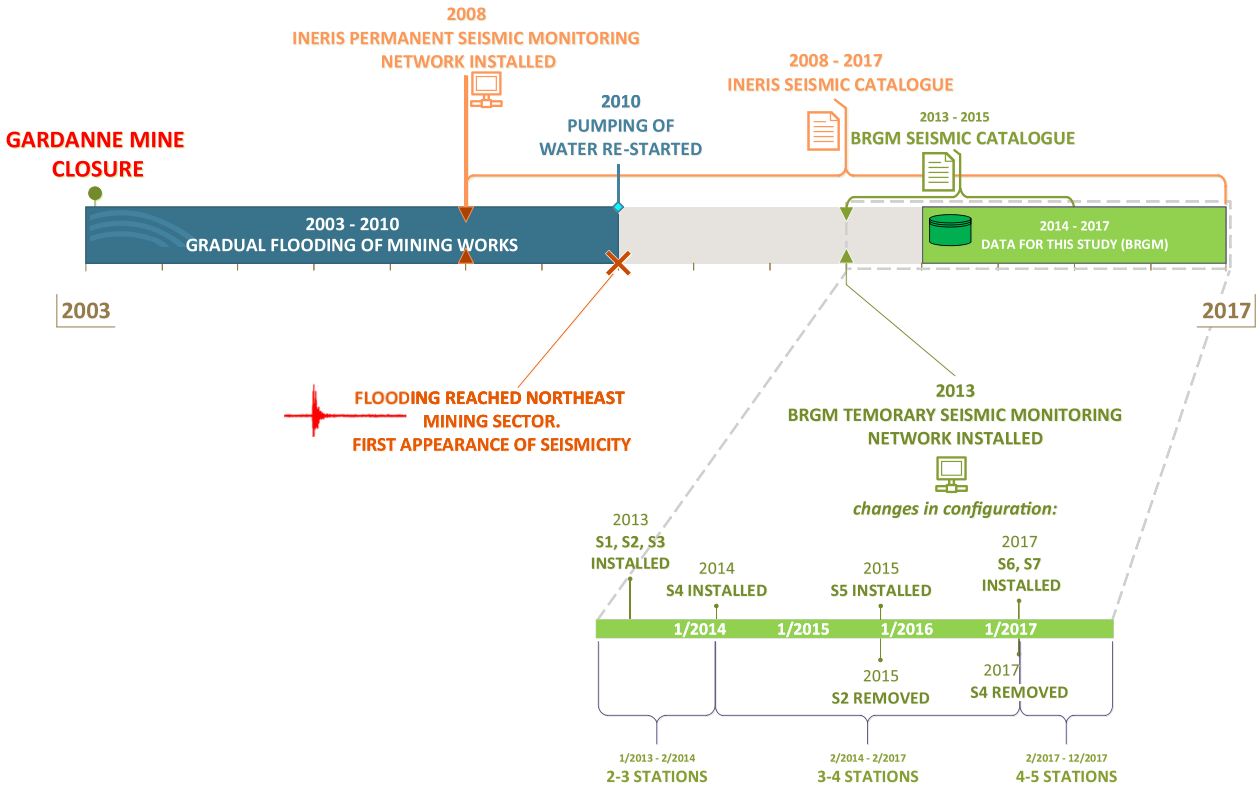

Figure A1. 2 Timeline of important events in the study area of Gardanne mine, and available data for this study: starting from the mine closure in 2003, followed by turning off the pumps and gradual flooding of mining works (blue line). Following the Geoderis risk analysis, Ineris installed a permanent monitoring network in areas classified as having the risk of ground instabilities (orange). Flooding front reaches the east part of the mine in 2010 and soon after first seismic activity starts appearing in the northeast part of mine, outside of monitoring zones (red). Pumping of water restarted in 2010 to control the flooding front (blue). Following again an increase of seismic activity in 2012, BRGM installed a temporary (sparse) monitoring network during 2013/2014 (green). Zoomed in period 2013-2017 shows BRGM network station configuration changes in time. Data available for this study cover the period 2014-2017 (green line). Ineris seismic catalogue is available for the period starting 2008 until today (orange), while BRGM seismic catalogue covers 2 years: 2014-2015 (green).

Seismic networks and used data

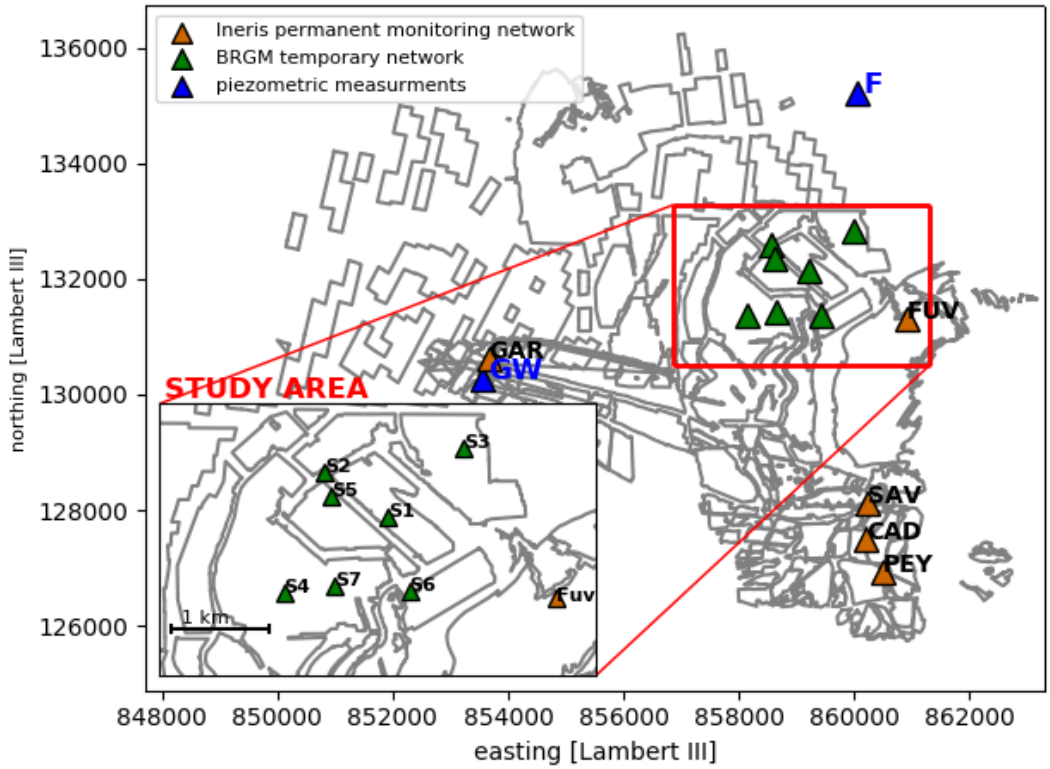

Figure A1. 3 Microseismic networks and piezometric measurements in Gardanne mine. Temporary seismic monitoring network of BRGM within the study area, permanent monitoring network of Ineris, piezometric measurements in Gerard well (GW) and Fuveau Régagnas well (F)

Temporary seismic network of BRGM (2013-)

The temporary network installed by the BRGM-DPSM is composed of stations identically equipped with GMS+ and GEOSIG AC-63 accelerometers (recording the signal in the frequency range from 0.1 to 400 Hz with the sampling frequency of 1000 Hz). Stations are installed at the surface and operate in a triggering and continuous recording mode (without remote data transmission) (Dominique 2016). The first three stations were installed in April 2013 in the zone of observed seismicity, west of the Fuveau. In the following years, however, station configuration did not have constant configuration, experiencing changes on multiple occasions. Figure A1. 2 provides a timeline of the BRGM station configuration changes during this period: from 3 initially available stations (installed in 2013) to five stations starting from the beginning of 2017, while Figure A1. 3 shows the map with location of all stations at once. Station configuration change during periods of three seismic crises can be seen in Figure A3. 2

BRGM seismic catalogue

Triggered data from the temporary network was partially manually analyzed for the period from June 2013 to 31st December 2015 (Dominique 2016b). The resulting seismic data catalogue lists a total of 756 events within the magnitude range $-1.3 \leq M_L \leq 1.7$, among which 606 are located within the study area. Locations of these events were determined based on standard techniques that include manual picking of P- and S- phases followed by an iterative location approach of minimizing the difference between the observed and predicted arrival times at a number of seismic stations. Estimated hypocentral depths are mostly several hundred meters beneath mine works (Dominique 2016a). Location errors were estimated up to yy m in horizontal and 100 to 300 m in depth.

Annex Part II

Data preparation

Continuous dataset (2014-2017): availability check and preparatory phase

For the development of the methodology that will be described in the following sections, continuous data of BRGM network, recorded during 4 years (2014-2017) on three to five stations with the sampling rate of 1000 Hz, in frequency range 1-400Hz, were used, total volume of 1.5 Tb of data.

As all the stations are equipped with identical instrumentation and the whole seismic frequency band of interest is inside a region of the flat frequency response of the instruments, the step of the instrument response removal from data is skipped for this dataset. The output record in counts is divided by the station gain (which equals 1), giving the ground acceleration.

However, another step of pre-processing was necessary to allow for automatic and simultaneous analysis on the ensemble of full-waveform traces together.

Data are continuously recorded, however, the raw data are stored in separated time-segments to multiple successive shorter time series. Available data, in this case, are (mostly) 1h length files. In total, the dataset comprised almost 35 000 files of 1h length time-series, per each station.

These files, time-series of raw data, on some stations are partially missing or incomplete during shorter or longer (not apriori known) time periods, due to station malfunctioning for example. Additionally, 1h segmentation of continuous-time series of recorded data between the stations is inconsistent. Hence to allow for analysis to be automatized if was necessary to obtain the consistent, equal length traces that would be used as the input files in further analysis. After checking of files availability, the time-series files of each station were adjusted (by merging or cutting of successive files) to correspond to desired time-segments i.e. successive time windows of equal length that covered the entire period of data availability. Data were also decimated to 500 Hz to reduce the computation time in further analysis. Processing code is developed in Python programming language and all steps are automatized.

BTBB principle

The following paragraphs provide a more detailed overview of the BTBB method, notably steps as defined in section 4.3.1

Part (i) CF construction

Designed to enhance the properties of the non-stationary impulsive signal such as the one generated by earthquake source (i.e., the arrival of P- or S-phases), for signal transformation to CF the higher-order statistics (HOS) function of fourth-order, i.e., kurtosis (a fourth moment about the mean, normalized by the square of the second moment i.e., variance) is used. CF HOS is therefore defined as follows:

$$CF\ HOS\ (t_i) = \frac{\frac{1}{M}\sum_{i=1}^{M}(u(t_i) - \hat{\mu})^4}{\left(\frac{1}{M}\sum_{i=1}^{M}(u(t_i) - \hat{\mu})^2\right)^2} \qquad \textbf{A2.1}$$

where $u(t) = \{u(t_1), u(t_2), .. u(t_M)\}$ represents a discrete signal, M is the number of samples, and $\hat{\mu}$ is the mean. In order to improve the computation efficiency, Poiata *et al.* (2016) implemented a recursive scheme of CF computation, following a principle similar to Langet *et al.* (2014). The final expression for CF HOF becomes:

$$CF\ HOS\ (t_i) = \frac{C\left(u(t_i) - \hat{\mu}(t_{i-1})\right)^4 + (1 - C)\widehat{m}_4(t_{i-1})}{\left(C\left(u(t_i) - \hat{\mu}(t_{i-1})\right)^2 + (1 - C)\widehat{m}_2(t_{i-1})\right)^2} \qquad \textbf{A2.2}$$

where $\widehat{m}_4$ is the fourth central moment, the exponential average is expressed in recursive form as $\hat{\mu}(t_i) = Cu(t_i) + (1 - C)\hat{\mu}(t_{i-1})$ and $C: 0 \leq 1 - C \leq 1$ is decay constant.

The HOS-CF are efficient in capturing and extracting changes in statistical properties of a signal as any transient change in the signal generates a temporary peak in the value. As this increase of this value can also come from other sources such as random noise arrival, coherency analysis across the network is implemented as a next step, taking into account the broadband nature of a seismic signal.

For calculating the CF of the original record $U(t)$, the frequency content of the signal is taken into account. The raw signal passes through several steps:

1. Using the approach of a multiband filter (MBF) decomposition of the signal (Lomax *et al.* 2012), a set of band-pass filtered time-series $(U(t,\ f_n))$ is created by running the original record $U(t)$ through the predefined bank of the narrow bandpass filters covering the frequencies between $fmin$ and $fmax$, with, having $n\ =\ 0, \dots, N$ band central frequencies fn (FIG).
2. Then, for each filtered signal, a CF is constructed by applying the recursive kurtosis, hence generating a set of CFs of each frequency band: $(CF(t, fn))$.

3. Single time-dependent broad-band, $HOS\ CF\ (CF^{TF}(t))$ is constructed as a maximum of a time-frequency dependent set:

$$CF_{HOS}\ (CF^{TF}(t))\ =\ max\ f\ CF(t,f), f\ \in\ [\ f_{min},\ f_{max}]. \qquad \textbf{A2.3}$$

4. In order to account for timing uncertainty, as HOS maximum is delayed with respect to the onset of the transient, generic CF for the problem is defined and calculated as a convolution of the positive derivative of HOS CF with a Gaussian window:

$$CF\ (t)\ =\ \dot{CF}^{+}_{HOS}(t) * e^{-t^2/4\sigma^2} \qquad \textbf{A2.4}$$

where $*$ is convolution operator, $\sigma = T_{decay}/2$ and

$$\dot{CF}^{+}_{HOS}(t) = \begin{cases} \dot{CF}_{HOS}(t)\ if\ \dot{CF}_{HOS}(t) \geq 0 \\ 0 \qquad elswhere \end{cases} \qquad \textbf{A2.5}$$

This time-frequency decomposition approach serves as a denoising scheme and allows the enhancing of the narrow-band energy arrivals in the case of low SNR, by retaining at each time the strongest HOS signature of short-duration, impulsive transients of different frequency bands.

Part (ii) Detection and location

As mentioned in the *Common basic principles* section, the full waveform methods base their location on the idea of 3D spatial likelihood images created from spatial mapping and stacking functions. In BTBB, stacking techniques correspond to the cross-correlation of CFs to compute station-pair time-delay estimate functions (TDEs), while exploiting the coherency of CFs for detection and location of sources of potential events, and further mapping of TDE functions onto 3D grids of theoretical travel time differences (TDOAs)

- **Station-pair time-delay functions estimations (TDEs)**

The calculation of the TDE distributions in BTBB is based on tracing of the time-dependent similarity between two signals by method of local cross-correlation (LCC method). The formulation of Birchfield & Gillmor (2002) presents the most common implementation of LCC used, however, as this approach can be computationally expensive, to reduce the calculation time, Poiata *et al.* (2016) implemented the LCC algorithm of Hale (2006) into BTBB, which allows recursive calculations (e.g., Young & van Vliet 1995). The LCC is expressed as:

$$LCC_p\left(t, \Delta\tau_p(q)\right) \equiv \int_{-\infty}^{+\infty} cf_i\left(t' - \frac{\Delta\tau_p(q)}{2}\right) cf_j\left(t' + \frac{\Delta\tau_p(q)}{2}\right) \qquad \textbf{A2.6}$$

$$\times\, \nu\left(t - t', \Delta\tau_p(q)\right) dt'$$

for a given station pair i and j and corresponding CFs, where $\nu\left(t - t', \Delta\tau_p(q)\right)$ is Gaussian filter defined as $\nu(t, l) = e^{-\Delta\tau_p(q)^2/4\sigma^2} e^{-t^2/\sigma^2}$ and variance σ^2 corresponds to the half-width of Gaussian function used for filtering.

The 2-D LCC function of lag $\Delta\tau_p(q) \in \left[-\Delta\tau_{p,max}, \Delta\tau_{p,max}\right]$ $(TDOA)$, and time defined t as defined in [*A2.6*] provides the TDE distribution at times $t = t'$.

The determine the final time-dependent function of the TDE distribution, used for the detection and location phase, for each station pair (i.e., pair of CFs), the local maximum of LCC is determined at a point with coordinates $\left[t_{LCC_{max}}, \Delta\tau_{LCC_{max}}\right]$. Time samples of the cross-correlated signals that correspond to this LCCmax are:

$$t_1 = t_{LCC_{max}} - \frac{\Delta\tau_{LCC_{max}}}{2}\ , and\ \ t_2 = t_{LCC_{max}} + \frac{\Delta\tau_{LCC_{max}}}{2} \qquad \textbf{A2.7}$$

In BTBB, direct mapping of LCC function into 3D space allows for faster performance by avoiding the computationally expensive explicit grid-search over all possible source locations as in the standard beamforming approach.

- **Spatial mapping and stacking of TDEs**

Before the summation in the next step, it is necessary to know the theoretical time difference of signals arrival between every two stations (TDOA) for a designed 3D space of interest. For the estimation of TDOAs of all station pairs, under the assumptions of a given velocity model and a seismic phase, associated with the 3D grid, the Grid2Time routine of NonLinLoc (Lomax 2005, 2008) can be used, which is based on the Eikonal finite-difference scheme of Podvin & Lecomte (1991).

A potential source location (SLF) is then estimated by mapping the TDE functions according to pre-calculated TDOAs and summing them over the pairs of stations. In the case of the constant velocity model, these SLF are reduced to hyperboloids passing through the hypocenter of the source (Figure A.1). As we can see in Figure A.2 showing imaging functions for the cases of the small number of stations (2,3,4) and 22 stations, that a minimum of 3 stations (i.e., 3 records of the visible event) are necessary for the location of an event.

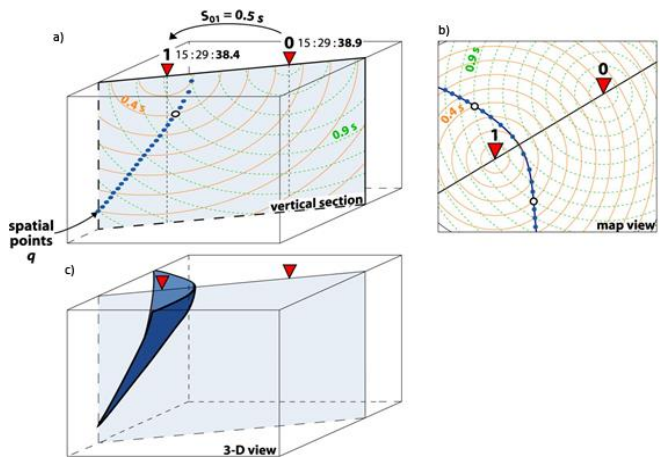

Figure A2. 1 Illustration of an equal differential time (TDE) surface in a homogeneous velocity model: a) collection of spatial points satisfying an arrival time difference of 0.5 s at the two stations 0 and 1, presented on a vertical section, b) collection of spatial points on the map view. c) schematization of the TDE surface on a 3-D view. Adapted from *Font* et al. *(2004)*

- **Source location determination**

The previous step leads to a time series of 3-D grids that provide the spatial (normalized) likelihood for the source to be located at a given position. The estimated position of the seismic source is the location with the highest likelihood.

Detection of an earthquake is declared when the normalized value of the final 3D spatial likelihood map (imaging function) exceeds the set threshold, which is determined by calibration analysis.

Once the position of the seismic source is determined, the origin time T_0 is estimated as the average of the observed arrival times t_i minus the predicted travel times $\tau_i(q)$, for the peaks of detection functions that contributed to the corresponding imaging function. Following Moser *et al.*(1992) this can be expressed as:

$$T_0(q) = \frac{\sum_{i=1}^{N_p} w_i\left(t_i - \tau_i(q)\right)}{\sum_{i=1}^{N_p} w_i} \qquad \textit{A2.8}$$

where N_p is the number of station pairs and w_i are weights attributed to the observed arrival times t_i.

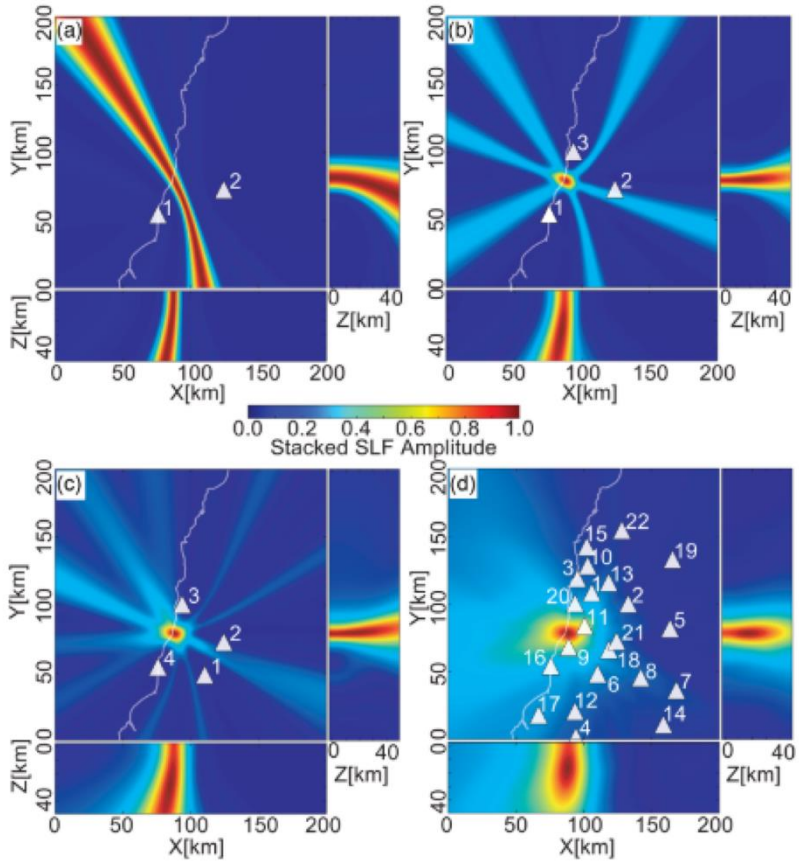

Figure A2. 2 Examples of imaging functions for the case of (a) two, (b) three, (c) four and (d) 22 stations. Adapted from *Poiata* et al. *(2016)*.

STA LTA method

In general, the STA/LTA algorithms process seismic signals in two moving time windows – a short-time average window (STA) and a long-time average window (LTA). The STA measures the 'instant' amplitude of the seismic signal and watches for earthquakes while the LTA takes care of the current average seismic noise amplitude (Trnkoczy 2012). The response of the STA/LTA function is dependent on the chosen lengths of the windows (Withers 1997).

To calculate CF, a recursive short-time average over long-time average (STA/LTA) algorithm implemented in Obspy (Beyreuther *et al.* 2010, Megies *et al.* 2011) was used. $CF_{STA/LTA}$ is defined as:

$$CF_{STA/LTA}\,(t_i) \;= \frac{STA_i}{LTA_i} \qquad \textbf{A2.9}$$

Following (Withers 1997, Withers *et al.* 1998), the STA_i and LTA_i windows are calculated in recursive algorithms:

$$STA_i = \; C \cdot u(t_i) + (1 - C)STA_{i-1} \qquad \textbf{A2.10}$$

and

$$LTA_i = \; C \cdot u(t_i) + (1 - C)LTA_{i-1} \qquad \textbf{A2.11}$$

Constant C is defined as

$$C = 1 - e^{S/T} \qquad \textbf{A2.12}$$

where S is the sample rate, T is characteristic decay time (i.e., the time required for the impulse response to decay to $\frac{1}{e}$ of its original value, $u(t_i)$ is the data point at time step i. However, it is common to use:

$$C = 1/N_{STA} \text{ or } C = 1/N_{LTA} \text{ accordingly.} \qquad \textbf{A2.13}$$

As the frequency content of seismic signals can vary considerably, due to the differences in source size and location, window lengths need to be adapted accordingly. Detailed explanations on how to determine the appropriate duration of both STA and LTA windows can be found in Trnkoczy 2012.

In my analysis, both STA and LTA windows lengths are adapted to each of the frequency bands to ensure the same level of sensitivity to events in all of them. Values are given in the table below:

Table A2. 1 STA and LTA windows lengths

	$f \in [1Hz, 100Hz]$	$f \in [1\ Hz, 20\ Hz]$	$f \in [20\ Hz, 60\ Hz]$
STA window length [s]	0.1	0.15	0.08
LTA window length [s]	1	1.5	0.8

Prior to their transformation to $CF_{STA/LTA}$, seismic records of all stations are filtered into predefined three frequency bands

Amplitude-ratio based method

Derivation of amplitude-ratio location approach

Also belonging to the group of migration-based algorithms, such as full waveform methods described in section 5.3**.**, amplitude-based location approaches (ASL) rely on the attenuation of seismic waves along the source-receiver travel path and do not require travel-time information (picking).

Apart from application to locate events, the modifications to the existing method introduced during this thesis work show that it can be used adequately with an additional purpose, as a noise removal method. These modifications and novel noise removal steps are presented in the following sections, as well as the application to testing the dataset resulting from the previous step.

Introduced by (Battaglia & Aki 2003), the ASL approach is derived directly from the attenuation relationship:

$$A(f) = s(f) \cdot A_0(f) \cdot \frac{1}{r^n} \cdot e^{\left(\frac{\pi f r}{Q V_p}\right)} \qquad \textbf{A2.14}$$

which states that recorded signal amplitude $A(f)$ on a certain station depends on site amplification effect $s(f)$, the amplitude at source $A_0(f)$, source-station distance r, quality factor for attenuation Q, P-wave velocity V_P (or S-wave velocity, respectively) and central frequency f. Estimation of the source position is determined by the minimization of measured and modelled seismic amplitude decay, recorded across a network of sensors.

The method has proved successful for a range of different types of events, such as emergent earthquakes [e.g. Battaglia and Aki, 2003], migration of volcanic tremor (e.g. Taisne *et al.* 2011, Ogiso & Yomogida 2012), volcano-tectonic earthquakes (e.g. Kumagai *et al.* 2013), long-period events (e.g. Battaglia & Aki 2003), volcanic tremor (e.g. Ogiso *et al.* 2015), explosion events (e.g. Kumagai *et al.* 2011), magma intrusions (e.g. Taisne *et al.* 2011), rockfalls (e.g. Aki & Ferrazzini 2000), debris flows (e.g. Ogiso & Yomogida 2015) or pyroclastic flows (e.g. Jolly *et al.* 2012).

In this thesis, modifications of the ASL approach introduced by (Taisne *et al.* 2011) was used.

Rather than estimating the seismic amplitudes at different stations, to avoid the estimation of the amplitude at the source $A_0(f)$ in equation [F.2] Taisne et al. (2011) introduced the estimation of location by the determination of the amplitude ratio of station pairs. Source amplitude $A_0(f)$ is eliminated by rewriting the equation as amplitude ratio of station pair (i, j):

$$\log_{10}\frac{A_i(f)}{A_j(f)} = \log_{10}\frac{s_i(f)}{s_j(f)} + n\log_{10}\frac{r_j}{r_i} - \frac{\pi f\left(r_i - r_j\right)}{Q V_p} \cdot \log_{10}(\exp 1) \qquad \textbf{A2.15}$$

Determination of event location with amplitude ratio approach works on a principle of finding the most probable source location based on misfit over all station pairs, minimizing the error between expected (theoretical) and observed values calculated on a grid of possible sources.

Introduced simplifications to approach of (Taisne et al. 2011) in application to study area

Considering the environment of the study area, further modifications to the approach were introduced. The attenuation law used is described exclusively with a geometrical spreading, ignoring contributions from anelastic attenuation and site amplification effect:

$$\log_{10}\frac{A_i}{A_j} = n\log_{10}\frac{r_j}{r_i} \qquad \textit{A2.16}$$

where A_i and A_j are the maximum amplitudes of signals at stations i and j, while r_i and r_j are the source-station distances of the same station pair.

Even though local site characteristics can, in general, significantly affect the amplitude of the recorded seismic signal, it was disregarded in the further calculation. Otherwise, the calibration with the training set, which is concentrated in the small area (hence providing limited azimuthal coverage of events), would be misleading as it would not include possible directional effects. Calculations of site effects would therefore improve location only locally for this particularly seismically active zone where events of the training set are localized, with a trade-off of introducing the bias in other areas, when seismic events originate from a different direction or more distant location in regards to stations. In addition, determination of horizontal-to-vertical spectral ratio (i.e., HVSR) showed a flat response and lacking significant peaks, for all stations (personal communication P. Dominique), indicating the site effect can be considered insignificant.

Reducing the number of parameters allowed to avoid the wrong calibration. Further, factor n was given value 2 under the assumption of a body wave geometric spreading behaviour (Lay & Wallace 1995).

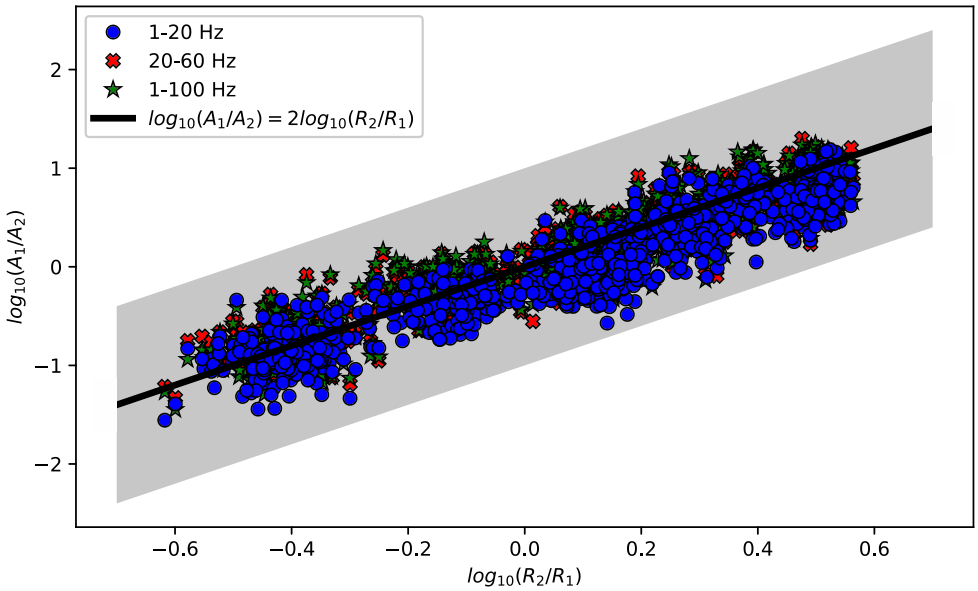

Figure A2. 3 Logarithm of amplitude ratios without frequency-dependent terms, shown in three different frequency ranges. Grey area corresponds to intercept of ±1

These modifications were evaluated with the training dataset and indeed provide a good fit to observed amplitude ratios, plotted as a function of the reversed distance ratios. The fit is equally good for all three frequency bands used (consistent with the previous, detection step), justifying also the choice of frequency-independent attenuation model).

New seismic data catalogue 2014-2017, 364 events of A class

Seismic data catalogue of A class events , result of analysis presented in Part II. following parameters:
T_ORIG: time of origin, result of BTBB analysis
Easting BTBB, Northing BTBB: Lambert III Sud coordinates, results of BTBB analysis
Easting AMP, Northing AMP: Lambert III Sud coordinates, results of amplitude ratio analysis
M_L:calculated local magnitude

Full catalog comprises additionall parameters for each event :
Moment magnitude Mw, Moment Mo,
P-phase arrival time picks (result of BTBB)
Parameters of STA/ LTA analysis (triggered 2 sec window, trigger time for each station in each frequency range, parameters MRMS and MAA (mean values and values for each frequency range and each station), Parameters of amplitude analysis, class based on new classification system, number of stations available with SNR>3, if in multiplet families.

Table A2. 2 Seismic data catalogue 2014-2017. A class events

T_ORIG	Easting BTBB	Northing BTBB	Easting AMP	Northing AMP	M_L
2014-03-21T12:01:10	858420,44	131615,28	857327,00	131315,00	0,22
2014-03-23T06:55:24	859034,74	131839,26	859227,00	131965,00	0,31
2014-06-27T23:23:29	860185,65	130643,34	861127,00	130765,00	0,14
2014-07-03T01:41:34	858925,86	131534,84	859627,00	130965,00	0,07
2014-08-27T20:08:29	858904,86	131554,04	859727,00	131015,00	0,12
2014-08-30T03:51:41	859105,50	132602,48	859077,00	132615,00	0,75
2014-09-16T05:20:59	858746,24	131507,85	859327,00	131065,00	0,06
2014-10-19T00:46:25	859044,87	132620,14	858977,00	132615,00	0,40
2014-10-29T07:36:58	858972,55	131896,88	859077,00	132015,00	0,13
2014-10-31T06:12:01	859082,16	132161,30	859127,00	132265,00	0,22
2014-11-11T08:51:33	859013,74	131858,46	859177,00	132015,00	0,30
2014-11-21T02:56:24	858147,58	131924,89	857827,00	132065,00	0,33
2014-11-23T08:21:31	859297,53	132309,77	859327,00	132315,00	0,06
2014-12-01T16:29:05	858892,44	131873,75	858977,00	132065,00	0,96
2014-12-01T17:10:51	858892,44	131873,75	859227,00	131965,00	0,06
2014-12-01T18:53:49	859035,51	131819,28	859127,00	131915,00	0,32
2014-12-01T19:42:30	858956,99	131776,20	859027,00	131915,00	0,41
2014-12-01T20:03:21	858892,44	131873,75	859077,00	131915,00	0,09
2014-12-02T13:32:55	858951,55	131916,08	858977,00	132015,00	0,98
2014-12-02T13:50:30	858891,66	131893,74	859127,00	131915,00	0,72
2014-12-02T15:13:04	859047,97	132019,89	859127,00	131815,00	0,10
2014-12-02T15:47:14	858872,25	131892,98	859027,00	131765,00	0,98
2014-12-02T16:19:13	858827,14	132011,30	858927,00	132015,00	0,51
2014-12-02T18:20:27	859013,74	131858,46	859077,00	131865,00	0,03
2014-12-02T23:19:44	859095,37	131821,61	859377,00	131965,00	0,18
2014-12-03T01:03:13	858851,25	131912,18	858927,00	131965,00	0,37
2014-12-03T01:04:27	859092,28	132421,86	859477,00	131615,00	0,40
2014-12-03T04:36:05	858829,47	131951,36	858777,00	132065,00	0,67

2014-12-03T05:36:10	858851,25	131912,18	858877,00	132115,00	0,35
2014-12-03T08:31:29	858806,92	132010,52	859127,00	131515,00	0,07
2014-12-03T09:03:46	858972,55	131896,88	859277,00	131865,00	0,06
2014-12-03T09:29:16	858809,25	131950,57	858927,00	131965,00	0,11
2014-12-03T11:25:51	858872,25	131892,98	858777,00	132215,00	0,60
2014-12-03T11:53:45	858891,66	131893,74	858977,00	132165,00	0,52
2014-12-03T14:27:46	858887,78	131993,65	859127,00	131665,00	0,07
2014-12-03T15:42:52	858787,51	132009,76	858777,00	132065,00	0,54
2014-12-03T17:49:08	858787,51	132009,76	858727,00	132065,00	0,23
2014-12-03T18:55:56	858788,28	131989,78	858877,00	132065,00	0,28
2014-12-04T03:54:54	858786,73	132029,74	858827,00	131865,00	0,09
2014-12-17T03:38:30	858681,63	130584,78	857727,00	130665,00	0,06
2014-12-26T12:11:01	858766,51	132028,96	858727,00	131815,00	0,02
2014-12-28T15:44:00	858803,78	131570,12	859627,00	130965,00	0,56
2015-01-09T22:51:37	859082,16	132161,30	859077,00	132115,00	0,34
2015-01-27T02:58:40	858788,28	131989,78	858977,00	131815,00	0,13
2015-01-27T23:54:30	859075,18	131840,83	859177,00	132015,00	0,60
2015-01-30T09:42:56	859013,74	131858,46	859027,00	132015,00	0,21
2015-02-06T04:44:27	858803,78	131570,12	859527,00	131015,00	0,22
2015-02-13T06:31:44	859173,16	132425,00	859277,00	132315,00	0,16
2015-02-25T10:25:21	858841,89	131631,64	859627,00	131015,00	0,18
2015-02-26T04:48:44	858589,33	132982,67	858727,00	133015,00	0,16
2015-03-24T06:57:41	858721,41	132147,28	857077,00	132965,00	0,46
2015-04-26T05:27:36	859112,50	132422,64	859477,00	131715,00	0,01
2015-05-26T02:48:14	858556,60	132260,96	858177,00	132965,00	0,12
2015-05-28T15:30:38	859089,14	131461,14	859777,00	131365,00	0,16
2015-05-29T18:25:02	858724,51	132067,35	859427,00	131465,00	0,07
2015-06-03T19:22:26	858556,60	132260,96	857427,00	133165,00	0,08
2015-06-07T21:33:25	858801,36	130589,43	858777,00	130615,00	0,09
2015-09-12T05:16:54	858821,59	130590,21	859927,00	130865,00	0,08
2015-10-07T08:44:10	858925,09	131554,83	860127,00	130865,00	1,70
2015-10-08T23:16:00	859088,36	131481,12	859727,00	130915,00	0,15
2015-10-09T18:46:30	858904,09	131574,02	859727,00	130665,00	0,86
2015-10-09T21:03:31	859119,48	131722,48	859327,00	131465,00	0,11
2015-10-10T15:55:50	858904,09	131574,02	859977,00	130915,00	0,88
2015-11-13T00:30:13	859012,94	131358,12	859577,00	130915,00	0,18
2015-11-28T17:38:56	858661,40	130583,99	856977,00	130665,00	0,32
2015-12-08T01:07:03	858721,41	132147,28	858677,00	132065,00	0,34
2015-12-25T06:11:30	857985,10	131978,64	857577,00	132365,00	0,24
2015-12-28T16:38:02	858619,56	132183,35	858727,00	132065,00	0,11
2015-12-31T06:40:09	858004,55	131999,40	856977,00	132165,00	0,46
2016-01-03T03:23:56	858966,33	132056,74	859127,00	132265,00	0,03
2016-01-10T18:46:43	858925,09	131554,83	859427,00	130865,00	0,98
2016-01-12T23:19:01	859149,83	132504,15	859277,00	132515,00	0,07
2016-01-17T16:24:01	859756,27	132407,69	859827,00	132615,00	0,08
2016-01-26T13:37:13	858691,13	132426,28	858927,00	131565,00	0,07
2016-02-17T04:43:08	858681,63	130584,78	858727,00	130615,00	0,70
2016-03-06T10:30:57	859149,83	132504,15	859477,00	132215,00	0,18
2016-04-01T05:07:56	858775,90	132829,82	858927,00	132865,00	0,11
2016-04-05T16:52:06	859072,07	131920,76	860727,00	131515,00	0,33

2016-04-06T02:32:17	859276,54	132328,97	859377,00	132365,00	0,08
2016-04-22T06:15:09	858721,41	132147,28	858727,00	131815,00	0,11
2016-05-15T16:14:50	858862,04	130591,78	859577,00	130765,00	0,51
2016-05-26T15:05:45	859066,65	132580,96	858977,00	132765,00	0,19
2016-06-19T08:18:07	859103,95	132642,45	858877,00	131965,00	0,10
2016-07-06T15:13:59	859151,38	132464,18	859277,00	132365,00	0,39
2016-07-12T17:23:10	858736,16	131767,62	859027,00	131565,00	0,40
2016-07-23T02:13:25	858641,17	130583,21	858877,00	130815,00	1,08
2016-07-24T20:09:06	858349,73	131892,71	857727,00	132565,00	0,51
2016-08-01T21:13:43	859026,95	131518,76	859577,00	131415,00	1,13
2016-08-02T16:36:24	858499,01	131678,36	858677,00	131065,00	0,41
2016-08-03T16:11:08	858684,83	131545,49	857127,00	132215,00	0,13
2016-08-03T23:35:08	858519,20	131659,13	857377,00	131715,00	0,38
2016-08-14T10:58:01	858441,44	131596,08	858627,00	131365,00	0,25
2016-08-17T18:23:17	859077,51	131780,89	859327,00	132115,00	0,20
2016-08-18T19:29:28	859272,67	132969,21	859427,00	132865,00	0,16
2016-08-25T18:42:01	859566,55	132640,45	860227,00	132465,00	0,35
2016-08-30T22:43:34	859429,73	132014,73	859527,00	132165,00	0,14
2016-09-01T23:39:41	859131,15	131943,07	859327,00	131865,00	0,49
2016-09-13T03:09:54	859035,51	131819,28	859177,00	132015,00	0,09
2016-09-17T01:03:04	857307,84	131832,37	857327,00	131615,00	0,22
2016-09-17T11:12:49	860061,08	131779,19	860727,00	132115,00	0,03
2016-09-19T04:02:57	859191,79	132445,74	859277,00	132265,00	0,91
2016-09-22T16:36:03	858936,76	131775,41	859377,00	131665,00	0,36
2016-09-24T18:03:44	858950,77	131936,06	859077,00	131965,00	0,27
2016-09-26T05:40:20	857943,88	131997,05	857927,00	132215,00	0,39
2016-09-27T11:19:20	859149,83	132504,15	859327,00	132315,00	0,41
2016-09-29T23:49:23	859171,60	132464,97	859277,00	132365,00	1,19
2016-10-04T03:23:54	858576,77	131741,42	858077,00	131965,00	0,48
2016-10-06T00:40:24	858625,71	131503,17	857277,00	132265,00	1,32
2016-10-12T21:09:10	858888,55	131973,66	859027,00	131965,00	1,63
2016-10-13T17:54:04	858430,59	131875,83	858677,00	131815,00	0,22
2016-10-16T12:41:01	858974,88	131836,93	859377,00	131965,00	1,43
2016-10-20T04:12:53	859130,39	132483,38	859277,00	132315,00	0,34
2016-10-20T22:46:07	859130,39	132483,38	859377,00	132415,00	1,59
2016-10-20T22:47:55	859066,65	132580,96	859277,00	132365,00	0,99
2016-10-21T08:27:10	859130,39	132483,38	859377,00	132415,00	0,96
2016-10-21T08:29:07	859157,60	131784,00	859327,00	131865,00	1,47
2016-10-21T10:16:22	859152,16	132444,20	859227,00	132365,00	1,08
2016-10-21T11:30:14	859091,50	132441,84	859277,00	132465,00	0,43
2016-10-21T17:58:02	858946,11	132055,95	859027,00	131965,00	0,36
2016-10-23T12:00:57	859155,27	132364,27	859327,00	132315,00	1,49
2016-10-23T13:26:29	858556,60	132260,96	858477,00	132615,00	0,48
2016-10-25T14:51:45	859130,39	132483,38	859327,00	132465,00	1,66
2016-10-28T13:45:22	858845,84	132572,37	858977,00	132865,00	0,20
2016-10-31T04:06:37	859066,65	132580,96	859127,00	132365,00	0,43
2016-10-31T20:01:25	858373,83	131793,58	858527,00	131765,00	1,13
2016-11-01T10:59:31	858273,53	131789,69	857877,00	132165,00	0,04
2016-11-01T16:50:30	858352,06	131832,76	857927,00	131965,00	0,57
2016-11-01T19:43:19	858231,53	131828,09	858277,00	131965,00	0,05

2016-11-01T22:36:23	858004,55	131999,40	857577,00	132265,00	0,09
2016-11-02T18:15:53	858273,53	131789,69	857427,00	132065,00	0,23
2016-11-05T13:58:52	858355,16	131752,83	857127,00	132065,00	0,55
2016-11-05T16:31:42	859172,38	132444,99	859327,00	132415,00	0,86
2016-11-06T09:59:03	858535,55	131759,83	857127,00	132565,00	0,52
2016-11-07T14:46:46	859276,54	132328,97	859377,00	132265,00	0,04
2016-11-08T00:50:37	859066,65	132580,96	859127,00	132365,00	0,42
2016-11-09T18:21:23	858599,34	132182,56	858177,00	132565,00	0,21
2016-11-10T14:13:29	858866,81	132032,86	858877,00	132115,00	0,15
2016-11-11T03:32:08	859292,86	132949,98	859427,00	132715,00	0,43
2016-11-11T13:25:46	859212,79	132426,55	859377,00	132265,00	1,27
2016-12-03T22:25:28	859191,79	132445,74	859227,00	132215,00	1,13
2016-12-04T06:28:29	858494,42	132318,58	858127,00	132465,00	0,16
2016-12-04T10:50:34	858744,77	132588,46	859227,00	132465,00	0,54
2016-12-06T21:15:19	858661,40	130583,99	858927,00	131315,00	0,01
2016-12-07T21:53:57	859168,49	132544,90	859377,00	132315,00	1,24
2016-12-08T14:15:55	858852,08	132932,84	859027,00	132465,00	1,27
2016-12-19T13:03:14	858661,40	130583,99	858927,00	130865,00	0,61
2017-01-21T06:04:11	858577,60	132241,76	858727,00	132115,00	0,67
2017-01-21T16:33:40	858580,70	132161,83	858727,00	132115,00	0,40
2017-01-21T16:33:47	858536,38	132260,17	858677,00	132865,00	0,17
2017-01-26T21:25:06	858557,38	132240,97	858677,00	132365,00	0,55
2017-01-27T04:38:14	858499,01	131678,36	858577,00	131015,00	0,13
2017-01-29T18:06:19	858721,41	132147,28	858677,00	132065,00	0,28
2017-01-29T22:23:38	858680,22	132185,71	858727,00	132615,00	0,50
2017-01-31T02:54:28	858809,25	131950,57	858877,00	132015,00	1,59
2017-01-31T02:57:33	858809,25	131950,57	858877,00	132065,00	0,22
2017-01-31T03:49:25	858727,62	131987,42	858577,00	132115,00	0,23
2017-01-31T04:15:30	858727,62	131987,42	858727,00	132015,00	0,19
2017-02-01T16:45:33	858725,29	132047,37	858877,00	132015,00	1,23
2017-02-01T16:45:55	858766,51	132028,96	858527,00	131965,00	0,14
2017-02-01T16:48:49	858705,84	132026,60	858877,00	132165,00	1,41
2017-02-01T23:11:15	858745,51	132048,16	858777,00	131965,00	0,31
2017-02-02T03:09:46	859040,19	132219,71	859077,00	132465,00	0,14
2017-02-02T05:01:23	857880,15	132094,65	858027,00	132265,00	0,91
2017-02-02T08:58:46	858707,40	131986,64	858677,00	132115,00	0,23
2017-02-03T11:39:27	858866,81	132032,86	858877,00	132065,00	0,28
2017-02-04T18:21:27	858742,41	132128,08	858727,00	131915,00	0,41
2017-02-06T01:54:24	858515,38	132279,37	858427,00	132615,00	0,58
2017-02-06T09:30:08	858684,10	132085,79	858877,00	132365,00	0,90
2017-02-06T09:42:07	858707,40	131986,64	858877,00	132115,00	0,31
2017-02-06T10:03:25	858707,40	131986,64	858727,00	132165,00	0,75
2017-02-06T10:06:01	858644,43	132064,24	858677,00	132315,00	0,02
2017-02-06T12:17:01	858707,40	131986,64	858727,00	132065,00	0,29
2017-02-06T12:39:36	858660,05	132705,24	858827,00	132565,00	0,21
2017-02-06T12:43:34	858727,62	131987,42	858677,00	132115,00	0,18
2017-02-06T13:22:14	858707,40	131986,64	858727,00	132065,00	0,73
2017-02-06T13:39:16	858620,33	132163,37	858777,00	132265,00	0,49
2017-02-06T18:05:34	858829,47	131951,36	858927,00	132015,00	0,10
2017-02-06T21:50:41	858621,11	132143,39	858727,00	132265,00	0,41

2017-02-06T22:30:58	858829,47	131951,36	858877,00	132065,00	0,69
2017-02-07T01:47:17	858848,14	131992,11	858827,00	132115,00	0,21
2017-02-07T02:32:49	858788,28	131989,78	858827,00	132065,00	0,45
2017-02-07T03:42:29	858640,55	132164,15	858777,00	132665,00	0,11
2017-02-08T18:10:35	858537,15	132240,19	858427,00	132365,00	0,51
2017-02-11T03:58:35	858457,85	132217,10	858277,00	132815,00	0,47
2017-02-13T21:57:31	859130,39	132483,38	859127,00	132465,00	0,48
2017-02-14T14:32:40	858457,85	132217,10	858727,00	132365,00	0,72
2017-02-15T03:26:00	858537,15	132240,19	858377,00	132565,00	0,58
2017-02-15T06:38:55	858847,36	132012,09	858927,00	132165,00	0,26
2017-02-15T10:57:29	858516,16	132259,39	858577,00	132465,00	0,03
2017-02-17T10:37:03	858557,38	132240,97	858427,00	132715,00	0,07
2017-02-17T14:25:33	858580,70	132161,83	858627,00	132165,00	1,02
2017-02-17T14:25:40	858580,70	132161,83	858627,00	132165,00	0,70
2017-02-17T14:25:52	858602,44	132102,64	858627,00	132165,00	0,36
2017-02-17T14:29:31	858642,88	132104,21	858727,00	132215,00	0,58
2017-02-17T14:30:59	858457,85	132217,10	858627,00	132365,00	0,29
2017-02-17T14:56:36	858457,85	132217,10	858827,00	132665,00	0,22
2017-02-17T15:56:06	858537,15	132240,19	858277,00	132665,00	0,42
2017-02-17T16:45:07	858481,95	132117,97	858477,00	132415,00	0,47
2017-02-18T14:11:19	858744,73	132068,14	858727,00	132065,00	0,34
2017-02-18T16:10:28	858350,58	132393,05	858377,00	132665,00	0,03
2017-02-18T20:11:31	858457,85	132217,10	858527,00	132515,00	0,10
2017-03-07T11:15:02	858398,00	132214,78	858777,00	132465,00	0,34
2017-03-08T12:45:33	858618,01	132223,31	858627,00	132465,00	0,21
2017-03-08T15:04:55	858659,22	132204,90	858477,00	132165,00	0,24
2017-03-09T01:05:21	858617,23	132243,30	858177,00	132515,00	0,54
2017-03-09T03:24:46	858499,07	132198,69	858477,00	132565,00	0,56
2017-03-09T04:11:05	858639,78	132184,14	858727,00	132165,00	0,88
2017-03-09T04:58:35	858700,41	132166,48	858877,00	132215,00	0,12
2017-03-09T05:01:37	858681,77	132145,74	858627,00	132115,00	0,87
2017-03-09T05:02:23	858458,63	132197,12	858727,00	132315,00	0,62
2017-03-09T05:07:14	858458,63	132197,12	858727,00	132215,00	0,85
2017-03-09T05:07:35	858520,03	132159,47	858777,00	132215,00	0,24
2017-03-09T05:08:20	858660,00	132184,92	858777,00	132415,00	1,03
2017-03-09T05:10:42	858479,63	132177,92	858727,00	132465,00	0,38
2017-03-09T05:11:24	858562,03	132121,08	858327,00	132415,00	0,91
2017-03-09T05:11:30	858498,30	132218,67	858427,00	132465,00	0,81
2017-03-09T05:12:39	858500,62	132158,72	858377,00	132565,00	0,30
2017-03-09T05:14:06	858500,62	132158,72	858727,00	132365,00	0,46
2017-03-09T05:16:15	858479,63	132177,92	858227,00	132865,00	0,11
2017-03-09T05:39:48	858722,18	132127,30	858777,00	132265,00	0,78
2017-03-09T05:49:38	858659,22	132204,90	858527,00	132565,00	0,34
2017-03-09T06:09:36	858643,66	132084,22	858627,00	132065,00	0,06
2017-03-09T06:49:58	858663,10	132104,99	858527,00	132165,00	0,02
2017-03-09T07:02:28	858459,40	132177,13	857877,00	132615,00	0,28
2017-03-09T07:22:03	858682,55	132125,76	858777,00	132115,00	0,08
2017-03-09T08:39:52	858643,66	132084,22	858677,00	132165,00	0,54
2017-03-09T09:11:53	858499,85	132178,70	858727,00	132215,00	0,19
2017-03-09T10:39:18	858721,41	132147,28	858727,00	132215,00	0,33

2017-03-09T10:57:26	858745,51	132048,16	858777,00	132115,00	0,29
2017-03-09T11:00:21	858642,88	132104,21	858777,00	132215,00	0,40
2017-03-09T11:46:38	858643,66	132084,22	858277,00	132215,00	0,37
2017-03-09T11:50:13	858722,18	132127,30	858577,00	132165,00	0,03
2017-03-09T14:52:15	858704,29	132066,57	858577,00	132115,00	0,70
2017-03-09T14:53:10	858722,18	132127,30	858827,00	132465,00	0,15
2017-03-09T15:01:10	858745,51	132048,16	858627,00	132115,00	0,01
2017-03-09T15:01:58	858701,96	132126,51	858777,00	132215,00	0,45
2017-03-09T15:02:20	858683,33	132105,78	858727,00	132265,00	0,49
2017-03-09T15:03:50	858701,19	132146,50	857977,00	132565,00	0,89
2017-03-09T15:04:51	858684,88	132065,81	858727,00	132515,00	0,80
2017-03-09T15:06:08	858643,66	132084,22	858527,00	132065,00	0,01
2017-03-09T15:08:05	858681,00	132165,72	858827,00	132515,00	1,11
2017-03-09T15:08:10	858427,55	132476,08	858977,00	132015,00	1,35
2017-03-09T15:08:19	858583,03	132101,88	858677,00	132715,00	0,10
2017-03-09T16:22:49	858745,51	132048,16	858727,00	132215,00	0,45
2017-03-09T16:27:30	858764,96	132068,92	858727,00	132215,00	0,02
2017-03-09T16:38:00	858746,29	132028,17	858877,00	132215,00	0,65
2017-03-09T18:02:51	858500,62	132158,72	857927,00	132615,00	0,39
2017-03-09T18:19:52	858825,59	132051,27	858827,00	132115,00	0,16
2017-03-10T13:40:11	858718,30	132227,21	857977,00	132315,00	0,10
2017-03-10T20:22:31	858846,59	132032,07	858927,00	132165,00	0,41
2017-03-12T00:06:04	858807,70	131990,53	858927,00	132165,00	0,06
2017-03-12T03:18:56	858328,74	131911,91	857627,00	131965,00	0,31
2017-03-15T01:47:51	858458,63	132197,12	858027,00	132515,00	0,46
2017-03-15T07:04:10	858884,70	132093,59	858927,00	132215,00	0,05
2017-03-16T11:45:47	858866,03	132052,84	858877,00	132215,00	0,01
2017-03-22T11:42:08	858451,59	131856,63	857827,00	131615,00	0,02
2017-03-24T04:23:39	858806,14	132030,50	858727,00	132165,00	0,43
2017-03-25T20:51:08	858927,42	131494,88	858627,00	131065,00	0,14
2017-03-28T11:44:12	859248,57	132548,01	859377,00	132465,00	0,43
2017-03-29T08:14:57	858785,18	132069,71	858727,00	132115,00	0,27
2017-03-30T07:42:43	858743,18	132108,10	858727,00	132015,00	0,24
2017-04-02T03:20:59	859003,62	131597,90	858877,00	130615,00	0,04
2017-04-07T23:07:24	858444,61	132036,47	858277,00	132565,00	0,31
2017-04-13T16:19:10	858624,21	132063,46	858777,00	132165,00	0,45
2017-04-20T15:20:02	858929,00	131975,24	858927,00	132065,00	0,08
2017-04-24T00:53:47	858329,51	131891,92	857777,00	131865,00	0,42
2017-04-25T18:04:23	858429,81	131895,81	857877,00	131915,00	0,89
2017-04-26T03:36:34	858146,80	131944,88	857977,00	131765,00	0,88
2017-04-26T03:45:33	858226,11	131967,96	857527,00	131715,00	0,10
2017-04-26T05:40:38	858246,33	131968,75	857577,00	131715,00	0,38
2017-04-27T16:02:51	859190,24	132485,71	859327,00	132415,00	0,31
2017-05-02T02:17:19	858826,37	132031,28	859027,00	132415,00	0,97
2017-05-03T16:17:07	859082,16	132161,30	859177,00	132165,00	0,46
2017-05-05T23:27:12	858612,57	132363,19	858477,00	132665,00	0,40
2017-05-06T13:57:15	858827,14	132011,30	859027,00	132465,00	0,64
2017-05-08T07:21:49	858825,59	132051,27	858877,00	132115,00	0,37
2017-05-09T19:10:55	858762,63	132128,87	858877,00	132215,00	0,09
2017-05-14T23:47:49	859235,35	132367,39	859327,00	132265,00	0,61

2017-05-19T04:14:55	858952,33	131896,09	859077,00	131965,00	0,07
2017-05-21T12:06:21	858686,43	132025,85	858777,00	132065,00	0,32
2017-05-23T02:44:32	858350,51	131872,73	857377,00	131715,00	0,14
2017-05-31T09:27:27	858327,19	131951,87	857877,00	131965,00	0,20
2017-05-31T11:47:58	859279,65	132249,04	859277,00	132315,00	0,53
2017-06-01T13:05:10	859085,28	132601,70	859077,00	132515,00	0,28
2017-06-05T20:40:31	859091,50	132441,84	859127,00	132315,00	0,66
2017-06-13T11:20:49	859075,20	132361,16	859127,00	132215,00	0,00
2017-06-19T03:45:34	859663,81	130622,98	860277,00	131115,00	0,25
2017-06-21T04:35:14	859087,59	131501,11	859177,00	131165,00	0,54
2017-06-27T23:29:51	859051,87	132440,30	859277,00	132265,00	0,15
2017-06-30T18:29:39	859166,14	131043,88	858127,00	130865,00	0,09
2017-07-03T00:18:04	859207,35	132566,42	859277,00	132415,00	0,75
2017-07-14T04:54:53	858558,10	131700,67	857527,00	131015,00	1,03
2017-07-14T22:02:11	858431,36	131855,85	857677,00	132065,00	0,35
2017-08-16T06:19:14	858986,56	133078,15	859177,00	132765,00	0,07
2017-08-22T01:27:07	858967,93	133057,42	859127,00	132765,00	1,31
2017-08-22T01:27:18	859044,11	133160,44	858977,00	133015,00	0,01
2017-08-22T01:27:29	858882,42	133194,18	859127,00	132615,00	0,30
2017-08-22T04:16:55	858995,89	132838,37	859227,00	132715,00	0,02
2017-08-22T09:52:42	859075,97	132341,17	859227,00	132415,00	0,02
2017-08-22T10:56:59	858985,78	133098,14	859177,00	133015,00	0,08
2017-08-22T10:57:52	858965,60	133117,36	859177,00	132915,00	0,17
2017-08-22T12:09:18	858845,09	133112,68	859277,00	132715,00	0,87
2017-08-22T17:12:17	858801,55	133191,03	859177,00	132765,00	0,07
2017-08-22T18:26:12	858781,36	133210,26	859077,00	132915,00	0,24
2017-08-22T20:39:52	858785,25	133110,35	859027,00	132765,00	0,24
2017-08-22T22:04:22	858869,97	132993,57	859127,00	132815,00	0,09
2017-08-22T23:33:00	858780,59	133230,24	859077,00	133015,00	0,41
2017-08-23T01:52:41	858788,35	133030,42	859177,00	132765,00	0,02
2017-08-23T02:38:15	858869,97	132993,57	859027,00	132965,00	0,59
2017-08-23T02:38:22	858771,98	132409,41	859027,00	132815,00	0,94
2017-08-23T02:40:03	858789,10	132990,43	859127,00	132815,00	0,55
2017-08-23T02:44:23	858995,89	132838,37	859127,00	132765,00	0,27
2017-08-23T02:57:04	858853,64	132892,87	858927,00	132815,00	0,27
2017-08-23T08:56:26	858737,01	132788,28	858977,00	132715,00	0,26
2017-08-23T09:08:08	858817,86	132771,41	859027,00	132715,00	0,09
2017-08-23T09:08:45	858730,02	132968,12	858977,00	132765,00	0,49
2017-08-23T09:15:25	858735,46	132828,25	858977,00	132765,00	0,45
2017-08-23T09:15:35	858737,01	132788,28	859027,00	132715,00	0,63
2017-08-23T09:37:22	858649,18	132984,99	859077,00	132815,00	0,08
2017-08-23T09:53:56	858751,02	132948,92	859127,00	132765,00	0,87
2017-08-23T09:54:07	858528,68	132980,31	858927,00	132465,00	0,20
2017-08-23T10:53:00	858785,25	133110,35	859127,00	132765,00	0,32
2017-08-23T16:29:08	858869,97	132993,57	859227,00	132865,00	0,05
2017-08-23T18:14:32	858837,98	131211,23	858777,00	130915,00	0,30
2017-08-23T20:56:40	858740,12	132708,35	858977,00	132665,00	0,32
2017-08-24T09:44:20	858897,93	132774,52	859127,00	132765,00	0,03
2017-08-26T13:27:05	858789,10	132490,12	858977,00	132765,00	0,18
2017-08-26T20:59:00	859075,20	132361,16	859277,00	132265,00	0,34

2017-08-27T09:48:31	858694,24	132846,66	859027,00	132765,00	0,34
2017-08-28T02:32:09	858674,06	132865,88	858927,00	132615,00	0,02
2017-08-28T07:03:57	858467,93	131957,33	858127,00	132715,00	0,41
2017-08-28T14:33:30	859196,46	132325,85	859277,00	132315,00	0,48
2017-09-01T12:30:00	858558,10	131700,67	858127,00	131015,00	0,01
2017-09-06T08:15:33	858411,92	131835,08	858027,00	131965,00	0,15
2017-09-08T19:34:35	858392,50	131834,33	857527,00	131715,00	0,80
2017-09-08T19:34:51	858516,10	131739,06	857627,00	131615,00	0,16
2017-09-08T19:44:41	858434,47	131775,92	857577,00	131465,00	0,54
2017-09-08T19:55:17	858373,83	131793,58	857627,00	132015,00	0,07
2017-09-08T20:28:35	858091,59	131822,66	857377,00	131415,00	0,01
2017-09-08T22:02:10	858534,77	131779,81	858027,00	131715,00	0,40
2017-09-08T22:18:26	858472,58	131837,44	857927,00	131515,00	0,13
2017-09-10T16:02:43	858431,36	131855,85	857977,00	131865,00	0,35
2017-09-13T21:44:25	858063,63	132021,70	857427,00	131665,00	0,00
2017-09-14T00:12:44	858536,32	131739,85	858727,00	131815,00	0,02
2017-09-21T17:05:53	858450,04	131896,60	857727,00	131315,00	0,20
2017-09-21T19:22:06	858866,03	132052,84	858927,00	132115,00	0,30
2017-10-01T21:59:36	858063,63	132021,70	857377,00	132665,00	0,30
2017-10-02T17:33:52	858572,89	131841,33	858427,00	131765,00	0,58
2017-10-08T09:08:00	859231,46	132987,62	859077,00	132365,00	0,81
2017-10-08T14:32:00	857350,60	131773,98	857177,00	131515,00	0,76
2017-10-08T16:30:56	858430,59	131875,83	857127,00	131565,00	0,13
2017-10-08T17:08:17	858431,36	131855,85	857577,00	132115,00	0,29
2017-10-08T19:46:38	858431,36	131855,85	857077,00	132215,00	0,52
2017-10-09T00:13:52	858431,36	131855,85	857827,00	132015,00	0,07
2017-10-18T15:15:55	858853,64	132892,87	859277,00	132615,00	0,10
2017-10-30T00:28:04	858562,80	132101,10	857827,00	132465,00	0,40
2017-11-04T08:33:49	859068,17	131500,35	859277,00	130665,00	0,75
2017-11-07T08:38:12	858541,81	132120,29	858277,00	132915,00	0,10
2017-11-07T20:31:50	859275,76	132348,95	859377,00	132415,00	0,11
2017-11-09T02:19:10	858969,44	131976,81	859077,00	132165,00	0,27
2017-11-13T05:55:43	858995,89	132838,37	859127,00	132965,00	0,00
2017-11-18T02:10:07	859320,87	132230,63	859427,00	132415,00	0,04
2017-12-03T04:21:10	859379,17	132272,92	859227,00	132165,00	0,32
2017-12-04T22:59:31	859511,32	133018,53	859077,00	132315,00	0,46

Annex Part III

Fitting the model of K-means algorithm to data catalogue 2014-2017

To apply the K-means algorithm to a dataset of A and B class events, Scikit-learn, a free software machine learning library for the Python programming language was implemented within the analysis code.

To find the best K value (which corresponds to the number of centroids and number of clusters), the Elbow method was applied first. It consists of fitting the model with to range of the potential number of clusters K and calculating the WCSS (Within-Cluster Sum of Square, the sum of squared distance between each point and the centroid in a cluster) for each. As the number of clusters increases, the WCSS value decreases. The point of the inflexion on the curve presents the point that best fits the model (used dataset). As shown in Figure A3. 1, and in correspondence to what can be easily observed "by eye" in Figure 6.2, the number of cluster K was estimated as 6. K-means algorithm is then applied to class A events, and B – class events are assigned to the same clusters based on the minimal distance to determined cluster centroids.

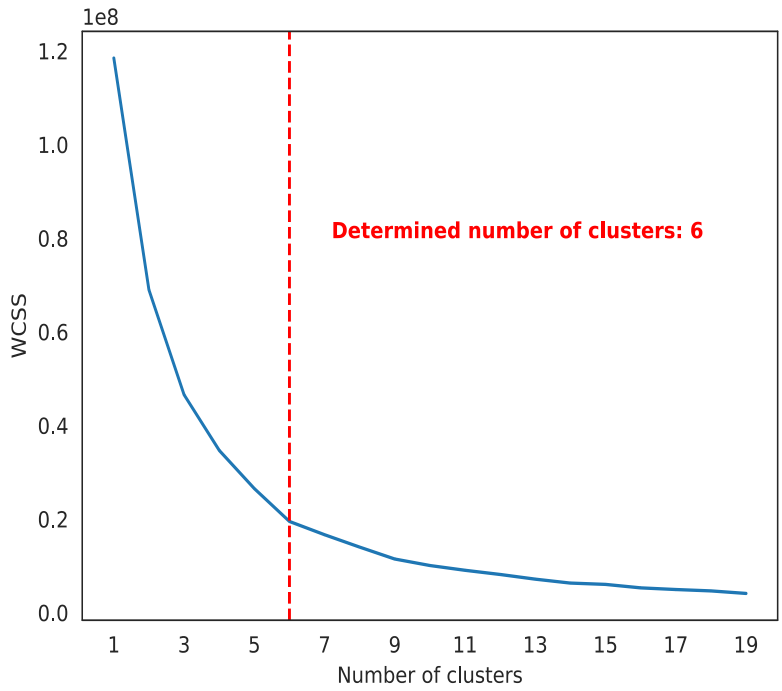

Figure A3. 1 Elbow method used to determine the optimal number of clusters (k). The procedure described in the text.

Influence of station configuration changes on the location of events and apparent migration of seismicity

Monitoring network configuration could potentially have biasing effect in locating of an event. Due to station changes in time during the observed period (timeline of changes shown in Figure A1. 2) it is necessary to examine its influence on apparent spatio-temporal migration of seismicity between two seismic crises (Figure A3. 2).

As it is not possible to conduct a test by determining the location of one event in the different configuration settings, we examine the influence of station configuration change on event locations by focusing on seismic clouds locations of A class events during three periods of seismic crises, in between which the station configuration had changes in settings.

First, we focus on a seismic crisis from late 2016 until March 2017. Within this period, the station configuration had a major change prior to the seismic activity in March, as station S4 was removed and two new stations (S6 and S7) were installed. Therefore, we separately observe the seismic cloud locations during one configuration setting (November 2016 – February 2017) and during a new configuration (March 2017). As we can observe in Figure A3. 2, the location of the events during the entire crisis period does not change albeit the station configuration changes, there is no migration of seismicity. Hence, we conclude that this configuration change did not have any effect on determining of location of seismic events.

However, migration is noticeable between the crisis of December 2014 and the crisis of November 2016-March 2017. To analyse the influence of the station configuration on this migration, we observe that the configuration of the crisis of December 2014 has almost the same station configuration as the first part of the observed crisis of November 2016 - February 2017, as the only change is the station transfer from S2 to S5 location.

Based on these observations, we conclude that station configuration changes do not have any meaningful influence on the location of events of class A and that migration of seismic cloud between two crises is not an artefact due to the change of station configuration.

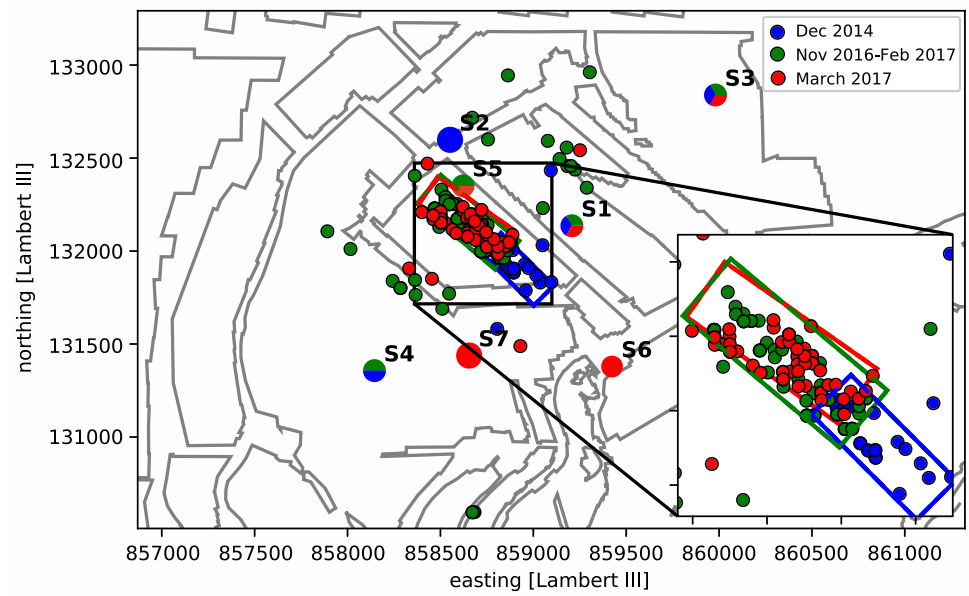

Figure A3. 2 Station configuration change during periods of three seismic crises and its influence on spatio-temporal migration of seismic cloud in the active area. Colours of seismic events, seismic stations and seismic cloud boundaries are corresponding to colours of observed periods shown in the label. Monitoring stations are marked with the name of stations and slightly bigger circles than seismic events, coloured with 1 to 3 colours indicating their active period(s). Seismic clouds areas are bounded with rectangles corresponding to their approximate area.

Finding the optimal value of the cross-correlation function

To determine the optimal value of the CC threshold to create doublets and families, a wide range of thresholds was tested. This criteria is very important as very high values indicate only tightly spaced events while too low CC threshold value groups events almost randomly (Cattaneo *et al.* 1999). The optimal value is found in the transition zone between the two, following the principle of (Aster & Scott 1993). As it can be observed in Figure A3. 3 , a high threshold results in a small number of grouped events and a small number of groups (e.g. for $CC = 0.9$ with only 151 events grouped, in 52 groups). As the threshold is lowered, the number of grouped events rises (e.g. $CC = 0.8$ with 388 events in 96 groups) but lowering the threshold further results in lowering of the number of groups, as they start merging and converge to one since group. The determined optimal range of CC values is between 0.7 and 0.9. The chosen threshold was set to $CC = 0.75$ (470 events grouped in 100 groups).

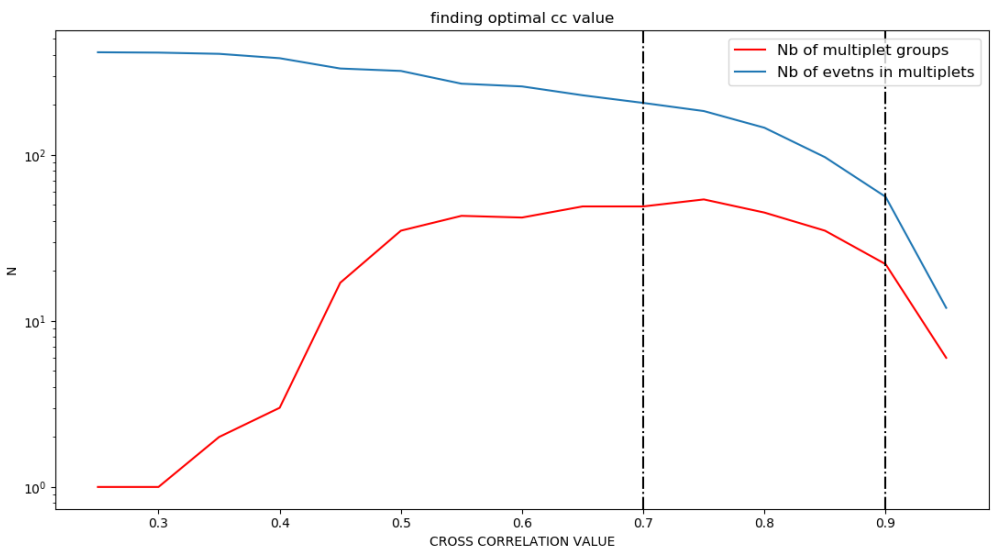

Figure A3. 3 Finding optimal cross-correlation value. The number of multiplet groups and a total number of events depending on the $\boldsymbol{CC}$ value.

Corner frequency estimation for families

Corner frequencies and moment magnitudes were estimated following the methodology proposed by Kinscher 2015. The approach is based on Brune's model (Brune 1970), implemented in the SYTMIS software.

The approach is based on the determination of the source parameters: moment magnitude M_W and corner frequency F_C , by minimizing the misfit between observed spectra and theoretic spectra of Brune's model (Brune, 1970). To find the best fitting set of parameters (M_W, F_C and quality factor Q) within the predetermined range, the grid search technique was applied, considering a weighting function based on the gap between signal and noise spectra.

Moment magnitude M_W variation range needed was set between -3 and 1 while the corner frequency range has been set between 1 and 100Hz, and the quality factor was set between 10 to 200.

Rather than obtaining an absolute measure of individual source spectra, we obtain relative shapes of spectra with respect to other earthquakes. We then stack the spectra in bins of the similar moment to obtain average spectra.

Rather than obtaining the values of parameters of individual source spectra of all events, here the shapes of spectra were determined with respect to all earthquakes within each family. The observed spectral curve of the S waves was created as stacking of spectral curves of all events within each of the 21 main families, assuming the waveforms similarity imply similarity of the shapes of the source spectra themselves. Only the waveforms recorded on station S1 were used.

Moment magnitude and corner frequency estimation for 21 families are shown in Figure A3. 4. Estimated corner frequency values range from 15 Hz to 73 Hz, while M_W ranges from -0.1 to 0.54.

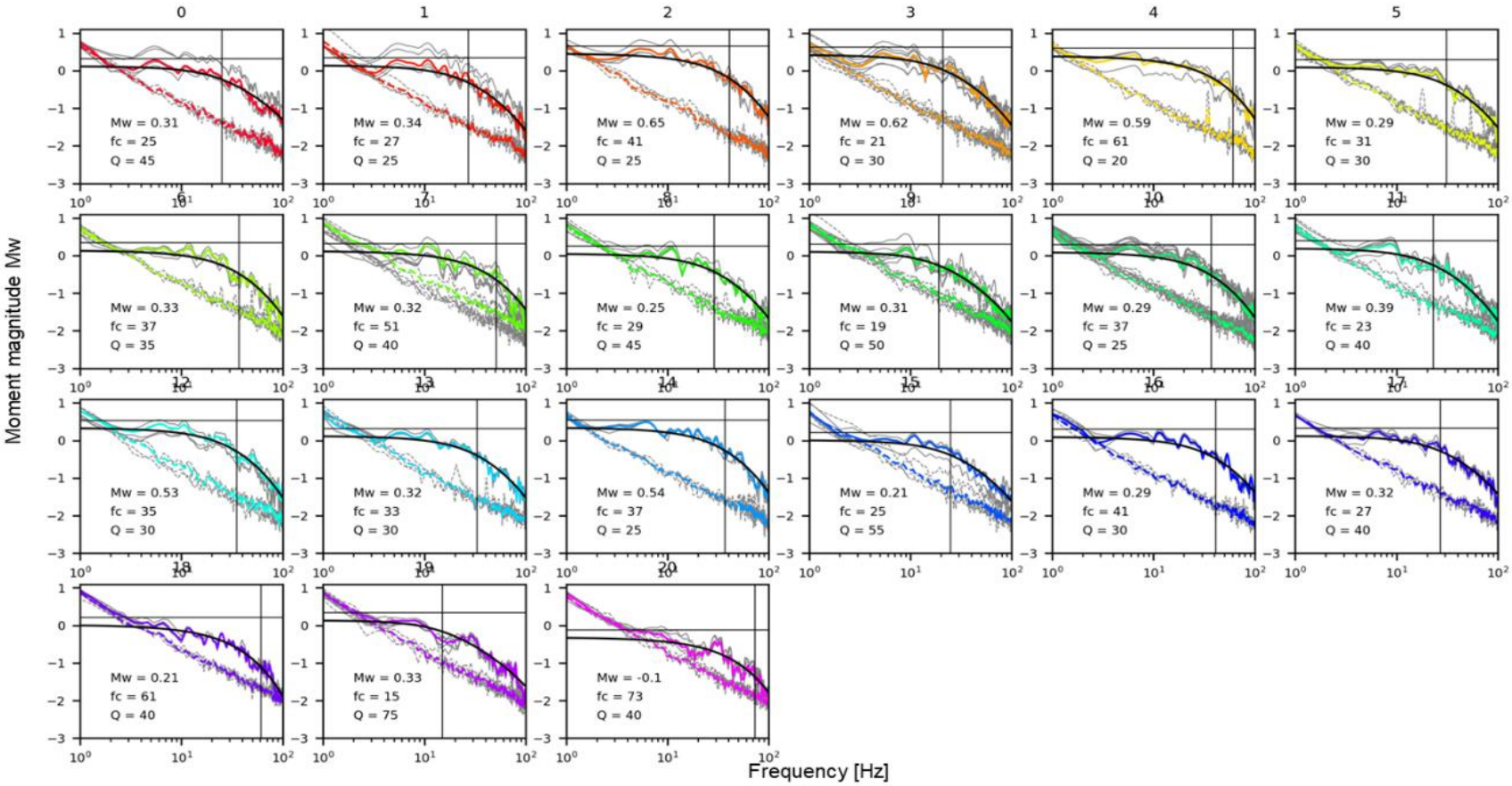

Figure A3. 4 Corner frequency and moment magnitude estimation for 21 main families. Coloured lines present observed stacked moment magnitude source spectra of all events within family, for seismic signal and background noise, respectively. Black curve represents the fitting of Brune's model synthetic spectra on the data. Grey lines indicate estimations of moment magnitude and corner frequency

Annex Part IV

Source mechanism

Seismic analysis done as complementary to the thesis (Kinscher *et al.* 2021) evaluated the source mechanism using 3 approaches:

I) Analysis of the direction of first motion (or polarity) of P waves on each station;

II) P and S wave amplitude ratio analysis;

III) Full waveform moment tensor inversion method.

Data used were fourteen strong events recorded during 2019/2020 chosen for analysis, located within clusters of new catalogues 2014-2017, as can be seen on Figure 14.1.

Analysis of the direction of first motion (or polarity) of P waves on each station

As described in section 14.2, dominance of P waves negative polarities (Figure A4. 1) could be explained as the effect of a low-velocity layer. Modelling with synthetic seismograms showed that this can be an effect of the mine layer and/or fluid in rock, which can result in changing of the wave polarity.

The Figure A4. 2 shows the influence of the work layer on the polarities of P waves based on a synthetic seismogram approach. To test the influence of the mining layer, the waveforms for a homogeneous velocity model (Figure A4. 2 c, without works) was compared with a model composed by a low velocity layer at the depth of the mining works (Figure A4. 2 c, with mining works). The normal fault mechanism (Figure A4. 2 a) was used at several different hypocenters. As the results, a clear conversion of positive polarities (visible in homogeneous models) into negative ones with the low velocity layer model can be observed, documenting its strong influence on wave propagation.

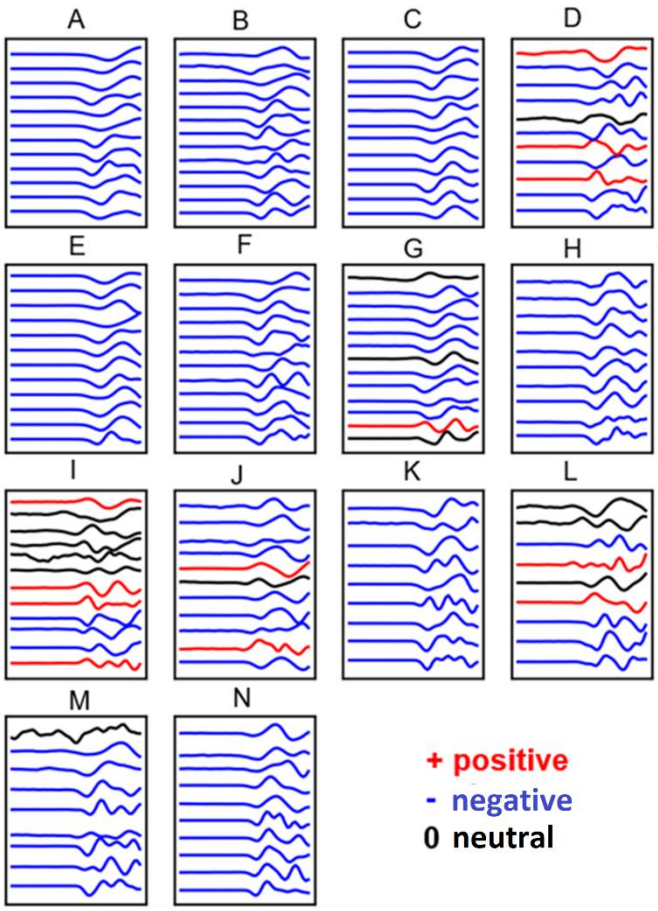

Figure A4. 1 Dominance of negative P waves polarities on the waveforms of 14 events (Kinscher *et al*. 2021)

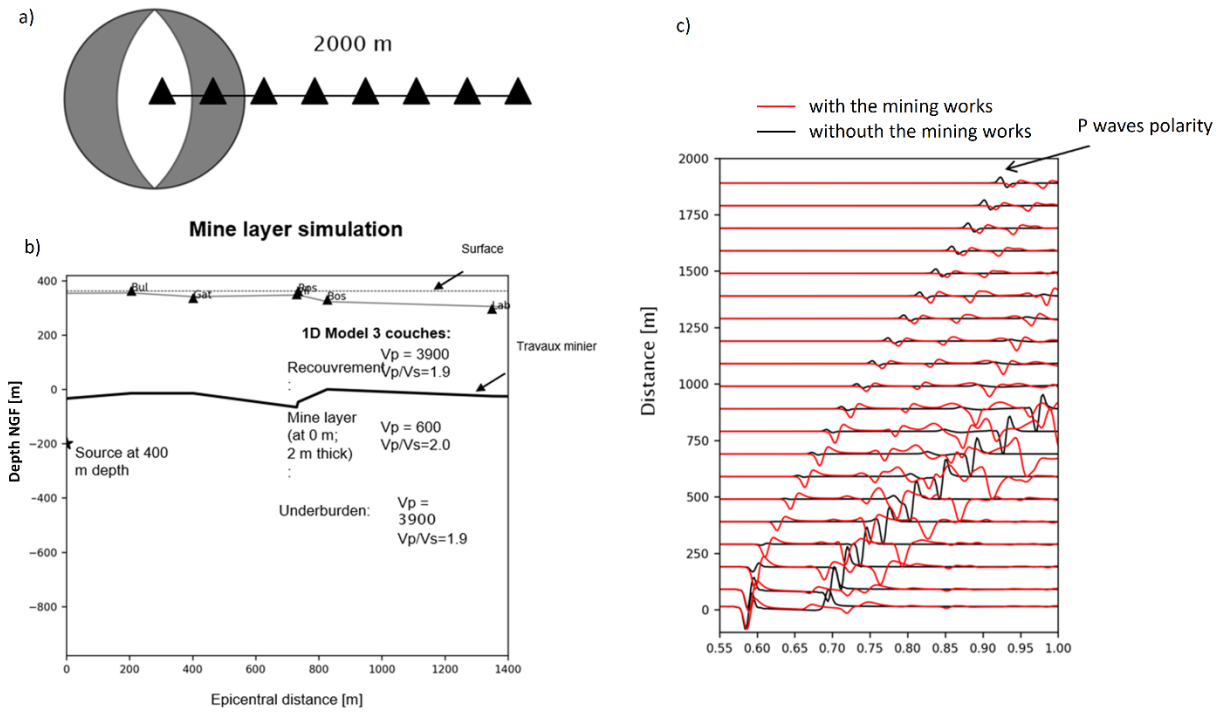

Figure A4. 2 Simulation of direction of first motion (or polarity) of P waves. a) The normal fault mechanism used at several different hypocenters, b) model composed by a low velocity layer at the depth of the mining works, c) conversion of the positive polarities (visible in homogeneous models) into negative ones in the model with the low velocity layer (Kinscher *et al*. 2021).

P and S wave amplitude ratio analysis

As described in section 14.2, an analysis of the S (SH, horizontaly polarized) and P wave ratios, was performed. Their ratios are estimated in terms of radiated seismic energy.

While the mechanism associated with a collapse (eg., pillar collapse, roof fall etc.), is a priori characterized by a dominance of P and SV waves (compared to SH waves), which results from the significant presence of tensile and compressive failure modes characteristic of an implosion (McGarr 1992a, Šílený & Milev 2008), the dominance of SH waves is a strong indication of the presence of a shear mechanism.

The obtained results show that the S/P ratios (Figure A4. 3) seem much less consistent with a tensile failure mode that is expected in the mine collapse model, however it appears to be in good agreement with a shear model. The dominance of the SH energy content (compared to P and SV) that has been observed in previous study (Kinscher *et al.* 2017) has been confirement here as well.

Addtionally, observed S/P ratios appear more compatible with a normal fault while the SH/P ratios are more related to the movement of a vertical and stalling fault. The mechanisms of the events therefore represent possibility of three types of faults, with a rake angle corresponding to a oblique slip.

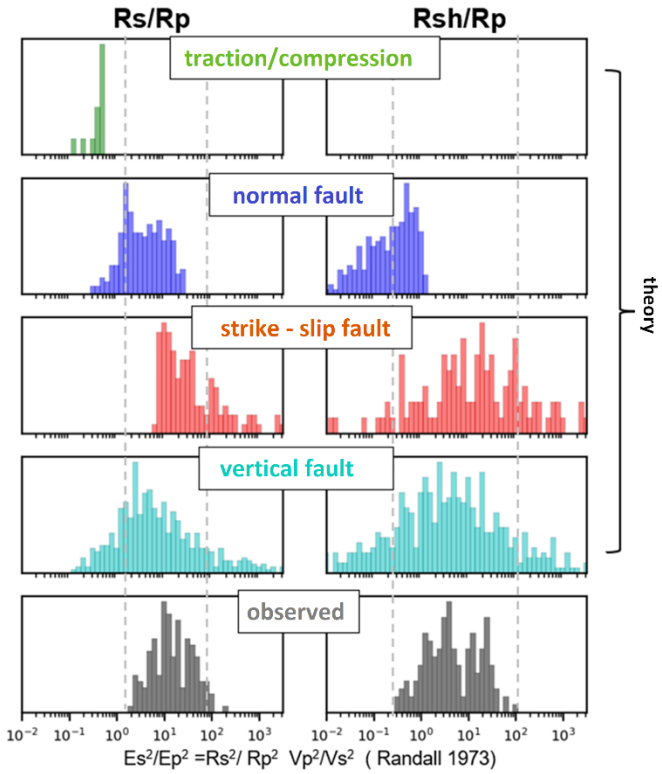

Figure A4. 3 Theoretical and observed S/P waves ratio values (Kinscher *et al*. 2021) .

Waveform based inversion

As described in section 14.2, results from waveform-based inversion were not satisfactory. The focal mechanisms are estimated quantitatively by the complete inversion of the wavefield by minimizing the differences between the observed and theoretical seismograms, for the 14 events and the three components (Z = vertical, R = radial, T = Transversal) of each available station.

The inversion is based on the theoretical DC source model (shear mechanism), which was indicated by the amplitude ratios, which allows to determine the orientation of a fault plane (azimuth and dip) and its direction of slip (rake) along this plane. The propagation model for the calculation of theoretical seismograms (Green function) is based on the AXITRA approach of (Coutant 1990), using the single-layer velocity model (1D) and the locations (in particular the depths as described in section 14.2). To minimize the propagation effects unexplained by this simplified model, the inversion was performed in a low frequency range, between 3 and 7 Hz, which was the best compromise in terms of signal-to-noise ratio and validity of the far-field approximation.

The results of the inversions are presented in Figure A4. 4, which shows a dominance of the strike-slip and normal fault mechanisms, with a dominance of vertical planes (> 70 °). As it can be observed, the stability

of the inversion (as well as the coherence between observed waveforms and theoretical on all the events) is not satisfactory, therefore the quality of the inversion results is poor.

The misfit, which reflects the difference between observed and theoretical seismograms in terms of L2 type standard, is quite high. Even when the signal-to-noise ratio is good on all the recordings, the best results of the inversion are either average quality (misfit <0.5), and very bad for the results of low quality (misfit> 1). A very good result would be for a misfit <0.1.

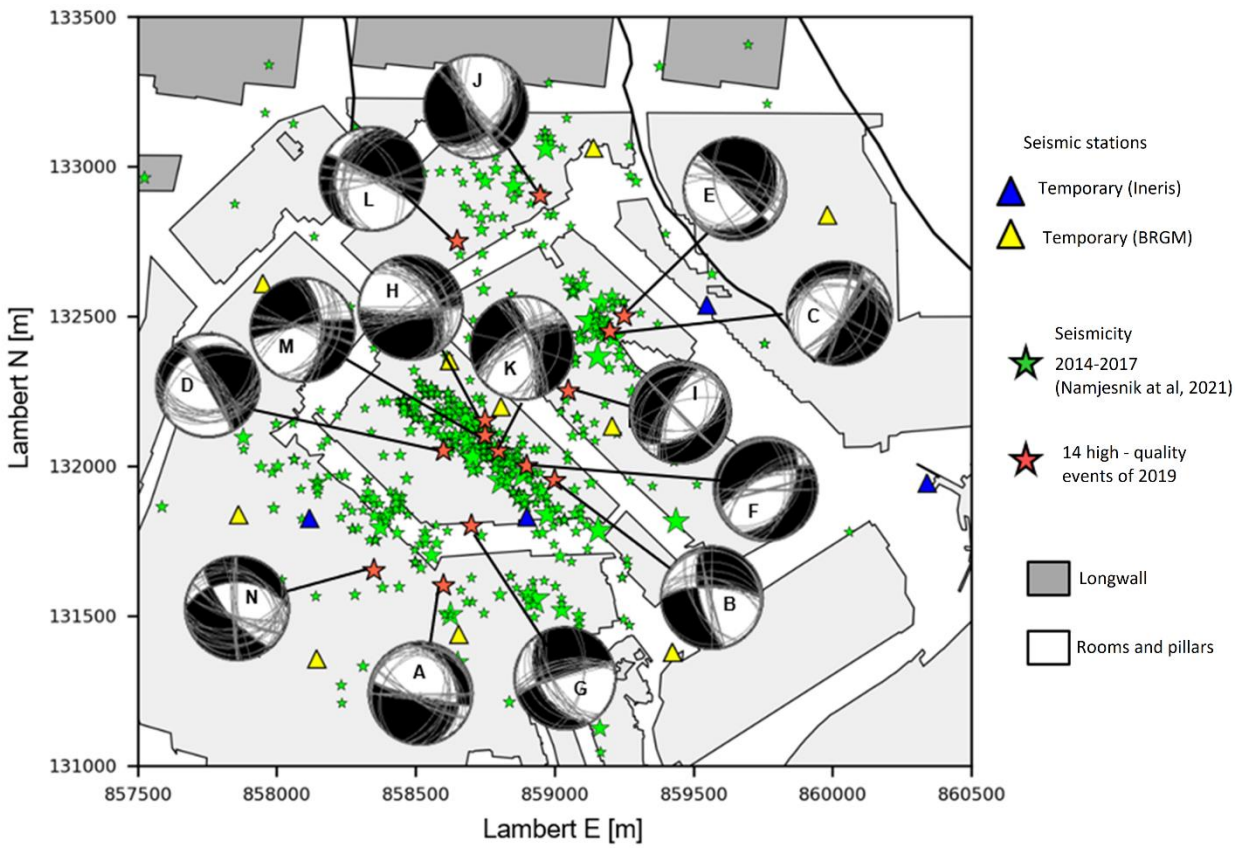

Figure A4. 4 Results of focal mechanisms for the 14 high quality events of 2019, presented in the form of a beachball, as well as the 25 best solutions obtained by inversion (gray circles within the beachballs) (Kinscher *et al*. 2021) .

Résumé

Origine de la sismicité observée dans le bassin houiller abandonné de Gardanne et son lien avec l'ennoyage des travaux miniers

La fermeture des mines et la gestion post-minière constituent aujourd'hui un défi majeur car les problèmes engendrés peuvent impacter grandement la sécurité publique. Lorsque les mines sont abandonnées, les systèmes de pompage des eaux souterraines sont généralement arrêtés et l'eau qui remplit progressivement les vides peut affecter la stabilité mécanique des structures souterraines. En général, les mécanismes de la sismicité observée dans les districts post-miniers inondés sont mal compris. Cette thèse porte sur l'étude de la sismicité enregistrée à la suite de l'ennoyage de l'ancien bassin houiller de Gardanne, en Provence, fermée en 2003, qui connaît des problèmes importants de sismicité post-minière. La distribution spatio-temporelle des événements sismiques suggère un lien avec les épisodes de précipitations intenses ainsi qu'avec le pompage actif. La connaissance de l'origine et des mécanismes de déclenchement de l'activité sismique est la clé pour l'évaluation des risques sismiques de l'ensemble du bassin de Gardanne. Les travaux de thèse ont porté sur des questions liées à l'identification précise de l'origine de la source sismique en évaluant deux hypothèses, à la détermination du mécanisme derrière la sismicité, et le lien entre la sismicité et le système hydrogéologique, et en améliorant la détection et la localisation de la microsismicité avec un réseau clairsemé. La nouvelle méthodologie de détection et de localisation développée adapte la méthode BTBB (Poiata) basée sur la forme d'onde complète en surmontant les défis du réseau de surveillance sismique clairsemé, et inclut une nouvelle approche d'élimination du bruit de l'ensemble des données continues ainsi qu'un système de classification basé sur la qualité de la localisation. Un comportement sismique sous forme de clusters a été mis en évidence par le nouveau catalogue sismique 2014-2017, qui a ensuite fait l'objet d'une analyse plus approfondie. L'ensemble des résultats sont en faveur de l'origine des sources sismiques sur la faille en dessous de la mine. Les caractéristiques spatio-temporelles des événements sismiques et les occurrences de multiplets/répéteurs ont fourni une image plus claire des structures géologiques actives et ont permis une interprétation préliminaire des mécanismes de déclenchement possible, basée sur la comparaison avec les données hydrologiques. Malgré la compréhension générale du mécanisme de la sismicité, la magnitude maximale des événements qui peuvent être déclenchés est actuellement difficile à quantifier et à prévoir en raison des limites des données disponibles. En tant que perspective et dans le but de mieux comprendre le risque sismique, des observations plus précises de la sismicité, des paramètres mécaniques et des changements de niveau d'eau dans la zone sismique active sont nécessaires pour améliorer la compréhension de ces facteurs et de leur interconnexion.

Les mots-clefs: après mine, mine abandonnée et ennoyée, microsismicité induite, origine de la sismicité, détection et localisation, multiplets et répéteurs, mécanisme de déclenchement

Abstract

Origin of seismicity related to a flooded abandoned coal mining district at Gardanne, Provence, France

The closure of mines and post-mining management nowadays present a major challenge as the problems that arise can greatly concern public security. When mines are abandoned, groundwater pumping systems are usually stopped and the water which progressively fills the remaining voids can affect the mechanical stability of underground structures. In general, mechanisms of observed seismicity in flooded, post-mining districts have been poorly understood. As a case study, this thesis focused on the abandoned, flooded coal mine in Gardanne, France, which has been experiencing significant post-mining seismicity problems. Seismic activity in Gardanne mine seems to originate from an interaction between rocks and fluids, as spatio-temporal distribution of events suggests the link with intense rainfall events as well as the active pumping. The knowledge on the origin and the triggering mechanisms of the seismic activity in Gréasque and Regagnas sector is the key for seismic hazard assessment of the entire Gardanne basin. Thesis work focused on questions concerning precise identification of seismic source origin evaluating two hypothesis, determination of the mechanism behind the seismicity, link between seismicity and the hydrogeological system, as well as improving of the detection and location of microseismicity with a sparse network. The new developed detection and location methodology adapts the full waveform-based method BTBB by Poiata by overcoming the challenges of the sparse seismic monitoring network, and includes a novel approach for noise removal from continuous dataset as well as location quality-based classification system. The seismicity clustering behaviour was indicated by the new seismic catalogue 2014-2017, which was further analysed more thoroughly. All results are in favour of the origin of the seismic sources on the fault below the mine. Spatial and temporal characteristics of observed seismic events and multiplet and repeater occurrences provided a clearer image of the active geological structures and allowed a preliminary interpretation of possible mechanisms affecting the initiation and driving of the repeating or after-shock like behavior of seismic events, based on comparison with available hydrological data. Despite the general understanding of the mechanism behind the seismicity, the maximum magnitude of the events that can be triggered is at this moment is difficult to quantify and predict due to limitations of available data. As a prospective, in order to better understand the seismic hazard, more accurate observations of the seismicity, mechanical parameters and water level changes in the seismically active zone are required to improve the understanding and the interconnection between these factors.

Key words: post-mining, abandoned and flooded mine, induced microseismicity, origin of seismicity, detection and location, multiplets and repeats, seismicity triggering mechanism